Fully Relaxed Heavy Ion Reactions in the Mass 80 Region



Philip Mark Evans
The Queen's College

A thesis submitted in partial fulfilment of the requirements
for the degree of Doctor of Philosophy
in the University of Oxford

Trinity term 1988

To my parents and my brother

While I have been fumbling over books
And thinking about God the Devil and all,
Other young men have been battling with the days
And others have been kissing the beautiful women.

Aldous Leonard Huxley

Fully Relaxed Heavy Ion Reactions in the Mass 80 Region

Philip Mark Evans
The Queen's College

A thesis submitted in partial fulfilment of the requirements
for the degree of Doctor of Philosophy
in the University of Oxford

Trinity term 1988

Abstract

This thesis describes a set of experiments to investigate the properties of fully relaxed reactions in the mass 80 region. Symmetric and asymmetric entrance channels, leading to similar compound nuclei, have been compared in order to determine the characteristics of the reaction mechanism.

The symmetric system $^{40}Ca + ^{40}Ca$ has been studied at laboratory energies of 197.3 and 230.5 MeV. The fissionlike products were detected by a series of six time of flight telescopes, placed at angles between 10° and 52.4° to the beam. and a Bragg curve spectrometer-multiwire proportional chamber telescope, situated at 30°. Data were collected in both singles and coincidence modes. To complement this measurement, fully damped yields from $^{28}Si + ^{50,52,54}Cr$ at 130 MeV and from $^{28}Si + ^{50}Cr$ at 150 MeV were measured using an array of four avalanche counter-silicon surface barrier detector telescopes spanning the angular range between 20° and 50°. The avalanche counters used in this experiment are of a new design which was developed in Oxford. We present the features of this design and discuss the detectors' operational characteristics.

Several possible interpretations of the data are considered. It is shown that diffusion models of deep-inelastic scattering tend to underpredict the measured fully relaxed cross sections. Rotating finite range model calculations of fission barriers point to the possibility of fast-fission in this mass region; a process hitherto associated with much heavier systems. Furthermore, such models also predict that these systems may fission asymmetrically. The more commonly employed rotating liquid drop model of the nucleus is unable to predict either of these effects. The data are compared with those reported in the literature for other systems in this mass region. It is argued that all these results are consistent with fast-fission and asymmetric fission, thus obviating the need for the previously proposed interpretation in terms of intermediate mechanisms.

ACKNOWLEDGEMENTS

It gives me great pleasure to express my thanks to those who have contributed to my time in Oxford; both from the physics and from the personal point of view.

I am grateful to Professor K. W. Allen and Professor D. H. Perkins for allowing me to use the excellent facilities of the Nuclear Physics Laboratory over the past four years. I would also like to thank Drs. P. J. Twin, W. Gelletly and J. S. Lilley for the opportunity to perform experiments at the S.E.R.C. Daresbury Laboratory, and I would like to express my gratitude to everyone at Argonne National Laboratory Physics Division for the chance to use the facilities there to carry out the experiment which forms the main part of this thesis.

I am thankful to the two people who have made indispensable contributions to this work: I am greatly indebted to my supervisor, Arthur Smith, for his cheerful help, guidance and encouragement throughout the course of this work and for many interesting discussions; both on physics matters and the more cultured aspects of life such as Volvo cars. I would also like to thank my original supervisor, Russell Betts, for helping to initiate the research programme, for maintaining a keen interest in the work (to the extent of many visits across the Atlantic to discuss the work, while beating me at pool!) and for considerable help and encouragement.

I owe a debt of gratitude to the people who have participated in the experiments described in this thesis: Chris Pass, Louise Stuttgé, Steve Sanders, Dale Henderson, Bruce Wilkins, Broniek Dichter, Birger Back, Flemming Videbaek, Dave Banes, the Bilwes, N. Poffé, Trigger 24 and of course, A.E.S. and R.R.B. In addition, I am extremely grateful to Steve Sanders for considerable help with both the interpretation of this work and many of the calculations presented. The avalanche counters would not have been built were it not for help from Keith Fifield and Kevin Connell in the early stages of their development.

It has been my great privilege to visit Argonne National Laboratory during the course of my studentship. I am grateful to Russell for organising both trips. The hospitality of everyone there – particularly Russell, Cathy, Nicholas and Alison – will always be appreciated, as will financial help towards the cost of the trips from the S.E.R.C., the Queen's College (especially Dr. Moffatt), the Nuclear Physics Laboratory and the Scott Fund.

Thanks are due to the people who have provided excellent computing facilities, both here in Oxford and elsewhere. They are Ian McArthur, John MacAllisteir and Sue Allcock at Oxford, Peter Noake at Daresbury and Lester Welch and Tom Moog at Argonne. The research support staff at all three places are gratefully acknowledged: especially the Oxford accelerator operators; Alec, John, Fred and the two Rays for cheerful conversation and plenty of hot tea during many nightshifts 'pushing back the frontiers of science.' Special thanks are due to Cyril Band for considerable help with the avalanche counter development (and for the odd game of cricket); to Colin Graham and the skilled engineers in the OEG workshop for help with many things, and to Peter Bromley Barrett and his boys for help with numerous electronics problems. The targets used

in these experiments, lovingly prepared by Chas Cherrill and Bob Darlington, provided many interesting hours finding out what was in them. I am grateful to Beverly Roger, the group 'secretry' and to Jock Barber, Derek Harvey and Vi Pearce of the finance department for their help in administrative matters.

It is my pleasure to thank the people who have taken on the difficult task of proof reading this work: Arthur Smith, Sue Allcock and Chris Pass (many thanks for the help with the translation into English and with the 'perestroika'). I am grateful to Susan Allcock, Tim Shaw and Paul Leyland for help both with computing and with TEX. Many of the figures used have been prepared by Irmgard Smith in the drawing office and Cyril Band and co. in the photographic department.

I would like to thank the people who have been my companions in various offices throughout the past few years for providing such a convivial atmosphere in which to work: they are Chris Pass, Paul Keeling, Simon Williams, Ramin Alizadeh and Dave Lewis. I have enjoyed the company of many people in the department during my stay here: particularly Slimane Ait-Tahar, Youcef Nedjadi, Tim Shaw, Hasnita and Sufyan Hashim, Sue Allcock, the boss, Austyn Rover and the NOG boys, Mark Chadwick, Alan Merchant and Paul Holmes.

Life in Oxford is not all work: even for a graduate student! and so my many happy times with Manlam, Ho, Tim, Youcef, Slimane, Arthur, Hasnita, Sufyan, Chris, Louise, Paul, Simon, Sandra and Manoel will always be remembered with much fondness and gratitude.

I would like to acknowledge the Science and Engineering Research Council for a grant which financed most of this work.

Most of all, I would like to thank my family for their undying love and support throughout the course of my education. Anything I have achieved is due to them.

Phil Evans
The Queen's College
Oxford
July 1988

Contents

page

Chapter 1. Introduction 1
1.1 Introduction 1
1.2 Plan of the Thesis 3

Chapter 2. Models and Motivations 5
2.1 Introduction 5
2.2 The Nucleus-Nucleus Interaction 6
2.2.1 The Interaction Potential 7
2.2.2 Dissipation and Friction 8
2.3 Fusion-Fission Reactions 9
2.3.1 Fusion 10
2.3.2 Competition Between Fission and Evaporation 12
2.3.3 The Fission Barrier 13
2.3.4 Experimental Signatures of Evaporation and Fission . . . 15
2.4 Deep-Inelastic Reactions 16
2.4.1 Models 16
2.4.2 Experimental Features of Deep-Inelastic Reactions 18
2.5 Fusion Without Compound Nucleus Formation 18
2.5.1 Fast-Fission 19
2.5.2 Quasi-Fission 19
2.5.3 Experimental Evidence 21
2.6 Evidence for a New Reaction Mechanism 22
2.7 Theoretical Explanations 26
2.7.1 Effects of the Potential Energy Surface 28
2.7.2 The Diffusion Model 28
2.7.3 Relaxation Times 30
2.8 Symmetric Entrance Channels 32
2.9 Other Possible Explanations 32
2.9.1 Asymmetric Fission 33
2.9.2 Q-Value Effects 35
2.10 Other Phenomena of Interest 36
2.10.1 Superdeformation 36
2.10.2 Alpha-Particle Clustering 38
2.11 Summary 40

Chapter 3. Detection Techniques 41
3.1 Introduction 41
3.2 Concepts of Particle Identification 42
3.2.1 Mass Determination by Time of Flight Measurement . . . 42
3.2.2 Charge Determination 43
3.3 Development of a Hybrid Avalanche Counter 44
3.3.1 Types of Timing Detector 44
3.3.2 Design and Construction 48

3.3.3 Operational Characteristics 52
3.3.4 Performance 54
3.4 The MWPC-Bragg Telescope 58
3.4.1 The Bragg Curve Spectrometer 58
3.4.2 The Multiwire Proportional Chamber 61

Chapter 4. Experimental Details 62
4.1 Introduction 62
4.2 Experimental Parameters 63
4.2.1 Beam Energies 63
4.2.2 Target Thicknesses 65
4.2.3 Positioning of Detectors 67
4.3 ^{40}Ca + ^{40}Ca at Argonne 67
4.3.1 Experimental Configuration 67
4.3.2 Electronics Setup 69
4.3.3 Procedure 78
4.4 ^{28}Si + ^{50,52,54}Cr at Daresbury 79
4.4.1 Experimental Configuration 79
4.4.2 Electronics Setup 80
4.4.3 Procedure 83

Chapter 5. Analysis and Results 85
5.1 Introduction 85
5.2 Singles Analysis of SSB Data 87
5.2.1 Energy and Time Calibrations 87
5.2.2 Mass Calibrations 88
5.2.3 Identification of ^{40}Ca + ^{40}Ca Fissionlike Yields 90
5.2.4 Mass Distributions 94
5.2.5 Q-Values Distributions 98
5.3 Singles Data from the MWPC-BCS Telescope 106
5.4 Coincidence Analysis 108
5.5 The ^{28}Si + ^{50,52,54}Cr Experiment 117

Chapter 6. Interpretation 124
6.1 Introduction 124
6.2 Information from Fusion Measurements 126
6.3 Statistical Model Calculations 132
6.3.1 Theoretical Background 132
6.3.2 CASCADE Calculations 135
6.4 Post-Scission Evaporation 140
6.4.1 The Code LILITA 140
6.4.2 LILITA Calculations 142
6.5 Diffusion Model Calculations 149
6.6 The Businaro-Gallone Transition 156
6.7 Mass and Energy Distributions 163
6.8 Fast-Fission and the Finite Range Model 168

6.9 Nuclear Shell Effects . . . 176
6.9.1 Alpha-Particle Clustering . . . 176
6.9.2 Ground State Q-Value Correlations . . . 177
6.9.3 Superdeformed Shell Effects . . . 178
6.10 Summary . . . 179

Chapter 7. Summary and Conclusions . . . 180
7.1 Summary . . . 180
7.2 Conclusions . . . 183

Appendix I . Finer Points of the Data Analysis . . . 186
I .1 Introduction . . . 186
I .2 Pulse Height Defect . . . 186
I .3 Plasma Delay . . . 188
I .4 Predicted Loci of Fission Events . . . 189
I .4.1 Total Kinetic Energies and Q-Values . . . 189
I .4.2 Mass Against Energy Plots . . . 190
I .5 Evaporation Residues . . . 191
I .6 Correction for $^{40}Ca + ^{nat}O$ Fission Products . . . 192
I .7 Laboratory to Centre of Mass Conversion . . . 192

Appendix II . The Program FLAME . . . 194
II .1 Introduction . . . 194
II .2 Program Details . . . 195
II .3 Analysis of the $^{40}Ca + ^{40}Ca$ Data . . . 196
II .4 Listing of Program . . . 197

Appendix III . Fusion Model Calculations . . . 204
III .1 Introduction . . . 204
III .2 Extra Push Model . . . 205
III .3 Critical Distance Model . . . 207
III .4 Statistical Yrast Model . . . 208

Appendix IV . Glossary of Terms . . . 209
IV .1 Introduction . . . 209
IV .2 Glossary . . . 210

REFERENCES . . . 213

List Of Tables

		page
2.1	Values of l_x and l_{xx} for mass ≈ 80	27
3.1	Advantages and disadvantages of various timing detectors	47
4.1	CASCADE predictions for the systems studied	65
4.2	Detector details for the Argonne experiment	69
4.3	Detector details for the Daresbury experiment	80
6.1	Thresholds predicted by fusion calculations	132
6.2	CASCADE predictions for ^{40}Ca + ^{40}Ca.	139
6.3	CASCADE predictions for ^{28}Si + ^{50,52,54}Cr.	140
6.4	Diffusion model calculations for ^{40}Ca + ^{40}Ca	151
6.5	Diffusion model calculations for ^{28}Si + ^{50}Cr	152
6.6	Diffusion model calculations for ^{32}S + ^{59}Co	155
6.7	References to labels in figure 6.12	158
6.8	Mass and energy FWHM values	167
6.9	Angular momenta of systems studied in this thesis	174
6.10	Angular momenta of systems studied in the literature	175
III .1	Parameters used in fusion calculations	205

List Of Figures

page

2.1 Interaction potential as a function of l 8
2.2 Competition between fission and evaporation 13
2.3 A solution to the Fokker-Planck equation 17
2.4 The four dissipative reaction mechanisms 22
2.5 Mass spectra for a series of systems 24
2.6 Mass distributions for $^{32}S + ^{59}Co$ 25
2.7 Results for $^{32}S + ^{63}Cu$ and diffusion model predictions . . 26
2.8 Saddle point energies as a function of mass asymmetry . . 33
2.9 Energy levels of a deformed harmonic oscillator 38
2.10 Shell corrections for mass ≈ 80 39
3.1 Hybrid avalanche counter construction 49
3.2 Construction of airtight gas box 50
3.3 Photograph of an avalanche counter 51
3.4 Electric field due to detector grids 53
3.5 Mass spectrum from 80 MeV $^{16}O + ^{40}Ca$ 55
3.6 Detection efficiency for a pair of ion species 56
3.7 Photo-etched counter performance 57
3.8 Schematic view of a Bragg curve spectrometer 58
3.9 Energy loss for heavy ions as a function of charge 59
4.1 CASCADE predictions for $^{28}Si + ^{50}Cr$ 64
4.2 Experimental configuration of the Argonne experiment . . 70
4.3 A photograph of the Argonne setup 71
4.4 Electronics used for the six surface barrier detectors 73
4.5 Electronics used for the MWPC 75
4.6 Electronics configuration for the Bragg curve spectrometer . 77
4.7 Type of experimental setup for a Daresbury experiment . . 81
4.8 Electronics configuration used in the Daresbury experiment 82
5.1 The effect of incorrect values for l and t_0 91
5.2 Mass against energy plot for 197.3 MeV $^{40}Ca + ^{40}Ca$ . . . 92
5.3 Fissionlike yields from $^{40}Ca + ^{40}Ca$ at 197.3 MeV 95
5.4 197.3 MeV $^{40}Ca + ^{40}Ca$ mass distributions 96

5.5 230.5 MeV ^{40}Ca + ^{40}Ca mass distributions 97
5.6 197.3 MeV ^{40}Ca + ^{40}Ca angular distributions 99
5.7 230.5 MeV ^{40}Ca + ^{40}Ca angular distributions 100
5.8 Average mass distributions from ^{40}Ca + ^{40}Ca 101
5.9 Two-body Q-values at 197.3 MeV 103
5.10 Two-body Q-values at 230.5 MeV 104
5.11 Deviations of measured Q-values from model predictions . . 105
5.12 Plot of B_P against R_1 for the BCS 107
5.13 BCS charge distribution at 197.3 MeV 109
5.14 BCS charge distribution at 230.5 MeV 110
5.15 Coincidence mass spectrum 112
5.16 Coincidence charge spectrum 113
5.17 Coincidence mass against energy spectrum 114
5.18 Charge against mass scatter plot 115
5.19 Barriers against the emission of light particles 118
5.20 Mass against energy plot for 150 MeV ^{28}Si + ^{50}Cr 120
5.21 Fissionlike yields from ^{28}Si + ^{50}Cr at 150 MeV 121
5.22 ^{28}Si + ^{50}Cr mass distributions 122
5.23 Q-value spectrum for 150 MeV ^{28}Si + ^{50}Cr 123
6.1 Extra push model analysis of ^{40}Ca + ^{40}Ca 128
6.2 Extra push model analysis of ^{28}Si + ^{50}Cr 129
6.3 CDM and SYM analysis of ^{40}Ca + ^{40}Ca 131
6.4 CASCADE calculations for ^{40}Ca + ^{40}Ca 137
6.5 CASCADE calculations for ^{28}Si + ^{50}Cr 138
6.6 LILITA mass distribution for 197.3 MeV ^{40}Ca + ^{40}Ca . . . 144
6.7 LILITA mass distribution for 230.5 MeV ^{40}Ca + ^{40}Ca . . . 145
6.8 LILITA mass distribution for 130 MeV ^{28}Si + ^{50}Cr 147
6.9 LILITA mass distribution for 150 MeV ^{28}Si + ^{50}Cr 148
6.10 Wilczyński plot for ^{40}Ca + ^{40}Ca at 197.3 MeV 153
6.11 Evolution of charge with time for 154 MeV ^{32}S + ^{59}Co . . 157
6.12 Fission barriers in the liquid drop model 159
6.13 Mass and energy full width half maxima in the LDM . . . 165
6.14 Spin distributions for ^{40}Ca + ^{40}Ca 172
6.15 Spin distributions for ^{28}Si + ^{50}Cr 173

Chapter 1

Introduction

We shall never get people whose time is money to take much interest in atoms.

Samual Butler

1.1 Introduction

When two nuclei collide, a broad spectrum of reaction mechanisms is possible. Which one prevails depends on the energy and angular momentum brought into the system. The nature of these mechanisms is the subject of much research in nuclear physics today.

Consider a heavy ion impinging on a target nucleus, at an energy just above[a] their mutual Coulomb barrier. Reactions between the particles can be classified according to the classical impact parameter b, which is related to the partial wave l by the expression

$$bp = \sqrt{l(l+1)}\hbar \tag{1.1}$$

where p is the momentum.

For small impact parameters, the two bodies can interact strongly and may completely amalgamate. This is known as the fusion regime. Fusion reactions

[a] i.e. 1 to 3 times.

can be divided into two sets, depending on how the compound nucleus loses excitation energy. It may emit nucleons or clusters of nucleons. This is called fusion-evaporation. For high angular momenta, the nucleus may split into two large parts. This known as a fusion-fission reaction.

At large impact parameters, their interaction is far weaker and so few, if any, particles flow between them. Thus they effectively retain their original identities. These reactions are termed quasi-elastic.

In between these two extremes are the collisions where there may be the exchange of many constituent particles and the dissipation of much of the energy of relative motion. These reactions are called deep-inelastic collisions.

This model begs several questions. Are there just the four types of reaction? Is the transition from one mechanism to another sharp and well defined? More specifically, could it be that there is a type of transition reaction between fusion-fission and deep-inelastic? The properties of this new mechanism would be intermediate between those of fusion-fission and deep-inelastic scattering.

Experimental evidence for intermediate processes exists and has been interpreted as fusion without compound nucleus formation. For instance, the nuclei might fuse, but the angular momentum of the system could be greater than the maximum value the compound nucleus can accommodate, and so the fission barrier is zero. This is known as fast-fission. An alternative process is quasi-fission, where the fused system is formed outside the saddle point of the compound nucleus, and so can decay without experiencing the fission barrier. Experimental studies of systems in the region of mass 80-120 suggest that there may be other intermediate processes, which arise because of the different times associated with equilibration of the various degrees of freedom.

This thesis describes an experimental search for intermediate mechanisms of the latter kind. The programme of research involved using both symmetric and asymmetric target and beam combinations to form similar compound systems

with mass ≈ 80. In this way the entrance channel dependence could be tested. The systems chosen were ^{40}Ca + ^{40}Ca and ^{28}Si + ^{50,52,54}Cr.

The fission decay of nuclei with mass ≈ 80 is interesting for other reasons. Calculations predict the possibility of superdeformed shell effects in this region. This would allow for similar nuclei to have very different potential energy surfaces, as a result of which, fission barrier heights, mass distributions and Q-values could show dramatic variations across a range of isotopes.

These nuclei are close to the Businaro-Gallone transition, below which fission barriers start to favour asymmetric decay. Experimental evidence shows this transition occurs at heavier masses than predicted by the liquid drop model.

The system ^{40}Ca + ^{40}Ca is particularly interesting, because the compound system populated (^{80}Zr) is the heaviest self conjugate nucleus that can be formed using stable ions and without particle evaporation. Experimental studies of lighter $N = Z$ nuclei reveal the existence of strong α-particle clustering, due to the α-particle's large binding energy. If such clustering exists in ^{80}Zr, it might give rise to α-particle structure in the fission decay.

1.2 Plan of the Thesis

In the next chapter we discuss the background to this work in more detail. The various theoretical models are described and an account is given of the experiment evidence for intermediate processes in the mass 80 region.

Chapter 3 is a review of the relevant charged particle detection techniques. The detector systems used in the experiments presented in this thesis are described. In particular, the development of a hybrid avalanche counter, used in the ^{28}Si + ^{50,52,54}Cr experiment, is presented. Details of the two experiments are given in chapter 4. After an explanation of the choices of experimental parameters, the discussion focuses on how each experiment was carried out.

Once the experimental data had been collected, the next task was to analyse them and present the results in a form readily accessible to interpretation. In chapter 5, we describe how this analysis was carried out for each experiment. As the data reduction for the two experiments followed very similar lines and as the $^{40}Ca + ^{40}Ca$ measurement is the major component of this work, the analysis of the $^{28}Si + ^{50,52,54}Cr$ data is only discussed in detail where different.

The interpretation of the results is the subject of chapter 6. Calculations carried out using some of the models discussed in chapter 2 are presented and compared with experiment. Chapter 7 is a summary of the thesis and a discussion of the conclusions to be drawn from the work.

Several appendices then follow, which focus on certain points of the discussion presented in the main body of the text. Appendix I discusses the finer details of the data analysis presented in chapter 5. The Monte-Carlo program FLAME, used in the $^{40}Ca + ^{40}Ca$ analysis, is described in appendix II. In appendix III we present further details of a set of fusion calculations shown in chapter 6. Some expressions used in the text may not be familiar to the reader, while others – such as fast-fission, quasi-fission etc. – are not defined uniquely in the literature. Hence, for clarity, a brief glossary of these terms is presented in appendix IV. Where a term is not defined uniquely in the literature, the meaning assigned to it is that given in this appendix.

This thesis ends with a list of references.

Chapter 2

Models and Motivations

A child of the new generation
Refused to learn multiplication.
He said 'Don't conclude
That I'm stupid or rude;
I am simply without motivation.'

Joel Henry Hildebrand

2.1 Introduction

We now discuss the experimental and theoretical motivations for this work.

Firstly, as the reaction mechanism is determined by the interaction between the impinging nuclei, we look at how a collision between two heavy nuclei is described and how dissipation can occur.

Traditionally there is a sharp distinction between fusion-fission and deep-inelastic scattering, with the possibility of certain intermediate processes (specifically fast-fission and quasi-fission) under the appropriate conditions. The next three sections discuss the experimental signatures of these reaction mechanisms and models to explain them.

In section 2.6 we discuss the large body of experimental evidence for a new type of intermediate reaction process, which cannot be described in terms of

either fast-fission or quasi-fission. The use of the diffusion model to explain these results is the subject of section 2.7.

In section 2.8, the possibilities of using a symmetric target and beam combination to study intermediate processes are discussed.

The experimental evidence for intermediate mechanisms is not wholly incompatible with other explanations. These other explanations are the subject of section 2.9.

The study of the fission decay of nuclei in the mass 80 region is of interest for other reasons. These are discussed in section 2.10.

This chapter ends with a summary of the salient points.

2.2 The Nucleus-Nucleus Interaction

Which reaction mechanism prevails for a particular impact parameter is determined by the nucleus-nucleus interaction. This has two distinct components: firstly conservative forces determine the trajectories of the particles before they come into contact and after they re-separate. Secondly secular forces account for the conversion of energy of relative motion to internal excitation energy of the system. These dissipative forces are well described in terms of the concept of friction.

2.2.1 The Interaction Potential

The nucleus-nucleus interaction has three parts: the nuclear force; Coulomb repulsion, and the centrifugal force. In the sudden approximation, where the potential maintains the same form throughout the reaction, its value $V_l(r)$ at a centre separation r can be written as:

$$V_l(r) = \frac{Z_1 Z_2 e^2}{r} + \frac{f^2 l(l+1)\hbar^2}{2\mu r^2} - V_N(r) \tag{2.1}$$

where Z_1 and Z_2 are the charges, μ is the reduced mass of the system and V_N is the nuclear potential. The Coulomb part is often modified for small r, to allow for the interpenetration of the two nuclei. f allows for reductions in the orbital angular momentum during the collision and depends on the moment of inertia of the system. Many forms can be chosen for V_N. Usually a proximity potential is used [1], which can be written:

$$V_N(r) = \frac{R_1 R_2}{R_1 + R_2} U_N(s) \tag{2.2}$$

where R_1 and R_2 are the nuclear radii and $U_N(s)$ depends on the surface separation ($s = r - R_1 - R_2$). The form of the interaction barrier for the system ^{40}Ca + ^{40}Ca is shown in figure 2.1. For low l values, the potential has a pocket. As l increases the pocket gradually disappears, due to the dominance of the centrifugal term.

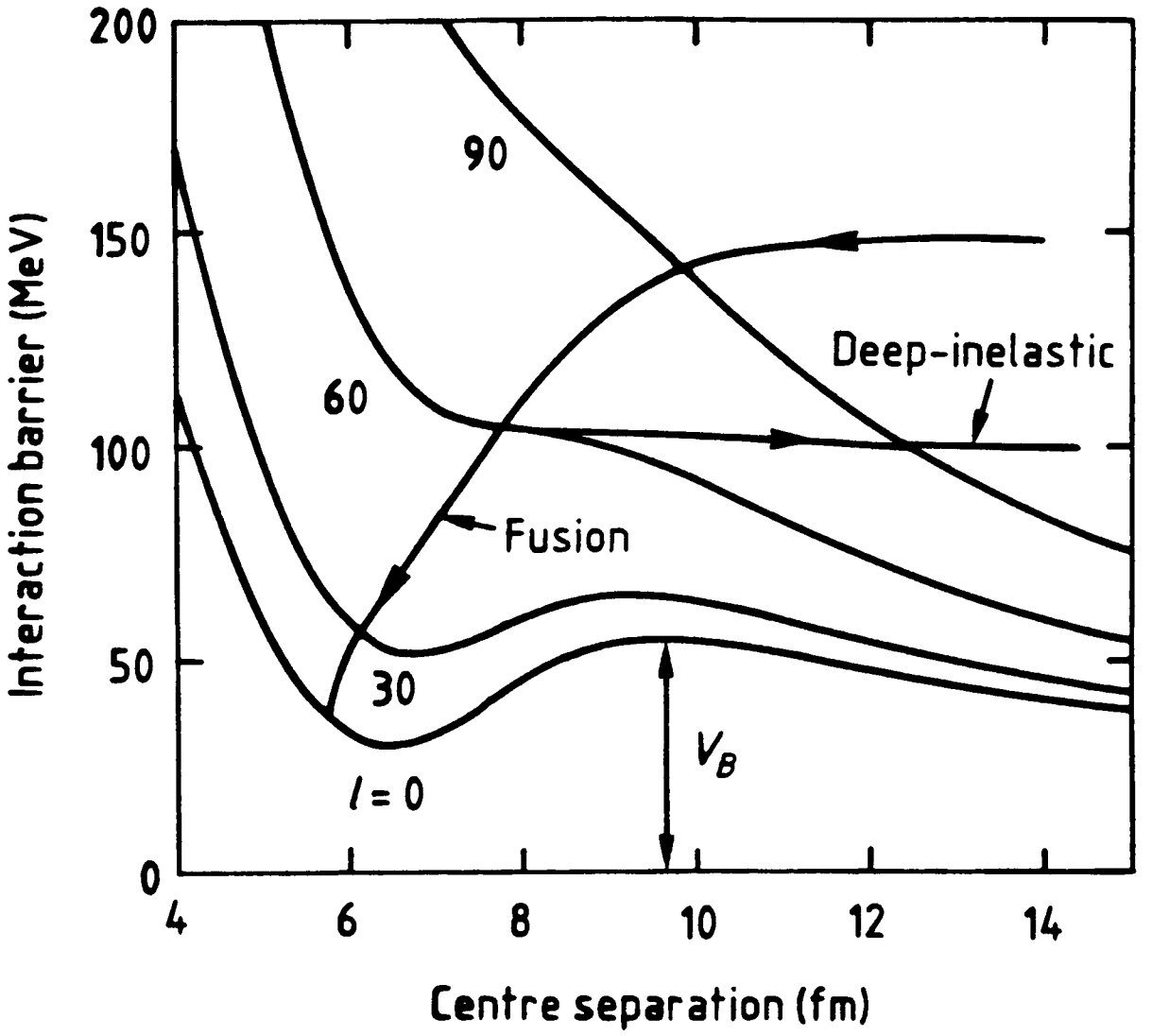


Figure 2.1. Interaction potential for the system ^{40}Ca + ^{40}Ca at different l values, calculated using the nuclear potential of Ngô [2]. V_B denotes the s-wave fusion barrier. Trajectories leading to fusion and deep inelastic scattering are illustrated.

2.2.2 Dissipation and Friction

Dissipation involves the irreversible change of energy from one form to another. On a microscopic scale, this can be understood in terms of interactions between nucleons within the target and projectile, which cause a large number of particle-hole excitations. The energy for these excitations is provided by the energy of relative motion. Furthermore there is the possibility of multiple particle transfer between the nuclei. Because of the large number of excitations involved, the process is essentially irreversible. Thus the distributions of matter and energy may be irrevocably changed during the reaction.

Most semi-classical models describe dissipation in terms of friction. The interacting nuclei can be thought of as gases within containers, defined by their

surfaces. When they come close enough to one another, the attractive nuclear force between their surfaces tends to cause a neck to form. The neck acts as a window, allowing the transfer of particles. This flow of particles between target and projectile equalizes their momenta. So the energy of relative motion is converted to kinetic energy of the gas particles, and hence to heat. This is known as window dissipation [1].

Kinetic energy may also be dissipated by the collisions of particles with the walls of the container. This is called wall dissipation [1].

Window and wall dissipation are both one-body mechanisms. An example of a two-body process is surface dissipation. Pauli blocking prevents interactions between nucleons in the nuclear interior. However particles at the Fermi surface may be scattered to states above it, thus converting collective energy to excitation energy [4].

Dissipation of angular momentum can be pictured in terms of friction. The surface force between the impinging nuclei is attractive and so, when their surfaces come into in contact, they will try to stick together. This causes the transfer of angular momentum from orbital motion to intrinsic spin of the target and projectile. In this way angular momentum is dissipated. The total angular momentum is conserved, but is redistributed amongst the reacting bodies.

2.3 Fusion-Fission Reactions

Before looking at the physics of intermediate processes, we consider the properties of fusion-fission and deep-inelastic reactions.

2.3.1 Fusion

Fusion is defined as a process in which two nuclei become trapped in their mutual interaction barrier and form a long-lived composite system (figure 2.1). It is usually, but not necessarily, synonymous with compound nucleus formation.

In fusion reactions, the energy of relative motion of the colliding nuclei is completely converted to other forms of energy. Furthermore, the system is so long-lived that all degrees of freedom are able to reach full equilibrium. This property of fusion reactions is usually termed full relaxation of all degrees of freedom and the total dissipation of kinetic energy is called full damping. Because of these features, the system's subsequent decay is independent of how it was formed.

Many theoretical models have been developed to describe fusion. In the simplest model, it is assumed that all partial waves up to a critical value l_{cr} fuse with unit probability while all those above do not fuse. Thus the total fusion cross section σ_{fus} is given by

$$\sigma_{fus} = \frac{\pi}{k^2}\sum_{l=0}^{\infty}(2l+1)T_l = \frac{\pi}{k^2}(l_{cr}+1)^2 \tag{2.4}$$

where T_l is the transmission coefficients for partial wave l and k is the de Broglie wavenumber of the system.

Classically, for fusion to occur, the centre of mass energy must be greater than the barrier height. If the barrier height is denoted by V_B (figure 2.1), and its radius is R_B, then the maximum partial wave that can fuse is given by

$$E_{cm} = V_B + \frac{l_{cr}(l_{cr}+1)\hbar^2}{2\mu R_B^2} \tag{2.5}$$

By combining equations 2.4 and 2.5, the expression

$$\sigma_{fus} = \pi R_B^2\left[1 - \frac{V_B}{E_{cm}}\right] \tag{2.6}$$

is obtained.

The foregoing discussion only holds for low energies. At higher energies, the disappearance of the pocket in the potential well limits fusion and equation 2.5 is no longer true. So l_{cr} is equal to the highest partial wave for which the interaction potential has a pocket. This is called the maximum critical angular momentum (l_{cr}^{max}).

Several models have been developed to describe this higher energy regime.

In the critical distance model due to Glas and Mosel [5], the nuclei have to reach a critical separation R_C in order to fuse. This is equivalent to saying they experience zero friction outside R_C and infinite friction inside. For low energies the cross section approximates to equation 2.6 and for high energies to

$$\sigma_{fus} = \pi R_C^2 \left[1 - \frac{V_C}{E_{cm}}\right] \tag{2.7}$$

where V_C is the value of the potential at R_C.

The statistical yrast model [6] assumes the compound nucleus is formed at an energy slightly above yrast, so that the level density is high. If ΔQ is the energy above the yrast line, then the excitation energy (E^*) is given by

$$E^* = E_{cm} + Q = \frac{l(l_{cr}+1)\hbar^2}{2J} + \Delta Q \tag{2.8}$$

Inserting this expression into equation 2.4 gives

$$\sigma_{fus} = \frac{\pi J}{\mu}\left[1 + \frac{Q - \Delta Q}{E_{cm}}\right] \tag{2.9}$$

where Q is the reaction Q-value, μ is the reduced mass and J is the moment of inertia of the yrast line.

The parameters in all the models discussed above are chosen empirically to reproduce experimental data over a wide mass range.

2.3.2 Competition Between Fission and Evaporation

The compound nucleus is generally formed in an excited state and so will emit radiation. Its decay can be described by statistical models [7]. The rate of emission for a particular type of radiation depends on the density of available levels in the initial and final nuclei and on the transmission coefficients for the reaction.

Fission is defined as the process where a nucleus splits into two (or possibly more) large fragments. It is not intuitively obvious how fission can be included in this framework, as the fission branch is determined by the minimal level density on the path to fission, and hence does not depend on the level densities of the residual nuclei. The minimal level density occurs when the potential energy on the path to fission is a maximum. At this point the nucleus becomes so deformed that it is committed to fission. This is called the saddle point configuration. For a given angular momentum, the energy difference between the ground state and the saddle point is called the fission barrier. Fission competition can be included in the statistical model by taking the level densities at the saddle point and using a suitable model to calculate the transmission coefficients, such as a parabolic barrier or a sharp cutoff approximation. Competition between fission and particle evaporation in this model is illustrated in figure 2.2.

In general fission only competes strongly with the evaporation of a particular type of particle when the fission barrier is smaller than the separation energy of that particle. The greater the angular momentum, the smaller the fission barrier. This is simply because the centrifugal force makes the nucleus less stable. So, as a result, for low angular momenta particle emission will dominate, whereas in the high angular momentum regime fission decay becomes favoured.

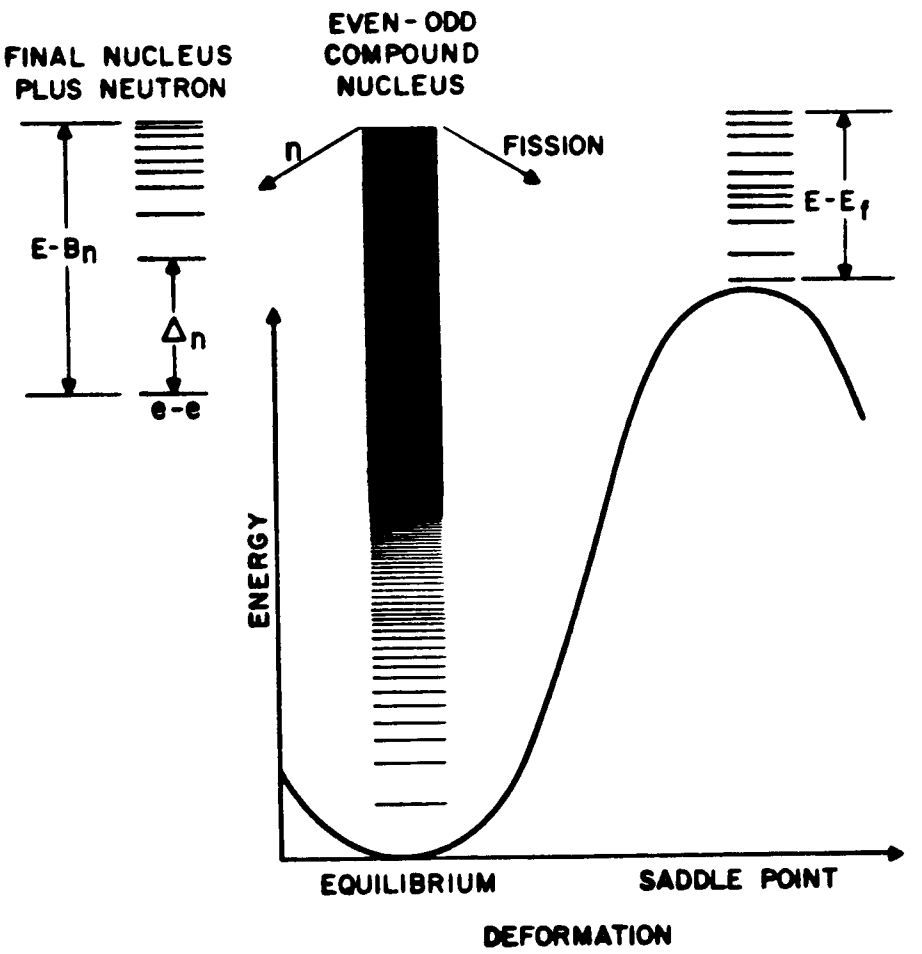


Figure 2.2. Competition between fission and neutron evaporation. The spectra of intrinsic states at the saddle point and in the residual nucleus following neutron emission are shown [8].

2.3.3 The Fission Barrier

The height of the fission barrier depends on how the nucleus responds to deformations and rotations. It can be calculated using the rotating liquid drop model (RLDM) [9].

In this model, the nuclear force is assumed to be of zero range. Furthermore, since we are only interested in the energy differences between shapes, the volume term is neglected. If $E^{(0)}$ denotes the energy of a spherical nucleus (mass A, charge Z), then two quantities can be defined:

$$x = \frac{E_C^{(0)}}{2E_S^{(0)}} = \frac{Z^2}{A} \Big/ \left(\frac{Z^2}{A}\right)_{crit} \tag{2.10}$$

and

$$y = \frac{E_R^{(0)}}{E_S^{(0)}} \sim \frac{l^2}{A^{7/3}} \tag{2.11}$$

where the various subscripts denote Coulomb, surface and rotational energies and $(Z^2/A)_{crit}$ depends on the parameters of the model. x is called the fissility parameter and is a measure of the relative strengths of the surface tension and the Coulomb repulsion. When x is 1, the spherical nucleus is unstable against fission. y is a measure of the rotational energy of the nucleus in terms of the surface energy. For a given x and y, the shape of the nucleus is varied and two quantities are calculated: the minimum energy (equated to the rotational ground state); and the maximum energy (equated to the saddle point). The ground state is stable with respect to all shape changes, whereas the saddle point is unstable against fission. The difference between these two quantities is the fission barrier.

Imagine a nucleus which is being rotated at higher and higher angular momenta. Eventually the centrifugal force becomes so great, that the surface tension can no longer counteract the combined effect of it and the Coulomb repulsion. At this point, the rotational ground state coincides with the saddle point and becomes unstable against fission. It is important to note that the maximum angular momentum a compound nucleus can accommodate ($l_{B_f=0}$) is not necessarily the same as the maximum critical angular momentum for fusion (l_{cr}^{max}) discussed above.

2.3.4 Experimental Signatures of Evaporation and Fission

Evaporation residues are the remains of compound nuclei, after they have de-excited by light particle emission. Their masses are slightly below that of the compound nucleus and tend to decrease the higher the initial excitation energy. Angular distributions for these reactions are very forward peaked: yields fall rapidly with angle. The particles evaporated are emitted in random directions in the centre of mass of the recoiling nucleus, and so the average velocity of the residues is equal to that of the compound nucleus.

For a fusion-fission reaction, all ingoing kinetic energy is dissipated and so the total kinetic energy (TKE) of outgoing fission fragments should only depend on the compound nucleus. The simplest model assumes that the total kinetic energy is solely determined by the Coulomb repulsion between the two fragments at scission, which for symmetric splitting (two equal fragments) is proportional to the Coulomb energy of the compound nucleus. A study of systematics by Viola [10] and co-workers supports this hypothesis. They obtained the empirical expression

$$E_K = 0.1189 Z^2/A^{1/3} + 7.3 \text{ MeV} \tag{2.12}$$

for the total kinetic energy. The Coulomb repulsion model is often modified by adding a centrifugal term and by including a separation between the nascent fragments' surfaces to account for deformation.

Fission fragment mass distributions, for highly excited nuclei, are usually Gaussian in shape and centred at half the compound nucleus mass.

Angular distributions for fission are close to $1/\sin\theta_{cm}$. This can be understood by making the analogy between the rotating compound nucleus and a fast spinning flywheel, with its axis of rotation perpendicular to the beam direction (i.e. in the θ plane). Due to the centrifugal force, any particles emanating from the flywheel will tend to do so at right angles to the rotation axis with equal

probability for all angles in the plane of rotation. So $d\sigma/d\theta_{cm}$ is constant. Hence $d\sigma/d\Omega_{cm}$ varies as $1/\sin\theta_{cm}$.

In reality, the flywheel model is only appropriate if the nucleus angular momentum is large or K (the projection of the angular momentum along the symmetry axis) is close to zero.

2.4 Deep-Inelastic Reactions

2.4.1 Models

Unlike the fusion process, deep-inelastic scattering does not involve the formation of a compound nucleus. These reactions correspond to partial waves for which there is no minimum in the nucleus-nucleus potential (figure 2.1). For such partial waves, the force at the point of contact is repulsive, and so the nuclei eventually re-separate.

The collision partners are made up of many particles and come into contact for a relatively long time ($\approx 10^{-20}$-10^{-21} s). Because of this, the properties of the two nuclei can change significantly: mass and charge may be transferred; energy may be dissipated, and the system's angular momentum may be redistributed.

In section 2.2.2, we make the analogy between nuclei and bags of gas in order to describe dissipation. This analogy can be carried further by describing the net transfer of matter between two colliding nuclei as a transport process, similar to diffusion in a gas. The evolution of the system can be described by a diffusion equation, known as the Fokker-Planck equation [11]:

$$\frac{\partial P(y_i,t)}{\partial t} = -\sum_i \frac{\partial}{\partial y_i}\{v_i \quad P(y_i,t)\} + \sum_{i,j} \frac{\partial^2}{\partial y_i \partial y_j}\{D_{ij} \quad P(y_i,t)\} \qquad (2.13)$$

where $P(y_i, t)$ is the population of the macroscopic variable y_i at time t. v_i and D_{ij} are known as drift and diffusion coefficients, respectively. They depend on level densities and transition probabilities, and thus are determined by the physical properties of the system.

As an illustration of the parameters v and D in the Fokker-Planck equation, consider the one-dimensional case when v and D are constant and the distribution at $t = 0$ is a delta function at $y = 0$. The solution is

$$P(y,t) = (4\pi Dt)^{-\frac{1}{2}} \exp\left[\frac{-(y-vt)^2}{4Dt}\right] \tag{2.14}$$

Equation 2.14 is a Gaussian with a mean value of vt and a variance of $\sqrt{2Dt}$. Thus the system has a constant drift velocity v and a variance which depends on D. This solution is illustrated in figure 2.3.

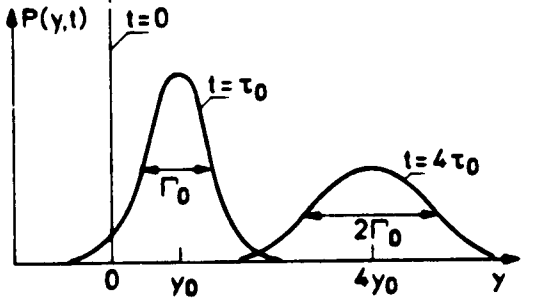


Figure 2.3. The solution to the Fokker-Planck equation for constant drift and diffusion coefficients [11].

Classical trajectory models [12] are well suited to describing the dynamical nature of these reactions. The evolution of each trajectory is determined by solving the equations of motion at small time intervals. Diffusion processes can be included within the context of the wall and window dissipation processes discussed above.

If a given trajectory stays trapped within the potential well for long enough then fusion is deemed to have taken place. The highest partial wave for which this happens (l_{cr}) can be used to evaluate the fusion cross section. Above l_{cr},

trajectory calculations predict that reaction times, the dissipation of energy and deflection angles all decrease as l is increased.

2.4.2 Experimental Features of Deep-Inelastic Reactions

As deep-inelastic reactions lie in the l-space between quasi-elastic reactions and fusion-fission, their Q-values can be anything from almost zero down to the fully relaxed value given by the Viola systematics (equation 2.12).

As a rule, they have mass distributions centred at target and projectile and angular distributions which are more forward peaked than $1/\sin\theta_{cm}$. However, for a fully relaxed deep-inelastic reaction, the angular distribution can tend to the $1/\sin\theta_{cm}$ form expected for fusion-fission. If a long-lived deep-inelastic reaction occurs, the system formed may rotate through a large angle: a process known as orbiting.

2.5 Fusion Without Compound Nucleus Formation

In the discussion of section 2.3.1, we mentioned that fusion does not necessarily lead to compound nucleus formation. It may be possible that although the system becomes trapped in a pocket in the interaction potential, there is no fission barrier to prevent prompt re-separation. Because of this the collision lasts longer than a deep-inelastic reaction, but for a shorter time than a true fusion-fission reaction. Typical time scales are: 10^{-19} s for fusion-fission; 10^{-20} s for this type of reaction, and 10^{-21} s for deep-inelastic collisions. Two examples of these processes are known as fast-fission [2] and quasi-fission [13].

2.5.1 Fast-Fission

We mentioned in the discussion on the fission barrier that the maximum angular momentum a compound nucleus can accommodate ($l_{B_f=0}$) is not necessarily the same as the maximum critical angular momentum for fusion (l_{cr}^{max}). If l_{cr}^{max} is greater than $l_{B_f=0}$ then the partial waves between $l_{B_f=0}$ and l_{cr}^{max} can still fuse, but a stable compound nucleus does not exist. This is called fast-fission.

2.5.2 Quasi-Fission

Quasi-fission is described by the extra push model [13]. In this model three configurations are important: first is the contact configuration. Second is the conditional saddle point, which is the maximum value of the potential energy, under the constraint that the mass asymmetry remains frozen. Third is the true saddle point of the compound nucleus – usually corresponding to two symmetric fragments. This is called the unconditional saddle point. The reaction mechanism depends on which configuration is reached.

To fuse, the system must get inside the potential barrier for the entrance channel (the conditional saddle point). For light systems, this is less compact than the contact shape, and so contact leads to fusion automatically. However, for heavy systems, the opposite may be true and extra radial energy could be needed for fusion. This energy is known as the extra push.

In analogy with equation 2.5, the maximum l value for fusion (l_x) is given by:

$$E_{cm} = V_B + \frac{l_x(l_x+1)\hbar^2}{2\mu R_c^2} + E_x \tag{2.15}$$

where R_c is the centre separation when the surfaces come into contact and E_x is the extra push energy. E_x depends on the effective fissility of the system

(x_e) – a quantity analogous to the fissility parameter for the compound nucleus (equation 2.10):

$$x_e = \left(\frac{Z^2}{A}\right)_e \Big/ \left(\frac{Z^2}{A}\right)_{crit} \tag{2.16}$$

with

$$\left(\frac{Z^2}{A}\right)_e = \frac{4Z_1Z_2}{A_1^{\frac{1}{3}}A_2^{\frac{1}{3}}\left(A_1^{\frac{1}{3}}+A_2^{\frac{1}{3}}\right)} \tag{2.17}$$

where $Z_{1,2}$ and $A_{1,2}$ are the charge and mass of the beam and target. The effects of rotation can be included by assuming the centrifugal force is equivalent to an increase in the Coulomb repulsion. So,

$$\left(\frac{Z^2}{A}\right)_e(l) = \left(\frac{Z^2}{A}\right)_e + \left(\frac{fl}{l_{ch}}\right)^2 \tag{2.18}$$

l_{ch} depends on the system. If the threshold for the extra push is given by x_{th}, then

$$E_x = \begin{cases} 0, & x_e(l) \leq x_{th}; \\ \propto [x_e(l) - x_{th}]^2, & x_e(l) > x_{th}. \end{cases} \tag{2.19}$$

The constant of proportionality can be estimated from experimental results, as can x_{th}.

Fusion is not sufficient to form a compound nucleus. For this to happen, the unconditional saddle point must be overcome. More energy still may be needed to get inside this barrier. This energy is called the extra-extra push (E_{xx}). The maximum angular momentum to form a compound nucleus (l_{xx}) can be calculated in the same way as l_x. E_{xx} is usually assumed to have a similar form to E_x:

$$E_{xx} = \begin{cases} E_x, & x_m(l) \leq x_{cl}; \\ \propto [x_m(l) - x_{th}]^2, & x_m(l) > x_{cl}. \end{cases} \tag{2.20}$$

with $x_m(l)^2 = x_e(l)x_{cn}$ (x_{cn} is the fissility of the compound nucleus) and x_{cl} is the threshold.

Quasi-fission occurs if the system fuses but decays without passing inside the unconditional saddle point, and so will take place for partial waves between l_{xx} and l_x.

2.5.3 Experimental Evidence

The main experimental evidence for fast-fission is a rise in the full width half maximum of the fissionlike mass distribution from ^{40}Ar + ^{165}Ho as excitation energy is increased [14]. Calculations suggest that at this point, a contribution from partial waves above $l_{B_f=0}$ becomes important. Because this component is not from a true compound nucleus, it does not have the variance expected for fission decay.

The most significant evidence for quasi-fission is the observation of discrepancies in the fissionlike angular distributions at high excitation energies. This can be accounted for if the state determining the angular distribution is less compact than the saddle point, and hence outside the compound nucleus [15].

The evidence for these mechanisms is inconclusive, since the observed rise in the mass width of ^{40}Ar + ^{165}Ho has not been seen for other systems and the deviations from calculated angular distributions can be explained in other ways. For a given system, the angular distribution depends on K (the projection of angular momentum along the symmetry axis). In the transition state model, K is determined at the saddle point. Recent results indicate that angular distributions can be explained in terms of this model [16], provided the fission barrier height (B_f) is greater than the nuclear temperature (Θ) When Θ is greater than B_f the disagreement between experiment and theory suggests that either shapes less compact than the saddle point determine the angular distribution or the transition to the final fission distribution is too fast to enable full equilibration of K.

2.6 Evidence for a New Reaction Mechanism

By the mid 1970s, the established picture of dissipative reactions was as follows: there is a sharp distinction between deep-inelastic reactions and fusion-fission, but in certain cases intermediate processes may occur. These correspond to reactions where the system becomes trapped inside the fusion barrier but is unable to form a compound nucleus due to either the absence of a fission barrier or the compactness of the saddle point. The four types of dissipative heavy ion reaction are shown in figure 2.4.

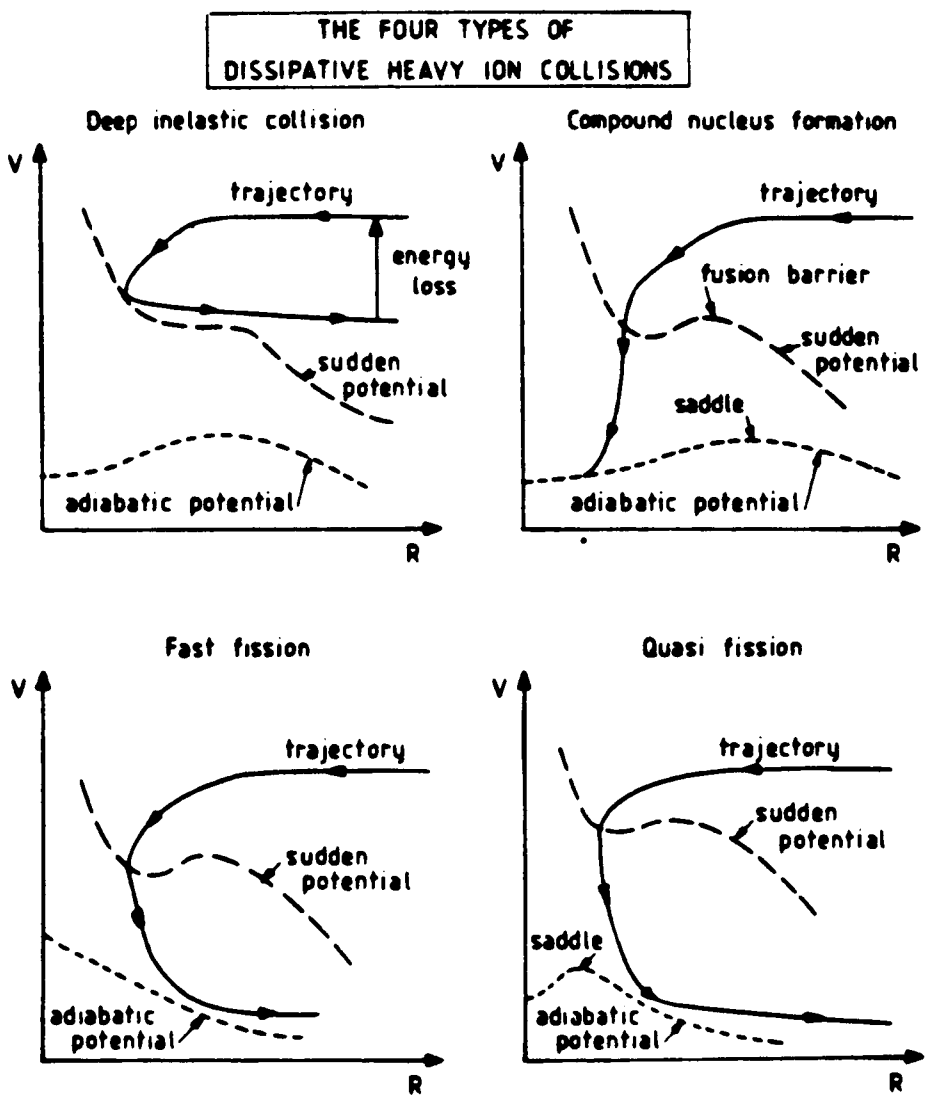


Figure 2.4. The four dissipative heavy ion reaction mechanism [2]. The sudden potential is the barrier in the entrance channel. The adiabatic potential corresponds to the compound nucleus.

Experimental investigations of the fission decay of nuclei in the mass 80

region have revealed some unexpected results which bring into question this picture.

Barrette and co-workers [17] investigated the system $^{32}S + ^{50}Ti$ at a series of energies. Most of their findings are completely consistent with a fission mechanism: the decay is two-body (with a small amount of neutron evaporation); the fragments have the correct energies for fission as predicted by the Viola formula; the energy widths agree with liquid drop model predictions; the angular distributions follow $1/\sin\theta_{cm}$, and furthermore the cross sections are consistent with fission. However the mass spectra exhibit a striking energy dependence. For the lowest energies (131 MeV) they observe target and beamlike decay, but at higher energies (166 MeV) the distribution becomes symmetric as expected for a fission reaction.

Oeschler et al. [18] carried out a study of the fissionlike decay of a series of systems from mass 91 to mass 121. They found in their experiments that lighter systems (e.g. $^{32}S + ^{59}Co$) show strong target and beamlike decay, whereas the heavier ones (e.g. $^{32}S + ^{89}Y$) show a narrow peak at symmetry, consistent with true fission. Interjacent target and beam combinations exhibit a monotonic transition between these two extremes. Their results are shown in figure 2.5.

Any energy dependence was ruled out, as for all reactions studied the centre of mass energy was about 1.7 times the Coulomb barrier.

A study of the reaction $^{32}S + ^{76}Ge$ (by Coffin, Guillaume and collaborators) revealed that the excitation functions for these reactions can be described using the statistical model of compound nucleus decay, if the rotating liquid drop model fission barriers are scaled by 0.6. By comparing their results with those of others, they were able to deduce that the full width half maxima (FWHM) of the mass distributions are strongly dependent on the entrance channel – being larger the greater the asymmetry of target and beam masses [19].

The same group discovered perhaps the most surprising evidence for a new mechanism, when they measured angular distributions for the system $^{32}S + ^{59}Co$

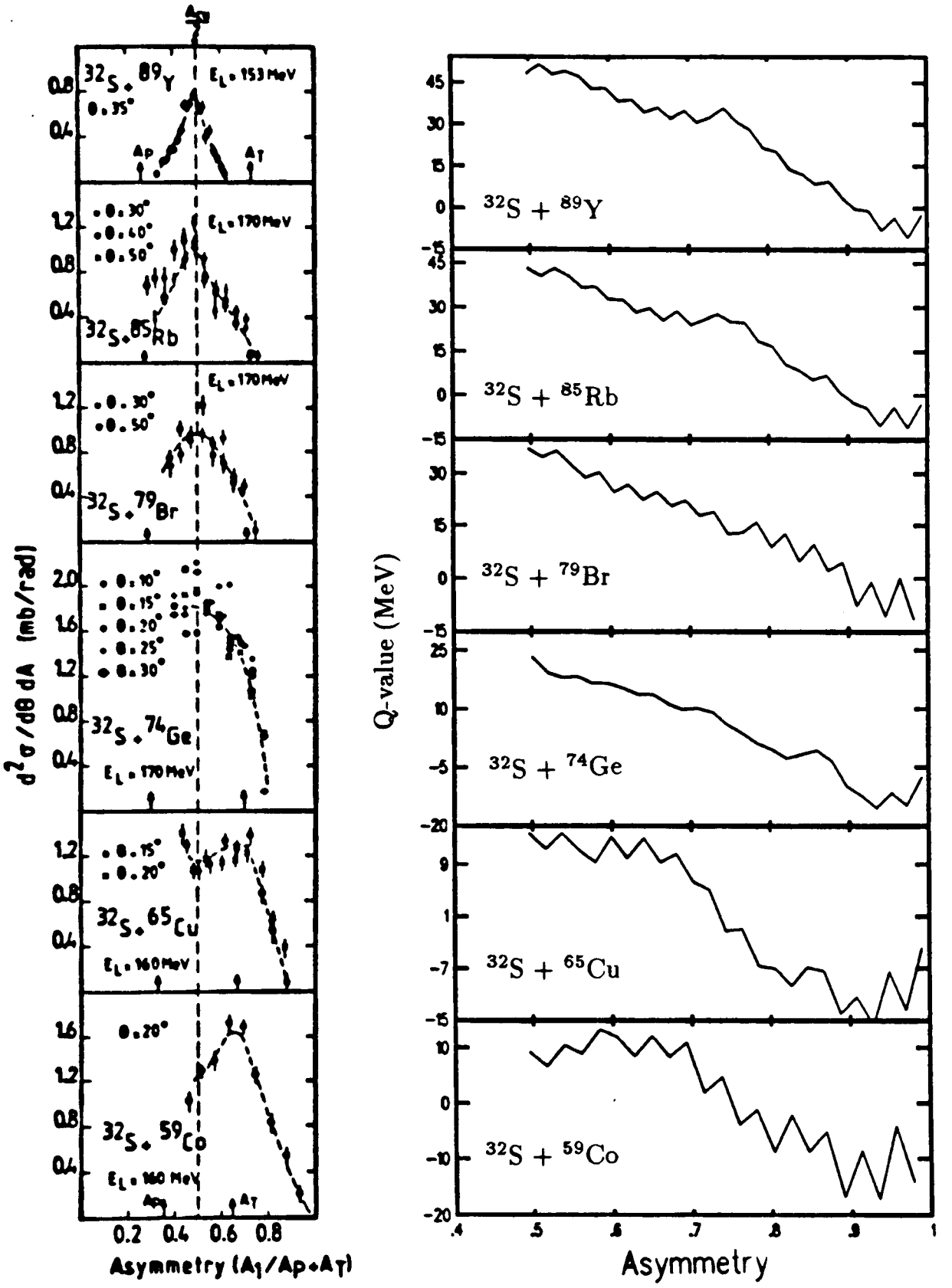


Figure 2.5. On the left are mass spectra, as a function of asymmetry, for a series of systems [18]. The target and projectile masses are shown. The dashed line indicates half the compound system mass. On the right are the corresponding ground state Q-values for division of the compound nuclei. The general trend in the Q-values follows the experimental data.

at a series of energies [20]. Their results are shown in figure 2.6. They found that backward angle data (e.g. $\theta_{lab} = 40°$) confirm the observation of target and

beamlike decay by Oeschler et al. However at more forward angles the entrance channel dependence grows weaker, until by $\theta_{lab} = 5°$ there is a narrow peak at half the compound nucleus mass. As with the results of Barrette et al., the entrance channel dependence decreases as energy is increased.

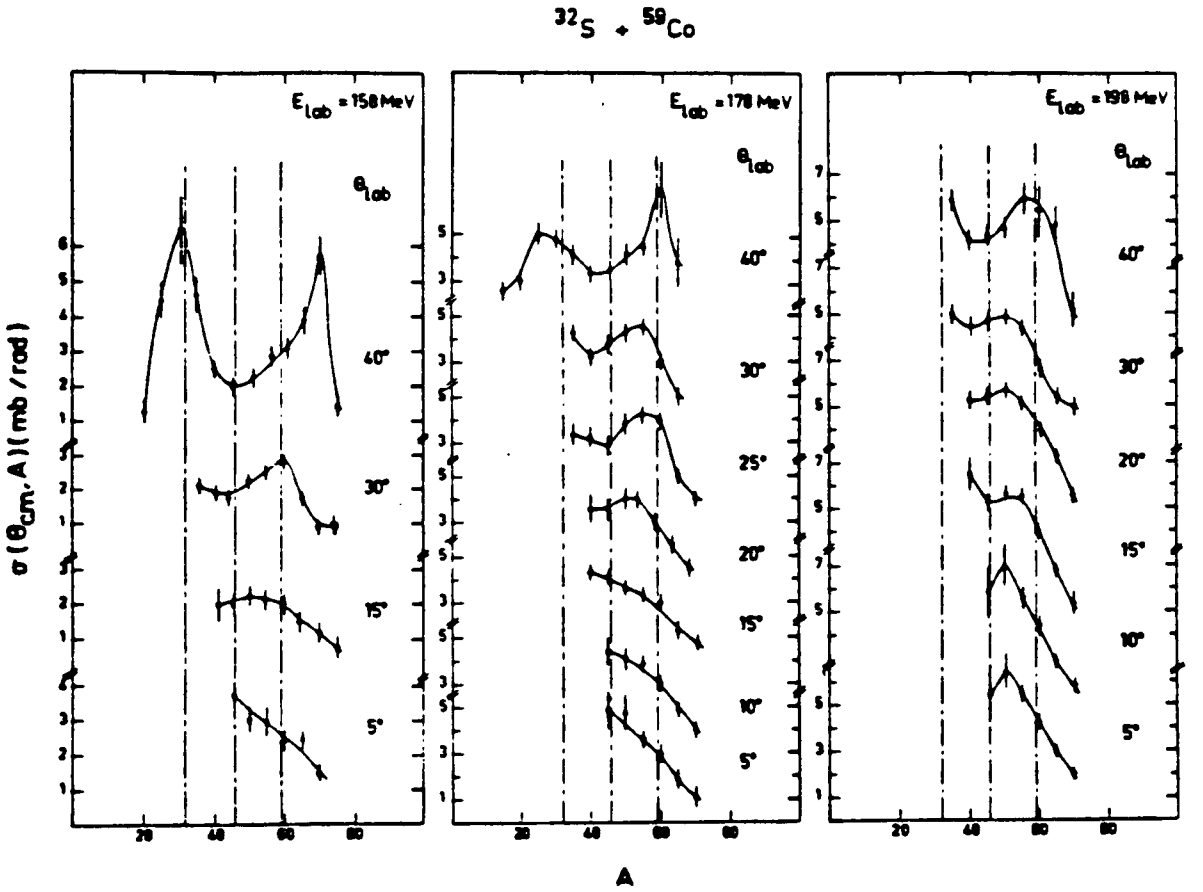


Figure 2.6. The results of Coffin et al. [20]. Mass distributions as a function of both angle and energy for $^{32}S + ^{59}Co$. The vertical dot-dashed lines indicate the projectile mass, half the compound system mass and the target mass. The solid lines are to guide the eye.

These results were substantiated by Agnoli et al. [21] who looked at $^{32}S + ^{59}Co$ and $^{32}S + ^{63}Cu$. Both systems reveal an evolution with angle and with energy. Their results for the system $^{32}S + ^{63}Cu$ are shown in figure 2.7.

In summary, experiments in the mass $\approx$ 80-120 region have revealed evidence for a reaction mechanism which has many hallmarks of fission, but which reveals an entrance channel dependence, in certain conditions. The fissionlike aspects of the mechanism are: two-body decay; fully damped Q-values; Q-value

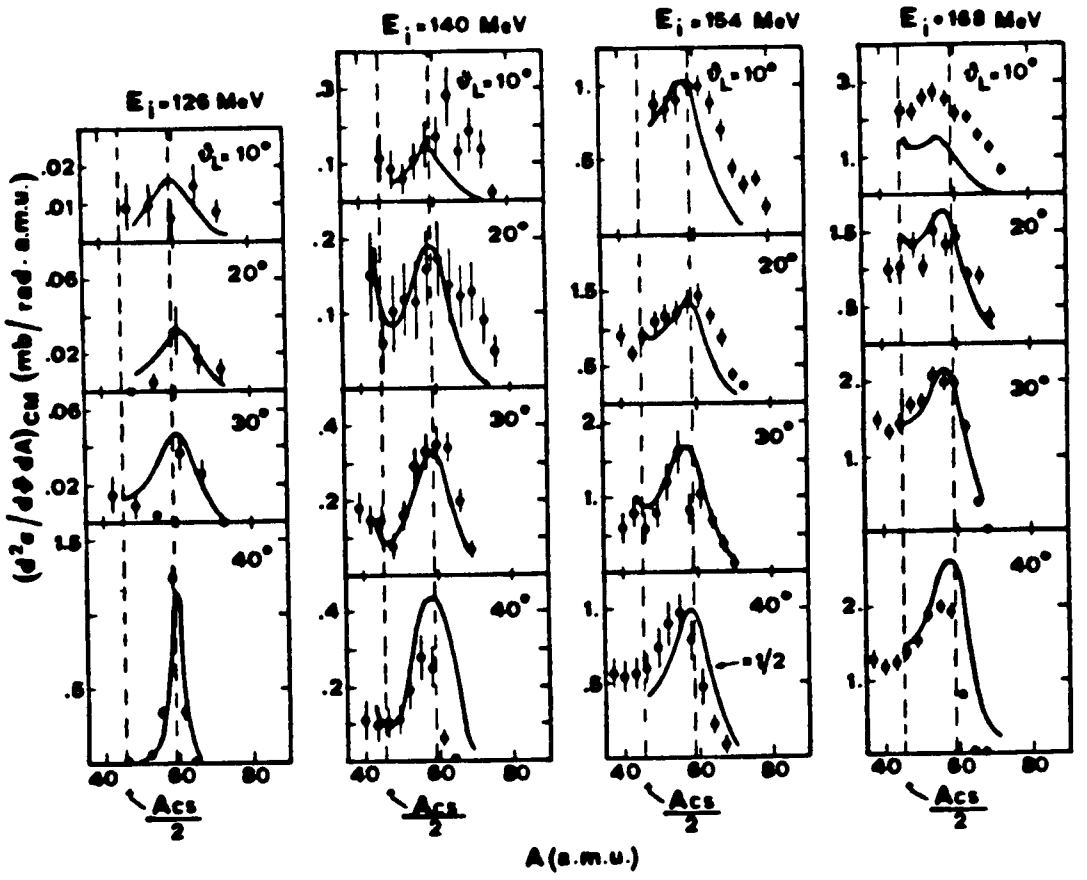


Figure 2.7. Mass spectra for the system $^{32}S + ^{63}Cu$ as a function of angle and energy [21]. The vertical dashed lines indicate half the compound system mass and the target mass. The solid curves are predictions of the diffusion model (see text).

widths; angular distributions, and cross sections given by statistical model calculations. The main entrance channel effect is target and beamlike decay, which gives way to symmetric fragmentation: at higher energies; for more forward angles, and for heavier systems. The mass widths also reveal an entrance channel memory.

2.7 Theoretical Explanations

We now consider the theoretical framework used to describe these intermediate processes.

Although these reactions have many of the properties of fission, the entrance channel effects point to the presence of a component which does not originate

from the decay of a compound nucleus. Furthermore the fact that this component becomes indistinguishable from fission under certain conditions indicates that it corresponds to fairly long-lived composite systems.

In view of this it would seem likely that fast-fission or quasi-fission might explain the results.

The simplest way of determining if fast-fission is an important mechanism is to compare $l_{B_f=0}$ and l_{cr}. $l_{B_f=0}$ can be calculated from the liquid drop model and l_{cr} can be estimated using the sudden approximation. It turns out that in this mass region and at the energies used, the rotating liquid drop model predicts that l_{cr} is generally smaller than $l_{B_f=0}$ ($\approx 70\hbar$) by several units of $\hbar$, and so fast-fission is not expected to occur.

The conditions for quasi-fission can be calculated using the extra push model. If l_x is much greater than l_{xx}, then this process will be important. However in the mass 80 region, $l_x \approx l_{xx}$ (see table 2.1) and so quasi-fission should not happen. Thus it seems the unique features of these fissionlike reactions cannot be explained by either quasi-fission or fast-fission.

Entrance Channel	Compound	E_{Lab} (MeV)	l_x	l_{xx}
$^{32}S+^{50}Ti$	^{82}Sr	166	62	62
$^{32}S+^{59}Co$	^{91}Tc	160	63	63
	^{91}Tc	168	65	65
$^{32}S+^{65}Cu$	^{97}Rh	170	68	68
$^{32}S+^{74}Ge$	^{106}Cd	170	72	72
$^{32}S+^{76}Ge$	^{108}Cd	178	75	75
	^{108}Cd	225	81	76
$^{52}Cr+^{56}Fe$	^{108}Sn	264	77	77
$^{32}S+^{79}Br$	^{111}Sb	170	72	72
$^{32}S+^{85}Rb$	^{117}I	170	74	74
$^{32}S+^{89}Y$	^{121}Cs	153	68	68
	^{121}Cs	184	77	75

Table 2.1 Values of l_x and l_{xx} for a series of systems with mass ≈ 80 [22].

2.7.1 Effects of the Potential Energy Surface

The transition from target and beamlike decay to symmetry – with increasing energy – can be understood by considering the interaction potential of the system. For a given angular momentum, the centrifugal term has a minimum at symmetry. As bombarding energy is increased, more angular momentum is brought into the system, and so the centrifugal potential becomes more significant. Thus for higher and higher centre of mass energies, the potential energy surface favours the equalization of target and projectile masses more and more strongly. In this way the potential 'drives' the system towards symmetry: hence the evolution with energy.

2.7.2 The Diffusion Model

Target and beamlike decay is associated with short-lived systems, whereas symmetric fragmentation is a feature of long-lived compound nuclei. Hence the evolution of the mass distribution suggests a strong link between interaction time and both energy and observation angle.

Because of this time dependence, the diffusion model (described in connection with deep-inelastic reactions) provides a convenient framework for the description of these reactions. Several forms of this model exist. We will describe the approach of Ricci [22].

The rotation angle ($\Delta\theta$) is related to the angle of observation (θ_{obs}) and the grazing angle (θ_{gr}) by the expression

$$\Delta\theta = \theta_{gr} - \theta_{obs} = \omega(l)\Delta t \tag{2.21}$$

where Δt is the interaction time and $\omega(l)$ is the mean angular velocity for partial wave l. In this way each value of θ_{obs} corresponds to a unique value of Δt

– assuming less than one complete rotation. The probability of the system surviving to time t ($P(t)$) is assumed to follow a statistical decay law. So,

$$P(t) \approx e^{-\frac{t}{\tau}} \tag{2.22}$$

where τ is its mean lifetime.

The Fokker-Planck equation (2.13) is solved for each partial wave in small time intervals ($\approx 10^{-23}$ s). The transport coefficients used (v_i and D_{ij}) are given by,

$$D_{ij} = d(y)\mu_{ij}(y,t) \tag{2.23}$$

and

$$v_i \quad = d^{-1}(y)\sum_{j=1}^{3}\frac{\partial}{\partial y_j}[d(y)D_{ij}, \quad] \tag{2.24}$$

where y_i denotes the macroscopic variables (in this case the mass of one fragment (A), the z component of the total intrinsic angular momentum (l_z) and (E) the total excitation energy), $d(y_i)$ is the level density and $\mu_{ij}(y,t)$ depends on the transition probability between macroscopic states y_i and y_j. For each step of the calculation, the transport coefficients and macroscopic variables of the previous step are used as initial values.

The transport coefficients are functions of the level densities and hence depend on the excitation energy, which, in turn, depends on the interaction potential. This presents a problem when trying to describe a system in the process of equilibration, as it is usually assumed that the entrance channel potential is given by the sudden approximation, whereas the fully relaxed system has all its constituent particles in their lowest possible energy state for a given set of collective variables (described by an adiabatic potential). To circumvent this difficulty it is assumed the potential (V) undergoes a monotonic change from one limit to the other:

$$V = V_{sudden}\chi(t) + V_{adiabatic}(1-\chi(t)) \tag{2.25}$$

where $\chi(t)$ is a time dependent function, which changes from 1 when $t = 0$ to 0 for large t.

The procedure outlined above is used to generate mass distributions for the range $l_{cr} \leq l \leq l_{gr}$. Distributions for the range $l_{B_f=B_n} \leq l \leq l_{cr}$ are calculated assuming a Gaussian distribution centred at half the compound system mass and with a variance given by the liquid drop model. So the fissionlike yield is divided into two parts: a fully equilibrated part for $l_{B_f=B_n} \leq l \leq l_{cr}$ and a partially equilibrated component for $l_{cr} \leq l \leq l_{gr}$.

In this way the kinetic energy, angular momentum and mass partition for a given observation angle can all be computed as a function of interaction time. Furthermore the statistical decay assumption can be used to evaluate the relative probability of a given final state.

Agnoli et al. [21] used such a prescription to describe the systems ^{32}S + ^{59}Co, ^{63}Cu at a range of laboratory energies to try to reproduce the evolution of the mass distributions with both energy and angle. Their results are shown by the solid curves on figure 2.7.

2.7.3 Relaxation Times

The fact that it is possible to have a reaction where the kinetic energy is completely dissipated, but the mass distribution evolves with angle shows that different times are associated with the relaxation of these degrees of freedom. Similarly, from studies of dissipative reactions in general, it has been possible to deduce the time scales for equilibration of other degrees of freedom. These times are summarized below [22]:

Charge to mass ratio	$\tau_{Z/A} \approx 10^{-22}$ s
Kinetic energy	$\tau_E \approx 3 \times 10^{-22}$ s
Angular momentum	$\tau_l \approx 1.5 \times 10^{-21}$ s

Deformation	$\tau_{def} \approx 5 \times 10^{-21}$ s
Mass	$\tau_A \approx 6 \times 10^{-21}$ s

This information makes it possible to describe the time evolution of a heavy ion collision.

When the two nuclei first come into contact, if their charge to mass ratios are different, the system looks very much like a giant dipole resonance and so oscillations might occur which are characteristic of such a resonance. The phonon energy of a giant dipole resonance in an ordinary nucleus is given by the empirical formula [23],

$$\hbar\omega \approx \frac{78}{(A_1 + A_2)^{1/3}} \text{MeV} \tag{2.26}$$

which is about 11 MeV in this mass range and much larger than the driving potentials associated with the equilibration of other degrees of freedom. So equilibration of Z/A can occur as a result of these oscillations in a very short time period.

During the next stage a neck is formed and kinetic energy is converted to excitation energy via nucleon exchange and angular momentum is dissipated. Although particles are exchanged, mass equilibration is as yet unfavoured for thermodynamic reasons: in a Fermi gas, the specific heat capacity is given by $C_V = 2aT$, where T is the temperature and a is the level density parameter. Suppose the fluxes of particles between the fragments are the same. The smaller fragment has the smaller heat capacity, and so will grow hotter, giving rise to a temperature gradient in the system. Because of this, a net flow of particles to the heavy fragment will develop to equalize the system's temperature. In this way energy may become equilibrated, but the mass asymmetry of the system can grow.

Once energy is fully dissipated, the net particle flow between the two fragments can lead to mass equilibrium.

2.8 Symmetric Entrance Channels

By using a symmetric entrance channel, it might be possible to obtain information on how the mass variance evolves as a function of time. If the variance were the same for all observation angles, this would show that it reaches the statistical limit before energy relaxation is achieved. Furthermore, might the mass distribution itself change as function of angle? As in this mass range and at these angular momenta, the sudden potential reaches its maximum value at symmetry, whereas the adiabatic potential has a minimum at symmetry. This would yield information on the time associated with the change from a sudden to an adiabatic potential.

By making similar systems with both symmetric and asymmetric entrance channels, it should be possible to determine unambiguously whether there really is an entrance channel dependence or if a gradual transition from asymmetric to symmetric fission takes place as energy is increased. The fission hypothesis could not explain the evolution with angle, but this has only been observed for two, very similar, systems and is not very well reproduced by the diffusion model.

For these reasons we examined the fissionlike yields of both symmetric and asymmetric entrance channels, leading to similar compound nuclei.

2.9 Other Possible Explanations

Other models exist which may be able to explain the results of Oeschler and others. These are fission models and so are inconsistent with the observation of a drift towards symmetry at forward angles. However it may be that several reaction mechanisms are involved and the mechanism leading to symmetry is forward peaked.

2.9.1 Asymmetric Fission

The fission saddle point's properties are determined by competition between the various forces within the nucleus.

The Coulomb force favours fission into two equal parts (symmetric fission), so that the total Coulomb energy of the system is minimized. However the surface tension will tend to make one nascent fragment suck the other up, in order to reduce the surface area and hence the surface energy.

Calculations of saddle point energies as a function of mass asymmetry for different fissilities are shown in figure 2.8.

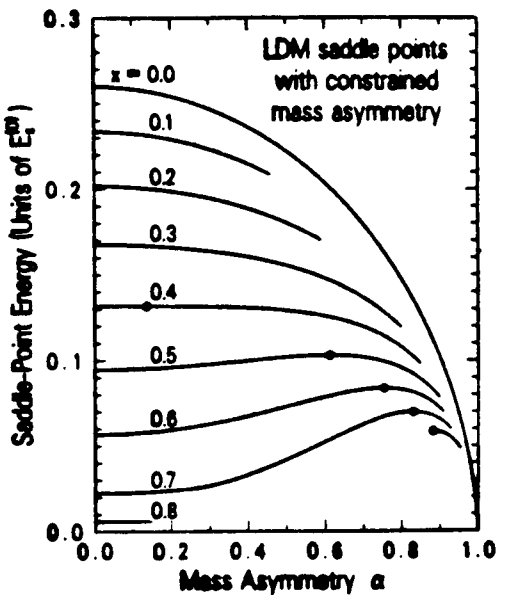


Figure 2.8. Saddle point energies as a function of mass asymmetry for different values of the fissility x. The dots indicate the Businaro-Gallone family of saddle points [24].

Consider a very heavy nucleus (large x). In this case, the Coulomb force is dominant and so symmetric fission prevails. If the masses of the two fragments are denoted by M_1 and M_2, then the mass asymmetry α is defined by

$$\alpha = \frac{M_1 - M_2}{M_1 + M_2} \tag{2.27}$$

$\alpha = 0$ for symmetric fission and $\alpha \approx 1$ for particle evaporation. As α increases from 0, the energy of the saddle point increases, until it reaches a maximum

value. This is known as the Businaro-Gallone saddle point [25]. The saddle point energy then falls to zero at $\alpha = 1$, due to the reduction of the Coulomb repulsion between the two fragments.

For lighter nuclei, the surface tension competes with the Coulomb repulsion more strongly. As a result the energy difference between the symmetric and Businaro-Gallone saddle points is smaller. For sufficiently small x, this energy difference becomes zero and the minimum at symmetry disappears, making asymmetric fission more favourable. The point at which this happens is known as the Businaro-Gallone transition and occurs at $(Z^2/A)_{BG} = 19$ (equivalent to $x = 0.394$) [9] in the liquid drop model. The centrifugal force is repulsive, like the Coulomb force, and so giving a nucleus angular momentum is, to a first approximation, like increasing its charge. Thus nuclei below the transition point may fission symmetrically if given enough angular momentum.

This value for $(Z^2/A)_{BG}$ of 19 is below the values for the systems discussed here and so they should fission symmetrically. However, a more realistic model of the nucleus (the rotating finite range model) predicts that the Businaro-Gallone transition should take place at a higher fissility.

Unlike the RLDM, the rotating finite range model (RFRM) takes into account the effects of the finite range of the nuclear force and the diffuseness of the nuclear surface.

The main differences between the predictions of this model and the RLDM are; that the fission barriers in the mass 80 region are lower [26], and the Businaro-Gallone transition is moved to higher fissility ($(Z^2/A)_{BG} \approx 23$) [27]. The value for $(Z^2/A)_{BG}$ is higher than for systems in the mass 80 region, so asymmetric fission might be expected, although the large angular momenta of the systems may bring them above the transition.

Such an effect could explain all the observations, except for the evolution with angle. An experiment by Sobotka [28] and co-workers provides evidence for the RFRM prediction of the Businaro-Gallone transition.

2.9.2 Q-Value Effects

When actinide nuclei fission – provided they are not too highly excited – the final fragment mass distributions tend to be slightly asymmetric. For a wide range of nuclei, the most probable light fragment mass increases linearly with the mass of the fissioning nucleus, while the most likely heavy fragment mass remains constant at ≈ 140 [8]. Fragment masses around 140 are especially favoured because of shell effects in the final nucleus. The existence of a closed proton shell at $Z = 50$ and a closed neutron shell at $N = 82$ make the final fragment almost doubly magic.

In this way the relative stabilities of each of the possible final products can have a dramatic effect on the final fission mass distribution. However this is only true for low excitation energy. As the nucleus is given more and more excitation energy, the distribution becomes more and more symmetric.

Comparison of the results of Oeschler et al. with the ground state Q-values for binary splitting of the compound nucleus reveals a strong correlation between the two (see figure 2.5). Could it be that the reactions have a large component which is Q-value dependent? This could happen if the systems are formed with low excitation energy above the rotational ground state, so that fluctuations in the potential energy surface due to nuclear structure become important. Lee et al. [29] propose such a mechanism to explain all the experimental results interpreted as evidence for intermediate processes.

The system ^{40}Ca + ^{40}Ca provides a stringent test of this. Its ground state Q-values have a small peak at ^{28}Si. So the observation of an enhancement of the ^{28}Si + ^{52}Fe decay channel would provide evidence for this.

2.10 Other Phenomena of Interest

The study of the fissionlike properties of nuclei in the mass 80 region is of interest for several other reasons. Most significant of these is the possible existence of superdeformation.

2.10.1 Superdeformation

The single particle levels within a nucleus are not evenly spaced, but fall into nearly degenerate groups known as shells. Because of the nonuniformity of the single particle energy levels, the nuclear binding energy does not vary smoothly with particle number, but exhibits variations depending on how full the shells are – closed shells being very tightly bound.

If we start with a spherical nucleus and deform it, the energies of the levels will change and the degeneracies will start to disappear. However, if the shape of the nucleus becomes highly symmetric (such as a prolate spheroidal shape with a 2:1 axis ratio), then new degeneracies will appear, giving rise to new shell structure at large deformations. This phenomenon is known as superdeformed shell effects. A closed shell at such deformations is especially stable.

Historically, the first direct evidence for superdeformation came with the discovery of low spin isomeric states in the fission decay of some of the actinide nuclei [30]. These states exhibit unusually short spontaneous fission half lives (tens of milliseconds compared with typical values of hundreds of years or more for this region of the periodic table) which suggests they decay without having to penetrate the whole fission barrier. This can be explained if the states occur in a second minimum in the nuclear potential energy surface, which is caused by the existence of superdeformed shell gaps in this mass region.

Both simple and complex calculations predict that such shell effects should also occur in the vicinity of $N \approx Z \approx 40$. Evidence for their existence could

be obtained by measuring the fission properties of a series of isotopes. Quantities such as fission barrier heights, total kinetic energies and mass distributions should show sharp variations characteristic of shell effects. Because of this the study of fission reactions in this mass range is of great importance.

The easiest way to understand superdeformation is to treat the nuclear potential well as a deformed harmonic oscillator. In particular consider the case of an axially symmetric oscillator. How the energy levels vary with deformation is shown in figure 2.9. The deformation can be described by δ.

$$\delta = \frac{\omega_\perp - \omega_z}{\widetilde{\omega}} \tag{2.28}$$

where ω_z is the oscillation frequency along the symmetry axis, $\omega_\perp$ is the oscillation frequency perpendicular to it and $\widetilde{\omega}$ is the average oscillation frequency.

The total single particle energy (E_{sp}) is not the same as the total nuclear energy. However, the deviation of E_{sp} from a smooth function of deformation and particle number (denoted by $\widetilde{E}_{sp}$) is expected to represent the shell structure (E_{sh}). $\widetilde{E}_{sp}$ can be obtained by smoothing the discrete levels into a continuous spectrum (this is known as the Strutinsky prescription [31]) or by taking the asymptotic form of the single particle energy corresponding to a very large number of particles [32]. To illustrate this figure 2.10 shows the predicted shell corrections for a series of zirconium isotopes in the harmonic oscillator model. Note the large negative energy corrections for a 2:1 axis ratio.

A more sophisticated model corrects for the fact that the harmonic oscillator does not represent the true nuclear potential well by adding a term proportional to l^2 and a spin-orbit term to the harmonic oscillator Hamiltonian. This is called the Nilsson model. Alternatively, a Woods-Saxon potential may be used. This model also predicts the occurrence of superdeformation in this mass region [33]. To obtain the total binding energy, the liquid drop model energy is added to the shell corrections.

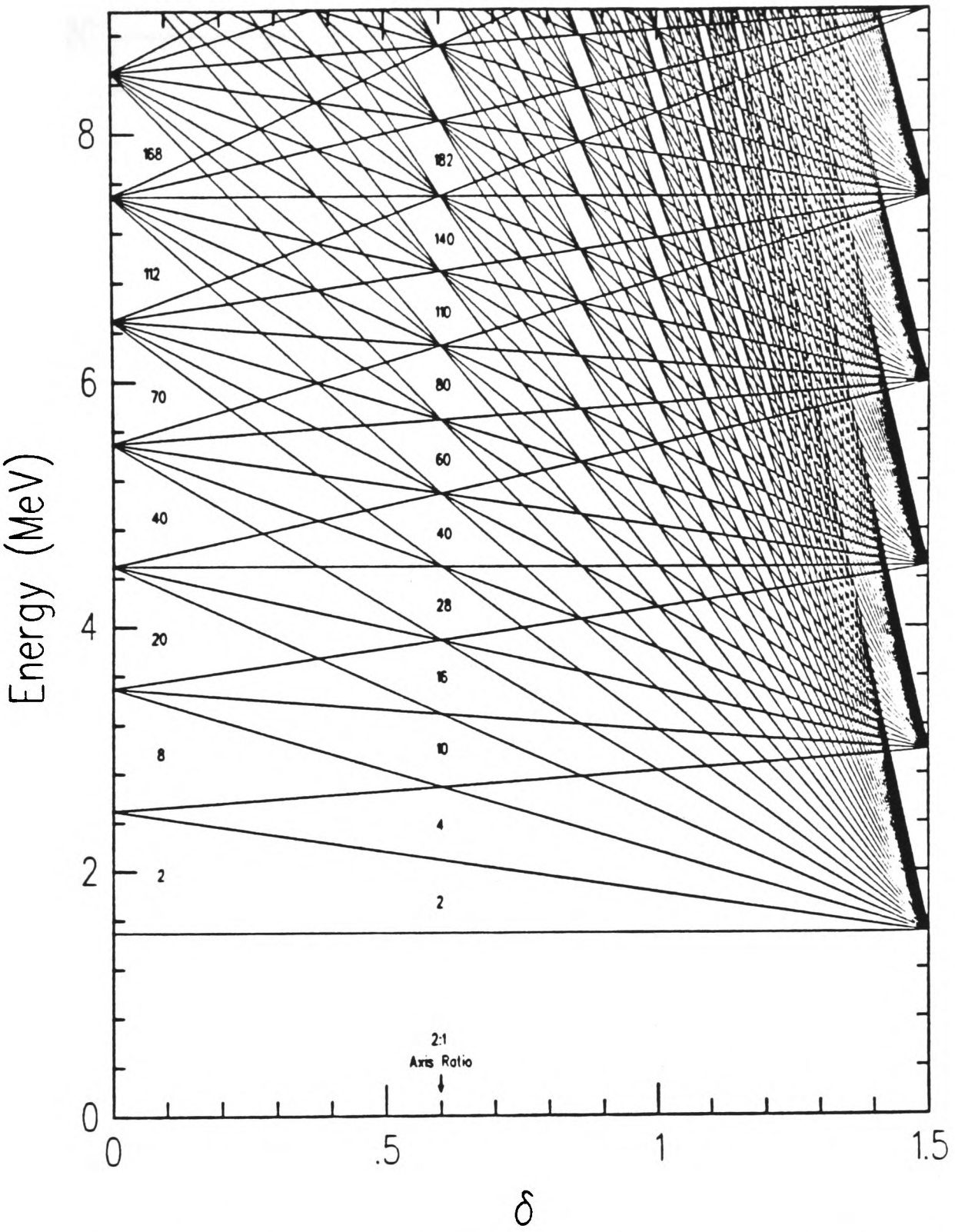


Figure 2.9. The variation of the harmonic oscillator energy levels with deformation, under the constraint of axial symmetry. Note the high degeneracies when the axis ratio is 1:1 (δ=0) and 2:1.

2.10.2 Alpha-Particle Clustering

The α-particle has a very high binding energy. Because of this, light nuclei can behave like clusters of α-particles.

When light $N = Z = even$ nuclei fission, they tend to do so preferentially

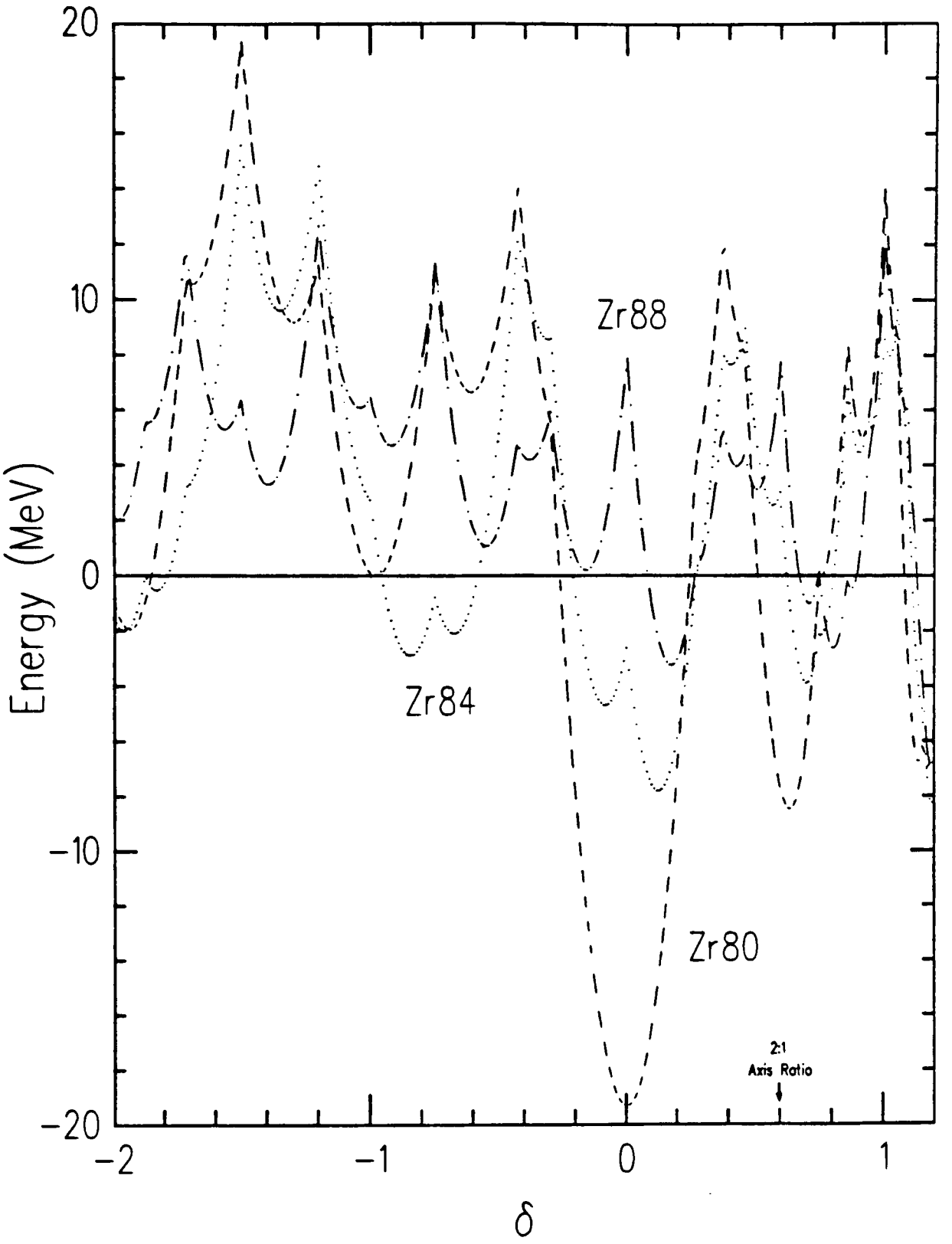


Figure 2.10. An illustration of shell effects. Shell corrections for ^{80}Zr (dashed line), ^{84}Zr (dotted line) and ^{88}Zr (dot-dashed line) calculated by subtracting a smooth function of deformation from the total single particle energies in a harmonic oscillator potential well.

into two sets of α-particles, again because of the high stability of the α-particle. ^{80}Zr is the heaviest $N = Z = \textit{even}$ nucleus that can be made using a stable beam and target, without primary decay. Does ^{80}Zr possess the properties of its lighter counterparts, or does no α-particle structure exist for such a heavy

system? Measurements of fission yields from ^{80}Zr can tell us which is the case.

2.11 Summary

In this chapter we discuss the reasons for carrying out the experiments described in this thesis and the models pertinent to the interpretation of the results from them.

Asymmetric entrance channel measurements suggest a target and beamlike decay with a fully relaxed Q-value. This is taken as evidence for an extreme kind of long-lived deep inelastic reaction, known as an intermediate process.

Other possible interpretations of these results exist; the most notable being the possibility of a ground state Q-value dependence and asymmetric fission due to the Businaro-Gallone transition.

Fission cross section measurements in this region are of interest because of the possibility of superdeformation and, in the case of the system ^{40}Ca + ^{40}Ca, because of the possibility of α-particle structure in the mass distributions.

Chapter 3

Detection Techniques

The gods are just, and of our pleasant vices
Make instruments to plague us.

William Shakespeare, *King Lear*

3.1 Introduction

The detection system is one of the most important parts of any experiment. A wide range of detectors has been developed for nuclear physics. Those used for heavy ions generally work by collecting some or all of the particle's kinetic energy in a volume of material. This energy is then converted to an electrical pulse. The use of sophisticated electronics, coupled with computer analysis, enables complex manipulation of these electrical signals, to extract the properties of the detected particle, such as its energy, mass and charge.

This chapter looks at how these properties may be measured and describes the particular types of detector used for the experiments described in this thesis. Section 3.2 deals with the concepts employed in mass and charge determination.

Mass determination is usually achieved by using a time of flight telescope in conjunction with an energy detector. The start signal is provided by a thin transmission detector. Section 3.3 describes the design, construction and development of a hybrid parallel plate avalanche counter for use as a start detector

in the ^{28}Si + ^{50,52,54}Cr experiment. Charge determination was achieved in the ^{40}Ca + ^{40}Ca experiment by using a detector telescope consisting of a multiwire counter and a Bragg curve spectrometer (BCS). These particular detectors are described in section 3.4.

3.2 Concepts of Particle Identification

3.2.1 Mass Determination by Time of Flight Measurement

The time of flight telescope is one of the most convenient ways of determining a heavy ion's mass, when used in conjunction with an energy detector. It consists of two transmission detectors separated by a large distance, with a thick stop detector – to measure the energy – placed behind them. These transmission (or Δ E) detectors are used to provide timing information. Often there is only one timing detector, in which case the stop detector is also used to provide the second timing signal.

Some types of accelerator, such as the linac, instead of delivering a continuous beam produce a series of pulses, which are typically 10^{-7} seconds apart. In this case, the accelerator itself can be used to provide the timing pulse, thereby eliminating the need for a start detector. By the use this method, very good timing resolution ($\approx$ 100 ps) is possible. However, the generally available Van de Graaff accelerators, such as the Nuclear Structure Facility at Daresbury Laboratory, produce a continuous beam.

For a non-relativistic particle of energy E and time of flight t, the mass A is simply given by

$$A_{amu} = 1.9297 E_{MeV} t^2_{ns} / l^2_{cm} \tag{3.1}$$

where l is the flight path.

As the errors in these quantities are uncorrelated, the uncertainty in A (denoted by δA) is given by the expression

$$\frac{\delta A}{A} = \left[\left(\frac{\delta E}{E} \right)^2 + \left(\frac{2\delta t}{t} \right)^2 \right]^{\frac{1}{2}} \tag{3.2}$$

assuming negligible uncertainty in l. δt and δE are determined by the properties of the detectors and so are fixed. To obtain optimum mass resolution, a large time of flight and thus a large flight path is needed. However the greater the flight path, the smaller the solid angle and hence the smaller the count rate. So a compromise has to be made between statistics and resolution. Furthermore, if $\delta E/E$ is greater than $\delta t/t$, then the mass resolution is dominated by the energy resolution and an increase in flight path produces no improvement. In practical situations, l is chosen so that $\delta t/t$ and $\delta E/E$ are roughly equal.

3.2.2 Charge Determination

At energies of several MeV, the main process by which a charged particle loses energy in passing through a volume of gas is the transfer of kinetic energy to atomic electrons. The rate of energy loss is given by the well known Bethe-Bloch formula [34]:

$$-\left(\frac{dE}{dx} \right) = \frac{n_1 Z_1 Z^2 e^4}{8\pi\epsilon_0^2 m_e v^2} \left[\log \frac{2m_e v^2 W_{max}}{I^2 (1-\beta^2)} - 2\beta^2 \right] \tag{3.3}$$

where Z is the particle's charge, v $(= \beta c)$ its velocity, m_e is the mass of the electron, Z_1 is the atomic number of the stopping material, which has n_1 atoms per unit volume, W_{max} is the maximum energy transferred to an electron and I is the mean excitation potential for the atoms of the stopping material. Now the logarithmic term varies slowly with energy and hence is approximately constant.

If we multiply the top and bottom of equation 3.3 by the mass of the charged particle (M) and take the non-relativistic limit for the energy, we get the relation

$$-\left(\frac{dE}{dx}\right) \propto \frac{MZ^2}{E} \tag{3.4}$$

Thus the ionization the particle produces depends strongly on its charge, mass and energy. A detailed measurement of this ionization can be used to identify the particle. Several detectors have been devised which measure the properties of particles in this way. The most common types are the Bragg curve spectrometer and the ionization chamber.

3.3 Development of a Hybrid Avalanche Counter

3.3.1 Types of Timing Detector

The most common type of timing detector are the silicon surface barrier, the microchannel plate, the parallel plate avalanche counter and the multiwire proportional chamber.

The timing resolution of E-ΔE telescopes comprising surface barrier detectors can be very good: values as low as 160 ps have been obtained [35].

Their main advantage is that they can be used for charge – as well as mass – identification. The use of these detectors to obtain timing information is made difficult by a process called plasma delay: the plasma produced in the detector, by heavy ions, is very dense and tends to shield electron-hole pairs from the external electric field, thus inhibiting charge collection at the electrodes. So there is a variable time difference between charge production and collection.

This variation is typically several nanoseconds. There are empirical formulae for plasma delay: examples include that due to Neidel et al. [36].

When a charged particle passes through matter, it produces secondary electron emission. The object of the channel plate is to collect the secondary electrons emitted from a thin foil and multiply them. Low energy electrons produced in the foil are accelerated towards the channel plate, where they are multiplied before being collected. Examples of these detection systems can be found in [37].

This type of detector must be operated in a high vacuum. Also the detector and the foil need to be well separated, as there has to be room for the incoming particles to pass through. Further problems include the vulnerability of the thin foils to vibrations and pressure fluctuations.

The parallel plate avalanche counter (PPAC) is an inexpensive, rugged device which can be built with the facilities available in the typical laboratory.

A PPAC consists of two thin ($\approx 100\ \mu g/cm^2$), metallized plastic films separated by an insulating spacer. This assembly is placed inside a vessel, through which gas is circulated and which has thin entrance and exit windows. A high voltage is applied across the films to produce a large internal field (≈ 500 $V(cm.mbar)^{-1}$). It is imperative the foils be as parallel as possible to ensure a uniform electric field. Any charged particle passing through the gas causes ionization. The primary electrons produced travel towards the anode, and on the way cause more and more ionization, giving rise to an avalanche. The external electric field does work in moving the electrons towards the anode. The energy for this is provided by the voltage source, which tries to maintain a constant potential difference by changing the charge on the electrodes. The variation in this charge constitutes a current signal.

Because of their ease of construction and robustness, very large avalanche counters can be made to cover large solid angles. But the larger the counter, the worse the timing resolution. They can accommodate count rates of up to $10^6\ s^{-1}$, but are susceptible to background electrons and must be shielded from

them. Position sensitive detectors can be made by placing grids of thin wires between the electrodes.

Their main disadvantage is the need for four windows (two electrode and two pressure). Ideally the metallized foils could act as pressure windows, but they would tend to buckle even under small gas pressures, thereby distorting the electric field. The passage of the detected ions through these windows leads to energy loss and energy and angular straggling, which degrade timing resolution. Fortunately it is possible to correct for most of these effects. Typical designs are given in [38].

The multiwire proportional chamber (MWPC) works in much the same way as the parallel plate avalanche counter, the main difference being that parallel planes of closely spaced, thin wires, are used to provide the field – although some designs consist of both grids and films. The spacing between the wires is small compared with the separation between planes, so that the electric field approaches that for parallel plates at large distances from the wires. These detectors have the advantage that only two gas windows are needed, rather than the two gas and two pressure ones required for a PPAC, and so the problems associated with energy loss within the windows are reduced.

Many types of multiwire counter exist. Some are fairly simple and similar to the PPAC in concept, while other designs consist of many grids. Examples can be found in [39].

Table 3.1 summarizes the types of detector discussed; their advantages; their disadvantages, and example values of the timing resolution obtainable.

A more detailed account can be found in [40].

Detector	Advantages	Disadvantages	Timing Resolution
Silicon Surface Barrier	Low band gap Charge information Commercially available	Radiation damage Plasma delay Expensive Pulse height defect	160-360 ps [35]
Channel Plate	Commercially available	Expensive High vacuum needed Foil fragile	200 ps or better [40]
PPAC	Can be made Rugged Inexpensive Position sensitive Large area	Cannot be bought Need for parallel plates Susceptible to electrons Four windows	200 ps [38]
MWPC	Can be made Inexpensive Position sensitive Rugged	Cannot be bought Susceptible to electrons Two windows	200-400 ps [39]

Table 3.1 Advantages and disadvantages of various timing detectors.

3.3.2 Design and Construction

The principal criteria in selecting the most suitable detector type for the experiments described in this thesis, were that the detection system should be able to withstand high count rates and should be inexpensive. To this end the most likely candidates were the parallel plate avalanche counter and the multiwire proportional chamber. However both have disadvantages: the PPAC has four transmission windows, which serve to degrade both energy and timing resolution, while multiwire counters often consist of many grids and so are complex in construction. Hence it was decided that a hybrid of the two types would be developed, so that both of these problems could be avoided.

The idea was to construct a detector which had the simplicity of the PPAC, but used parallel grids in place of the conventional metallized foils. The design of the detector is shown in figure 3.1.

Thin wire was wound onto a 1.5 mm thick piece of G10 (printed circuit board material) which had a layer of copper on each face and a 1cm diameter hole drilled through the centre. The wire was then glued with conducting Epoxy Resin adhesive and allowed to dry. When dry, the wires at the edges were cut, so that the two faces were electrically insulated. Conventional, non-conducting Epoxy Resin adhesive was then put on all sharp edges to prevent breakdown. The detector was then baked at 200 °C for two hours to cure the adhesives.

When dry, the grid was placed inside an airtight gas box with thin entrance and exit windows, which were made by stretching 25 μm thick polypropylene to ≈ 0.8 μm with a heated hydraulic ram [41]. The gas box is shown in figure 3.2.

Isobutane gas was circulated through the box at a typical pressure of 10 torr. The face of the grid closest to the beam was held at -500 V. The other face was connected to ground via a 15 MΩ resistor, across which the signal was extracted. A large magnetic shield was attached to the front of each detector to deflect electrons. A photograph of a completed detector is shown in figure 3.3.

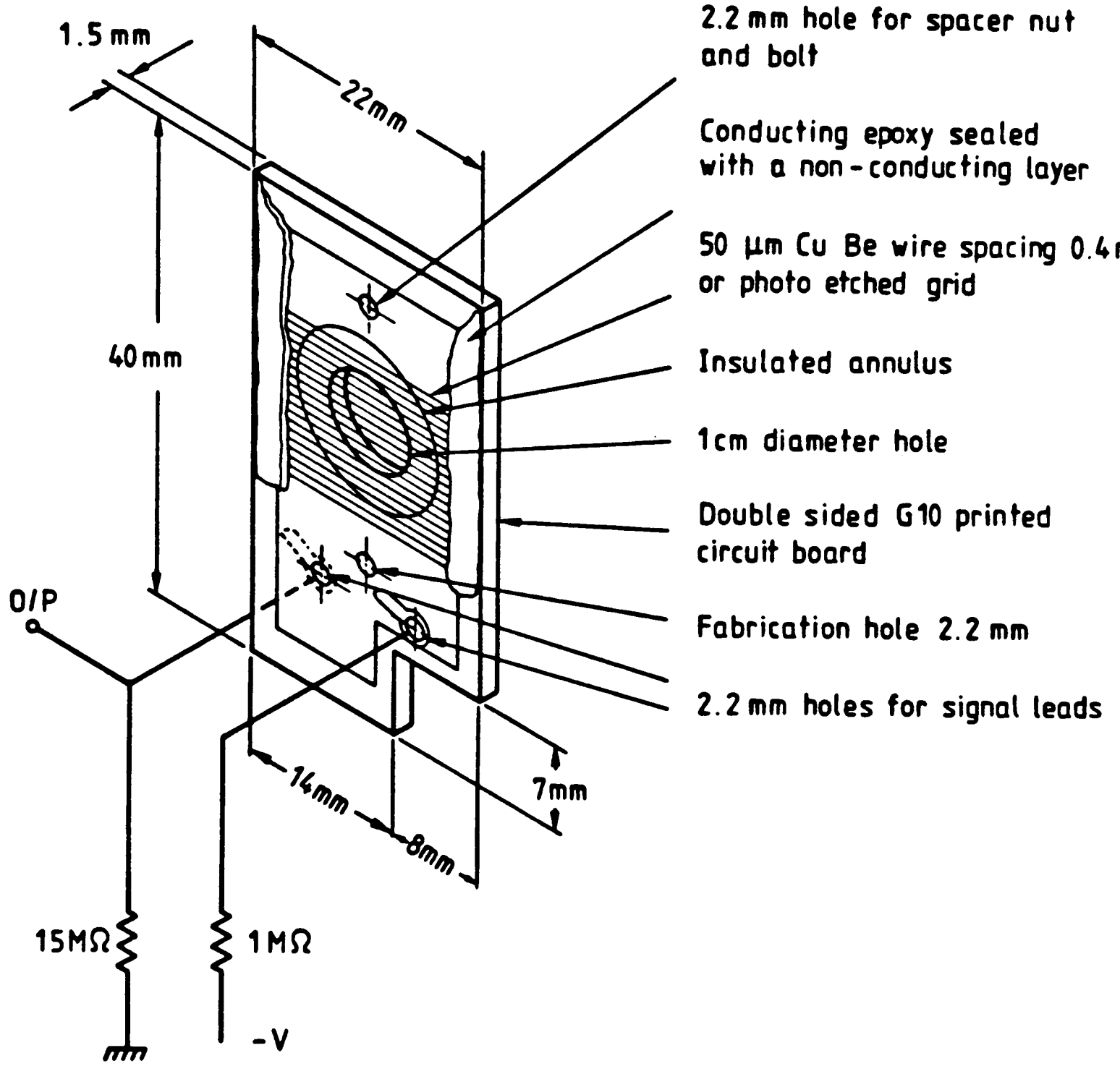


Figure 3.1. Hybrid avalanche counter design and construction details.

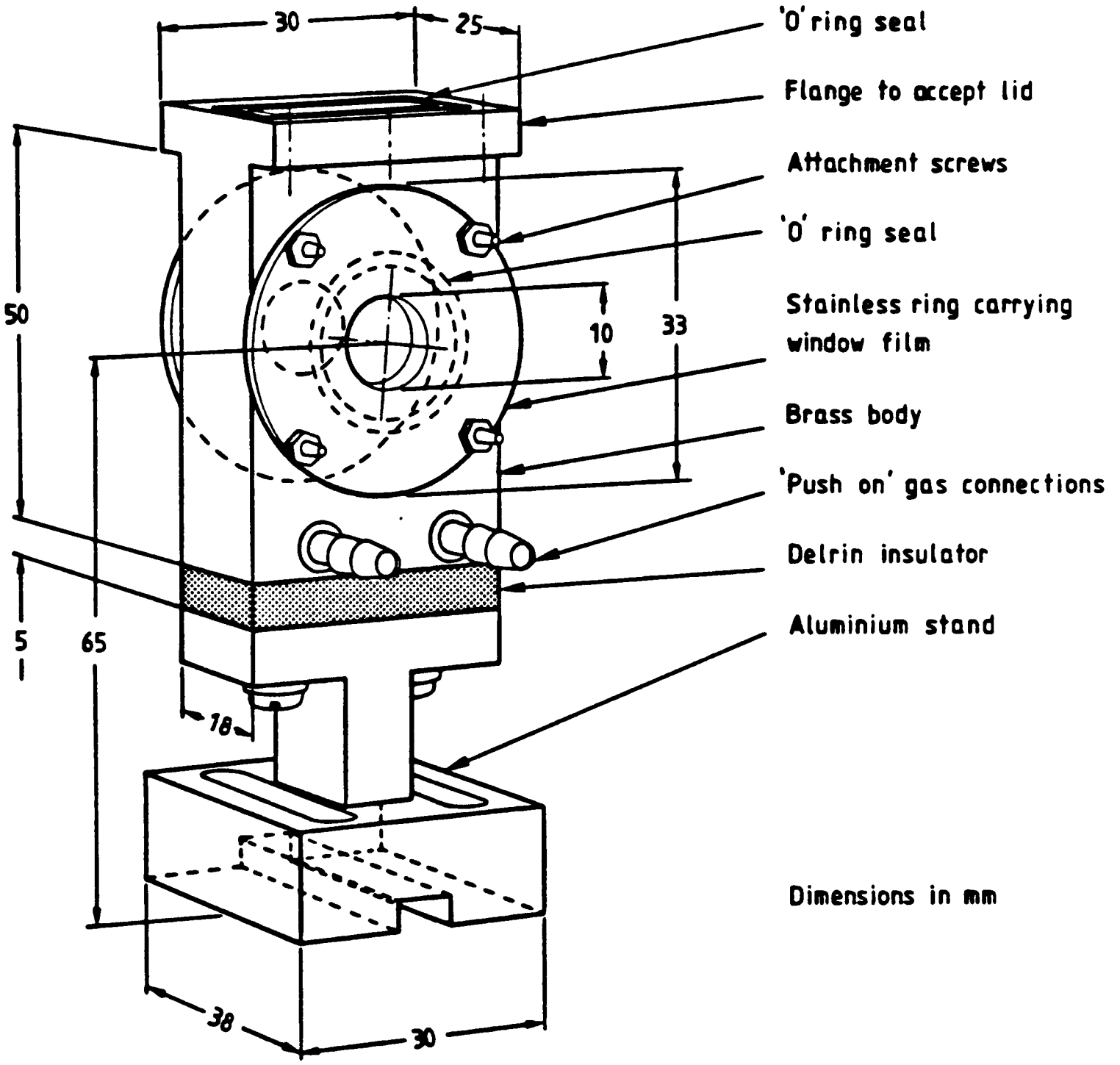


Figure 3.2. Construction of the airtight gas box. A grid would be attached to a lid and mounted in the top of the box.

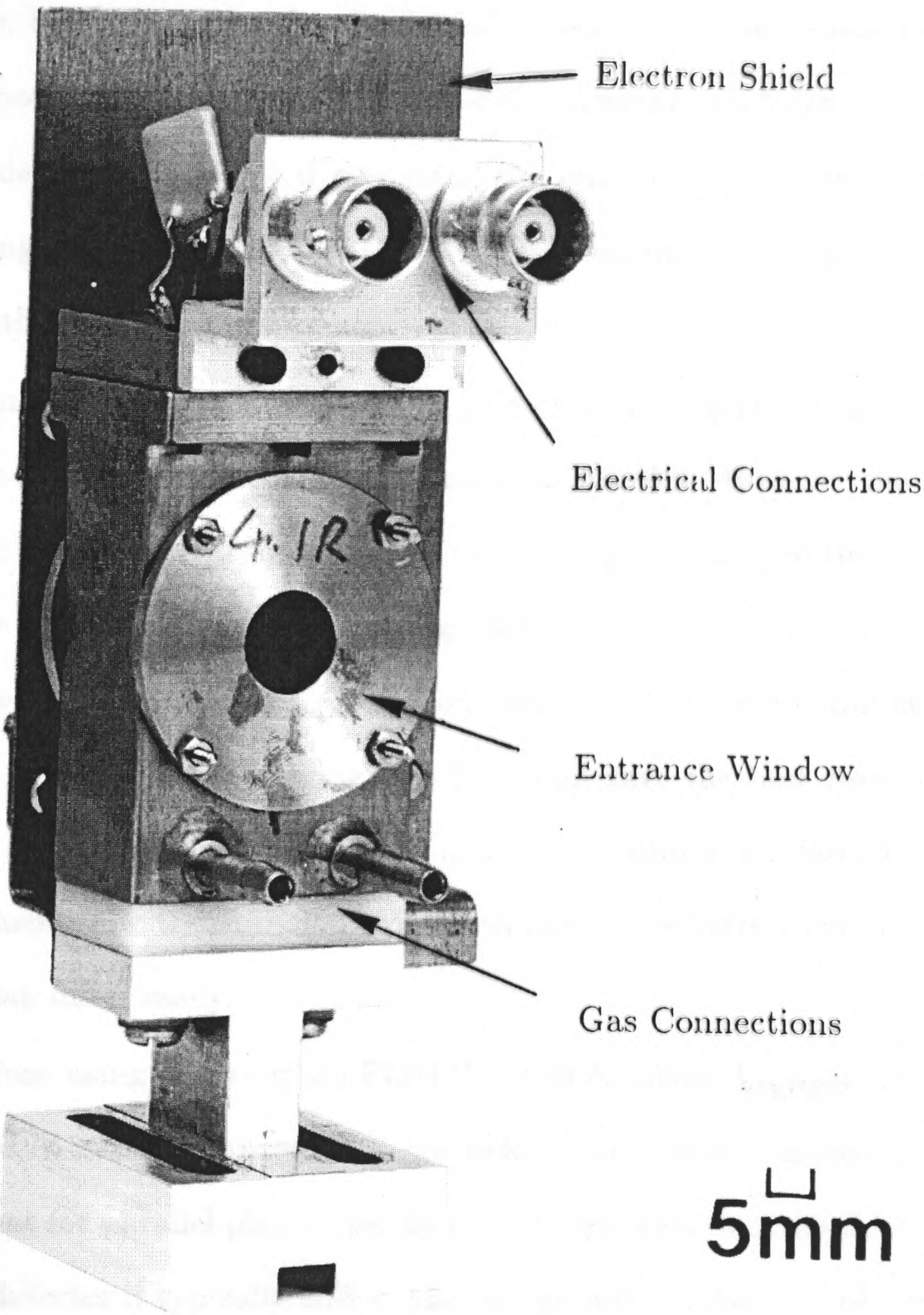


Figure 3.3. Photograph of a completed avalanche counter. Note the electron shield and the gas inlet connections near the base. The electrical connections are attached to the lid.

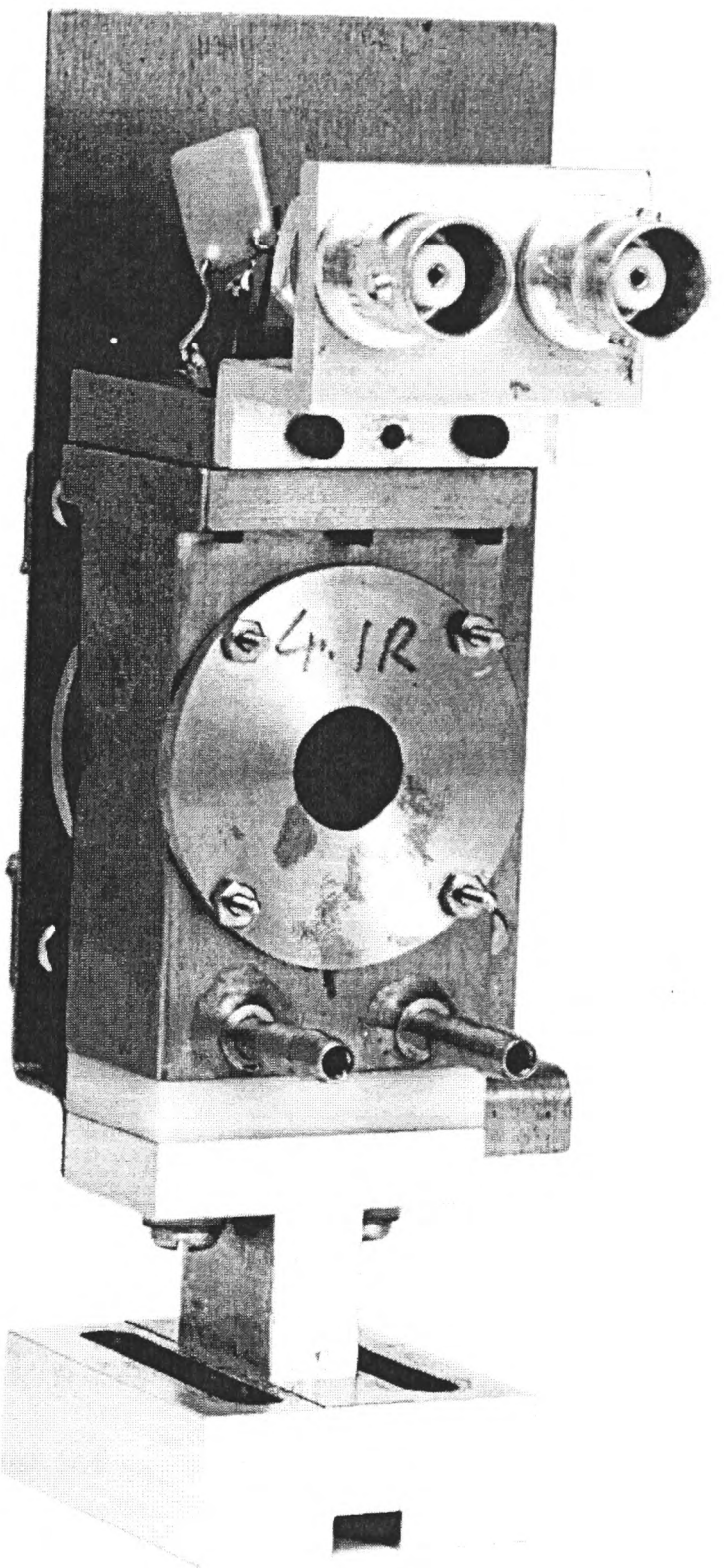


Figure 3.3. Photograph of a completed avalanche counter. Note the electron shield and the gas inlet connections near the base. The electrical connections are attached to the lid.

3.3.3 Operational Characteristics

The operation of any detector based on the PPAC concept is the subject of a compromise: too high a value for the field E causes breakdown, while too low a value does not give a large enough pulse; if the pressure p is large the timing resolution is degraded, whereas if p is small the pulse size is too small again; and the spacing x must be chosen so that it is small enough to give good timing resolution, without causing breakdown.

To obtain a high enough field with a pair of parallel grids, it is essential that the wires in each plane be as closely spaced as possible. However the closer the wires, the lower the transmission. So the wire spacing has to be carefully chosen to give good transmission and a high field.

Several wire thicknesses and separations were tried. It was found that 50 μm thick Cu-Be wire with a spacing of 0.3-0.4 mm gave the best results. For thicker wires it was impossible to get a high field without a relatively small spacing and hence low transmission. When thinner wires were used, the grids tended to break down easily.

Calculations using the program FISH [42] (which solves Laplace's equation by the method of iteration) reveal that the field for such a wire spacing closely approaches that for parallel planes (see figure 3.4) and also that the field at the centre of the detector is typically 80% of that for parallel planes. So the detector should behave very much like a PPAC. The electric field for each of the wires should be identical, and so there should be perfect symmetry between left and right and top and bottom on figure 3.4.

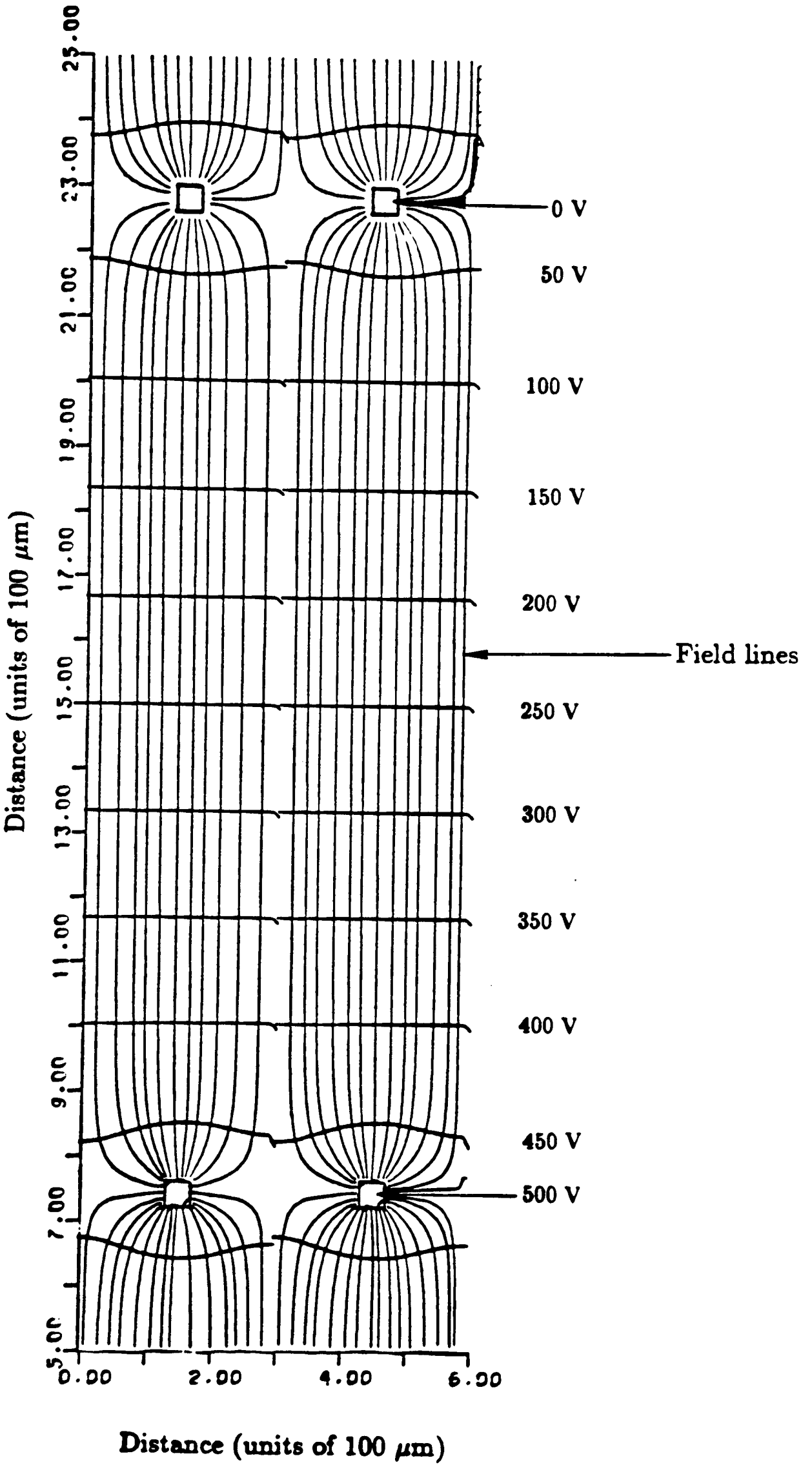


Figure 3.4. FISH calculation of the electric field due to a pair of grids made up of 40 μm wires, separated by 0.3 mm. The spacing between the grids is 1.5 mm. The potential difference across the grids is 500 V.

3.3.4 Performance

Measurements with a ^{37}Cl beam revealed that timing resolution values of as low as 350 ps could be obtained from telescopes consisting of these counters and surface barrier detectors.

As a further test, the fission yield from the reaction $^{16}O + ^{40}Ca$ was measured at 80 MeV. A typical mass spectrum is shown in figure 3.5. The results are consistent with a mass resolution ($\delta A/A$) of 0.1 for a flight path of as little as 20 cm.

In spite of these good performance characteristics, there was a problem with the detectors: after several hours continuous use, the detectors tended to become susceptible to breakdown. This could only be cured by reducing the bias voltage, which resulted in a significant reduction in efficiency. The variation of efficiency with voltage is a strong function of ion species (see figure 3.6), so to obtain reliable mass distributions, the detectors had to be operated at 100% efficiency for all species.

In an effort to remove the breakdown problem, a new method of grid manufacture, using photo-etching, has been tried. A number of photo-resist masks of the grid were placed onto 70 μm thick copper sheet. The uncovered areas were then chemically milled with ferric chloride, leaving a set of thin copper grids. With the aid of alignment holes, two of these grids were thermally bonded onto G10. In this way thin, uniform 'wires' spaced by 0.3 mm have been made. This method has significantly reduced the breakdown problem, enabling the efficient detection of α-particles from a ^{252}Cf fission source (figure 3.7).

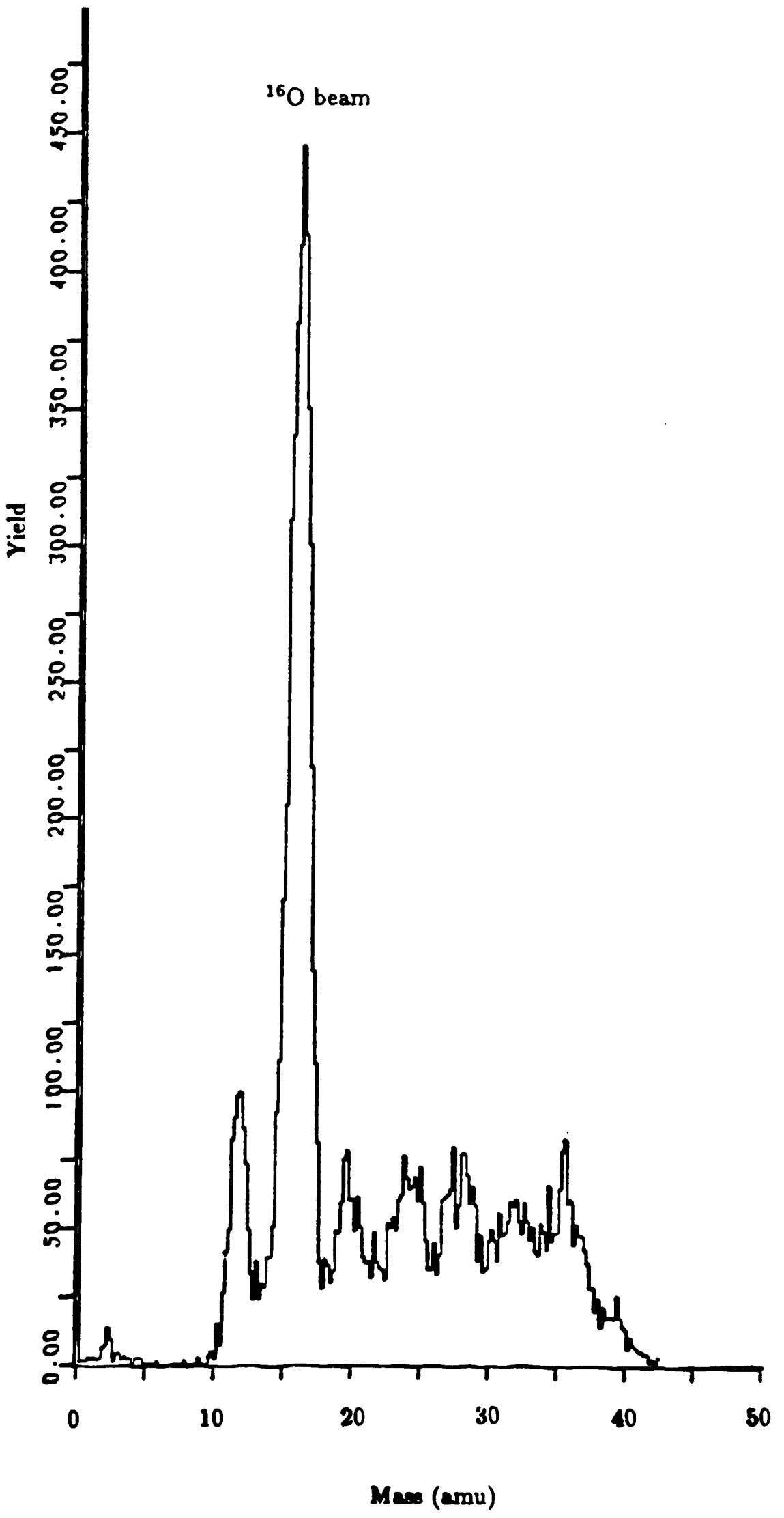


Figure 3.5. Mass spectrum from 80 MeV ^{16}O + ^{40}Ca obtained at 50°, with a flight path of 20 cm. The results are consistent with those of Sanders et al. [43].

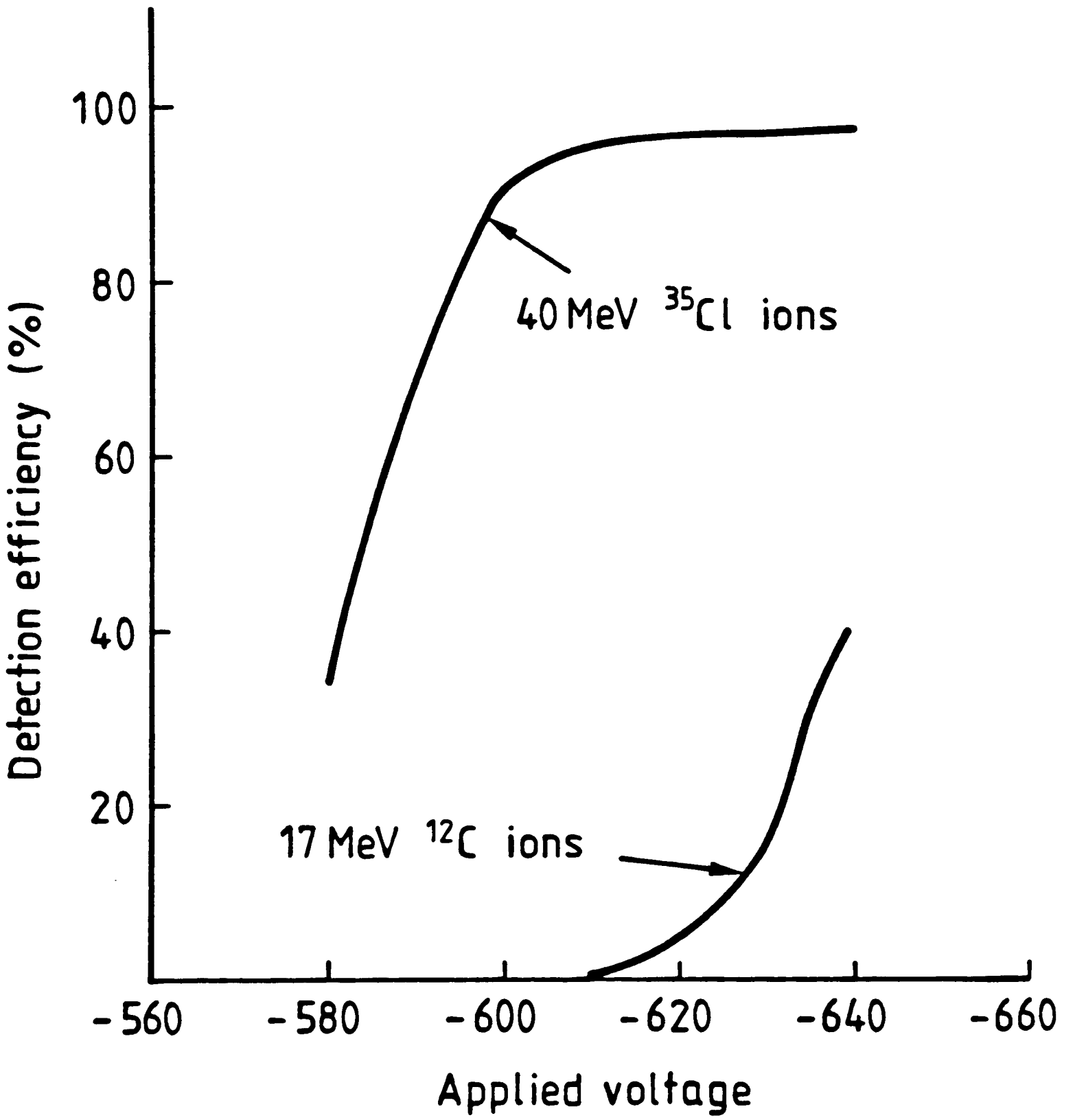


Figure 3.6. Detector efficiency as a function of bias voltage for a series of ion species. These results were obtained with a wire spacing of 0.6 mm.

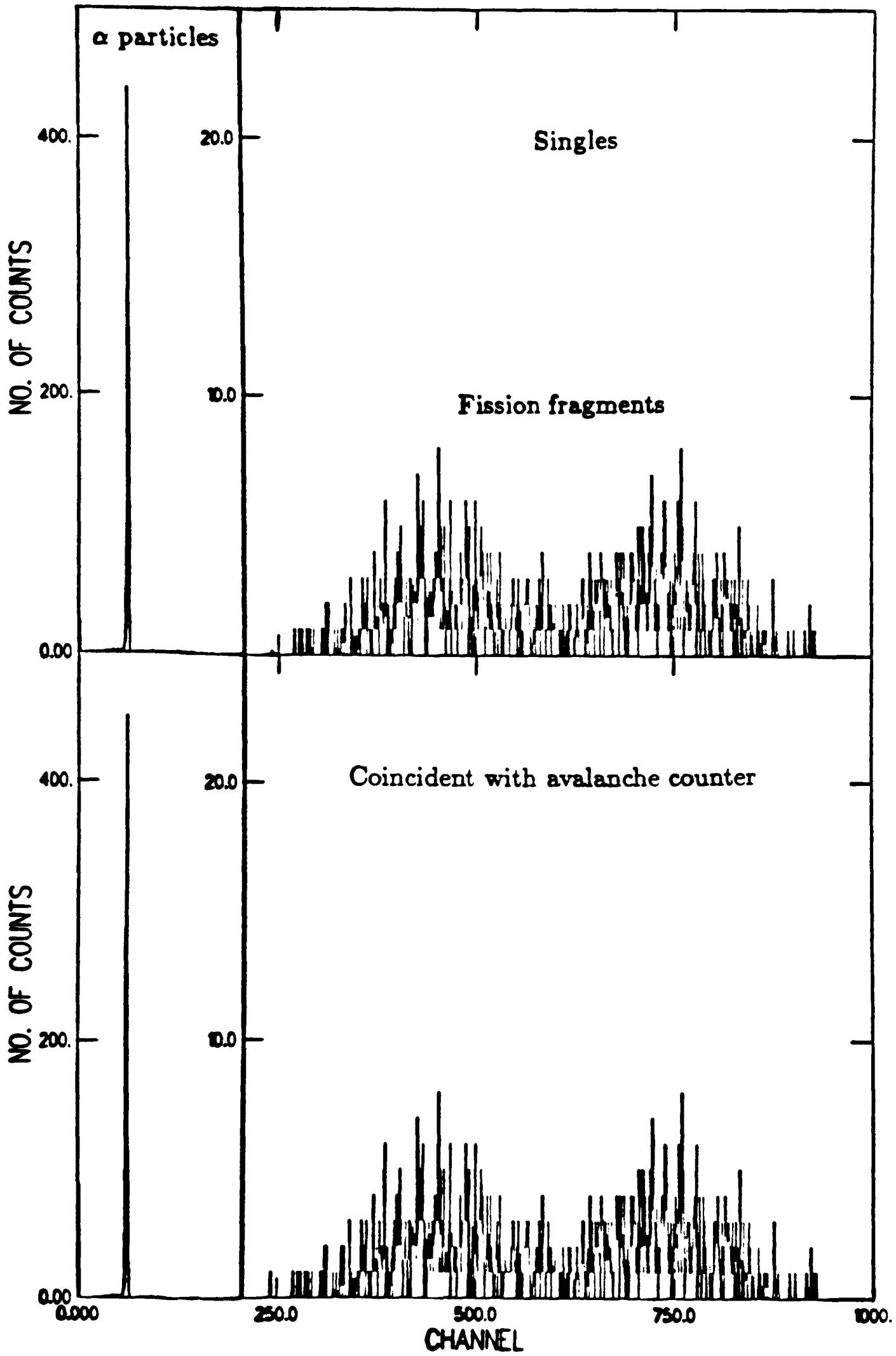


Figure 3.7. Singles and coincidence spectra from a ^{252}Cf source, obtained with a SSB-photo-etched counter telescope. The top half shows an SSB energy spectrum. The bottom half shows the same spectrum, but with the condition that the avalanche counter should fire. (Note the different scales for α-particles and fission fragments).

3.4 The MWPC-Bragg Telescope

3.4.1 The Bragg Curve Spectrometer

A schematic view of a Bragg curve spectrometer is shown in figure 3.8. It consists of a large, gas filled chamber, with a plane electrode situated at each end and a Frisch grid close to the anode. A series of guard rings is used to ensure a uniform field.

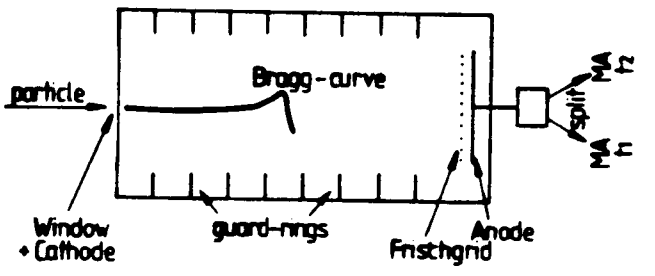


Figure 3.8. A Bragg curve spectrometer [44]. The charged particle enters through the cathode window and produces a trail of ionization known as a Bragg curve. The electrons produced then drift towards the anode, where they induce a signal, after passing through the Frisch grid.

A charged particle enters through a window in the cathode and loses energy by ionization, until it comes to rest. The primary ionization produced drifts towards the electrodes. If the electron drift velocity is constant, the electron cloud travelling towards the anode will maintain the profile of the primary ionization. This profile is known as the Bragg curve and has a distinctive shape (see figure 3.8). From the moment the particle enters the detector, its energy loss per unit distance rises steadily, until it reaches a maximum, known as the Bragg peak, it then falls to zero, as the particle comes to rest. The height of the Bragg peak (and hence the energy loss around it) is a smoothly varying function of

the ion's charge Z and is approximately proportional to it over a small region of charge (figure 3.9). So measurement of the Bragg peak can be used to determine the particle's charge. The total area under the curve (i.e. the total number of electrons liberated) is proportional to the energy E of the ion.

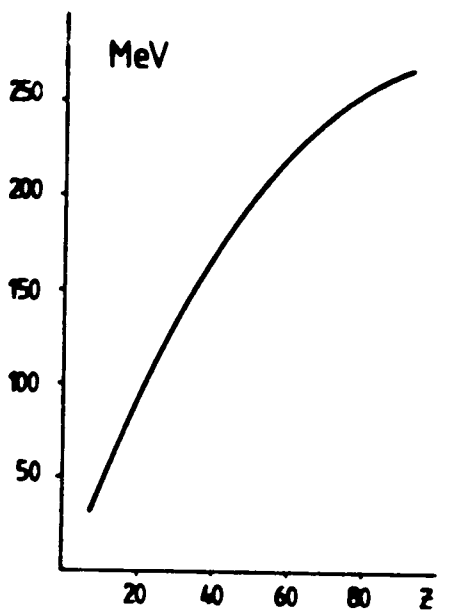


Figure 3.9. Energy loss for heavy ions in the last 20cm of their path in methane gas at 200 mbar, plotted against charge [44].

To establish the charge of the particle from the Bragg peak, it is necessary to be able to sample the electrons produced in the last few centimeters of its flight path, that is the first electrons to reach the anode. The presence of the Frisch grid makes this possible. The object of the Frisch grid is to shield the anode from the region in which the ionization is produced. Without the grid, the size of the anode signal would depend on the position of the electrons. The electrons induce little signal on the anode until they pass through the grid. So, at any given time, the signal induced on the anode only depends on the number of electrons between it and the Frisch grid.

Two signals are derived from the output pulse: firstly a long time constant amplifier is used to measure the total charge produced and hence the total energy

of the particle; secondly a short time constant amplifier is used to determine how many electrons are produced in the final portion of the particle's flight path, thus integrating around the Bragg peak, and producing a signal roughly proportional to the charge of the ion. The time constant of the second amplifier is chosen to be about the time it takes electrons from the Bragg peak to drift from the Frisch grid to the anode.

For this sort of detector to work most effectively, the charged particle must stop within the gas and ideally it should have sufficient energy such that the ionization produced reach its full Bragg peak. Since the range of an ion depends strongly on its charge, mass and energy, the gas pressure used has to be carefully chosen to ensure the particles of interest stop. This kind of detector is typically operated with an electrode spacing of 20-40 cm, a reduced field (E/p) of $\approx$ 0.1-0.5 V(cm.torr)$^{-1}$, and an anode potential of $\approx$ 2 kV.

ment is described in the paper by Vineyard et al. [45]. The details of its design are described below. It is slightly different from the conventional design, in that a wire plane, positioned 2 cm inside the entrance window, acts as a cathode. The cathode and Frisch grid are 36 cm apart and are made of 20 μm diameter tungsten wires, coated with Au and separated by 1mm. The field spacing rings are 1 cm apart and are connected to a divider chain of 100 MΩ resistors between the cathode and the Frisch grid. The anode is a copper-clad piece of G10, 3 cm behind the Frisch grid. A high field region is obtained between the Frisch grid and the anode by two field spacing rings, with 300 MΩ resistors across the gaps. As a result, the field between the Frisch grid and the anode is three times that between the cathode and the Frisch grid. The entrance window is 1.5 μm aluminized mylar foil. The entrance aperture is 8 cm by 10 cm. A photograph of the Bragg curve spectrometer is shown in figure 4.3 of the next chapter.

3.4.2 The Multiwire Proportional Chamber

The multiwire proportional chamber was built at Argonne National Laboratory [46]. Its design is similar to that of the Stelzer detector [44]. It has a biased cathode plane with grounded position sensitive anodes. It is made of three planes separated by 3.2 mm. The outer two planes (anodes) consist of wires 20 μm thick separated by 1 mm. The central plane (cathode) is a 200 $\mu g/cm^2$ foil metallized on both sides with 40 $\mu g/cm^2$ of gold. The advantage of this arrangement is that the grids electrically shield the cathode foil. 70 $\mu g/cm^2$ polypropylene foils act as gas windows. The entrance aperture is 10 cm wide and 8 cm high. A photograph of this detector is shown in figure 4.3.

Chapter 4

Experimental Details

I came to know God experimentally.

George Fox

4.1 Introduction

The object of this work was to obtain mass, energy and angular distributions from the fissionlike reactions of the systems $^{40}Ca + {}^{40}Ca$ and $^{28}Si + {}^{50,52,54}Cr$ at two bombarding energies. To achieve this, the accurate measurement of energy and time of flight at a series of observation angles was needed. Because of these objectives, it was important to ensure the experimental parameters facilitated such measurements. For example, the range of useful bombarding energies was limited by two considerations: firstly if the energy were too low, the fission cross section would be too small to obtain good statistics in a reasonable amount of time; and secondly too high an energy would see the predominance of other effects, such as deep-inelastic scattering. Other parameters of importance included detector angles and target thicknesses.

In section 4.2 we indicate how beam energies and other experimental conditions were chosen.

Section 4.3 describes each aspect of the $^{40}Ca + ^{40}Ca$ experiment at Argonne National Laboratory. First of all the experimental apparatus and setup are discussed. Then an account is given of the electronics configuration used, after which we describe the procedure followed.

In section 4.4, we present details of the $^{28}Si + ^{50,52,54}Cr$ experiment at Daresbury Laboratory. The discussion follows the pattern of section 4.3.

4.2 Experimental Parameters

4.2.1 Beam Energies

The program CASCADE [47] was used to calculate expected fission cross sections (σ_f) for a range of beam energies. The results of these calculations for the system $^{28}Si + ^{50}Cr$ are shown in figure 4.1. They predict that these cross sections should rise rapidly in the laboratory energy region between 130 MeV and 150 MeV. Below 130 MeV the cross section is small, as particle evaporation becomes dominant. Above 150 MeV the cross section reaches a plateau, because higher partial waves are unable to fuse. Thus laboratory energies of 130 MeV and 150 MeV were chosen. In all these calculations, the fission barriers were estimated by taking the values given by the RLDM of Cohen et al. [9] and scaling them by 0.6 as suggested by Guillaume et al. [19]. The level density parameters for fission and for particle evaporation were both set to $A/8$ MeV^{-1}, where A is the mass of the compound nucleus. All other parameters used in these calculations were determined in the same way as those for the calculations described in section 6.3.

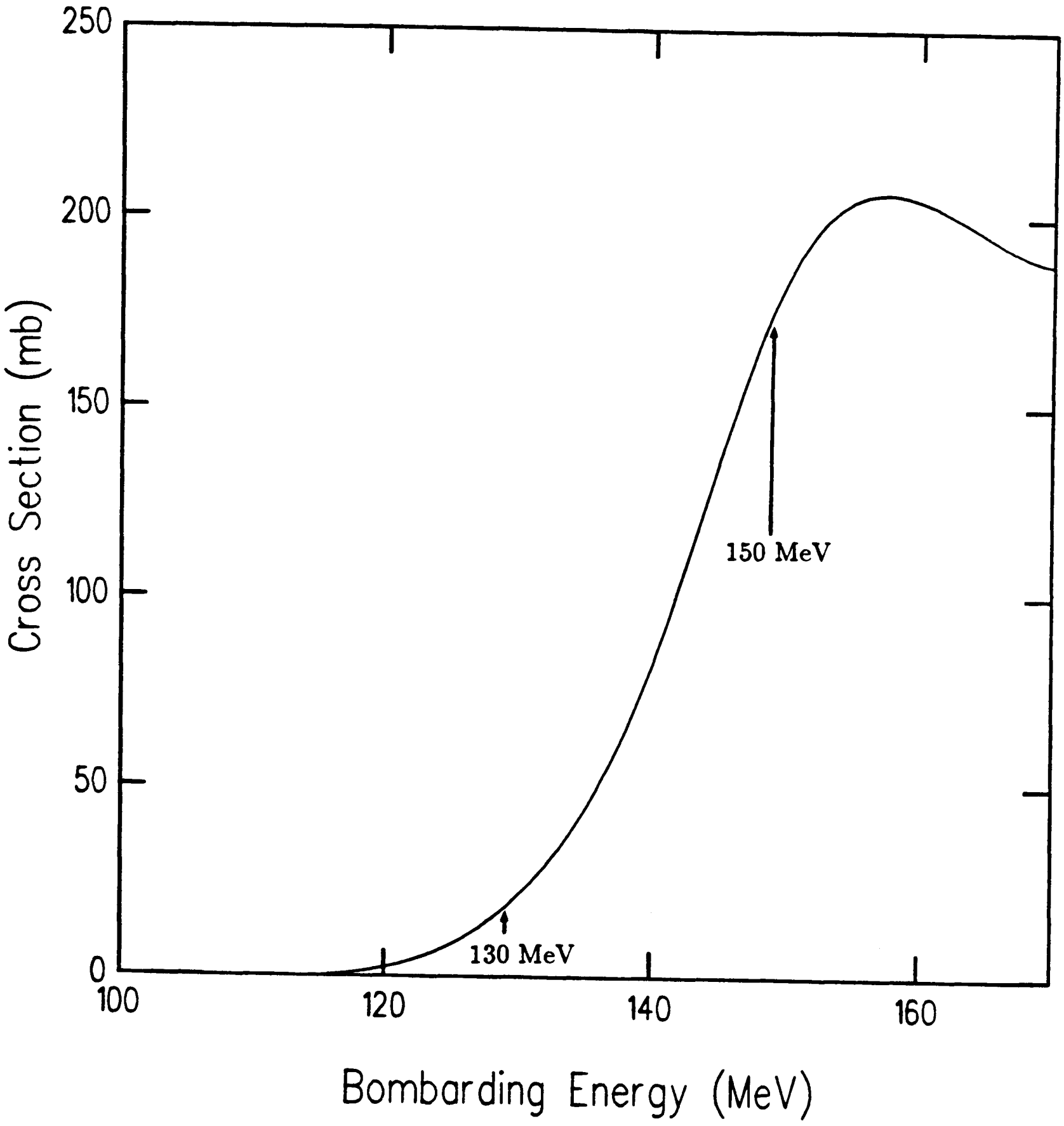


Figure 4.1. CASCADE predictions of fission cross section, as a function of bombarding energy, for the system $^{28}Si + ^{50}Cr$. Bombarding energy is in the laboratory frame. The two beam energies used in the experiment are indicated.

When Oeschler et al. [18] compared different systems, they carefully chose the centre of mass energy E_{cm} for each system such that the ratio of E_{cm} to the Coulomb barrier V_C was constant. The same criterion was used in this work. For the ^{28}Si + ^{50,52,54}Cr measurement, at energies of 130 and 150 MeV, $E_{cm}/V_C \approx 1.6$ and 1.9 respectively; with corresponding energies for the ^{40}Ca + ^{40}Ca system of 200 and 230 MeV. A summary of the salient information is listed in table 4.1.

System	$\mathbf{E}_{lab}$ (MeV)	$\mathbf{B}_n$ (MeV)	$\mathbf{B}_f$ (MeV)	$\boldsymbol{\sigma}_f$ (mb)	E_{cm}/V_C
^{28}Si + ^{50}Cr	130	13.8	6.5	21.68	1.62
	150		2.5	183.63	1.87
^{28}Si + ^{52}Cr	130	12.9	7.4	19.70	1.65
^{28}Si + ^{54}Cr	130	12.3	7.4	21.23	1.69
^{40}Ca + ^{40}Ca	200	15.0	1.7	101.07	1.66
	230		1.3	154.44	1.91

Table 4.1 CASCADE predictions for the systems studied, along with other relevant information. $\mathbf{E}_{lab}$ denotes the bombarding energy in the laboratory frame, $\mathbf{B}_n$ is the neutron binding energy, $\mathbf{B}_f$ is the fission barrier, $\boldsymbol{\sigma}_f$ signifies the predicted fission cross section and E_{cm}/V_C is the ratio of centre of mass energy to Coulomb barrier.

4.2.2 Target Thicknesses

The target thicknesses were governed by two factors: high count rates were needed to get good statistics, yet if the rates were too high (i.e. above 10 kHz) pile-up would become a problem; secondly thick targets would degrade energy resolution.

Count rate is related to target thickness by the formula

$$Y = \frac{\rho J \Delta\Omega}{2.67ZA} \times \frac{d\sigma}{d\Omega_{lab}} \tag{4.1}$$

where; Y is in counts per second, ρ is the target thickness in μg/cm^2, $d\sigma/d\Omega_{lab}$ is the differential cross section in mb/sr, $\Delta\Omega$ is the detector's solid angle in units of 10^{-4} sr, J is the beam current in eμA, Z is the charge state of the beam and A is the atomic mass of the target.

In the case of these measurements, the most prolific contribution to the count rate was expected to come from Rutherford scattering to the most forward detector. Thus the Rutherford scattering cross section at this detector ($d\sigma_R/d\Omega_{lab}$) was equated to $d\sigma/d\Omega_{lab}$ in equation 4.1. The former is given by the formula

$$\frac{d\sigma_R}{d\Omega_{lab}} = 1.296 \left(\frac{Z_1 Z_2}{E_{cm}}\right)^2 \left[\sin\left(\frac{\theta_{cm}}{2}\right)\right]^{-4} \frac{d\Omega_{cm}}{d\Omega_{lab}} \tag{4.2}$$

where; Z_1 and Z_2 are the target and projectile atomic numbers, E_{cm} is the centre of mass energy in MeV, θ_{cm} is the centre of mass angle of the detector and $d\Omega_{cm}/d\Omega_{lab}$ is the Jacobian for conversion from the centre of mass to the laboratory frame.

Typical values were: 10 enA for the beam current; 10×10^{-4}sr for the solid angles; 10^6 mb/sr for the Rutherford cross section at forward angles, and 40 to 52 for A. The charge state of the beam was typically 10. However, this value may change as the beam passes through the target, and so 10 is the maximum value for Z. These values indicate that target thicknesses of order 100 to 200 μg/cm^2 should give acceptable count rates of several kHz.

4.2.3 Positioning of Detectors

As the chief objective of the experiments described in this work was to obtain detailed angular distributions, it was necessary to use several time of flight telescopes to measure yields at a series of angles. The range of angles was determined from both kinematic considerations and limits on maximum count rates. Kinematics show that if these systems split into two equal fragments, with the Viola TKE, the maximum observation angle is about 50° in the laboratory frame. Also, as the Rutherford scattering cross section rises sharply at forward angles, putting the detectors too close to 0° could result in severe radiation damage. In view of these problems, detector angles were limited to the range ≈ 10° to ≈ 50°. Another primary consideration when choosing detector positions was that flight paths should be as long as possible to facilitate accurate mass determination.

4.3 ^{40}Ca + ^{40}Ca at Argonne

4.3.1 Experimental Configuration

This experiment was carried out using the ATLAS (Argonne Tandem-Linac Accelerator System) accelerator and the Large Scattering Facility at Argonne National Laboratory in the United States.

As ATLAS is a linac, the beam it produces is delivered in pulses. The production of each pulse can be used to provide a reference timing signal. So the accelerator itself provided the start signals for time of flight measurement, eliminating the need for a set of detectors to carry out this function. The Large

Scattering Facility is a 36 inch ($\approx$ 1 m) circular scattering chamber, with an extension piece at forward angles.

On one side of the beam axis, six silicon surface barrier detectors, each of area 400 mm^2 and active depth 60 μm, were placed at angles of 10°, 15.4°, 20.2°, 32.4°, 42.4° and 52.4°. They were situated at distances of 79.4, 76.5, 58.6, 41.9, 41.6 and 41.8 cm from the target and so subtended solid angles of 0.63, 0.68, 1.17, 2.28, 2.31 and 2.29 msr respectively. The three forward detectors were situated inside the chamber extension, enabling long flight paths and hence good mass resolution (see equation 3.2).

The MWPC-Bragg telescope was mounted on the other side of the beam, at an angle of 30°. Owing to the large entrance aperture of the Bragg curve spectrometer (8 cm by 10 cm), a mask 3.2 cm high by 10 cm wide was placed in front of it to reduce the incident particle flux. The entrance window of the proportional counter had dimensions 8 cm high by 10 cm wide. The Bragg detector was at a distance of 48 cm from the target, with the MWPC just in front of it – 42 cm from the target. So, the Bragg counter, being the further from the target, provided the defining solid angle.

The MWPC-Bragg spectrometer telescope was used for two reasons: firstly to obtain charge information; and secondly to obtain coincidence data. If the total solid angle of all detectors on the right of the beam axis is S_R and the total solid angle of those on the left is S_L, then the coincidence rate depends on $S_R \times S_L$. So, to a first approximation, for a given total solid angle S_R and S_L should be similar for the best coincidence yield.[b] The large entrance aperture of the MWPC-BCS telescope meant that to achieve this, it had to be placed on one side of the beam axis, with all six SSB detectors on the other side.

For this experiment, the Bragg curve spectrometer was biased at 1700 V and had 20 torr of isobutane flowing through it. This pressure of 20 torr was

[b] Particle correlations are also important.

carefully chosen to stop ions of atomic mass 40 to 60 and energy 3 to 5 MeV/amu within 36 cm (i.e. within the active range of the detector). The cathode plane of the proportional chamber was held at −500 V. The isobutane pressure was 2 torr for this detector.

Table 4.2 lists details of detector angles and other information.

Detector	**Angle** (deg.)	**Solid Angle** (msr)	**Bias** (V)
SSB1	10.0	0.63	+90
SSB2	15.4	0.68	+55
SSB3	20.2	1.17	+55
SSB4	32.4	2.28	+55
SSB5	42.4	2.31	+55
SSB6	52.4	2.29	+55
BCS	30.0	≈13.9	+1700
MWPC	30.0	≈45.4	−500

Table 4.2 Details of each of the detectors used in the Argonne experiment. SSBn denotes the nth surface barrier detector, MWPC the multiwire proportional chamber and BCS the Bragg curve spectrometer.

A schematic diagram of the experimental configuration can be found in figure 4.2. A photograph of the setup is shown in figure 4.3.

4.3.2 Electronics Setup

Usually in a nuclear physics experiment the electrical signals from the detectors have to be processed to extract the relevant physical information, before being fed into a computer for further sorting and storage on tape or disk. To communicate with the computer, two things are needed; the analogue to digital converter (ADC), and the master gate or strobe. The ADC converts an analogue electrical pulse into a digital signal which can then be read by the computer.

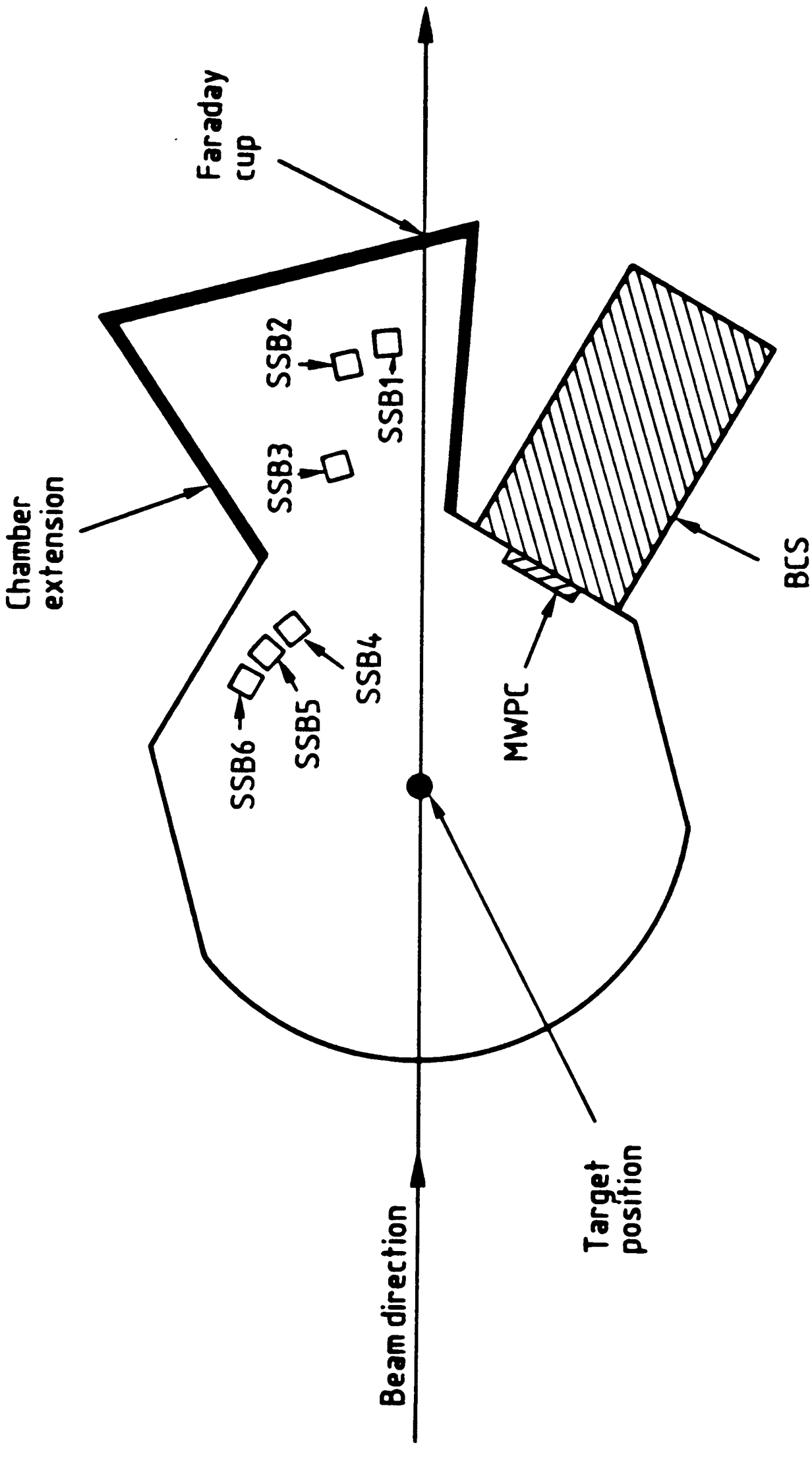


Figure 4.2. A schematic diagram of the experimental configuration used in the $^{40}Ca + ^{40}Ca$ experiment at Argonne. Detector positions are shown. The arrow indicates the beam direction. The symbols are the same as in table 4.2.

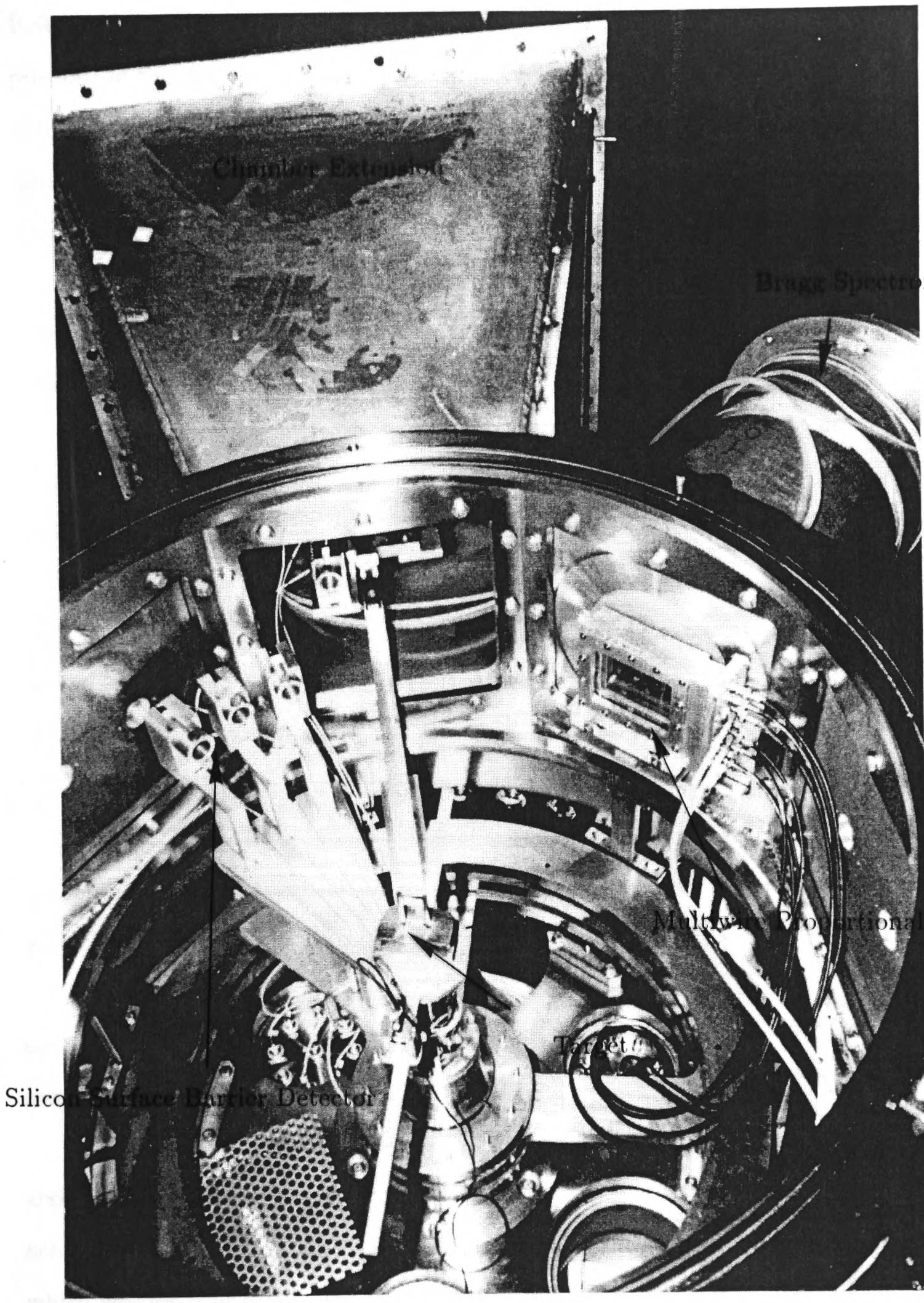


Figure 4.3. A photograph of the inside of the large scattering facility at Argonne. The beam travels from bottom to top in the picture.

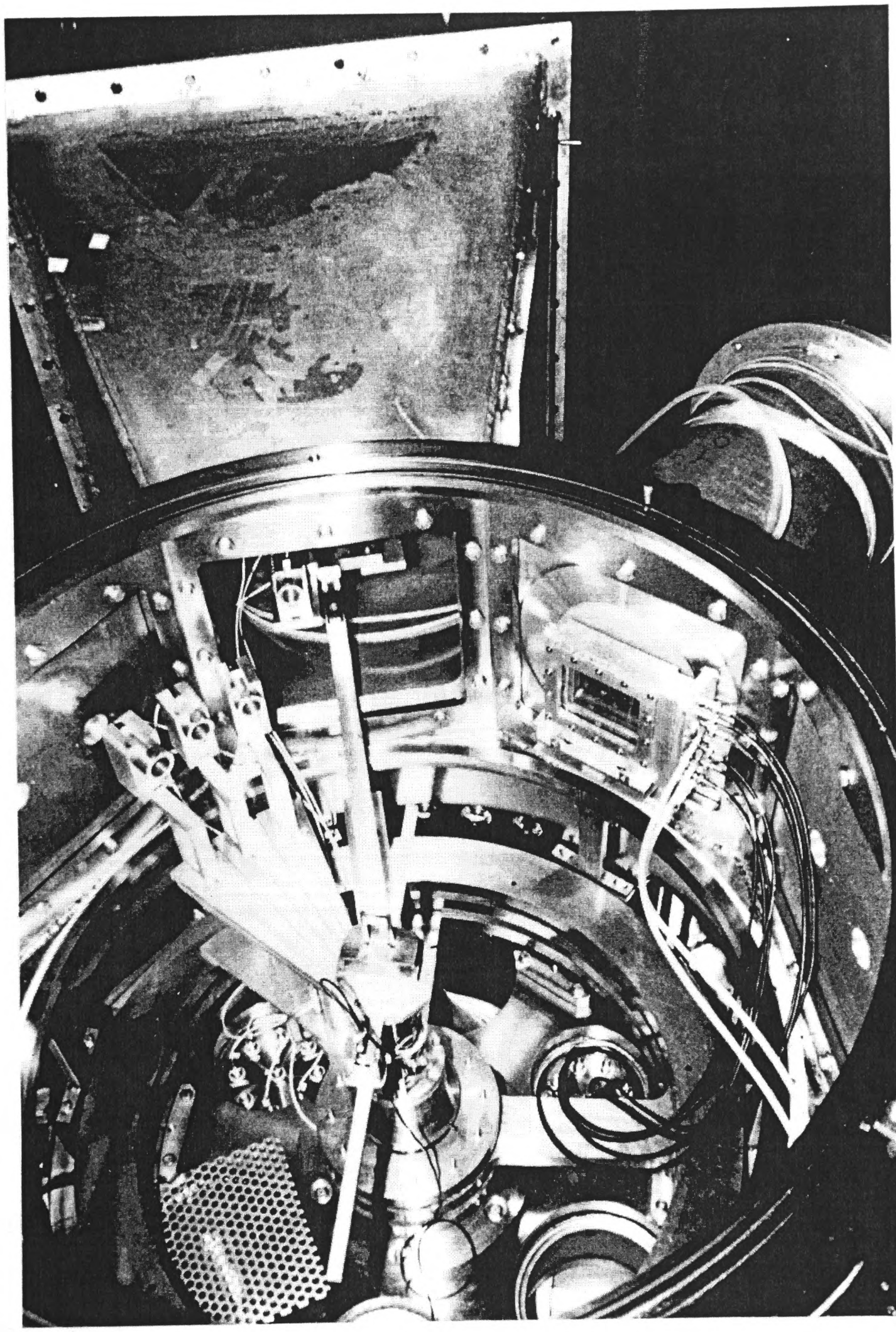


Figure 4.3. A photograph of the inside of the large scattering facility at Argonne. The beam travels from bottom to top in the picture.

Before the ADC can do this, it must be told of the arrival of a signal. The purpose of the master gate is to do just this. So if the signals from a particular detector are to be read by the computer, as well as being fed to an ADC, they must provide an input to the master gate. In this experiment the computer wrote the data to tape for analysis later.

The electronics setup used for the experiment at Argonne can be split into three parts, corresponding to: the six silicon surface barrier detectors; the multiwire proportional chamber, and the Bragg curve spectrometer.

The electronics configuration for each of the six surface barrier detectors is shown in figure 4.4. The object was to extract time of flight and energy information.

The rise time of the output pulse from a typical charge sensitive pre-amplifier is too slow for accurate time of flight measurement. For instance, the surface barrier detectors used in the ^{40}Ca + ^{40}Ca and ^{28}Si + ^{50,52,54}Cr experiments had capacitances of 400 pF. The output pulse produced by an Ortec 142B pre-amplifier (used in the experiments) for such a detector capacitance has a rise time of order 8 ns. A suitable fast signal (rise time $\approx$ 3 ns) was produced by placing an inductive pick-off in series between the surface barrier detector and the pre-amplifier. This is denoted by TPO in figure 4.4.

The slow signal (top of figure 4.4) was connected to a charge sensitive pre-amplifier (PREAMP) and an amplifier (AMP). In this way an energy signal was produced, which was fed into an ADC.

The rest of the SSB electronics measured time of flight, by comparing the arrival of the fast signal from the TPO with the corresponding beam pulse. To achieve this, the TPO signal was connected to a fast $\times$10 amplifier, the output of which was fed into a constant fraction discriminator (CFD). A constant fraction discriminator produces a walk-free timing pulse which is independent of the input signal's amplitude and rise time. The output signal from the CFD was used to start a time to amplitude converter (TAC), the stop signal for which

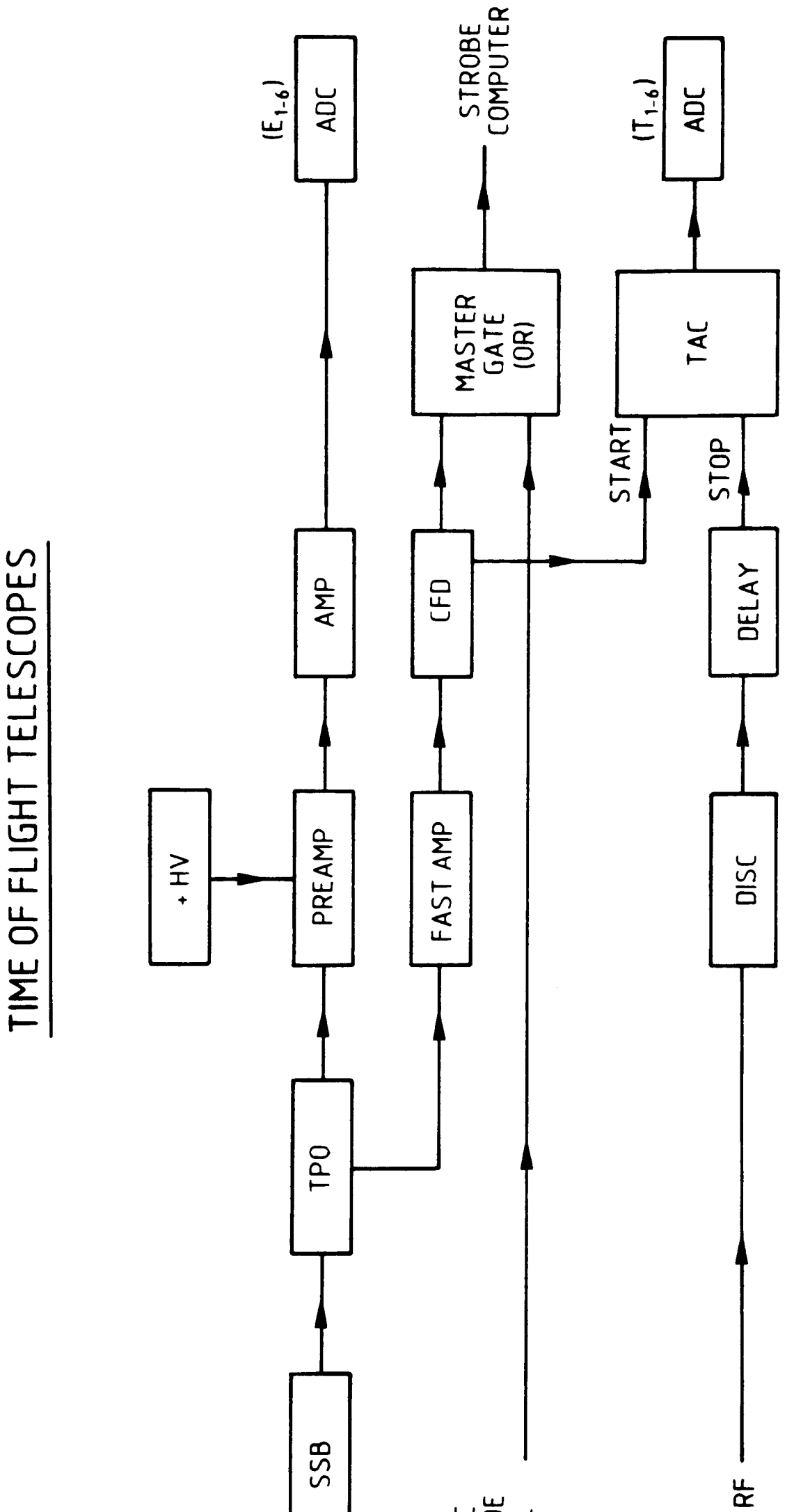


Figure 4.4. Electronics used for the six surface barrier detectors and the master gate. All symbols are explained in the text.

was provided by a radio frequency (RF) signal from the accelerator. This signal, equivalent to a constant minus the time of flight, was then fed into an ADC. The SSB was used to start the TAC, so that it would only be triggered if a particle were detected. To correct for the wrong chronological order of the signals the RF signal was delayed. This configuration: FAST AMP, CFD, TAC is frequently used for accurate timing, and indeed was employed throughout these experiments.

This whole setup was repeated for each of the six SSB detectors, to obtain six energy and six time of flight signals. The fast signal from each of the TPOs was also fed into an OR box to provide the master gate. In figure 4.4, HV signifies high voltage bias supply and DISC denotes discriminator.

Seven signals were extracted from the multiwire proportional chamber, as shown in figure 4.5. Three were electrode signals: cathode, first grid (G1) and second grid (G2); and four were position signals: X-left (X_L), X-right (X_R), Y-up (Y_U) and Y-down (Y_D). The four position signals were extracted from the grids.

The three electrode signals were used for time of flight measurement, in much the same way as the fast outputs from the SSBs were. The time of flight signals are labelled CRF, G1RF and G2RF in figure 4.5. The cathode signal was also connected to the master OR gate (see figure 4.4).

Position determination was achieved by measuring the difference in time between the arrival of the cathode signal and each position signal with time to digital converters (TDC). A TDC is equivalent to a TAC plus an ADC.

The electronics configuration used for the Bragg curve spectrometer is shown in figure 4.6. The anode signal was fed into a charge sensitive pre-amplifier. As explained in section 3.4, two energy outputs were taken from the pre-amplifier. The first one was fed into a long time constant ($\tau = 10$ μs) amplifier, the output of which provided an energy signal E_B. The second signal was fed into an amplifier with a short time constant ($\tau = 0.5$ μs). One output

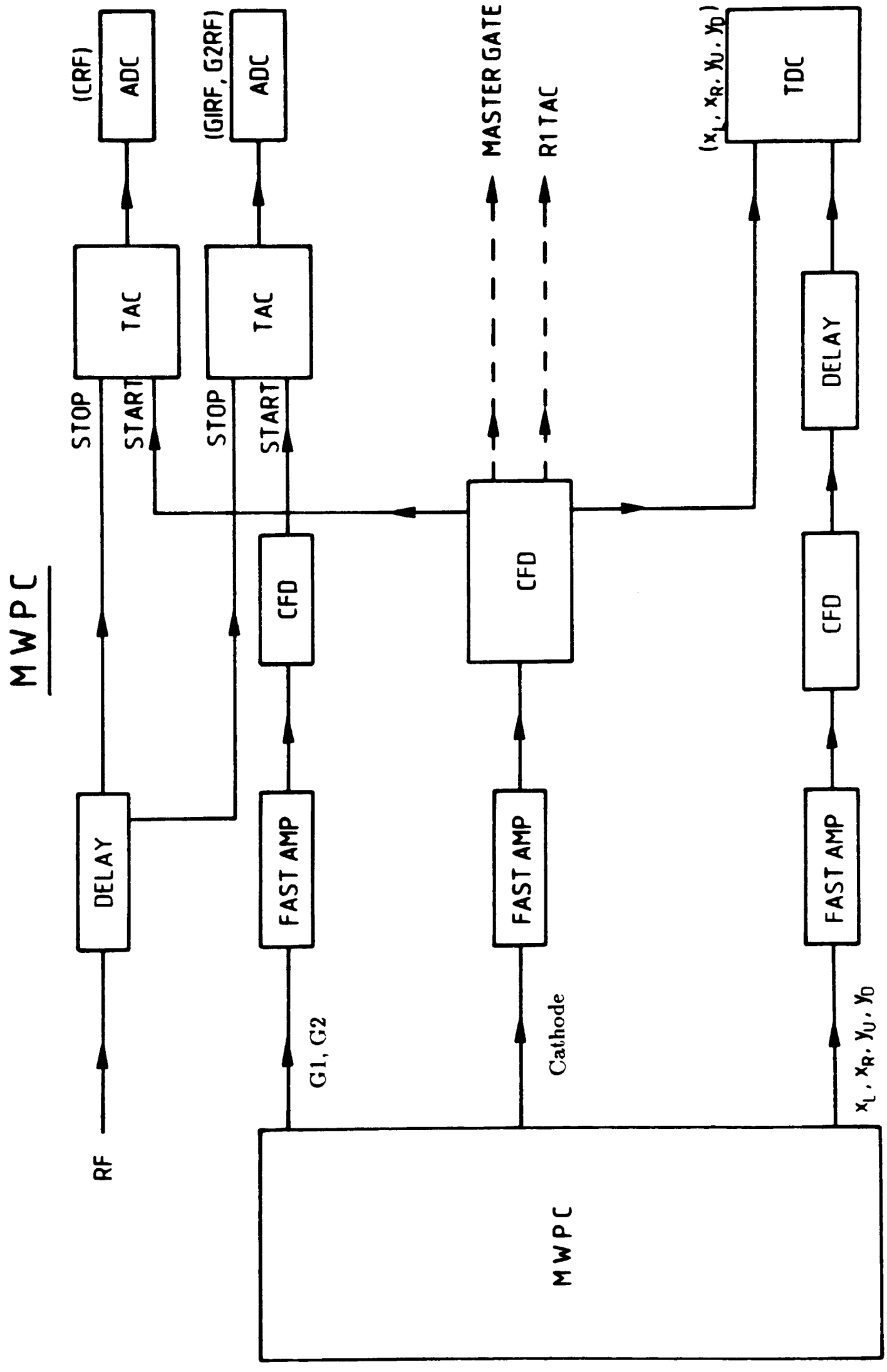


Figure 4.5. Electronics used for the multiwire proportional chamber. See text for explanation of symbols.

from this amplifier was electronically stretched before being fed into an ADC, to produce a signal corresponding to the Bragg peak B_P.

The time output of the Bragg curve spectrometer's pre-amplifier was fed into a timing filter amplifier (TFA) and then to a leading edge discriminator (LED). The output of the LED was used to extract two range signals. The first one (R1) was obtained from a TAC which was started with the cathode signal from the MWPC (see figure 4.5) and stopped with the output of the LED. The leading edge discriminator was also used to start the TAC for the second range signal (R2). The stop signal was obtained from the falling edge of the signal from the $\tau = 0.5$ μs amplifier. The falling edge signal was obtained using a timing single channel analyser (TSCA).

If an ion's energy is too low, it will stop in the Bragg spectrometer, without reaching its Bragg peak. This presents a problem when charge identification is required. In an effort to overcome this difficulty, by providing a means of resolving the charges of ions which fail to reach their Bragg peak, the rate of rise, or slope, of the short time constant signal was measured. This was done by taking two outputs from the $\tau = 0.5$ μs amplifier. One was delayed and the other inverted. The two signals were then summed and inverted. The amplitude of the output pulse produced by such an arrangement is proportional to the slope of the B_P signal. The output was fed into a biased amplifier and then an ADC, to provide the SLOPE signal.

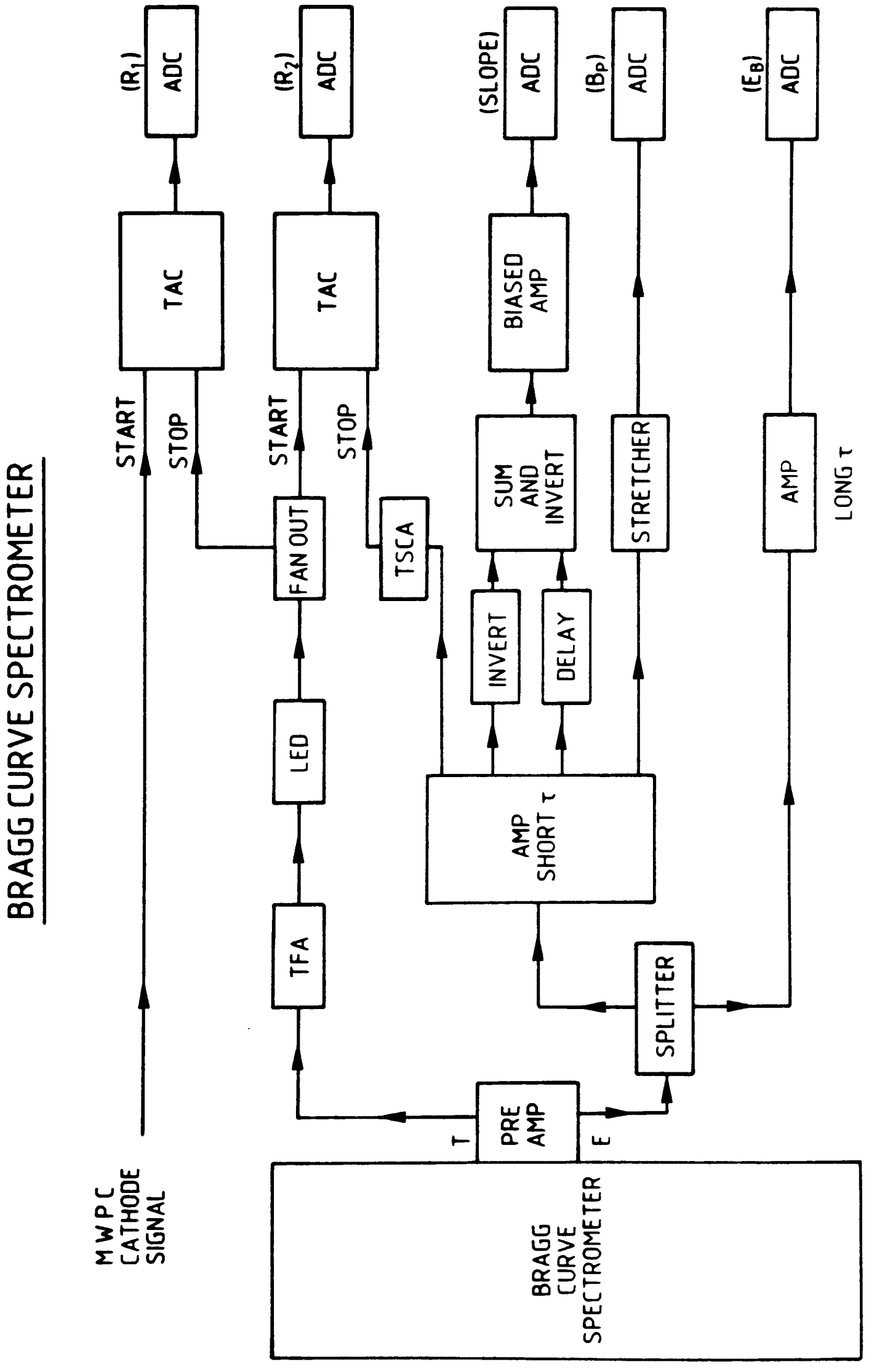


Figure 4.6. Electronics configuration used for the Bragg curve spectrometer. See text for explanation.

4.3.3 Procedure

A 200 μg/cm^2 thick target of ^{40}Ca was bombarded with a ^{40}Ca beam at energies of 197.3 and 230.5 MeV. The target, which was made by evaporating ^{40}Ca onto a 20 μg/cm^2 carbon backing, was kept under vacuum at all times to prevent oxidization. Energies of 197.3 and 230.5 MeV were used, because fine tuning the Linac to achieve energies of exactly 200 and 230 MeV would have been very time consuming and the characteristics of these fissionlike reactions are expected to change by little over a few MeV. Using the electronics configuration described above, electrical signals from the detectors were transferred to a VAX 11/750 computer, which wrote the data to tape in an event by event format.

In addition to the ^{40}Ca + ^{40}Ca measurements, elastic scattering of the ^{40}Ca beam off a flash gold target was also measured, at both energies. These data provided high energy calibration points for all detectors. The gold target was 15 μg/cm^2 thick, and had a 20 μg/cm^2 thick carbon backing. Scattering of the beam off the edges of a small hole target was also measured for the purposes of mass calibration.

Throughout the experiment, the biases on all SSBs were continually corrected for leakage current effects and the isobutane pressures in the Bragg counter and MWPC were monitored for any variations. Several measurements were made at the end of the experiment. To obtain low energy calibration data, α-particle spectra were collected from a ^{241}Am source (α-particle energy = 5.5 MeV) mounted in the target position. A precision time calibrator was used to check the linearity of each TAC and to calibrate them.

4.4 ^{28}Si + ^{50,52,54}Cr at Daresbury

4.4.1 Experimental Configuration

The fissionlike reactions of the systems ^{28}Si + ^{50,52,54}Cr were studied at the Nuclear Structure Facility (NSF), Daresbury Laboratory. The NSF is a 20 MV van de Graaff accelerator. The experiment was performed in the 79° scattering chamber, which has a diameter of 1 meter.

Four avalanche counter-silicon surface barrier telescopes were mounted in the chamber. Two were placed at 20° and 40° on one side of the beam and two were placed at 30° and 50° on the other side.

In all four telescopes, the avalanche counters were put as close as possible to the target (i.e. 10 cm away), to maximize flight paths. They had entrance windows of 10 mm diameter and thus subtended solid angles of 7.85 msr. The particular type used for this experiment had wire wound grids, with a wire spacing of 0.4 mm. Each avalanche counter was biased at −500 V and had 10 torr of isobutane circulating through it. The detectors were connected to the gas supply in parallel. This was for two reasons: firstly to prevent any deposits removed from one counter being transported to others; and secondly so that if one counter should fail, or its gas windows break, it could be isolated, allowing the others to continue in operation.

The SSB detectors each had surface areas of 400 mm^2, active depths of 60 μm and were situated 41 cm from the target. They all subtended 2.38 msr and hence provided the defining solid angle for each telescope.

A monitor detector was also used, to provide a means of cross section normalization. The SSB in one of the time of flight telescopes could have been used for this, but the degradation of energy resolution associated with straggling in the avalanche counters made this undesirable. The monitor was a 400 mm^2, 100

μm thick SSB placed at 41.5 cm from the target, at an angle of 8.3°. It was collimated with a 1 mm diameter hole, giving it a solid angle of 4.6×10^{-3} msr.

Table 4.3 lists details of each telescope and the monitor.

Detector	**Angle** (deg.)	**Solid Angle** (msr)	**Bias** (V)
AC1	20.0	7.85	-500
AC2	40.0	7.85	-500
AC3	30.0	7.85	-500
AC4	50.0	7.85	-500
SSB1	20.0	2.38	+80
SSB2	40.0	2.38	+110
SSB3	30.0	2.38	+110
SSB4	50.0	2.38	+125
MON	8.3	4.6×10^{-3}	+108

Table 4.3 Details of the detectors used in the Daresbury experiment. ACn means the nth avalanche counter and SSBn the nth surface barrier detector. MON denotes monitor.

A photograph of a typical experimental setup used for one of these experiments is shown in figure 4.7.

4.4.2 Electronics Setup

The electronics configuration used for each telescope in the ^{28}Si + ^{50,52,54}Cr experiment, at Daresbury Laboratory, can be found in figure 4.8. The setup was very similar to that used for one of the SSB detectors in the Argonne experiment, the main difference being that an avalanche counter (PPAC) was used to provide the stop signal for time of flight measurement, rather than an RF signal.

Although the avalanche counter was the front detector, the SSB was used to start the TAC, as it constituted the defining solid angle. Doing this ensured

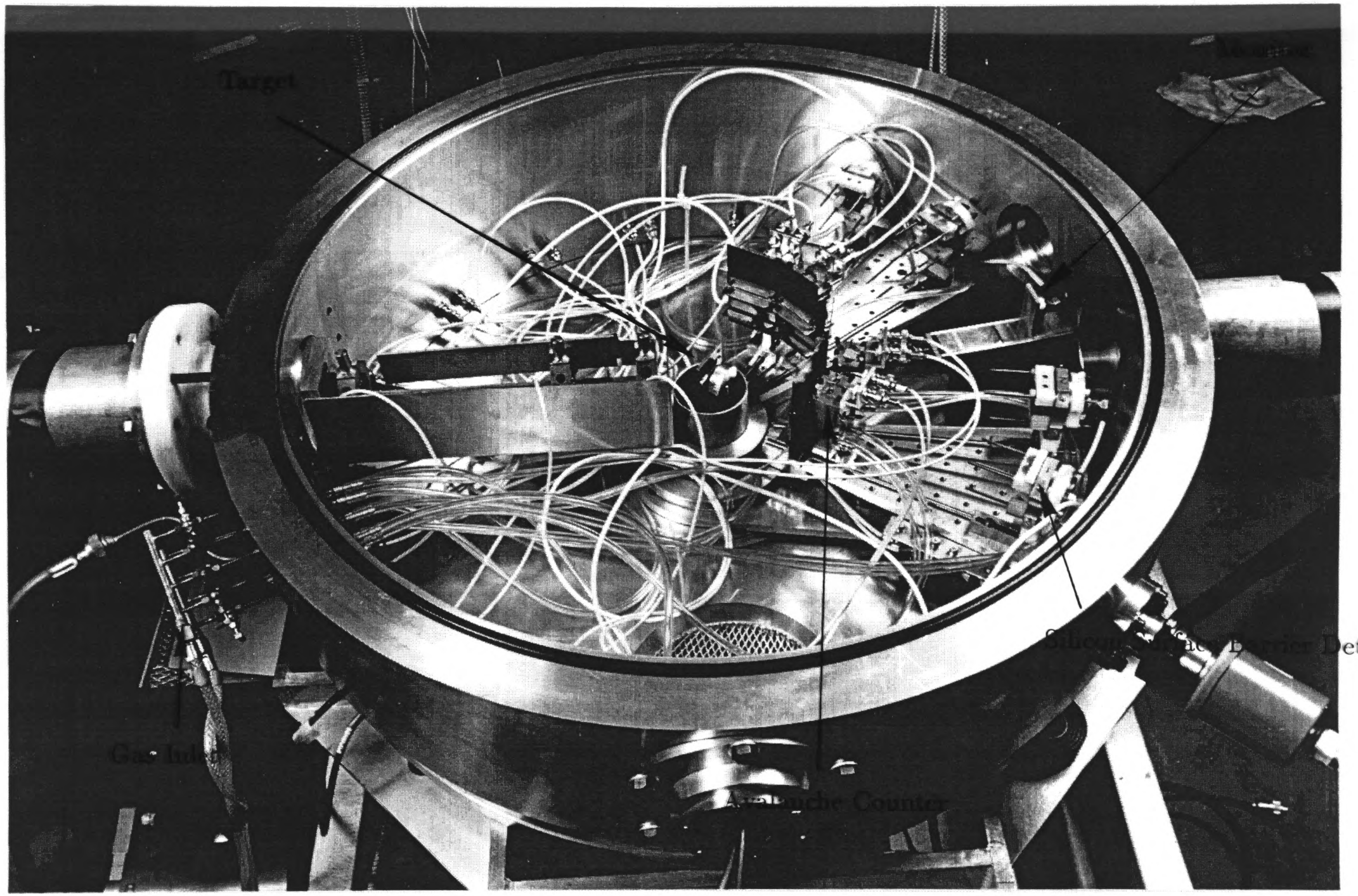


Figure 4.7. A photograph of a typical experimental setup for a Daresbury experiment. This particular figure shows the Oxford scattering chamber, which is smaller than that at the NSF. However the basic detector configuration used in the ^{28}Si + ^{50,52,54}Cr measurement was identical. The beam travels from left to right. .

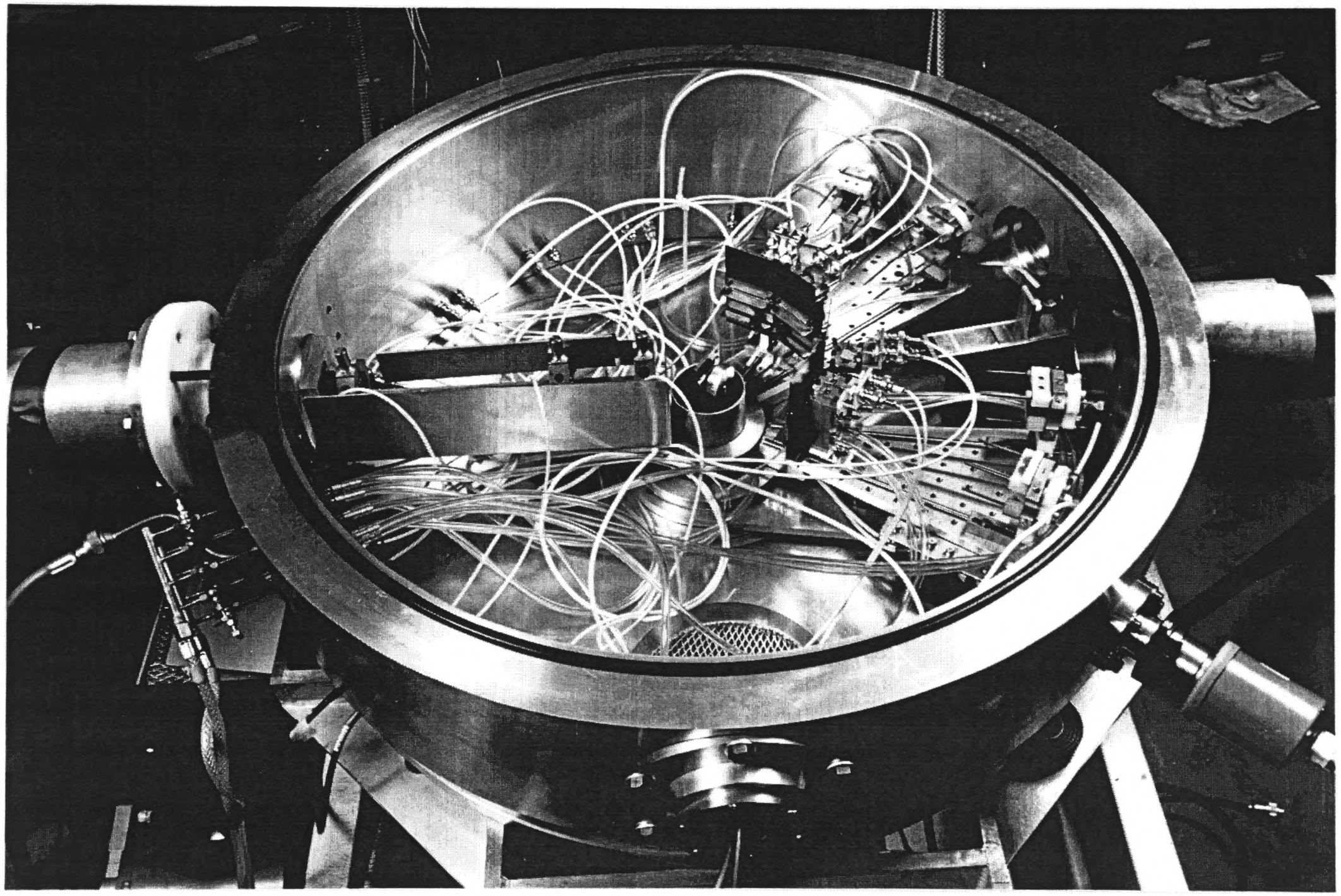


Figure 4.7. A photograph of a typical experimental setup for a Daresbury experiment. This particular figure shows the Oxford scattering chamber, which is smaller than that at the NSF. However the basic detector configuration used in the $^{28}Si + {}^{50,52,54}Cr$ measurement was identical. The beam travels from left to right.

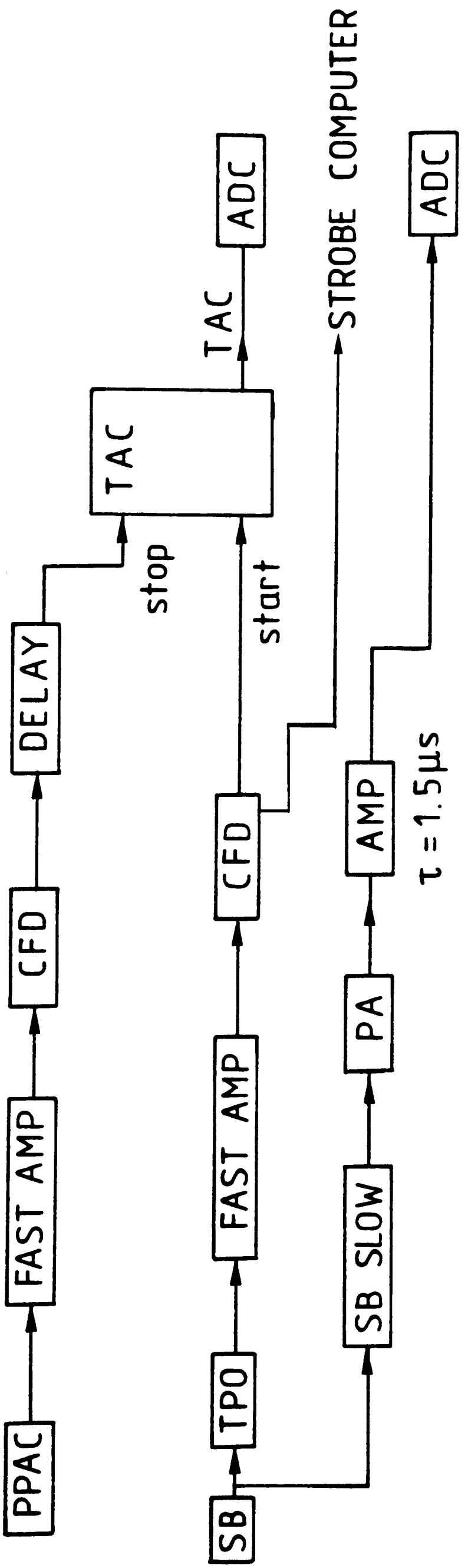


Figure 4.8. The electronics configuration used in the $^{28}Si + {}^{50,52,54}Cr$ experiment at Daresbury laboratory. See text for explanation.

the TAC would not be started by a particle passing through one detector and missing the other. Because the order of the signals was reversed, the output from the TAC was not time, but a constant minus time. The output signal from the TAC was fed into an ADC.

This setup was duplicated for each of the four avalanche counter-SSB telescopes. Thus eight digital signals were produced in total – four energy and four time. The circuit for the monitor detector consisted of a pre-amplifier, an amplifier and an ADC.

A second output was taken from each SSB's constant fraction discriminator. These signals were then fed into an OR box, the output of which was used to provide the master gate or strobe signal for the ADCs and to trigger the computer. This procedure enabled the convenient measurement of the avalanche counters' efficiencies.

4.4.3 Procedure

The procedure followed in this experiment was very similar to that adopted in the $^{40}Ca + {}^{40}Ca$ measurement at Argonne.

^{28}Si beams of 130 MeV and 150 MeV were focused on to 100 $\mu g/cm^2$ thick targets of $^{50,52,54}Cr$ (at 150 MeV only reactions with ^{50}Cr were studied), which were made by evaporating each chromium isotope onto 20 $\mu g/cm^2$ thick carbon backings. A GEC 4190 computer was used to collect the data and write it to tape for analysis later.

Elastic scattering from a flash gold target was also measured, to obtain a high energy calibration point for all detectors. The gold target was 5 $\mu g/cm^2$ thick, and had a 20 $\mu g/cm^2$ thick carbon backing.

As with the Argonne experiment, biases on all SSBs were continually corrected for changes in leakage current. The isobutane pressure in the avalanche

counters was continually monitored to ensure its constancy. Several measurements were made at the end of the experiment. To obtain low energy calibration data, α-particle spectra were collected from a ^{252}Cf source (α-particle energy = 6.1 MeV). The TACs were calibrated as at Argonne.

Chapter 5

Analysis and Results

I pass with relief from the tossing sea of Cause
and Theory to the firm ground of Result and Fact.

Winston Spencer Churchill

5.1 Introduction

Details of the data analysis and the results obtained are described in this chapter. The presentation of the analysis and results focuses on the principal component of the thesis, the ^{40}Ca + ^{40}Ca experiment, with any differences pertinent to the ^{28}Si + ^{50,52,54}Cr measurement being emphasised at the end of the chapter.

Once the data from these experiments had been written to tape by the computers at Argonne and Daresbury, the next task was to read them back, using the computers at Oxford. The data were then manipulated, or 'sorted,' in order to extract the relevant physics. This was achieved using a sophisticated analysis program known as GENDAT [48]; run originally on the OEG VAX 11/780 and, more recently, on the VAX 8700 at the Oxford Nuclear Physics Laboratory.

GENDAT (GENeral DATa aquisition program) is a FORTRAN package, written in a modular form so that the user can tailor it to his own requirements

with the minimum of difficulty. The data tapes from the ^{40}Ca + ^{40}Ca experiment were written in the appropriate format for the Argonne analysis program, and so were incompatible with the existing versions of GENDAT. Hence the tape reading routines in GENDAT had to be extensively modified to read the data. Once data are read from tape, a sub-program, known as the 'virtualization' routine, manipulates the raw parameters to calculate the relevant derived quantities (known as virtual ADCs). In the discussion that follows, most data manipulation referred to was carried out at the virtualization routine level.

The next few sections describe the analysis of the ^{40}Ca + ^{40}Ca experiment, starting with the extraction of singles mass and Q-value distributions from the six SSB detectors in section 5.2. The singles analysis of the multiwire proportional chamber-Bragg curve spectrometer telescope is described in section 5.3, and in section 5.4 the coincidence analysis is presented. Due to the complexity of the singles analysis, certain points are only mentioned briefly in this chapter. However, in such circumstances a detailed discussion of the relevant point is presented in the appropriate section of appendix I.

The analysis of the data from the ^{28}Si + ^{50,52,54}Cr experiment is discussed in section 5.5. To avoid repetition the discussion focuses on the points which differ from the ^{40}Ca + ^{40}Ca data.

5.2 Singles Analysis of SSB Data

5.2.1 Energy and Time Calibrations

The first step in analysing the data from the SSB detectors was to calibrate the energy and time signals (denoted by E_{1-6} and T_{1-6} in figure 4.4).

Energy calibrations were carried out using 5.5 MeV α-particles and elastic scattering of ^{40}Ca from ^{197}Au and ^{40}Ca, as referred to in section 4.3.3, to obtain several points spanning the range of interest. Energy calibration of the ^{40}Ca + ^{197}Au,^{40}Ca points involved several stages:

1) Firstly the energy of the elastically scattered beam was calculated assuming two-body kinematics.
2) This was corrected for energy loss in the target (typically 1-2 MeV), using stopping power tables (Northcliffe and Schilling [49] and Ziegler [50]).
3) The surface barrier detectors had thin entrance windows, consisting of 40 μg/cm^2 of evaporated gold. The energy loss in these gold layers (on average less than 0.5 MeV) was also corrected for using the stopping power tables.
4) Once these corrections have been made, the true energy of the elastically scattered beam entering the active region of a given detector (E_t) is known. However, for heavy ions, this is not equal to the energy measured (E_m), as part of the energy imparted may not be detected due to a phenomenon known as pulse height defect. Allowance for this was made using an empirical formula (appendix I.2). Thus $E_m = E_t - \Delta E$, where ΔE is the predicted energy defect.

The channel where the α-particle peak fell was assigned the energy 5.5 MeV, and a linear least squares fit calibration performed for each energy spectrum. The fits yielded maximum errors of 0.5 MeV on each calibration point. No corrections were needed for the α-particles since very little energy ($\approx$ 10 keV)

was lost in the SSB entrance windows and because pulse height defect is not a problem for such light particles (see the discussion of appendix I.2).

A precision time calibrator was used to produced a set of TAC spectra consisting of a series of sharp peaks separated in time by 10 ns. A linear least squares fit calibration was carried out for each TAC, to evaluate its time gain and dispersion. On average these calibrations were good to 100 ps.

5.2.2 Mass Calibrations

The next stage of the analysis was to generate mass spectra for each detector. As discussed in section 3.2.1, once energy E and time of flight t are known, a mass spectrum can be produced using the formula (equation 3.1)

$$A_{amu} = 1.9297 E_{MeV} t_{ns}^2 / l_{cm}^2 \tag{5.1}$$

In section 4.3.2, we mention that the time of flight TACs were started with the fast signals from the SSBs and stopped with the delayed RF signal from the accelerator. Because of this the TAC outputs were, in fact, equivalent to a constant (t_0) minus time of flight (t). So if T is used to denote a TAC signal, then $t = t_0 - T$ and the mass is simply

$$A_{amu} = 1.9297 E (t_0 - T)^2 / l^2 \tag{5.2}$$

This formula was used to calculate a first order mass calibration for each detector. The elastic scattering data were used to obtain a first order estimate for the unknown t_0.

All of the first order mass estimates were then corrected using the following procedure:

1) Firstly a pulse height defect correction was made for each detector. The correction for pulse height defect described in the previous section was subtracted from the calculated energy to get an accurate estimate of the final

energy detected. It was now necessary to make a second correction to convert this detected, or measured, energy to the true energy of the particle. Hence, the method outlined in appendix I.2 was used to obtain an energy defect (ΔE), which this time was added (ΔE was subtracted in the initial energy calibration) to the measured energy (E_m) to produce an estimate of the true energy (E_t). Thus $E_t = E_m + \Delta E$. These two corrections were needed as pulse height defect depends on energy and mass, and so a simple calibration of elastic scattering data would be incorrect for non-elastic events. For elastically scattered beam this simply negated the first pulse height defect correction to yield the true energy entering the detector.

2) The plasma delay time (τ_p) (see section 3.3.1 for a discussion on plasma delay) was calculated as a function of the first order mass estimate (A) and of the corrected energy (E_t), using the procedure of appendix I.3. However the t_0 value for each detector had already been chosen to give the ^{40}Ca elastic peak the correct mass calibration, and so its plasma time $\tau_p(^{40}\mathrm{Ca})$ was already accounted for implicitly. Thus the important quantity was $\tau_p(A) - \tau_p(^{40}\mathrm{Ca})$, which we shall call $\delta\tau_p$.

3) These corrected time and energy signals were now used to obtain a more accurate estimate of the mass, given by the formula

$$A = 1.9297 E_t (t_0 - T - \delta\tau_p)^2 / l^2 \tag{5.3}$$

4) After these corrections had been carried out, they were tested by generating plots of mass against energy for the scattering of ^{40}Ca off the edges of a hole target, a process which gave a broad range of detected energies.

If the calibrations were correct, the spectrum for each of the six SSBs would consist of a straight line at mass 40, with a broad energy distribution, extending to low energy. Small errors in the measurement of flight path (l) or t_0 determination could cause significant deviations from this ideal case. This is illustrated

in figure 5.1 for the case of a mass 40 particle. Errors in l would tend to shift the mass line, whereas if t_0 were wrong, the mass line would become curved, but tend to the correct mass at low energy. With these considerations in mind, the parameters l and t_0 were adjusted (within reasonable limits) and steps 1 to 4 repeated, until a good straight mass 40 line, extending to low energy, was achieved for each time of flight spectrum.

The elastic scattering data were also used to measure the mass resolution ($\delta A/A$) of each detector. For the three forward detectors ($\theta = 10°$, 15.4° and 20.2°), with the longest flight paths, values of $\delta A/A \approx 0.05$ were obtained and for the three backward detectors ($\theta = 32.4°$, 42.4° and 52.4°) $\delta A/A \approx 0.07$.

5.2.3 Identification of ^{40}Ca + ^{40}Ca Fissionlike Yields

Once all these calibrations had been performed, contamination reactions were investigated. Figure 5.2 shows a plot of mass against energy ($\theta_{lab} = 20.2°$) for ^{40}Ca + ^{40}Ca, at a bombarding energy of 197.3 MeV. This spectrum shows a profusion of data from several types of process. Likely contaminants include oxygen (from the atmosphere), zirconium (used as a reduction agent when making the targets), and tantalum (from the reduction boat). Reactions with the carbon target backing may also be important.

In order to establish which events are the products of the fissionlike decay of the ^{40}Ca + ^{40}Ca system, the method described in appendix I.4 was used to determine where they should fall on a mass against energy spectrum for each detector. The predicted locus of these events for the 20.2° detector is shown on figure 5.2, along with similar plots for the fissionlike reactions of ^{40}Ca + ^{90}Zr and ^{40}Ca + ^{16}O (the most common isotopes of zirconium and oxygen). These curves clearly indicate which are the fissionlike events from each reaction. Evaporation residues from reactions with ^{40}Ca, ^{16}O and ^{90}Zr were identified using the method outlined in appendix I.5.

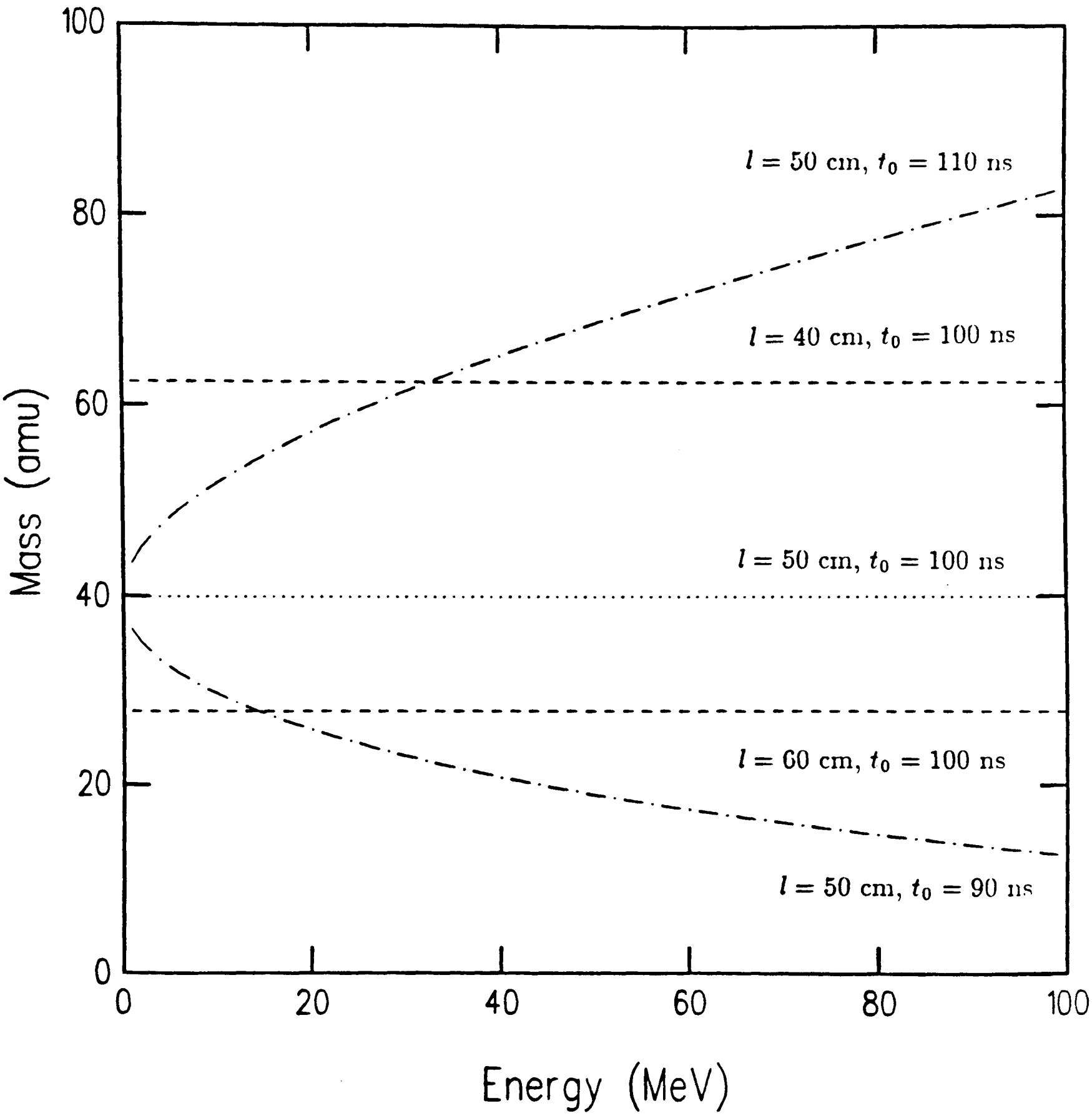


Figure 5.1. An illustration of the effect of incorrect determination of l and t_0 on a plot of mass against energy. For the hypothetical example shown, the detected particle has mass 40, l is 50 cm and t_0 is 100 ns.

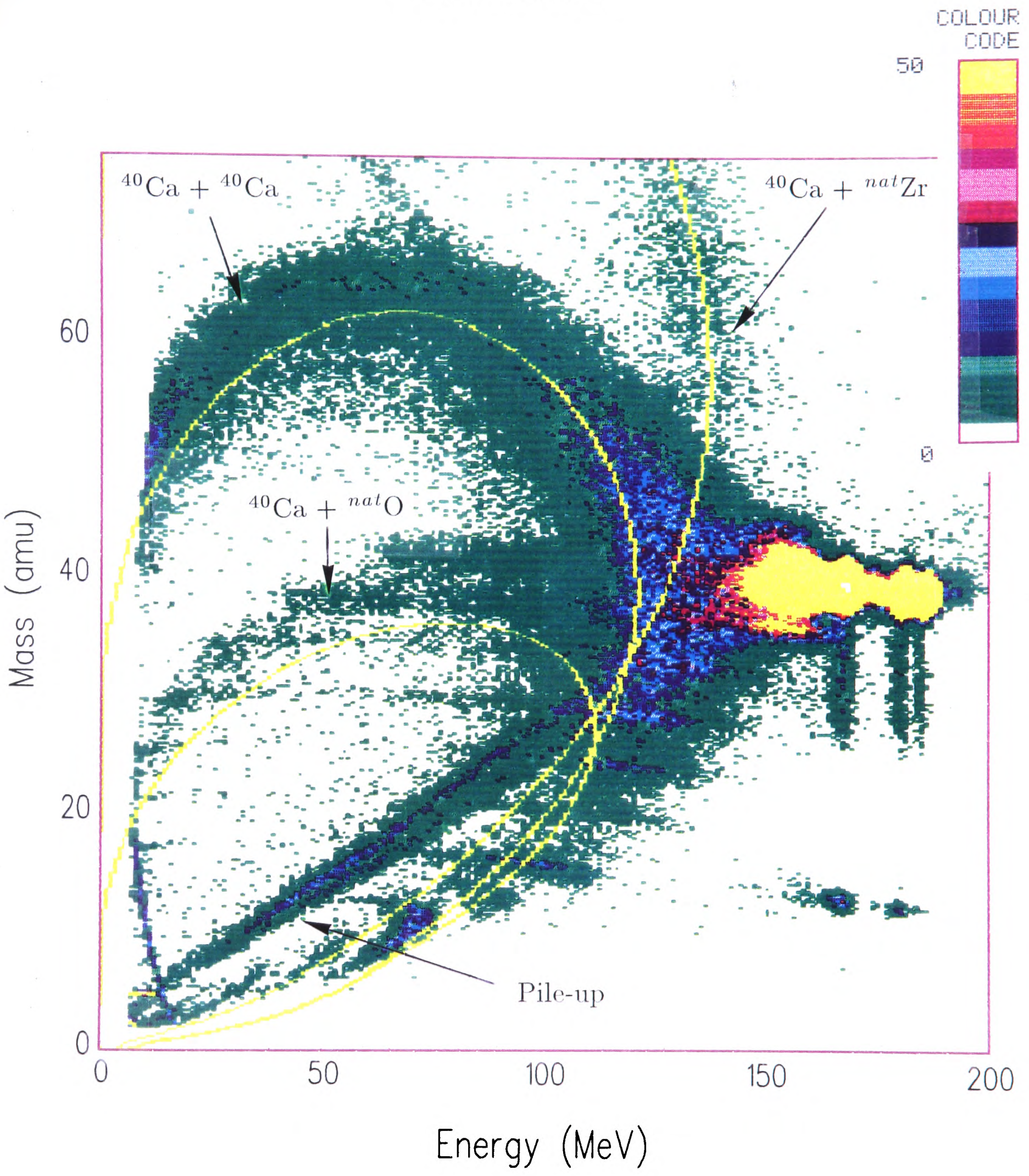


Figure 5.2. A scatter plot showing mass against energy for 197.3 MeV ^{40}Ca + ^{40}Ca, obtained from the 20.2° detector. The various components of the data are labelled. The curved lines indicate the predicted loci of fissionlike events from reactions with each isotope present in the target.

Comparison of the predictions of these simple calculations with the experimental mass against energy spectra (e.g. figure 5.2) indicate that fusion-fission of the systems ^{40}Ca + ^{nat}O,^{nat}Zr and evaporation residues from fusion of the beam with ^{40}Ca and ^{nat}O are the main sources of contamination from nuclear reaction processes.

There was no experimental evidence for contamination from reactions with the carbon target backing. Calculations using the statistical model program CASCADE (see section 6.3) predicted that at the energies studied, the fission cross sections for the system ^{40}Ca + ^{12}C should be less than 1 mb. Furthermore, the grazing angle in the laboratory frame is less than 10° (the smallest observation angle).

Other sources of 'contamination' came from instrumental effects, primarily pile-up and slit scattering. As its name suggests slit scattering occurs when a component of the beam is scattered by the collimation system. This scattered component has a longer flight path than the rest of the beam and hence appears spuriously heavy when its mass is calculated. Pile-up occurs when the count rate is so high that a signal arrives at the amplifier before the preceding one has been processed. Its hallmark is a random energy, but the correct time of flight signal for an elastically scattered event (as most pile-up originates from the profuse elastic scattering). The shaping times of the amplifiers used were 2 μs, whereas the ranges of the TACs were one tenth of this. Thus pile-up in time was less likely than pile-up in energy. Pile-up events are indicated in figure 5.2.

To separate the ^{40}Ca + ^{40}Ca component, a two-dimensional software window was applied to the region of interest and the corresponding mass spectrum projected out.

The fissionlike component from ^{40}Ca + ^{40}Ca, at an energy of 197.3 MeV, is shown in figure 5.3 for each detector. Two corrections have been made in order to produce these spectra; pile-up has been removed, and the fissionlike events from ^{40}Ca + ^{nat}O have been corrected for. The pile-up correction was

obtained by extrapolating the yield observed in areas of pure pile-up to the region of interest. Two groups of $^{40}Ca + ^{16}O$ products are present, corresponding to two different centre of mass angles. As the low energy group is clean, it was used to estimate the yield of the high energy component, overlapping with the $^{40}Ca + ^{40}Ca$ fissionlike events (see appendix I.6). Contributions from the fission decay of $^{40}Ca + ^{90}Zr$ and from slit scattering are negligibly small in the region of interest (typically at the 1% level).

The data obtained from the backward detectors are much cleaner. No evaporation residues were observed beyond 20.2°, little or no pile-up occured and only the lightest $^{40}Ca + ^{16}O$ products were detected.

5.2.4 Mass Distributions

The most noticeable feature of the mass spectra shown in figure 5.3 is their strong periodic structure, with maxima at every four mass units (i.e. 20, 24, 28 etc.). These spectra show the mass calibrations are good to 1 amu.

These mass spectra were converted to the centre of mass frame using the method described in appendix I.7. Before transformation they were binned in groups of four mass units, corresponding to the peaks in the laboratory spectra.

$d\sigma/d\theta_{cm}$ for each detector at 197.3 MeV is shown in figure 5.4. The corresponding spectra for 230.5 MeV are shown in figure 5.5. In both sets of spectra, the errors are taken to be $\sqrt{N}$, where N is the number of counts in a given bin. There are gaps in the spectra for the 10° detector because the yield around mass 40 is contaminated beyond correction by evaporation residues from reactions of ^{40}Ca with ^{16}O.

For each mass bin, $d\sigma/d\theta_{cm}$ is plotted as a function of centre of mass angle for energies of 197.3 MeV and 230.5 MeV in figures 5.6 and 5.7 respectively. The grazing angle is indicated in both figures. The 197.3 MeV data clearly follow

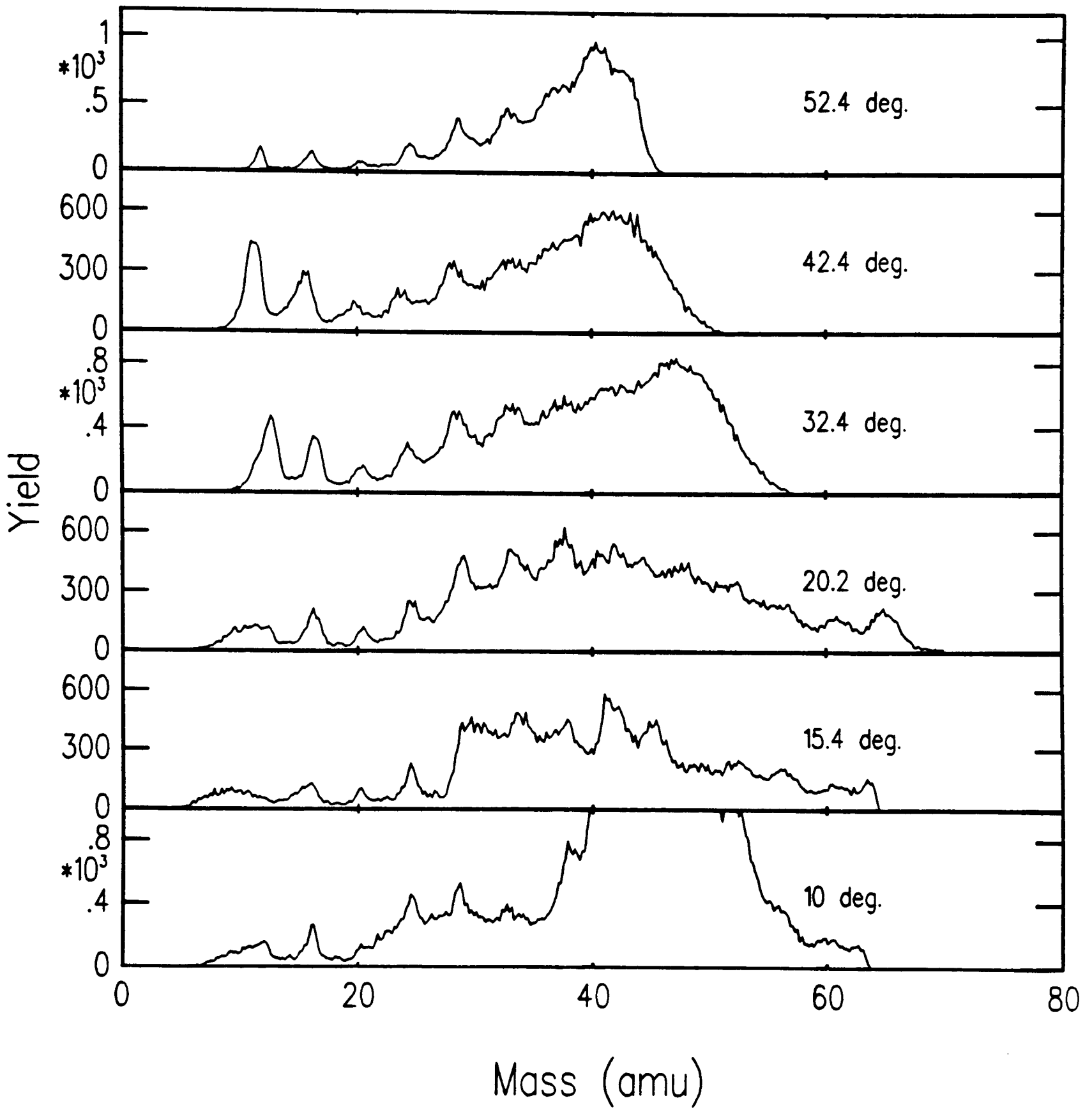


Figure 5.3. Fissionlike yields from the system $^{40}Ca + {}^{40}Ca$ at 197.3 MeV. Note the strong periodic structure.

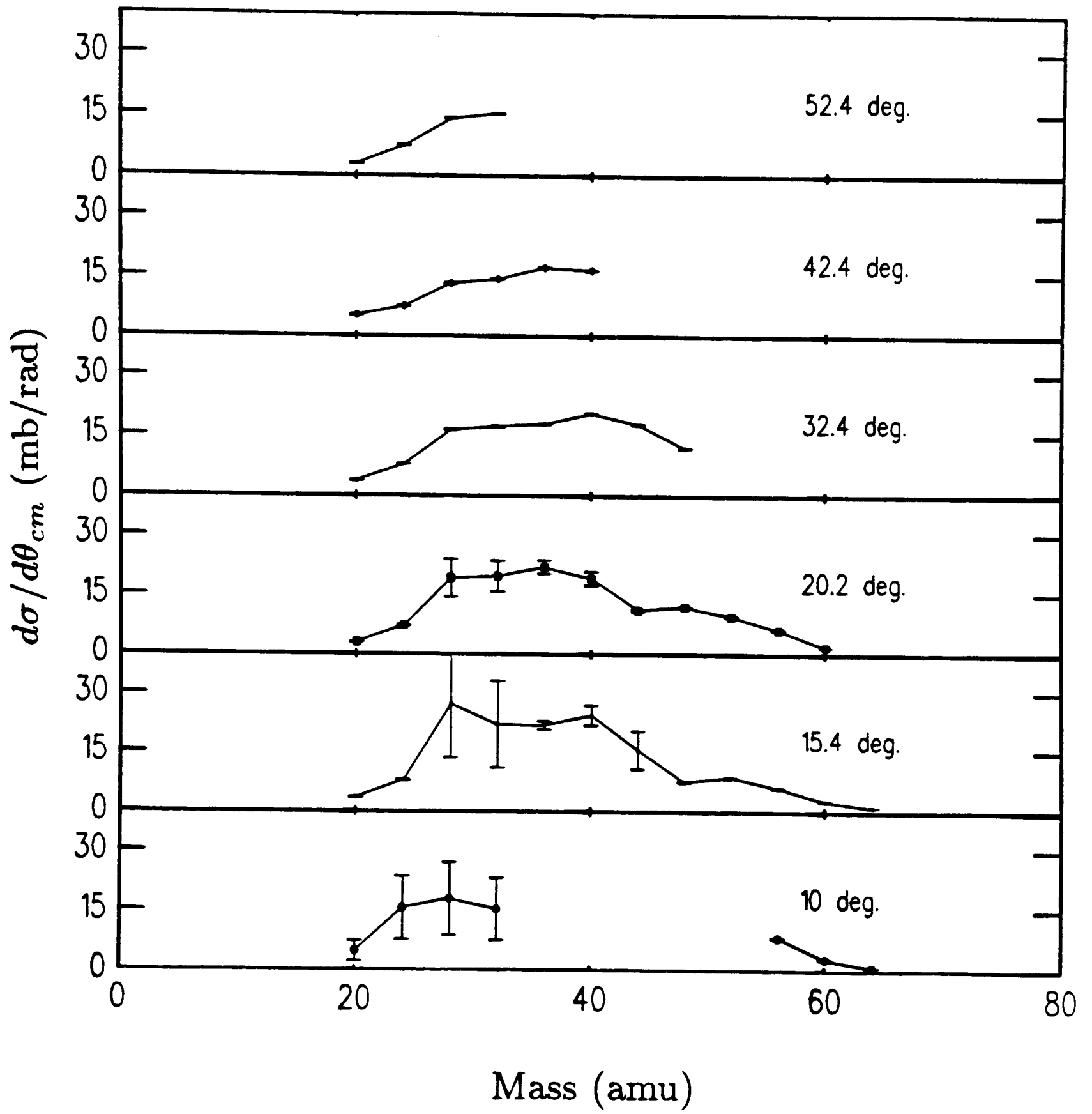


Figure 5.4. Mass distributions in the centre of mass frame from the system ^{40}Ca + ^{40}Ca at 197.3 MeV.

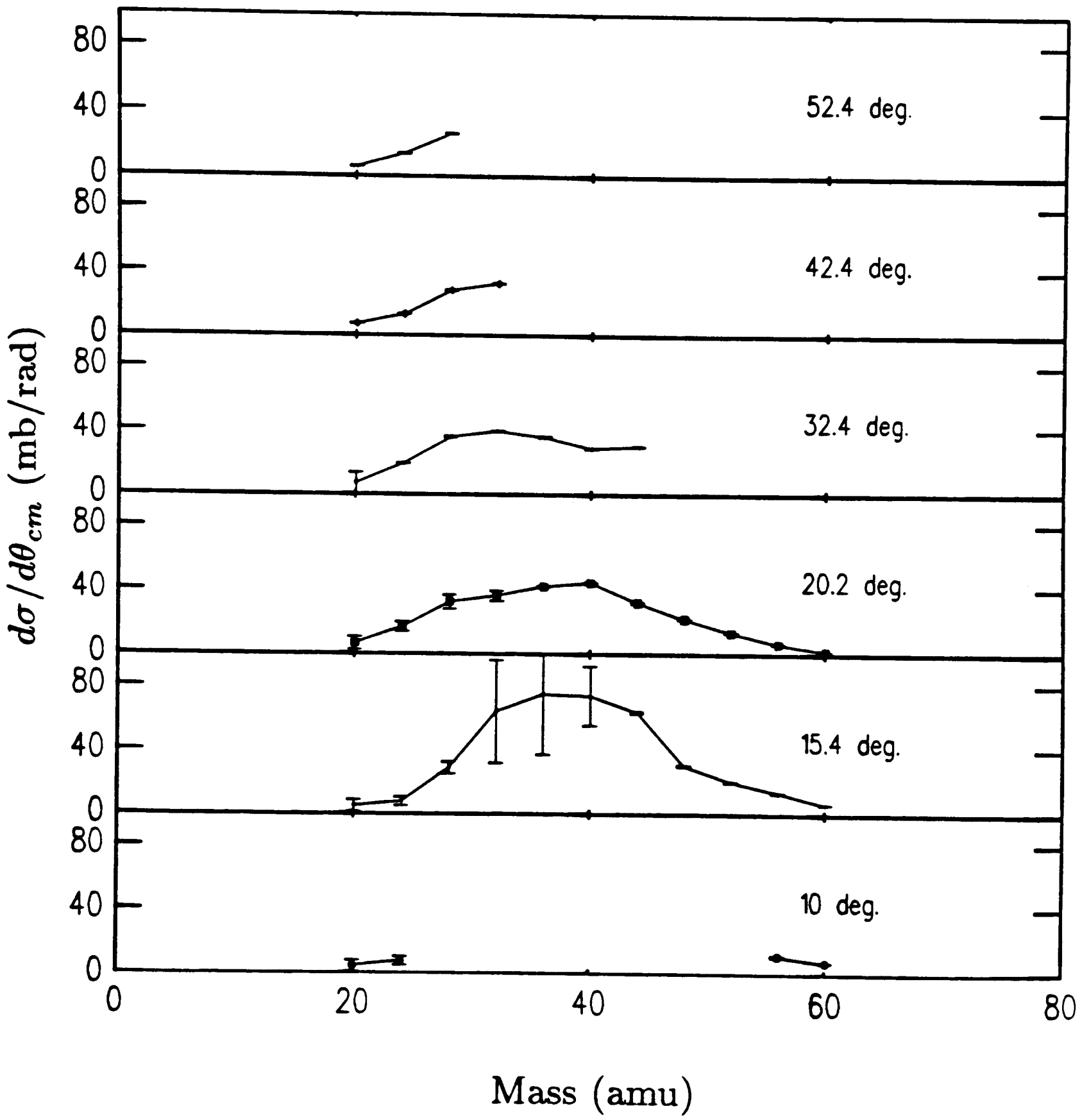


Figure 5.5. Mass distributions in the centre of mass frame from the system ^{40}Ca + ^{40}Ca at 230.5 MeV.

the form $d\sigma/d\theta_{cm} = constant$ – as expected for a fusion-fission reaction in the medium mass region. In the case of the 230.5 MeV data there is a hint of a rise in $d\sigma/d\theta_{cm}$ forward of the grazing angle for masses close to 40.

Figures 5.6 and 5.7 were used to extract average mass distributions. This was achieved by taking the weighted mean value of $d\sigma/d\theta_{cm}$ across the whole angular range for a given mass bin. The weighting factor used was the number of counts in the laboratory frame yield for each bin. The data points with the largest errors were neglected for the purposes of this procedure. Figure 5.8 shows the average mass distribution, and a Gaussian fit, for each energy. The Gaussian for 197.3 MeV has a centroid of 38 amu and a full width half maximum of 26 amu, while the fit for the 230.5 MeV data has the same centroid, but a slightly narrower full width half maximum of 24 amu. The shifts in centroids of the mass distributions indicate that, on average, about four nucleons are evaporated.

The weighted mean values of $d\sigma/d\theta_{cm}$ for each energy were summed and multiplied by $\pi/2$ to obtain (assuming $d\sigma/d\theta_{cm} = constant$) the total fissionlike cross section (σ_f) at each energy.

$$\text{At 197.3 MeV, } \sigma_f = 197.6 \pm 35.4 \text{ mb.}$$

$$\text{At 230.5 MeV, } \sigma_f = 403.1 \pm 64.1 \text{ mb.}$$

5.2.5 Q-Values Distributions

For a two-body reaction, the Q-value is given by the expression

$$Q = E_3 + E_4 - E_{lab} \tag{5.4}$$

where E_{lab} is the bombarding energy and the subscripts 3 and 4 indicate the detected and undetected reaction products respectively. E_4 is given by

$$E_4 = \frac{1}{M_4}\left[M_p E_{lab} + M_3 E_3 - 2\cos\theta\sqrt{M_p M_3 E_{lab} E_3}\right] \tag{5.5}$$

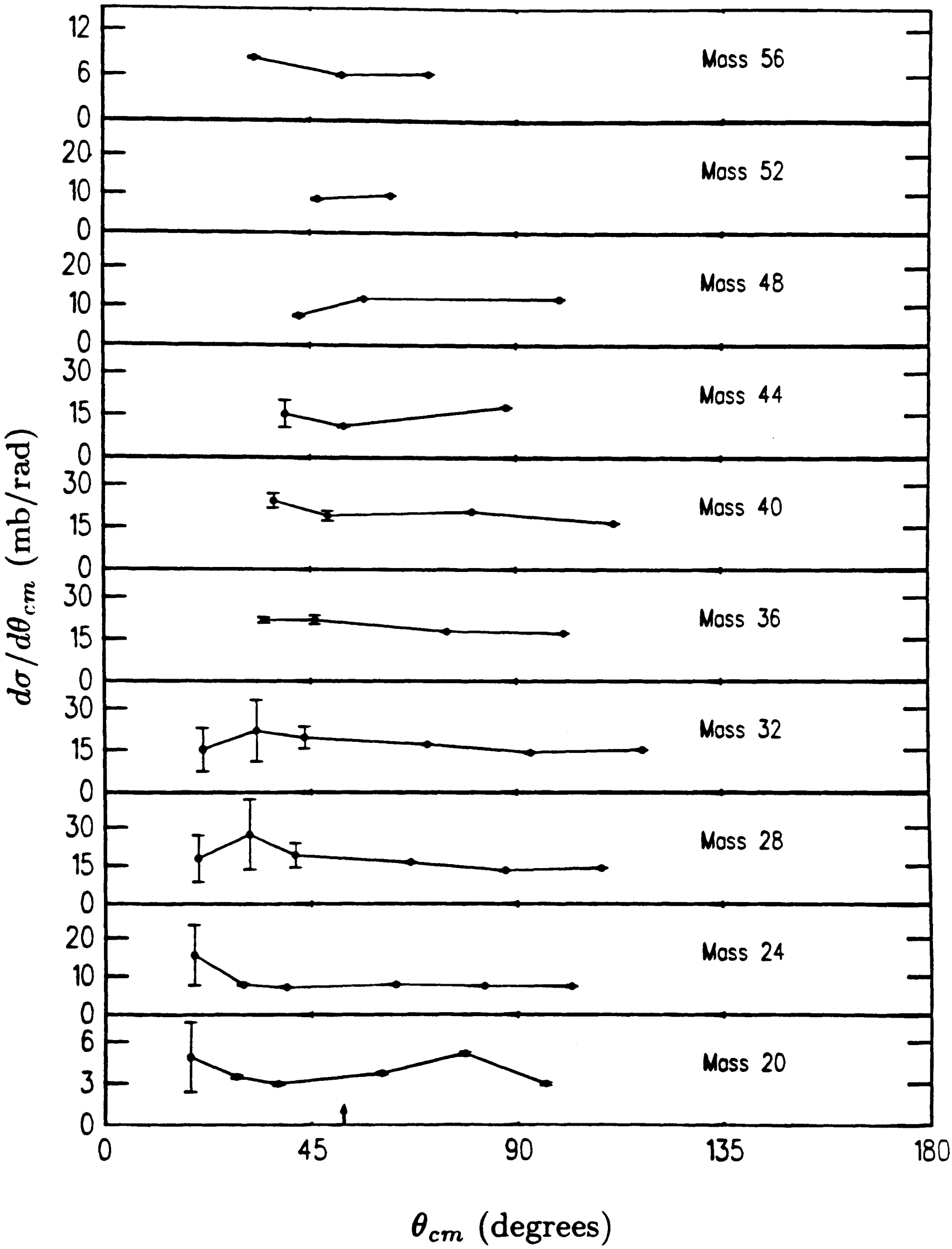


Figure 5.6. Angular distributions in the centre of mass frame from ^{40}Ca + ^{40}Ca at 197.3 MeV. The arrow in the mass 20 distribution indicates the grazing angle.

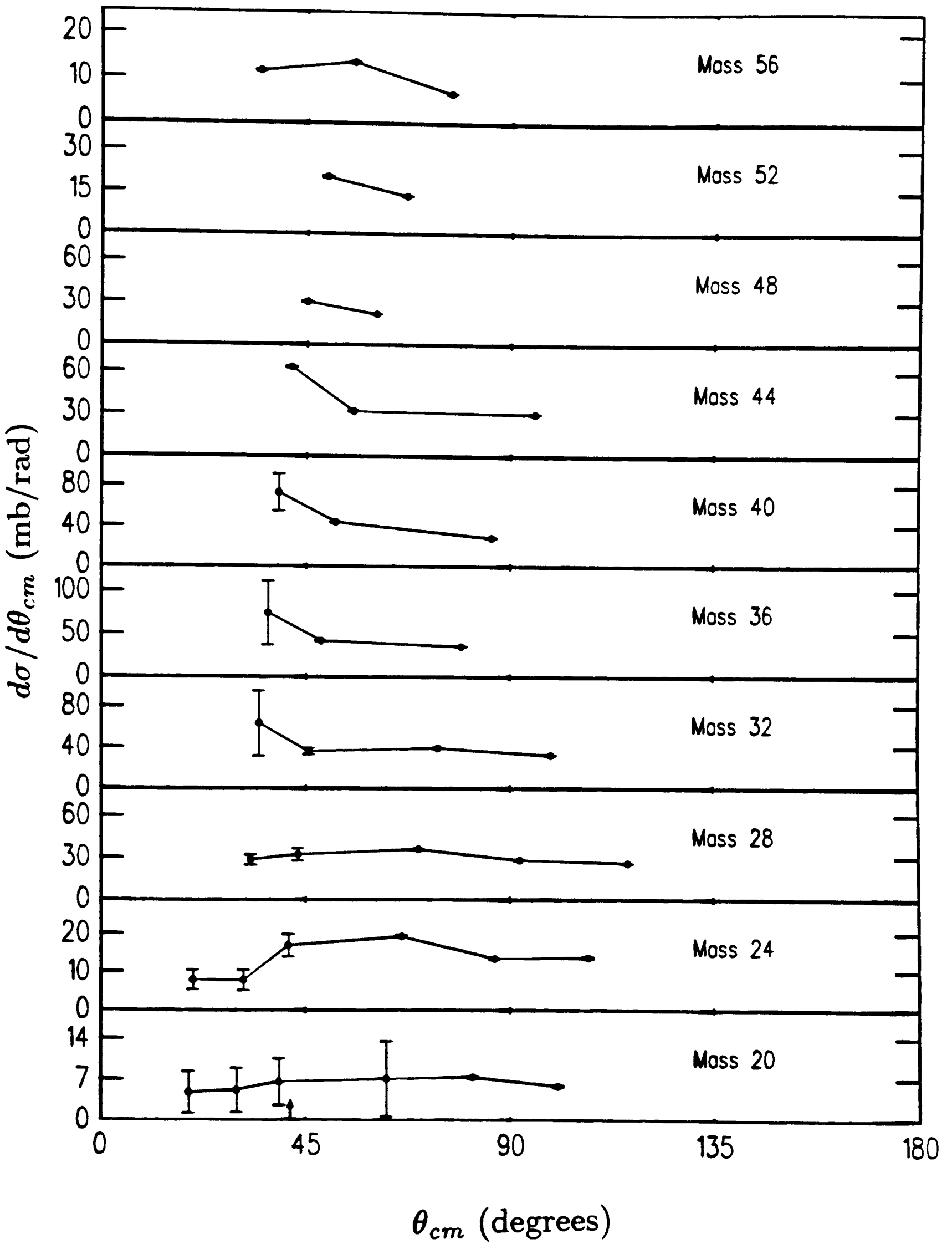


Figure 5.7. Angular distributions in the centre of mass frame from ^{40}Ca + ^{40}Ca at 230.5 MeV. The arrow in the mass 20 distribution indicates the grazing angle.

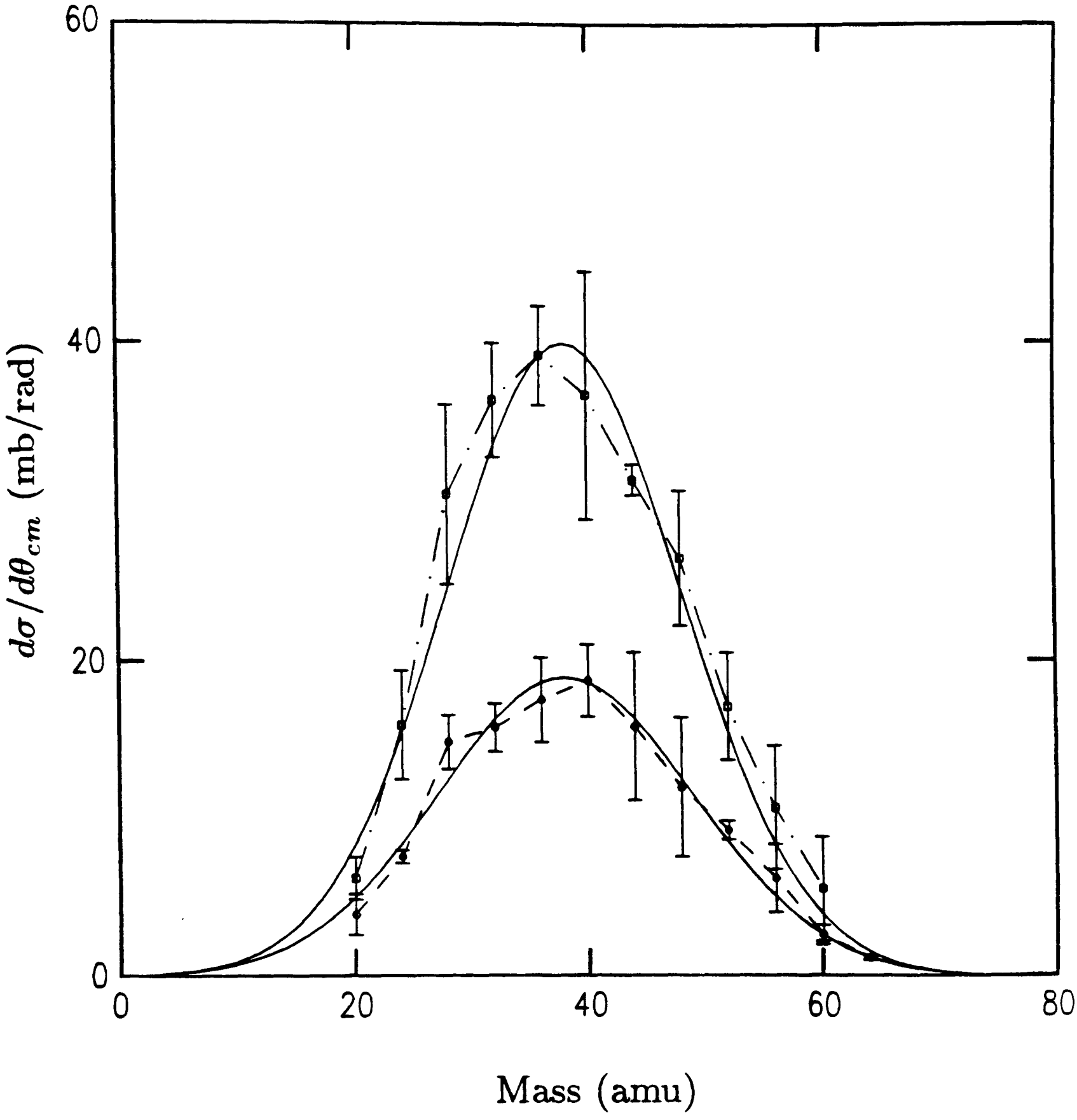


Figure 5.8. The average mass distribution from $^{40}Ca + ^{40}Ca$ for each bombarding energy. The dashed line shows the distribution for 197.3 MeV and the dot-dashed line that for 230.5 MeV. The solid curves are Gaussian fits to each distribution and are discussed in the text.

where M_p denotes the projectile mass. This method was used to calculate Q-values for the six silicon surface barrier detectors, as a function of mass, for both energies: they are relatively flat as a function of angle, as shown in figures 5.9 and 5.10.

For the backward angle detectors, where the data are cleanest, the procedure outlined in appendix I.4 was used to calculate a predicted Q-value for each mass bin (Q_{pred}). This quantity was subtracted from the measured Q-value (Q_{exp}) to obtain a Q-value difference (ΔQ). A plot of ΔQ against mass for the 42.4° detector at an energy of 197.3 MeV is shown by the dashed line in figure 5.11. The ground state Q-values (Q_{gs}) for the reaction

$$^{40}\mathrm{Ca}+^{40}\mathrm{Ca} \Rightarrow {}^{M}_{Z}\mathrm{X}+\mathrm{Y}+Q_{gs}$$

are also shown in figure 5.11 (solid line). M indicates the mass of reaction product X with $Z = M/2$, and Y denotes the complementary fragment. The results display a strong correlation between ΔQ and the ground state Q-values. A similar plot for the 230.5 MeV data (dot-dashed line in figure 5.11) shows a rise in ΔQ close to mass 40, indicating the Q-values become slightly more positive in the vicinity of symmetric fragmentation at higher energy. It should be emphasised that these variations in ΔQ represent fluctuations of order 1 MeV in quantities whose standard deviations are over 6 MeV. Also, the predicted Q-values are calculated assuming sticking friction, and so fluctuations in ΔQ could be indicative of the inadequacies of this assumption and thus might not be correlations with the ground state Q-values. Nevertheless, the strong correspondence is interesting.

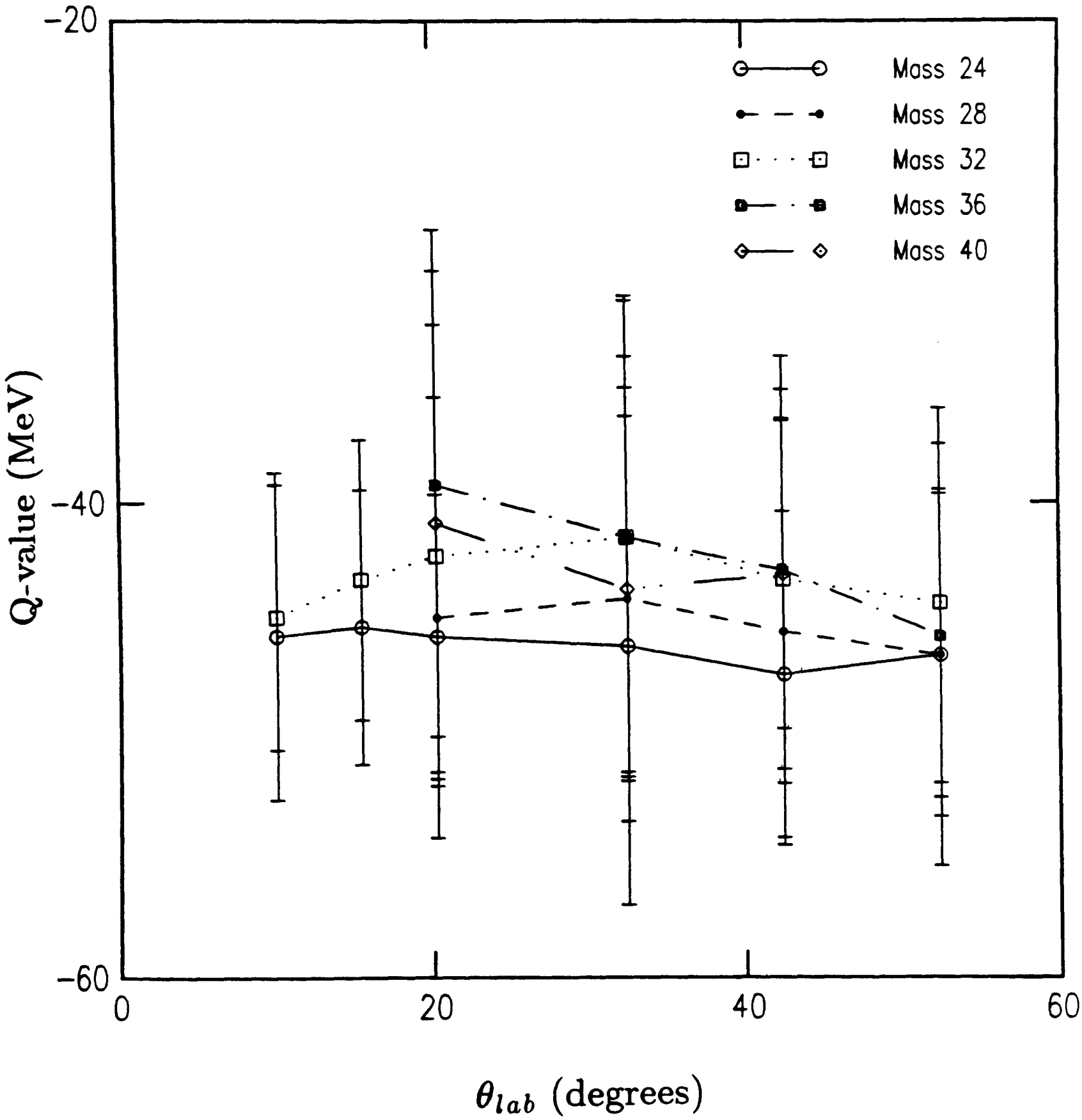


Figure 5.9. Two-body Q-value for each mass bin plotted as a function of angle in the laboratory frame, for the 197.3 MeV data. The error bars indicate full width half maxima.

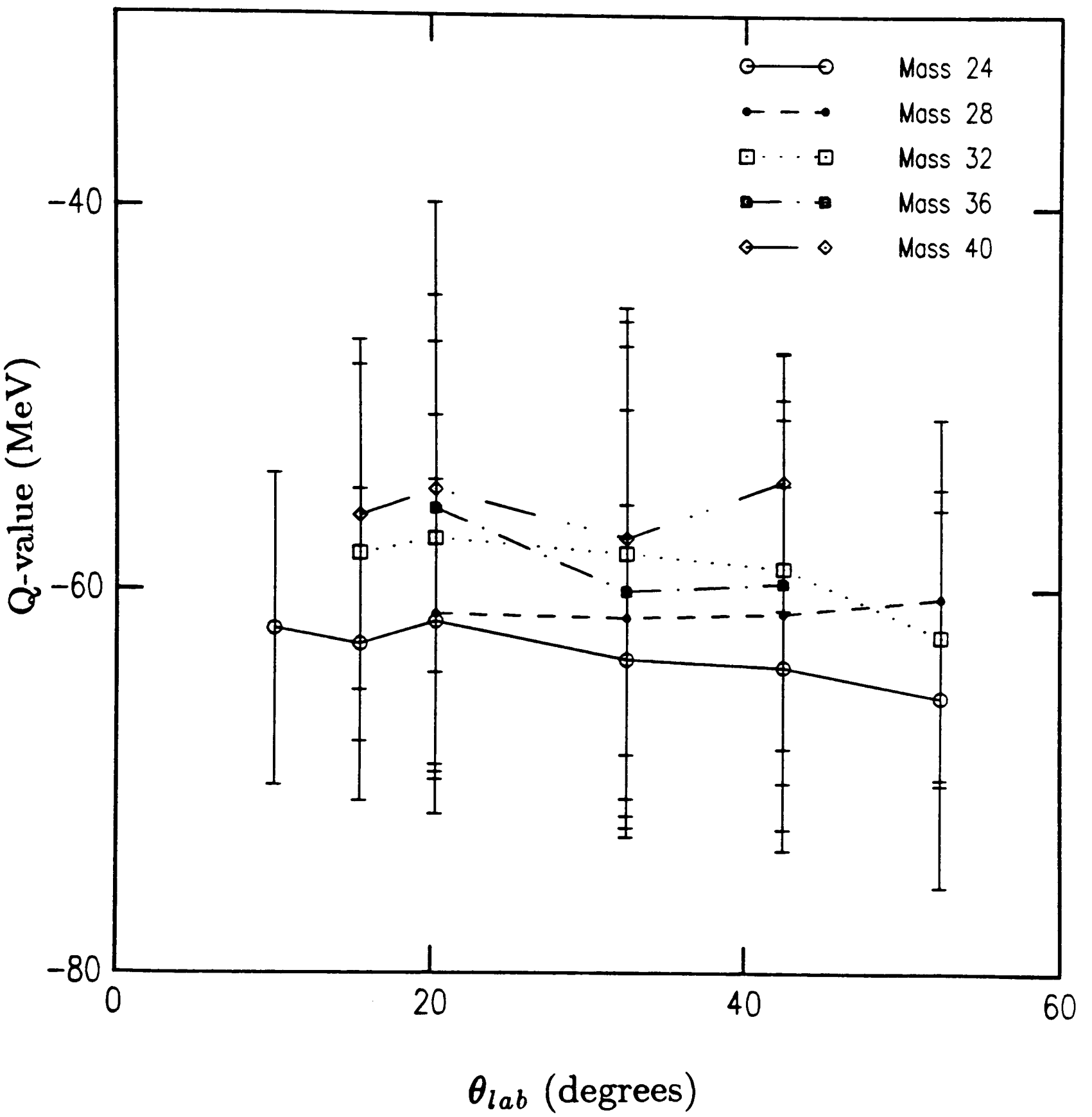


Figure 5.10. Two-body Q-value for each mass bin plotted as a function of angle in the laboratory frame, for the 230.5 MeV data. The error bars indicate full width half maxima.

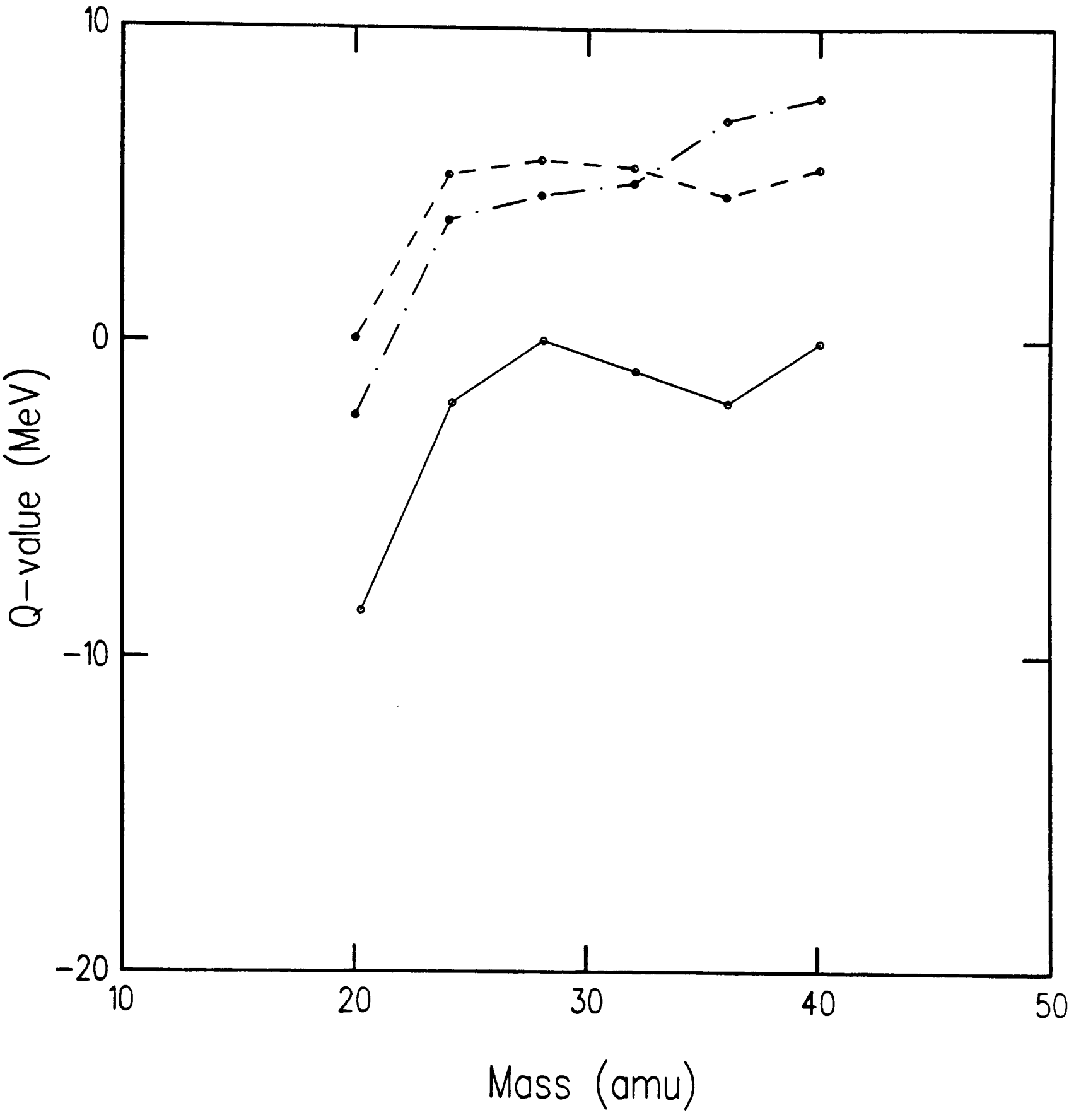


Figure 5.11. Deviations of the measured Q-values from model predictions. The dashed line shows the deviation at 197.3 MeV and the dot-dashed line that at 230.5 MeV. The solid line shows the ground state Q-values (see text).

5.3 Singles Data from the MWPC-BCS Telescope

The main purpose of the multiwire proportional counter Bragg curve spectrometer telescope was to obtain charge identification. We point out in section 3.4.1 that the height of the Bragg peak is approximately proportional to charge Z. Therefore, the B_P signal contains Z information. All symbols referred to in this section are explained in section 4.3.2 and the associated figures.

B_P was plotted against Bragg energy (E_B), range 1 (R_1), range 2 (R_2) and cathode time (CRF), to see which gives the best charge separation. This criterion was best satisfied by a plot of B_P against R_1, which is shown in figure 5.12. R_1 is a measure of how far the incident particle is from the Frisch grid when it comes to rest and hence is proportional to a constant minus its true range. The data fall into three regimes as indicated in figure 5.12. The vertical line for low R_1 corresponds to particles which travel through the counter without stopping. This is known as punch through. Ions which do this are generally energetic and light. The solid diagonal line for the highest R_1 corresponds to events which do not have enough energy to reach their Bragg peak. Heavy, slow ions are expected to be the main contribution to this yield. The region in between these two extremes corresponds to events which reach their Bragg peak and stop within the active region of the counter. Charge identification can readily be achieved for these 'good' events.

In figures 5.13 and 5.14 we show calibrated charge spectra for the good events (solid lines) at 197.3 and 230.5 MeV respectively. The data display an odd-even structure, with even charges being favoured. This is consistent with the α-particle-like structure observed in the singles mass spectra. To verify that these data are consistent with the singles yields, a series of Monte-Carlo simulations has been performed using the program FLAME, which is described in appendix II. For each energy, the charge distribution in the MWPC-BCS telescope was calculated, assuming a primary mass distribution given by the

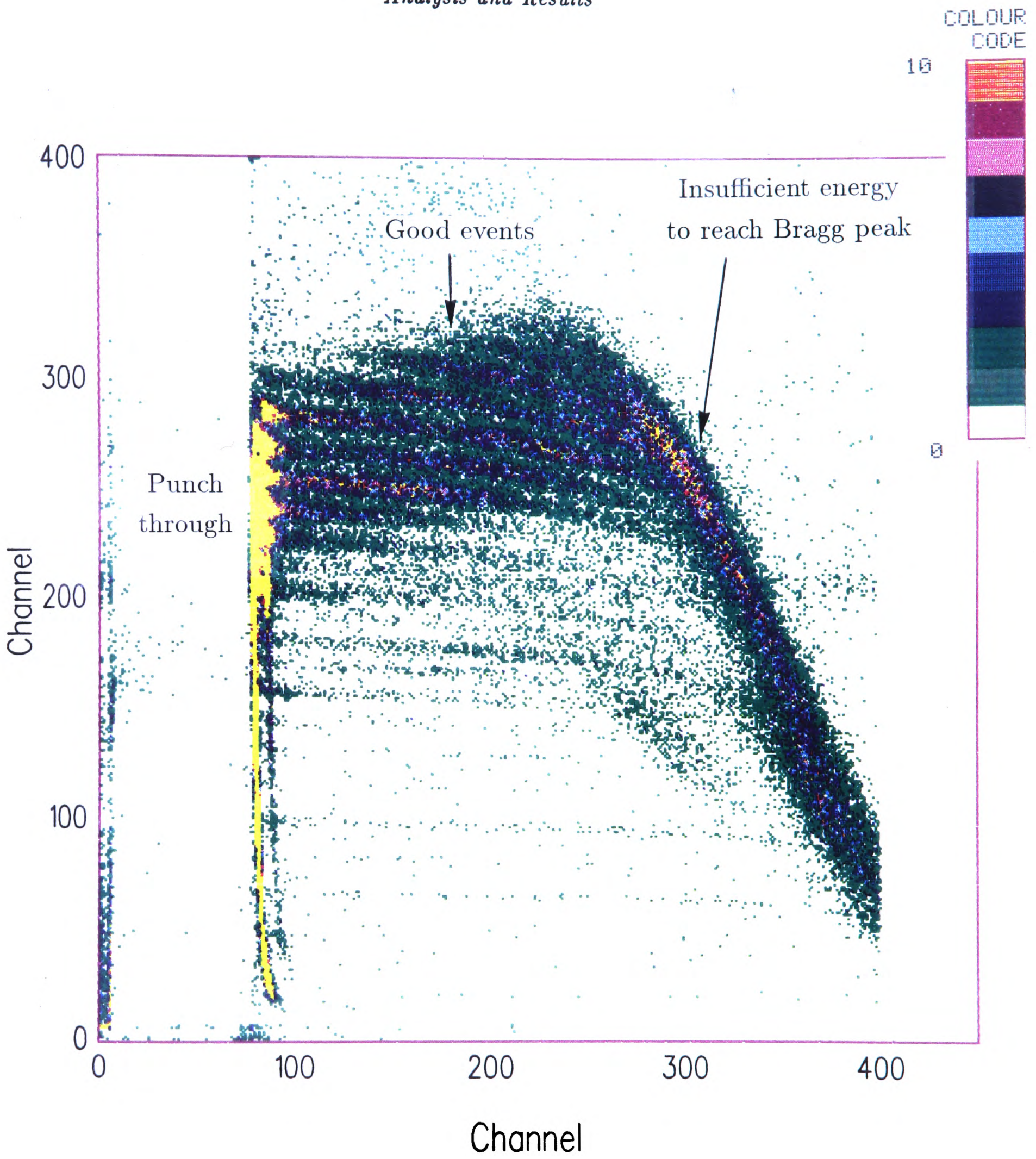


Figure 5.12. A scatter plot of B_P against R_1 obtained from the Bragg curve spectrometer for a bombarding energy of 197.3 MeV. The various regions of the data are indicated.

Gaussian fit in figure 5.8 and $Z = M/2$. These predictions are shown by the dashed lines in figures 5.13 and 5.14. Data and calculation are in good agreement for high charge values, but for small Z the Monte-Carlo overpredicts the data, as many of the lighter particles punch through. Thus, these charge distributions are generally consistent with the singles mass spectra.

Analysis of the plots of B_P against E_B, R_1, R_2 and CRF for the punch though data confirms that these events generally correspond to light ions, as can be seen in figure 5.12. We point out in section 4.3.2 that the slope of the B_P signal was measured in an effort to resolve events which do not reach their Bragg peak. Thus, the SLOPE signals from such events were plotted against E_B, R_1, R_2 and CRF. Unfortunately, no separation of ions which fail to reach their Bragg peak was achieved. In principle a knowledge of the Bragg energy and time allows the fragment mass to be determined. Such a procedure requires a reliable energy calibration, which we could not achieve in the limited experimental time available.

5.4 Coincidence Analysis

Once it had been established that the singles spectra from the SSB and MWPC-BCS telescopes are consistent, the data were analysed in coincidence mode. The mass distributions from the 6 surface barrier detectors were compared with the charges of the complementary fragments detected by the MWPC-BCS telescope.

Figures 5.15 and 5.16 show typical mass (from the 42.4° SSB detector) and charge (from the Bragg spectrometer) spectra in coincidence. The spectra are shown by the solid lines. To verify their consistency with the singles data, distributions predicted by the Monte-Carlo program FLAME are also shown, by

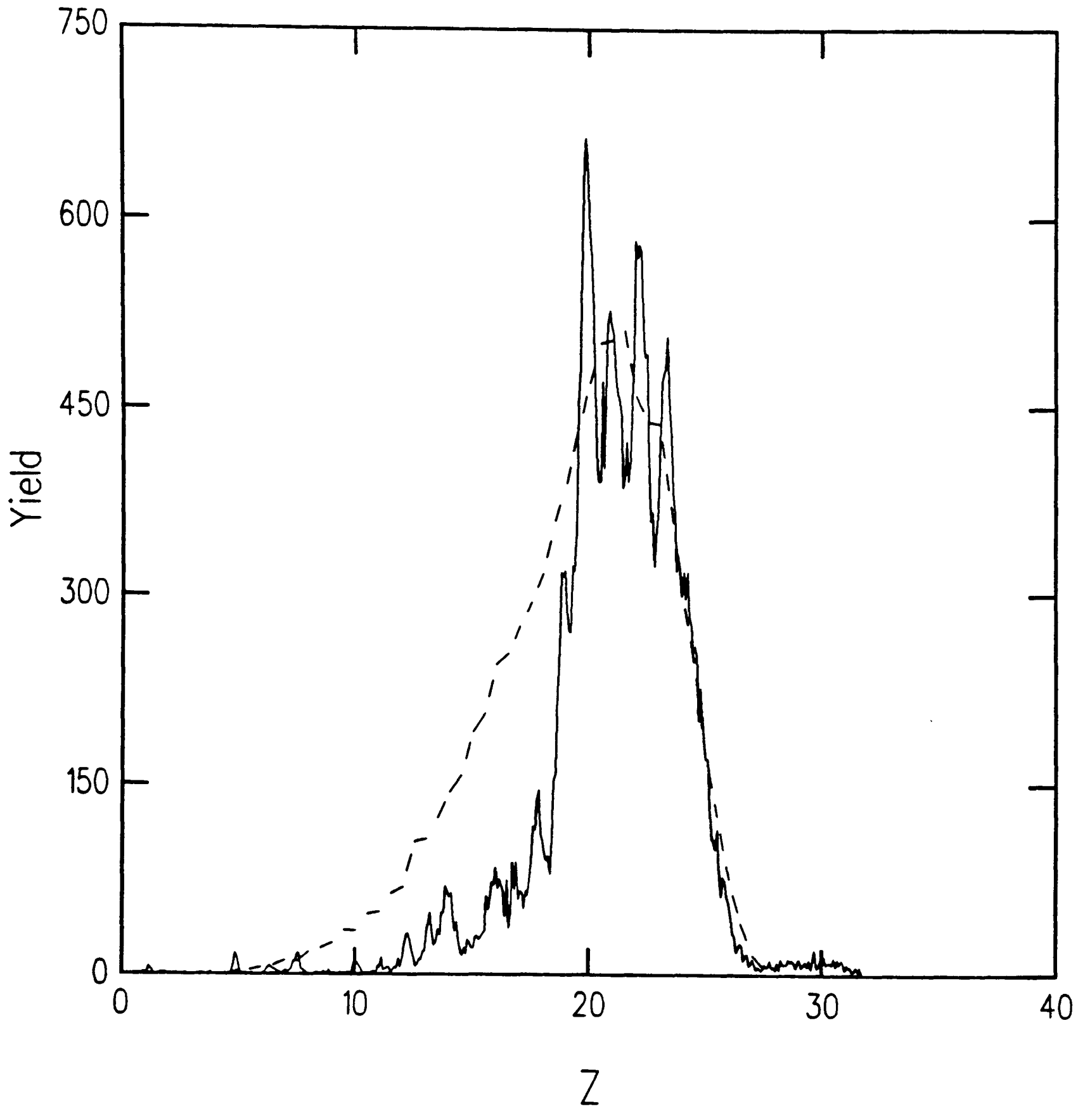


Figure 5.13. A charge distribution from the Bragg curve spectrometer for the good events at 197.3 MeV (solid line). The dashed line shows a Monte-Carlo simulation.

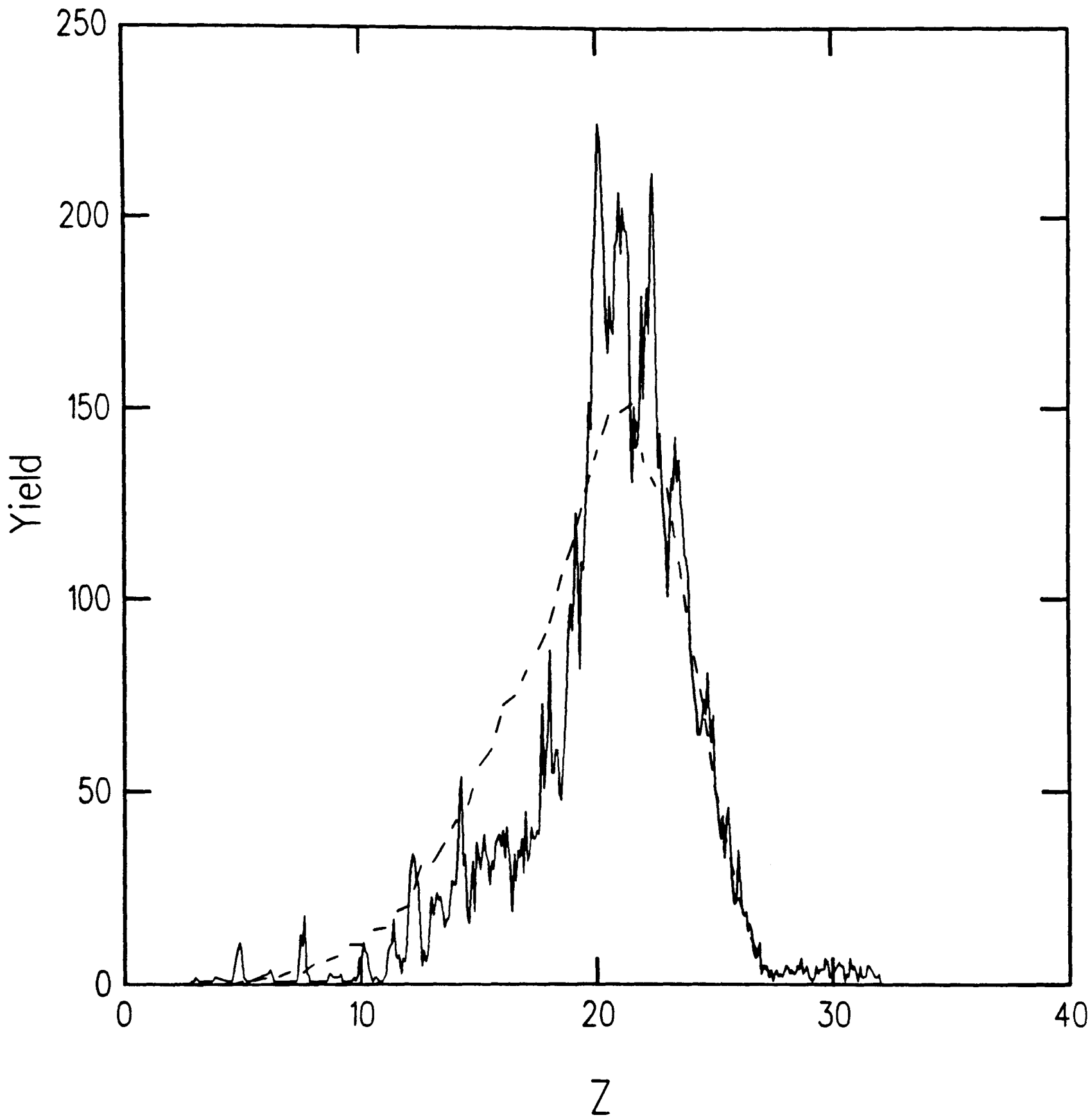


Figure 5.14. A charge distribution from the Bragg curve spectrometer for the good events at 230.5 MeV (solid line). The dashed line shows a Monte-Carlo simulation.

the dashed lines. The inputs to these calculations are exactly as described in the previous section and appendix II.

In figure 5.17 we present a plot of mass against energy for the 32.4° silicon surface barrier detector, in coincidence with the Bragg curve spectrometer. Since the MWPC-BCS telescope was situated at a similar angle – i.e. 30° – one would expect that if the reaction mechanism is two-body the mass distribution would be approximately symmetric about mass 40. This is borne out in figure 5.17, which has maxima at masses of 29 and 48. Furthermore, the coincidence requirement has noticeably cleaned up the data.

Figure 5.18 shows a plot of charge Z_1 against the mass of the coincident partner M_2 at 197.3 MeV. This figure was obtained by combining the yields in each of the 6 silicon surface barrier detectors. A small amount of contamination from ^{40}Ca + ^{nat}O can also be seen in figure 5.18. The dashed line corresponds to $2Z_1 + M_2 = 80$, i.e. to no evaporation, assuming $Z_1 = M_1/2$ for each fragment. The solid line shows where events with $2Z_1 + M_2 = 76$ should fall according to the $Z_1 = M_1/2$ assumption. Clearly the latter line gives the best description of the data. Thus, the data are consistent with the evaporation of about 4 amu – in agreement with the singles results. A similar analysis of the 230.5 MeV data suggests the evaporation of up to 6 amu. Thus these data are consistent with the evaporation of between 4 and 6 atomic mass units, on average. However, these results are dependent on the assumption that $Z = M/2$ for each fragment. Unfortunately, this cannot be verified from the data directly.

Both singles and coincidence data provide compelling evidence for the evaporation of several nucleons. Thus, it is interesting to ask whether the evaporation occurs before, or after, the compound system bipartitions. At whatever stage the evaporation occurs during the reaction it should, on average, have no effect on the trajectories of the residual particles. Assume the system emits an α-particle: if the particle is emitted after the system splits into two, the average kinematics should be those for the binary fission of ^{80}Zr, however if the

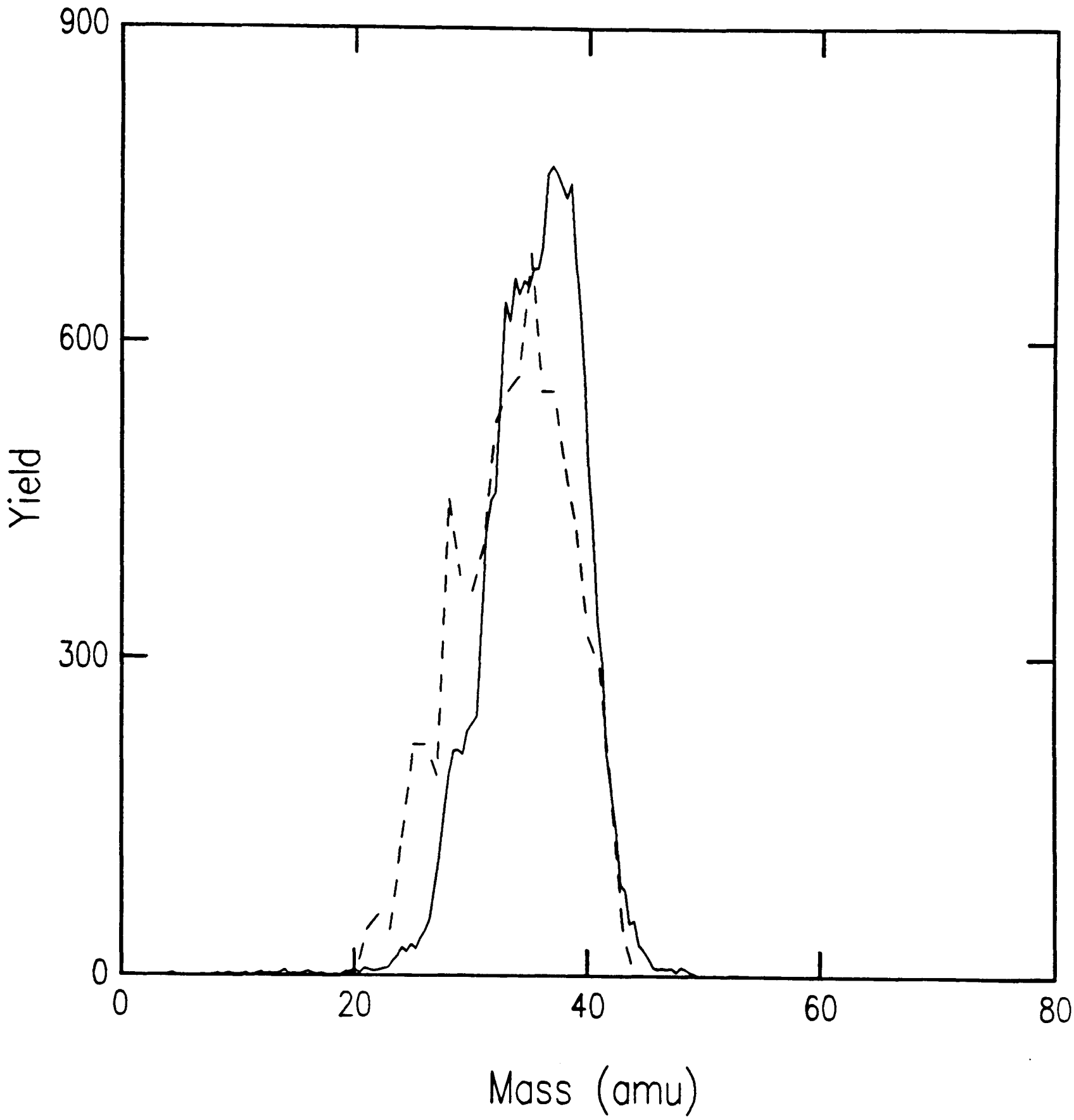


Figure 5.15. Mass spectrum from the 42.4° detector in coincidence with the MWPC-BCS telescope at a bombarding energy of 197.3 MeV (solid line). The dashed line shows a Monte-Carlo simulation.

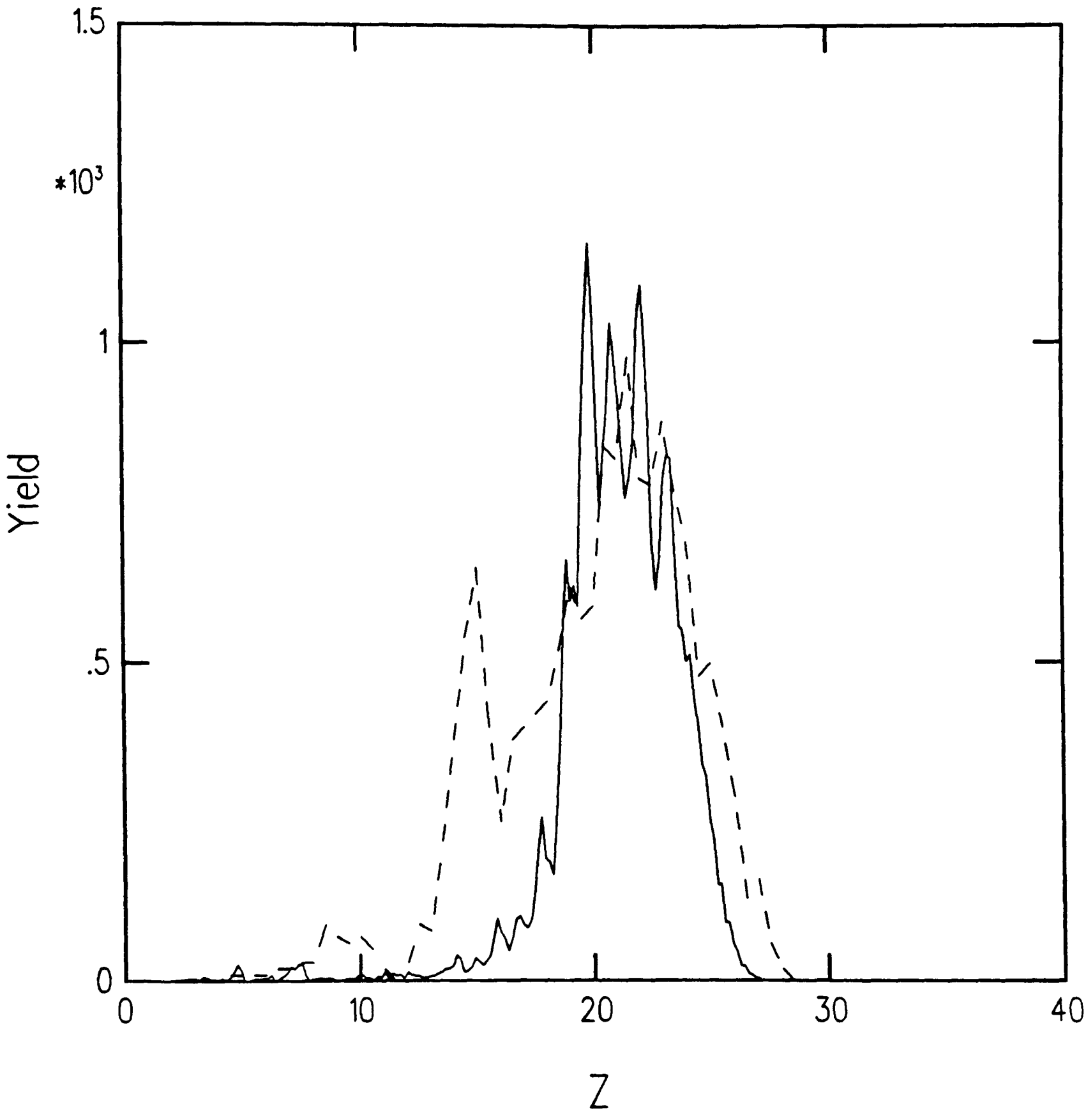


Figure 5.16. Charge distribution from the Bragg curve spectrometer in coincidence with all six SSB detectors at 197.3 MeV (solid line). The dashed line shows a Monte-Carlo simulation.

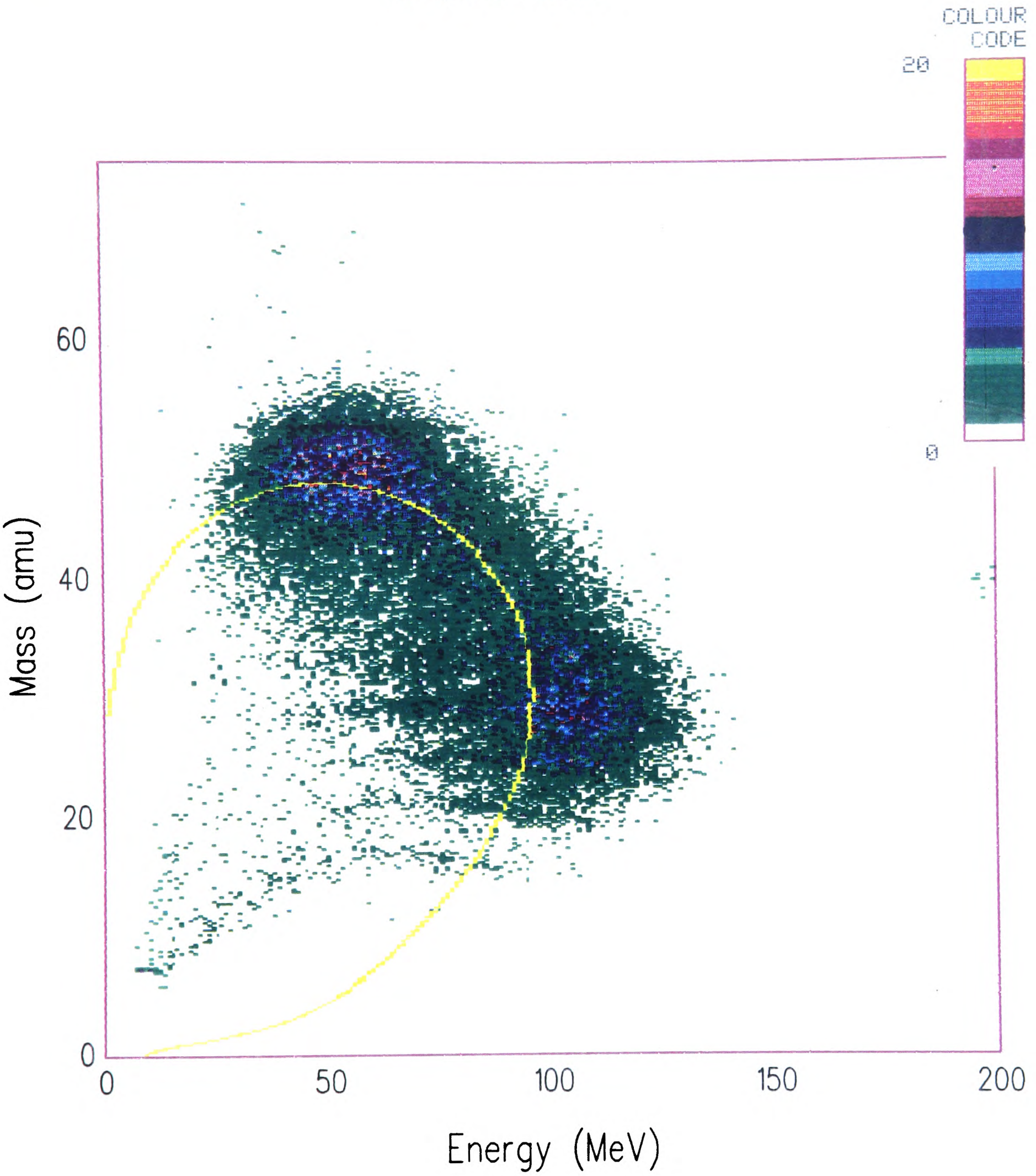


Figure 5.17. Scatter plot showing mass against energy for the 32.4° SSB detector at 197.3 MeV, in coincidence with the Bragg spectrometer. The curve shows the predicted locus of fissionlike events from $^{40}Ca + {}^{40}Ca$.

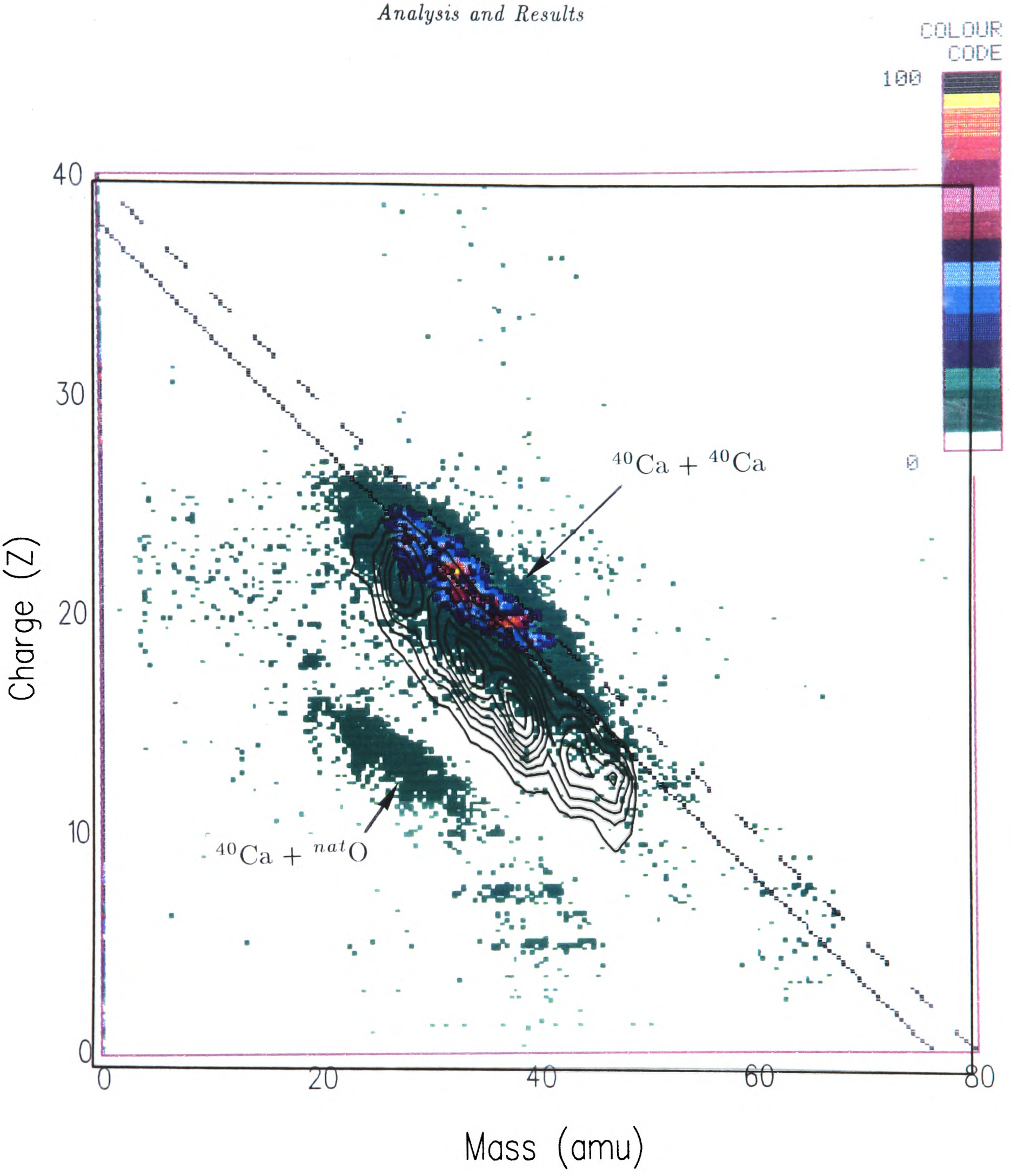


Figure 5.18. Plot of charge in the Bragg counter against mass in the array of time of flight telescopes at 197.3 MeV. The dashed line shows the limit $N=Z=40$ (i.e. no evaporation from the ^{40}Ca + ^{40}Ca system) and the solid line $N=Z=38$. Events from reactions of the beam with oxygen in the target are indicated. The overlay shows a model prediction, which is discussed in section 6.4.

evaporation takes place before, the system is described by the kinematics for the fission of a ^{76}Sr nucleus moving with the same velocity as the compound system. If the total kinetic energy for each of these systems is estimated using the procedure outlined in appendix I.4, then the most likely coincidence angles for the two processes can be deduced. Calculations along these lines reveal that if one reaction product is detected at a certain angle, then the complementary fragment angles predicted for each of the evaporation mechanisms differ by as much as 3°. To investigate this possibility, for a series of charges and masses, a gate was placed on a particular charge in the Bragg counter and a particular mass in an SSB detector and the position signal in the multiwire proportional chamber analysed. The position spectra obtained were broad and showed no evidence for two peaks.

If it is assumed that $N = Z$ (i.e. number of neutrons = number of protons) for the primary fragments, then further information about the evaporation process can be obtained from consideration of the energy barriers against emission of light particles. In figure 5.19 we present the energy barriers for the emission of s-wave protons, neutrons and α-particles from $N = Z$ nuclei between ^{12}C and ^{80}Zr. The s-wave energy barrier is equal to the sum of the binding energy and the Coulomb barrier (calculated here assuming $r_0 = 1.25$ fm) for each type of radiation. Clearly, in the case of heavy $N = Z$ nuclei, which are very neutron deficient, proton emission is the most favoured decay mode, while α-particle evaporation should be important for very low Z values. However, these plots are for s-wave particles. For finite angular momentum, the centrifugal barrier against α-particle decay will be smaller than that against proton or neutron emission. Thus, for increasing angular momentum α-particle emission will start to become more and more favourable. Hence, it seems most likely that the heavier fragments from the fissionlike decay of ^{40}Ca + ^{40}Ca will predominantly

emit protons or α-particles, whereas lighter species will preferentially emit α-particles. This is to be expected if the evaporation process takes the $N = Z$ fragments towards the valley of β-stability.

5.5 The ^{28}Si + ^{50,52,54}Cr Experiment

The analysis of this experiment followed much the same pattern as that of the singles data from the ^{40}Ca + ^{40}Ca experiment described in section 5.2. However there were several small differences. The stopping power tables of Northcliffe and Schilling and of Ziegler were used to correct all energies for losses in the avalanche counters' windows and the isobutane counter gas (which is typically $\approx$ 2 MeV in total).

Very little, or no, pile-up occured in this experiment. This fact coupled with the low yields from reactions with target impurities simplified the data analysis significantly, obviating the need to correct for these effects.

A plot of mass against energy for the system ^{28}Si + ^{50}Cr, at a bombarding energy of 150 MeV and a laboratory angle of 30°, is presented in figure 5.20. The locus of fissionlike events is also shown. As with the ^{40}Ca + ^{40}Ca, the fissionlike events are well described by the Viola systematics if the sticking model is used to extrapolate to asymmetric splits. Figure 5.21 shows the fully damped yields in the four telescopes from this system. In figure 5.22 we present typical one-dimensional mass spectra in the centre of mass frame for ^{28}Si + ^{50}Cr: again only the fully damped events are shown. These mass distributions clearly have a different character to those for ^{40}Ca + ^{40}Ca. The strong asymmetric component appears to be centred at target and beam. The spectra contain some contamination around mass 28 from slit scattering. Problems with the reliability of the avalanche counters meant that no more than two points were available for

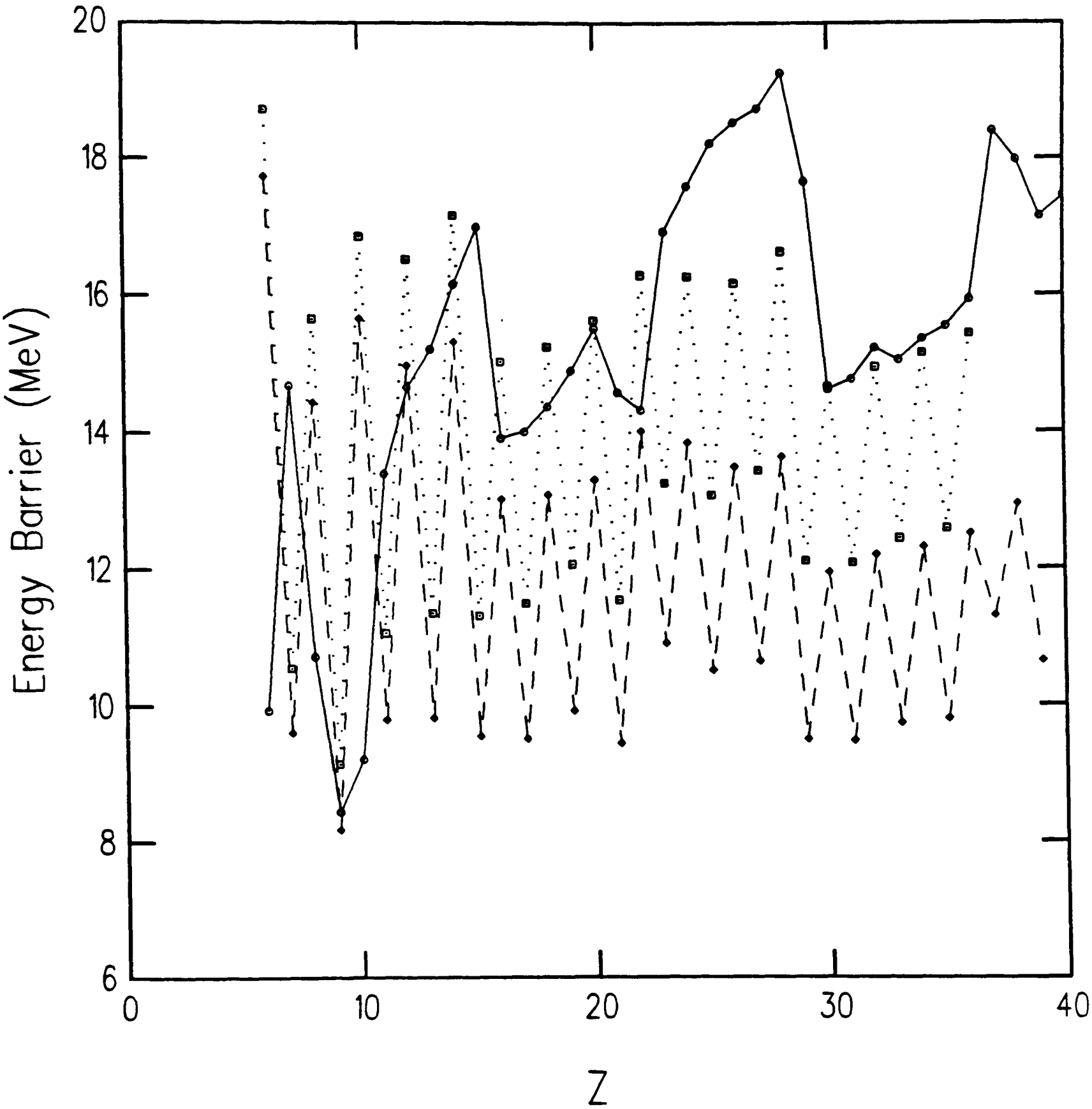


Figure 5.19. s-wave barriers against the emission of protons (dashed line), neutrons (dotted line) and α-particles (solid line) for $N = Z$ nuclei.

each angular distribution. However, this limited data is consistent with constant $d\sigma/d\theta_{cm}$, as can be seen in figure 5.22.

A typical Q-value spectrum is shown in figure 5.23. The centroid expected on the basis of the Viola systematics is also indicated. This confirms that the data have fully relaxed total kinetic energies. Variations of the fissionlike Q-values with mass split show no evidence for any correlation with the ground state Q-values.

The 130 MeV data for ^{28}Si + ^{52,54}Cr are similar in all respects to those for the isotope ^{50}Cr at the same energy and so are not presented. The total fissionlike cross sections (σ_f) for these systems were estimated by assuming constant $d\sigma/d\theta_{cm}$.

For 130 MeV ^{28}Si + ^{50}Cr, $\sigma_f = 33.8 \pm 9.2$ mb.

For 130 MeV ^{28}Si + ^{52}Cr, $\sigma_f = 25.0 \pm 6.8$ mb.

For 130 MeV ^{28}Si + ^{54}Cr, $\sigma_f = 26.9 \pm 7.3$ mb.

For 150 MeV ^{28}Si + ^{50}Cr, $\sigma_f = 143 \pm 42$ mb.

These data are consistent with those of Barrette et al. [17] for the system ^{32}S + ^{50}Ti at a similar range of energies (110 to 166 MeV).

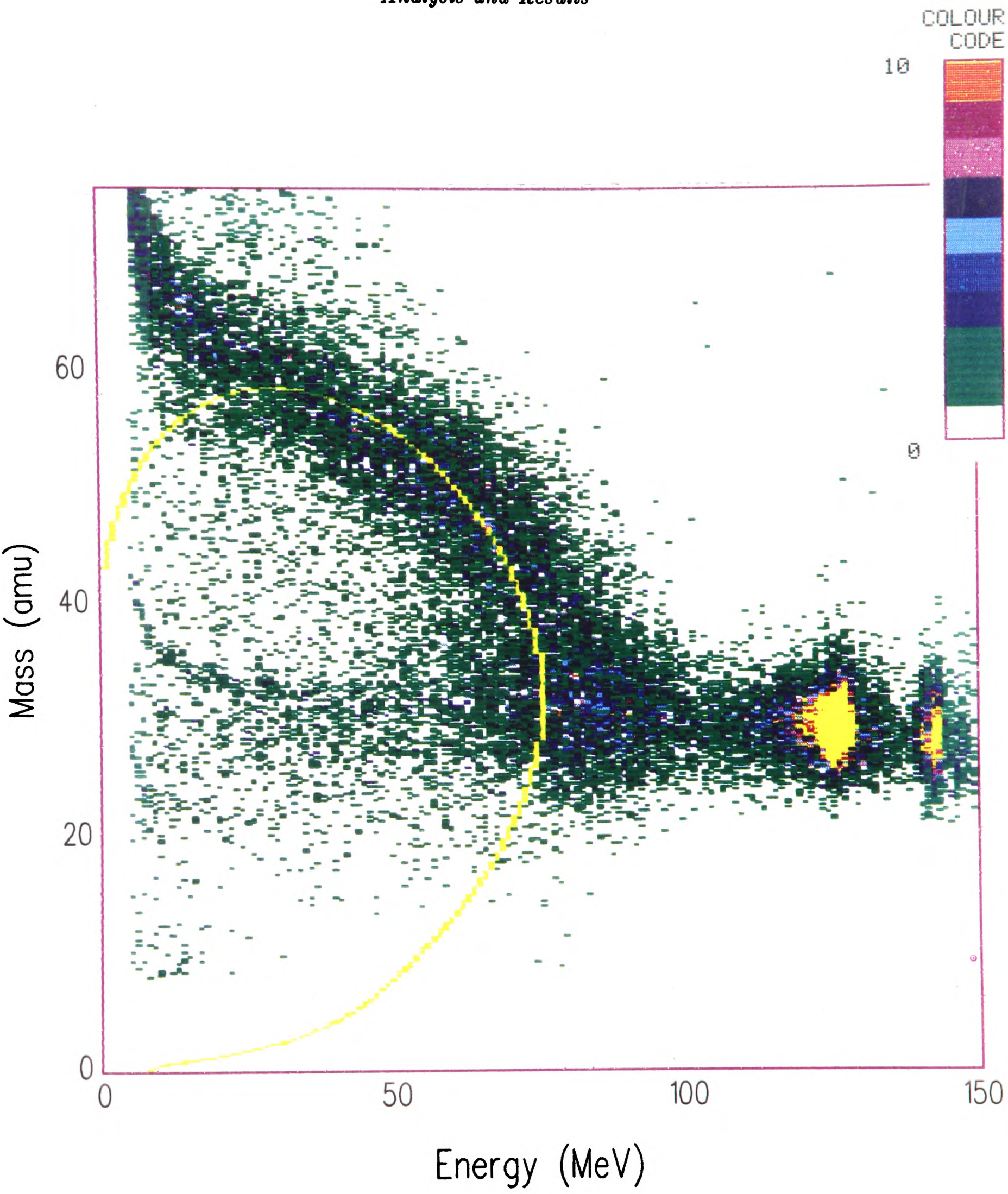


Figure 5.20. Scatter plot showing mass against energy for 150 MeV ^{28}Si + ^{50}Cr. The curve shows the predicted locus of fissionlike events.

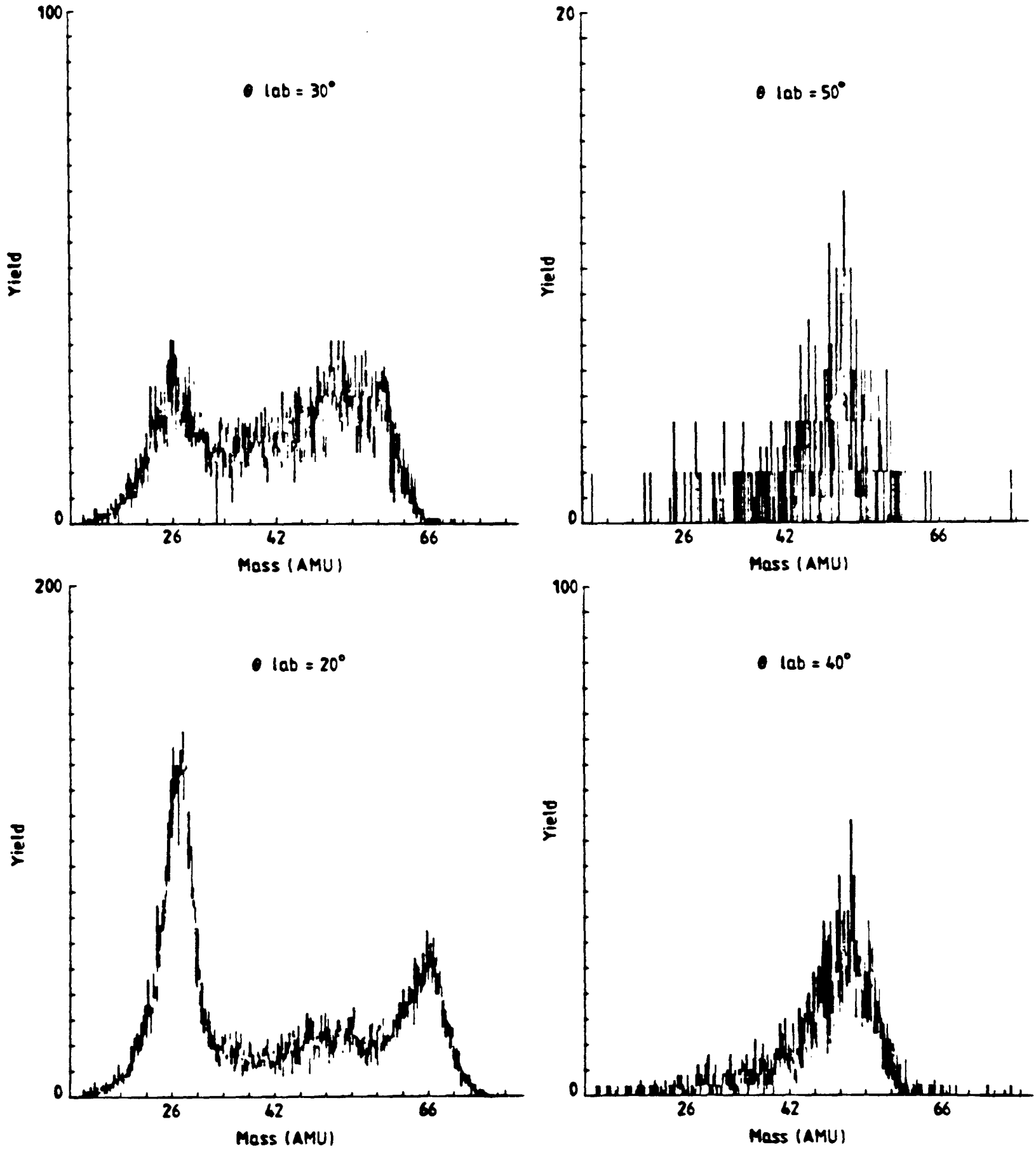


Figure 5.21. Fissionlike yields from 150 MeV ^{28}Si + ^{50}Cr in the four telescopes.

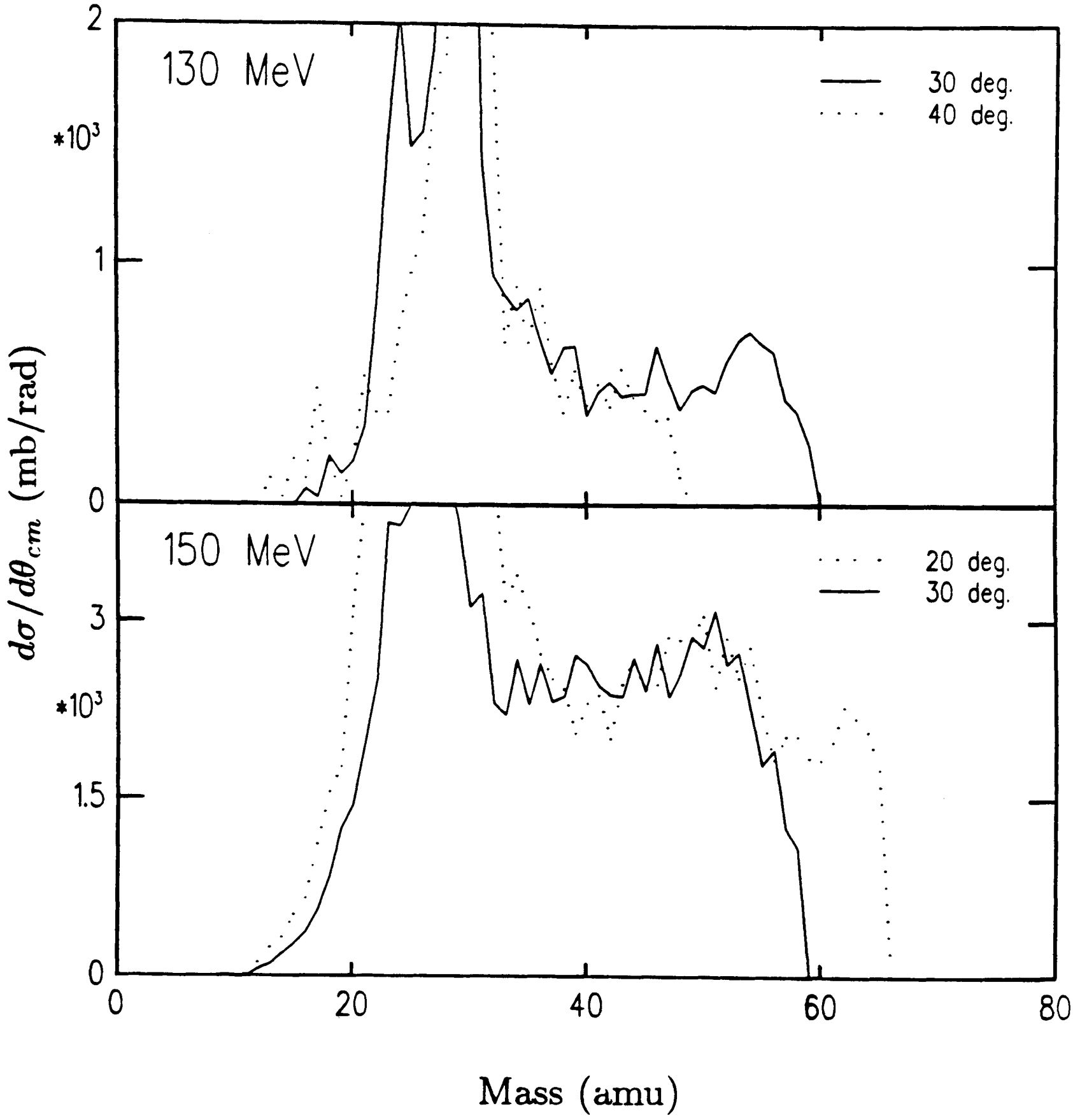


Figure 5.22. Mass distributions in the centre of mass frame for ^{28}Si + ^{50}Cr at both 130 and 150 MeV. The corresponding laboratory angle for each spectrum is indicated. The peaks at mass $\approx$ 28 are due to slit scattering. The cut-offs in backward angle spectra are due to kinematic effects.

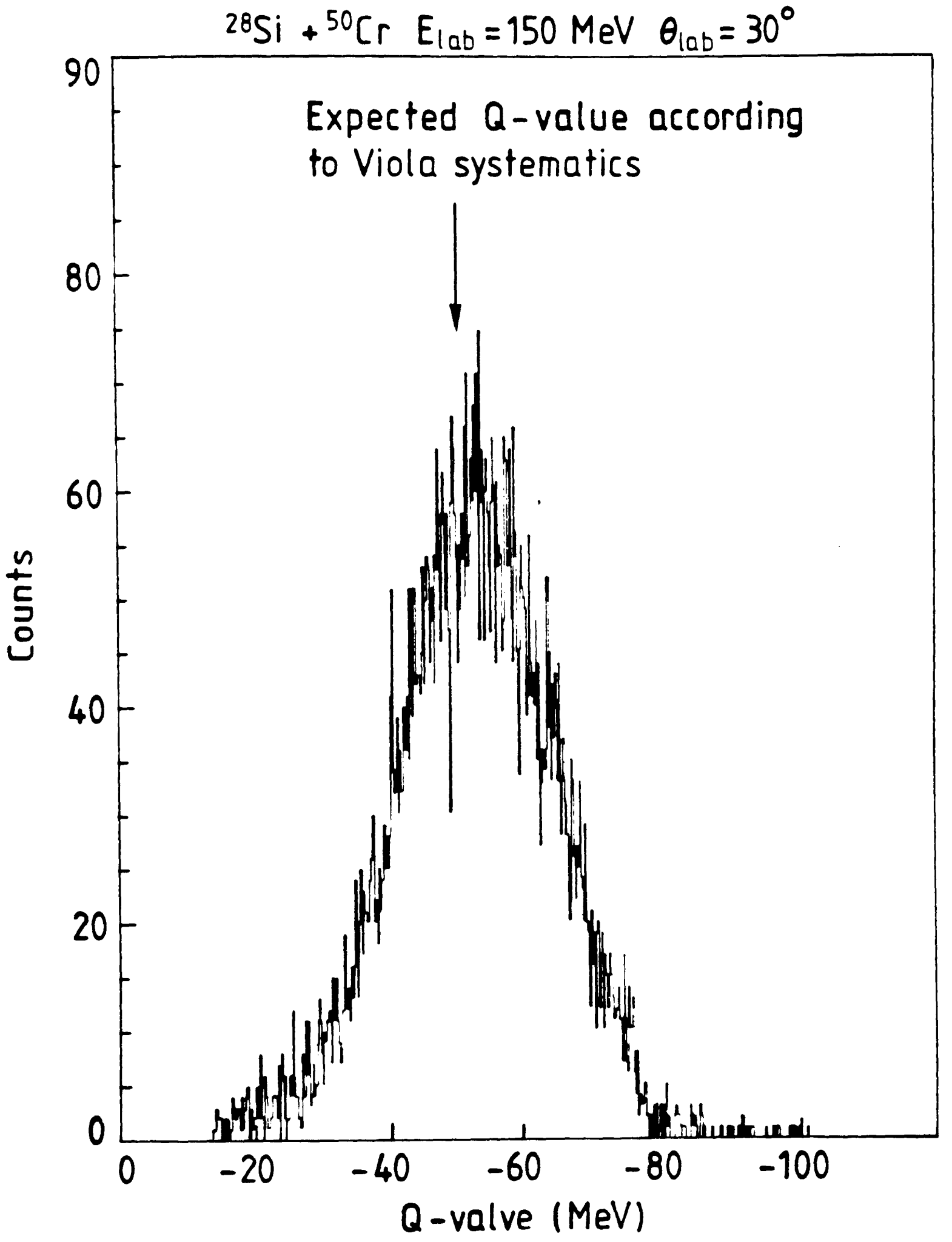


Figure 5.23. Q-value spectrum for 150 MeV ^{28}Si + ^{50}Cr. The Q-value predicted by the Viola systematics is indicated.

Chapter 6

Interpretation

When you have eliminated the impossible, whatever remains, however improbable, must be the truth.

Arthur Conan Doyle, *The Adventures of Sherlock Holmes*

6.1 Introduction

Once the data had been analysed, the experimentally deduced quantities – such as mass, charge and Q-value distributions – were compared with the predictions of theoretical models. The object of this process was to try to identify the reaction mechanism, or mechanisms, giving rise to the observed results. In this chapter we report on the theoretical analysis, much of which involved computer calculation and was carried out on the Oxford Nuclear Physics Laboratory's OEG VAX 11/780 and VAX 8700.

The comparison of fusion data with model predictions can be used to obtain information on the relative strengths of competing mechanisms. To this end the fusion cross sections for the systems studied are discussed in section 6.2 and compared with calculation.

As all reaction products analysed in this work have fully relaxed Q-values, they may all emanate from true fusion-fission reactions in which short-lived compound nuclei are formed. To investigate this possibility, calculations were

performed using two versions of the statistical model program CASCADE [47]. The first version uses the rotating liquid drop model (RLDM) fission barriers to calculate competition between fission and particle evaporation while the second version uses the rotating finite range model (RFRM) barriers [51]. Section 6.3 is a discussion of these calculations; the results and their sensitivity to the input parameters.

The fact that the centroid of the $^{40}Ca + ^{40}Ca$ fissionlike mass distribution is shifted slightly below 40 ($\approx$ 38) indicates that some evaporation occurs from the system. In order to deduce the primary fissionlike mass distributions for the systems studied a series of calculations was performed with the Monte-Carlo statistical model program LILITA [52]. These calculations are discussed in section 6.4.

A principal objective of this work has been to establish the evidence for intermediate reaction mechanisms. As intermediate mechanisms have been most successfully described in terms of diffusion model analyses, a set of model calculations has been performed for the systems investigated in this work. These calculations are presented in section 6.5.

We mention in chapter 2 (section 2.9) that much of the data on fissionlike reactions in the mass 80 region may be explainable in terms of asymmetric fission. This would happen if the systems were below the Businaro-Gallone transition, a situation made feasible for these systems by the effects of finite range forces. This possibility is discussed in more detail in section 6.6.

As a further test of the character of the reaction mechanism, the variances of the mass and energy distributions were compared with the predictions of the liquid drop model (given in the papers of Nix [53] and Nix and Swiatecki [54]). This is the subject of section 6.7.

As we point out in section 2.9.1, RFRM calculations reveal that fission barriers in the mass 80 region are lower than RLDM calculations suggest. Furthermore, finite range model calculations [51] also reveal that the fission barriers

for the systems studied in this thesis vanish at angular momenta of order $10\hbar$ lower than predicted by the RLDM. Thus it is interesting to ask whether the RFRM can provide an explanation for these data. Specifically, could it be that fast or quasi-fission is taking place? This possibility is considered in section 6.8.

In section 6.9 we consider the evidence for shell effects; in particular whether the α-particle structure observed for ^{40}Ca + ^{40}Ca indicates the existence of α-particle clustering in the compound nucleus, and if a correspondence between ground state Q-values and fissionlike mass distributions is seen. The relevance of this work to searches for superdeformation in this region is also discussed.

A summary of the salient points discussed in this chapter is presented in section 6.10.

6.2 Information from Fusion Measurements

As models of fusion can be used to yield estimates of the thresholds for the different competing processes and also give some indication of their relative strengths, it is informative to compare the measured fusion cross sections with the predictions of these models. In this short section on fusion all energies quoted are in the centre of mass frame, unless otherwise stated. Technical details of these calculations are given in appendix III.

The evaporation residue cross sections for ^{40}Ca + ^{40}Ca have been measured over a wide energy range by several groups. However only one set of results exists for the energy region of interest (Doubré et al. [55]) and this is inconsistent with other measurements at lower energies, which yield cross sections up to a factor of three lower (e.g. see Tomasi et al. [56]). Furthermore no published data exist for the systems ^{28}Si + ^{50,52,54}Cr. In view of this consideration, the input parameters for the ^{28}Si + ^{50,52,54}Cr calculations were obtained by extrapolation of those for ^{40}Ca + ^{40}Ca.

The processes of quasi-fission and fast-fission are discussed in section 2.5. The extra push model [13] can be used to extract estimates of their thresholds and magnitudes. The extra push model prediction for ^{40}Ca + ^{40}Ca, along with the experimental data, is shown in figure 6.1. In this diagram the single-dot-dashed line indicates the limitation to the fusion cross section brought about by the need for the extra push energy. The difference between this line and the solid line gives an indication of the size of the deep-inelastic cross section. Thus deep-inelastic scattering is expected to be small in magnitude at the energies studied (i.e. 98.7 and 115.3 MeV). For a symmetric system, the conditional and unconditional saddle points are identical, and so quasi-fission should not occur. The dashed line indicates the limiting condition for compound nucleus formation, corresponding to zero fission barrier (i.e. $B_f = 0$) according to the RLDM. The region between this line and the dot-dashed line corresponds to fast-fission – i.e. a fusion-fission type of reaction, but without the existence of a stable compound nucleus. The threshold for this process is expected to be of order 125 MeV for ^{40}Ca + ^{40}Ca, which is some 10 MeV above the highest energy used in this work. The double-dot-dashed line indicates the limit where the fission barrier is equal to the neutron binding energy. Fusion-fission is expected for the region between this line and the $B_f = 0$ limit.

A similar analysis has been performed for each of the ^{28}Si + ^{50,52,54}Cr systems. Figure 6.2 presents the calculations for the isotope ^{50}Cr. Those for the other isotopes differ only slightly. The beam energies used in this experiment were 83.3 and 96.2 MeV. In this figure, the dotted line corresponds to the limit $B_f = 0$ and the double-dot-dashed line shows where the fission barrier is equal to the neutron binding energy. The extra push is shown by the single-dot-dashed line. The extra-extra push is predicted to become important at $\approx$ 240 MeV, and hence the quasi-fission cross section should be zero at the energies studied. The threshold for deep-inelastic scattering is 93 MeV and fast-fission is not expected to occur until very high energies (above 150 MeV).

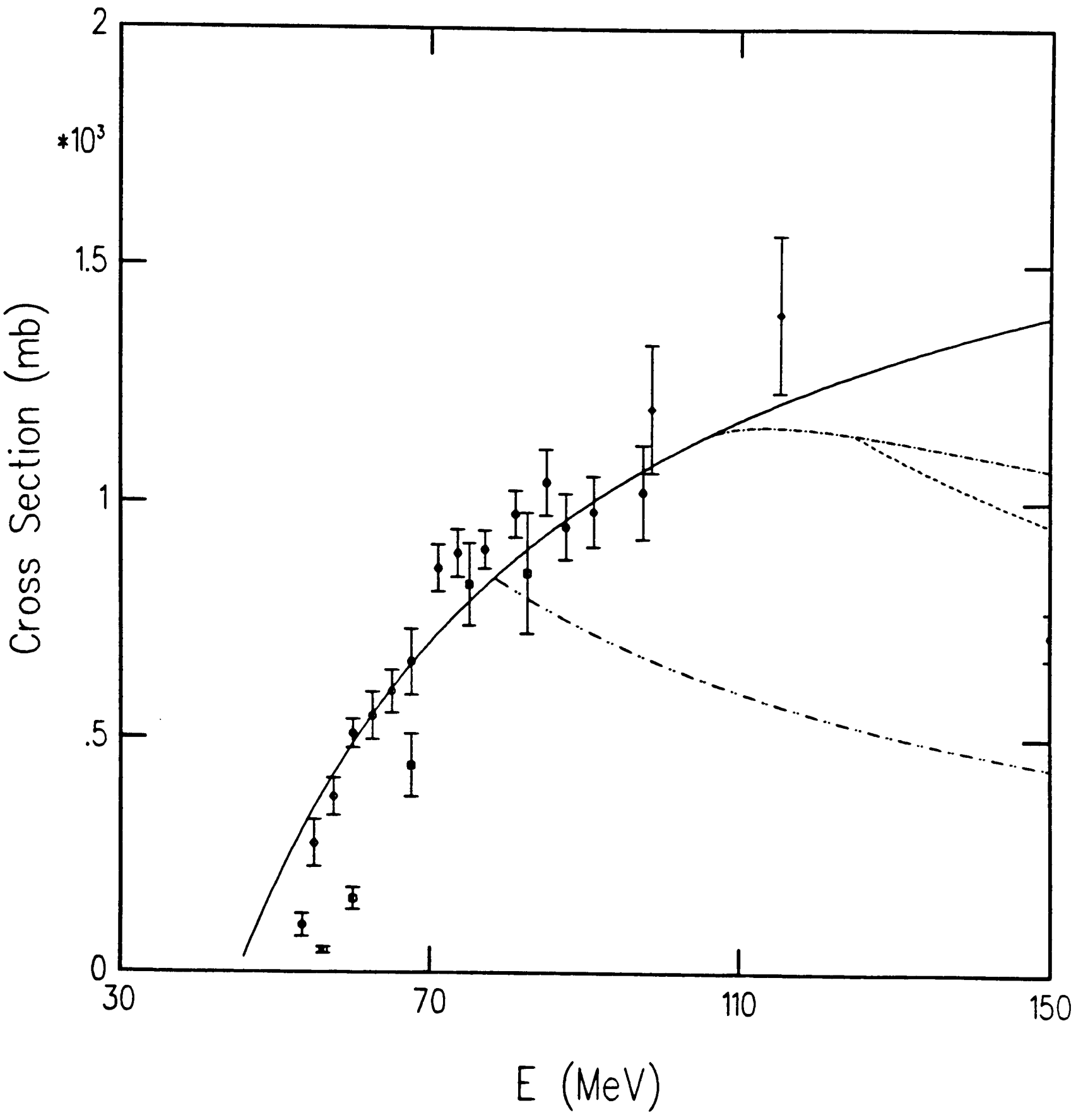


Figure 6.1. Extra push model prediction of fusion cross sections for the $^{40}Ca + ^{40}Ca$ system. The square symbols denote the data of Tomasi et al. [56], the circles the data of Doubré et al. [55] and the diamonds are obtained by adding an evaporation cross section deduced from the study of Doubré to the fissionlike cross sections measured in this work. The lines are explained in the text.

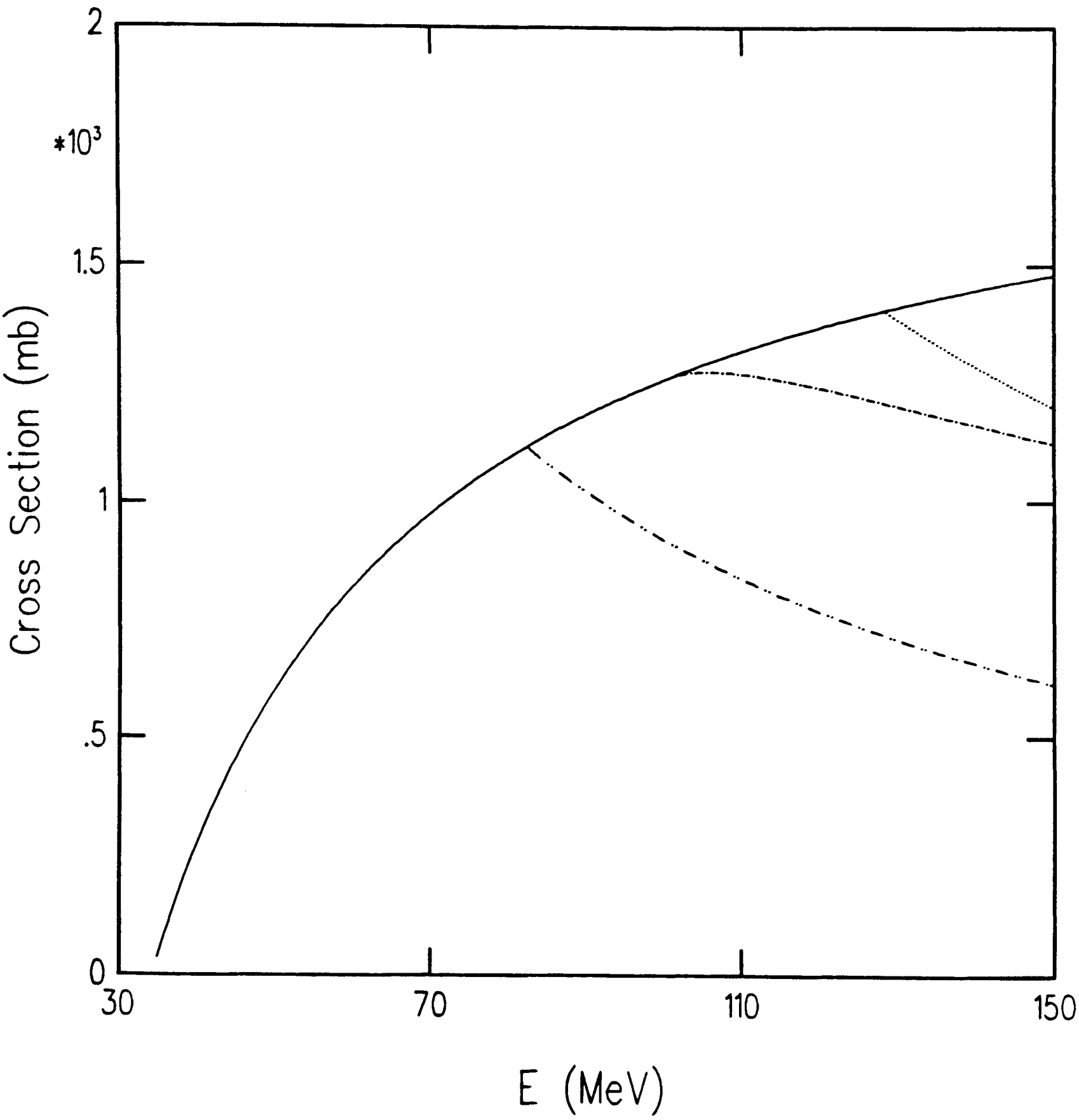


Figure 6.2. Extra push model prediction of fusion cross sections for the $^{28}Si + ^{50}Cr$ system. The lines are explained in the text.

From the above it is seen that the extra push model predicts that neither fast-fission or quasi-fission should occur for the systems studied in this thesis. However, this model employs many parameters from the rotating liquid drop model. Furthermore, a RLDM prescription was used to determine the limit at which the fission barrier vanishes.

The critical distance (CDM) [5] and statistical yrast (SYM) [6] models furnish convenient methods of calculating the higher energy fusion regime (see section 2.3.1). Calculations for ^{40}Ca + ^{40}Ca in terms of these two models are shown in figure 6.3. The solid line indicates the results of the critical distance model analysis. This calculation predicts that the high energy regime starts at $\approx$ 82 MeV. The statistical yrast model results are indicated by the dotted line. Similar calculations were performed for ^{28}Si + ^{50,52,54}Cr. They yielded results comparable to those for ^{40}Ca + ^{40}Ca.

Both sets of calculations for ^{40}Ca + ^{40}Ca are in reasonable agreement with experiment, underpredicting the data of Doubré et al., as expected from the measurements of other workers taken at lower energies. These analyses confirm that ^{40}Ca + ^{40}Ca has a large fusion cross section ($\sim$1 barn) at the energies used in this work and that the high-energy limitations to fusion are only just starting to set in. Similar calculations for ^{28}Si + ^{50,52,54}Cr suggest the same is true for this system at the bombarding energies employed. The important thresholds deduced from this set of calculations are listed in table 6.1.

All these fusion calculations were performed using the standard model parameters. In the case of the ^{40}Ca + ^{40}Ca system, better agreement between experiment and theory could be obtained by optimizing these parameters, a process which would change the thresholds calculated by small amounts (typically no more than 10%).

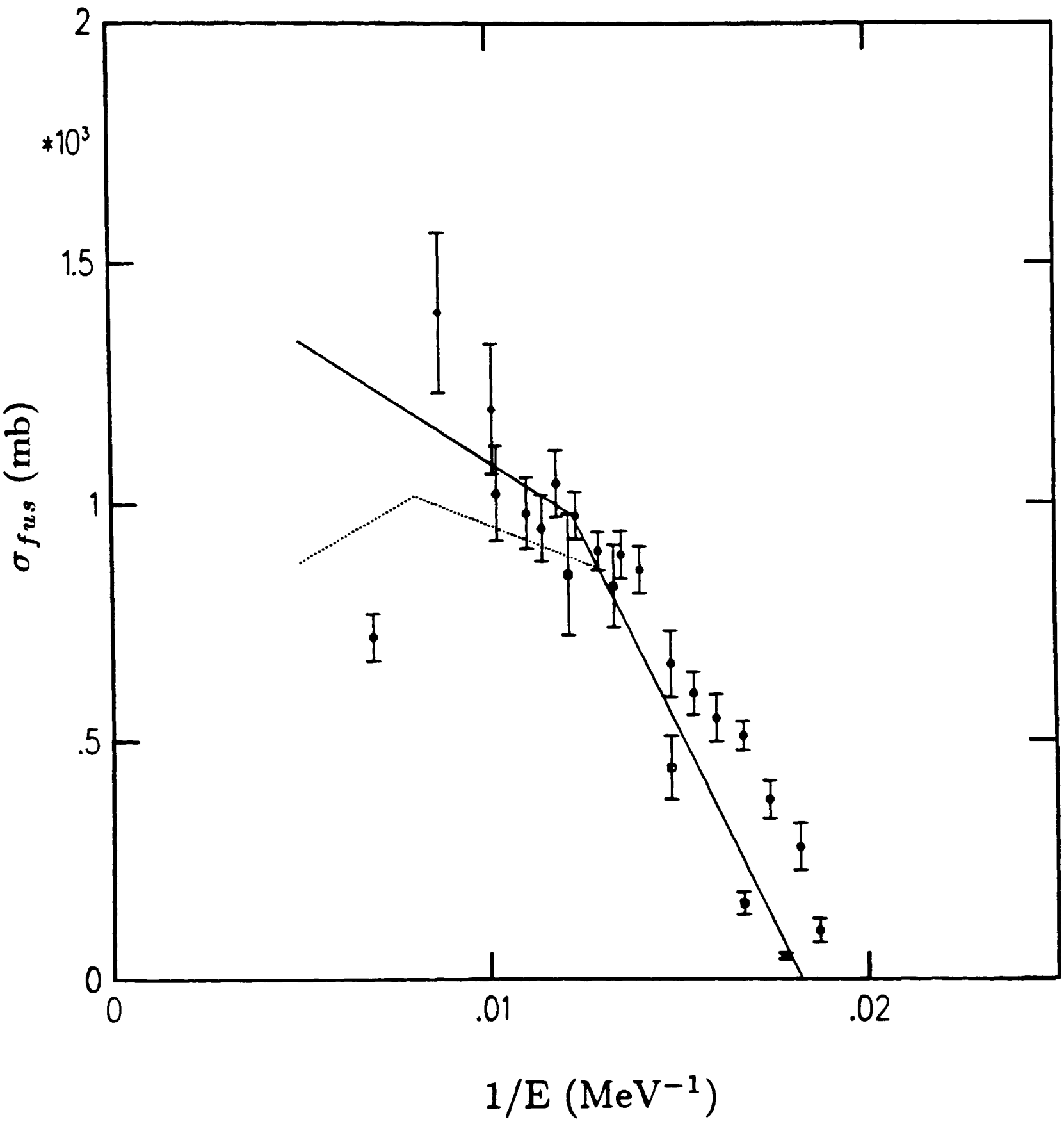


Figure 6.3. Critical distance model (solid line) and statistical yrast model (dotted line) analysis of the system $^{40}Ca + ^{40}Ca$. The various data points are explained in the caption to figure 6.1.

Model	Threshold	$^{40}Ca + ^{40}Ca$	$^{28}Si + ^{50}Cr$
Extra Push	Deep-Inelastic	98	93
	Fast-Fission	125	150
	Quasi-Fission		242
Critical Distance	Second Region	82	72
Statistical Yrast	Second Region	69	62
	Third Region	125	100

Table 6.1 Thresholds predicted by fusion calculations. All values quoted are in MeV and for the centre of mass frame. Second Region denotes the high energy fusion regime and Third Region the fusion entry line (appendix III).

6.3 Statistical Model Calculations

6.3.1 Theoretical Background

The measured fissionlike cross sections were compared with the predictions of statistical model calculations, using the program CASCADE. CASCADE employs the formalism of Hauser and Feshbach [57]. Full information on the program is given in the paper of Pühlhofer [47]. A few relevant details are presented here.

First of all we consider fusion. The cross section for formation of a compound nucleus of spin J and parity π_J from a target of spin J_T and a projectile of spin J_P, at a centre of mass energy E, is given by

$$\sigma(J,\pi_J) = \frac{\pi}{k^2}\frac{2J+1}{(2J_P+1)(2J_T+1)}\sum_{S=|J_P-J_T|}^{J_P+J_T}\sum_{L=|J-S|}^{J+S} T_L(E) \qquad (6.1)$$

where S and L are given by the equations $\mathbf{S} = \mathbf{J_P} + \mathbf{J_T}$ and $\mathbf{J} = \mathbf{L} + \mathbf{S}$ and T_L is the transmission coefficient for angular momentum L. The summation over L is subject to the parity condition $\pi_J = \pi_P \pi_T (-1)^L$. S is called the channel spin.

Expression 6.1 is a generalization of equation 2.4 to include the effects of finite target and projectile angular momenta. The spin-dependent factor is equal to the probability of coupling $\mathbf{J_P}$ and $\mathbf{J_T}$ to obtain $\mathbf{S}$, multiplied by the probability of coupling $\mathbf{S}$ and $\mathbf{L}$ to obtain $\mathbf{J}$, summed over all values of L.

A Fermi function is used for the transmission coefficients.

$$T_L = \frac{1}{1 + \exp[-(L - L_0)/d]} \tag{6.2}$$

where L_0 is the critical partial wave for fusion and d is a diffuseness parameter. Unless specified, d is given the default value $2\hbar$ and L_0 is calculated approximately by equating the centre of mass energy E_{cm} with the sum of Coulomb and rotational energies of touching target and projectile nuclei, which yields the formula

$$L_0 = \sqrt{2\mu(E_{cm} - V_C)} \times (R_{12} + D) \tag{6.3}$$

where V_C is the Coulomb energy, μ is the reduced mass, R_{12} is the sum of their radii and D is a distance parameter. An upper limit for L_0 is set by the requirement that the fission barrier be at least 8 MeV. A parameterization deduced from the work of Cohen et al. [9] is used to calculate this limit. The total fusion cross section is the summation of equation 6.1 over both J and π_J.

The de-excitation of the compound nucleus can take place via three types of process: light particle evaporation, fission and γ decay. As γ decay is an electromagnetic process, it is typically $\sim 10^7$ times weaker than particle evaporation.

The rate of emission of a light particle x (proton, neutron or α) from excited nucleus 1 (excitation energy E_1, spin J_1, parity π_1) to form a product nucleus 2 (E_2, J_2, π_2) is given by the expression

$$R_x d\varepsilon_x = \frac{1}{\hbar}\Gamma_x(\varepsilon_x) = \frac{1}{h}\frac{\rho_2(E_2, J_2, \pi_2)}{\rho_1(E_1, J_1, \pi_1)} \sum_{S=|J_2 - s_x|}^{J_2+s_x} \sum_{L=|J_1-S|}^{J_1+S} T_L^x(\varepsilon_x) d\varepsilon_x \tag{6.4}$$

where ε_x is the kinetic energy of particle x, s_x is its spin, L its orbital angular momentum and $\mathbf{S} = \mathbf{J_2} + \mathbf{s_x}$ is the channel spin. ρ_1 and ρ_2 are the level densities in initial and product nuclei respectively. A derivation of this rate expression is given by Thomas [58]. The transmission coefficients are take from calculations using the optical model [59] and the level densities are calculated within the framework of the Fermi gas model. Many expressions can be used for the level density, but in general they have the form

$$\rho(U, J) = C(U, J) \exp\left[2\sqrt{aU}\right] \tag{6.5}$$

where J is the angular momentum, U is the net excitation energy and a is the level density parameter (usually taken as $A/8$ MeV^{-1}). CASCADE uses the level density prescription of Dilg et al. [60]. If B_x is the separation energy of particle x, then

$$\varepsilon_x = E_1 - E_2 - B_x \tag{6.6}$$

Expressions similar to 6.4 and 6.6 can be obtained for both fission and γ decay [7]. In the case of fission,

$$R_f = \frac{2J_1 + 1}{h} \frac{\rho(E_2, J_2)}{\rho(E_1, J_1)} \tag{6.7}$$

and E_1 and E_2 are related through the expression

$$\varepsilon_{sp} = E_1 - E_2 - B_f(J) \tag{6.8}$$

where ε_{sp} is the kinetic energy at the saddle point and B_f is the fission barrier. It is a general rule of thumb that for fission to compete with evaporation $B_f(J) \leq B_x$. The fission barrier decreases with J and so fission only becomes an important process for high angular momenta.

The total rate for a given type of radiation is obtained by summing R_f, R_x etc. over all possible transitions. The probability of a particular process is directly proportional to its total rate. Thus, if the cross section for population

of a given state is known, the cross section for its depopulation by a particular process can be determined from its rate.

6.3.2 CASCADE Calculations

Two versions of CASCADE were used for these calculations: the first one[c] utilises fission barriers from the rotating liquid drop model, while the other[d] uses finite range model barriers. In all instances where the RLDM barriers were used, they were scaled by a factor of $k = 0.6$ (see section 2.6 for discussion).

The initial philosophy of these calculations was to scale L_0 and choose d such that fissionlike and total fusion cross sections were well reproduced as a function of energy for both ^{40}Ca + ^{40}Ca and ^{28}Si + ^{50,52,54}Cr, using a consistent set of input parameters. Since fission only occurs for higher partial waves, a small change in d can dramatically alter the predicted fission cross section without changing the fusion cross section by much. As evaporation residue data only exist for ^{40}Ca + ^{40}Ca, the calculations were initially performed for this system. The program input parameters for these calculations were then used to determine those for the ^{28}Si + ^{50,52,54}Cr systems.

The first set of calculations was performed using the finite range model barriers. For ^{40}Ca + ^{40}Ca, it was impossible to reproduce both fissionlike and evaporation residue cross sections (discussed in section 2 of this chapter) solely by changing the values of L_0 and d. At both energies, the fissionlike cross sections were grossly overpredicted by factors of 3 or 4. Furthermore, the fission barrier calculation routine BARFIT [51] predicts that at both energies the fission barrier vanishes for several partial waves which fuse. The statistical model of compound nucleus decay is not applicable in such a regime. The best agreement between

---

[c] Used for the calculations described in sections 4.2.1 and 5.2.3.

[d] Modified by K. T. Lesko at Argonne.

experiment and theory was obtained by increasing the level density parameter for particle evaporation (a in equation 6.5) from $A/8$ MeV^{-1} to $A/7$, while keeping the level density parameter for the saddle point fixed at $A/8$ and using the default values of L_0 and d. These calculations are shown by the solid line in figure 6.4. Agreement at 230.5 MeV is not so good, but this is to be expected, as most of the fissionlike cross section at this energy comes from partial waves for which the fission barrier is zero. These calculations were repeated for the systems ^{28}Si + ^{50,52,54}Cr. The fissionlike cross sections, predicted by the RFRM version of CASCADE, for the isotope ^{50}Cr are plotted in figure 6.5 (solid line). The same level density parameters were used as in the ^{40}Ca + ^{40}Ca calculations. BARFIT predicts the disappearance of the fission barrier for this system at the higher energy (150 MeV), also.

The rotating liquid drop model does predict a finite fission barrier for both systems at the energies studied. A set of calculations for ^{40}Ca + ^{40}Ca, using the RLDM barriers, is shown by the dashed line in figure 6.4. Here the level density at the saddle point has been enhanced in order to reproduce the data ($a = A/7.2$), with the value of a for particle evaporation set to the default value of $A/8$. These data can only be reproduced using the default level densities if very different spin distributions are assumed at the two energies. In contrast, the fissionlike cross sections for the ^{28}Si + ^{50,52,54}Cr systems are well described using the default values for all parameters. The prediction for the isotope ^{50}Cr is shown by the dashed line in figure 6.5. The results of these calculations for ^{40}Ca + ^{40}Ca and for ^{28}Si + ^{50,52,54}Cr are listed in table 6.2 and 6.3 respectively.

In conclusion, these calculations are able to describe the fissionlike cross sections for both systems fairly well. The version of CASCADE with the finite range model fission barriers predicts that the barriers fall to zero for several partial waves in nearly every case (the only exception being 130 MeV ^{28}Si + ^{50,52,54}Cr). In order to reproduce the data the level densities for particle evaporation have had to be enhanced by a factor of ≈ 1.14. This is consistent with

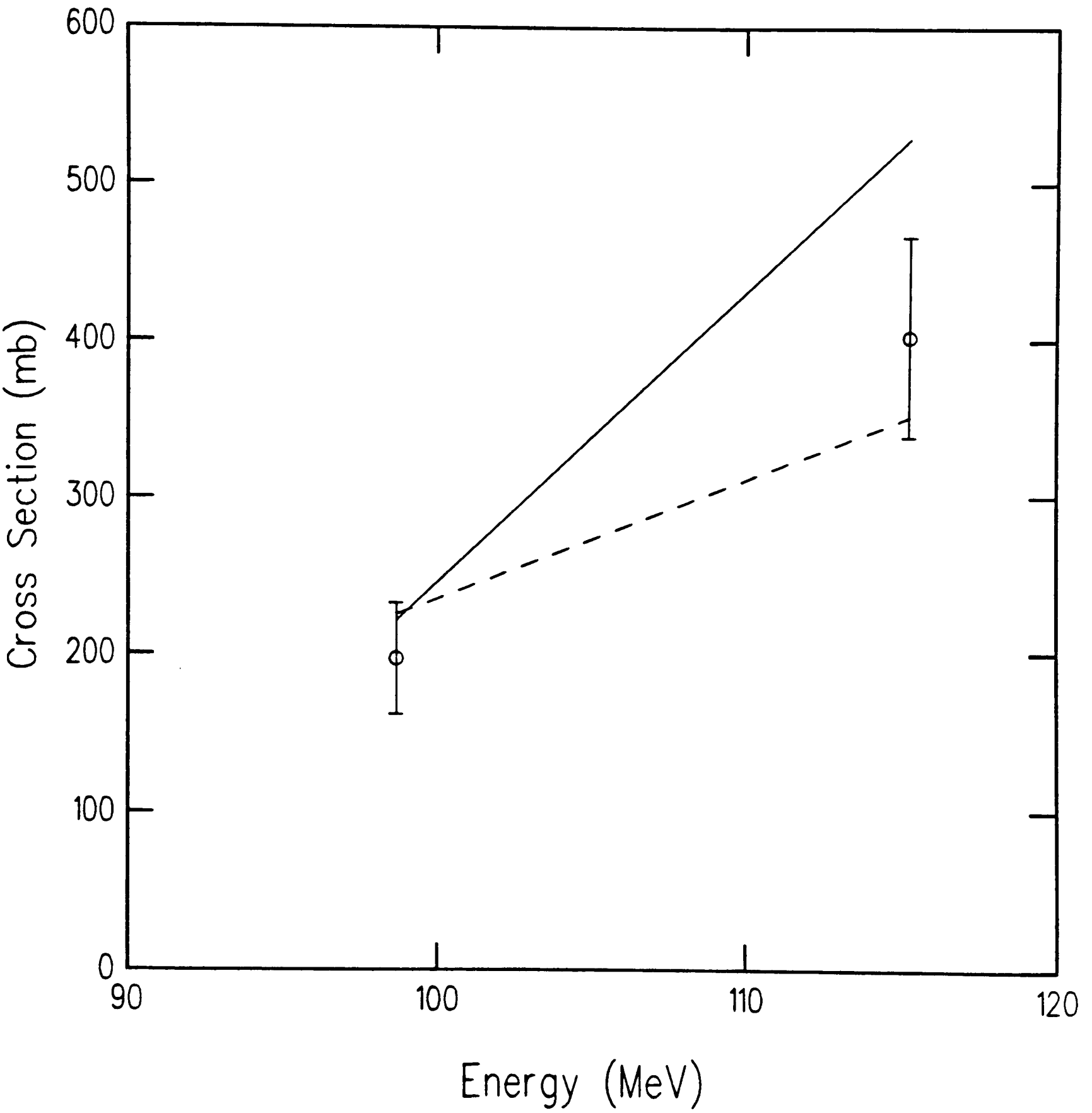


Figure 6.4. CASCADE calculations of fission cross sections for $^{40}Ca + ^{40}Ca$ compared with experimental data. The solid line indicates the cross sections predicted using the finite range model fission barriers, and the dashed line those obtained with the rotating liquid drop model barriers.

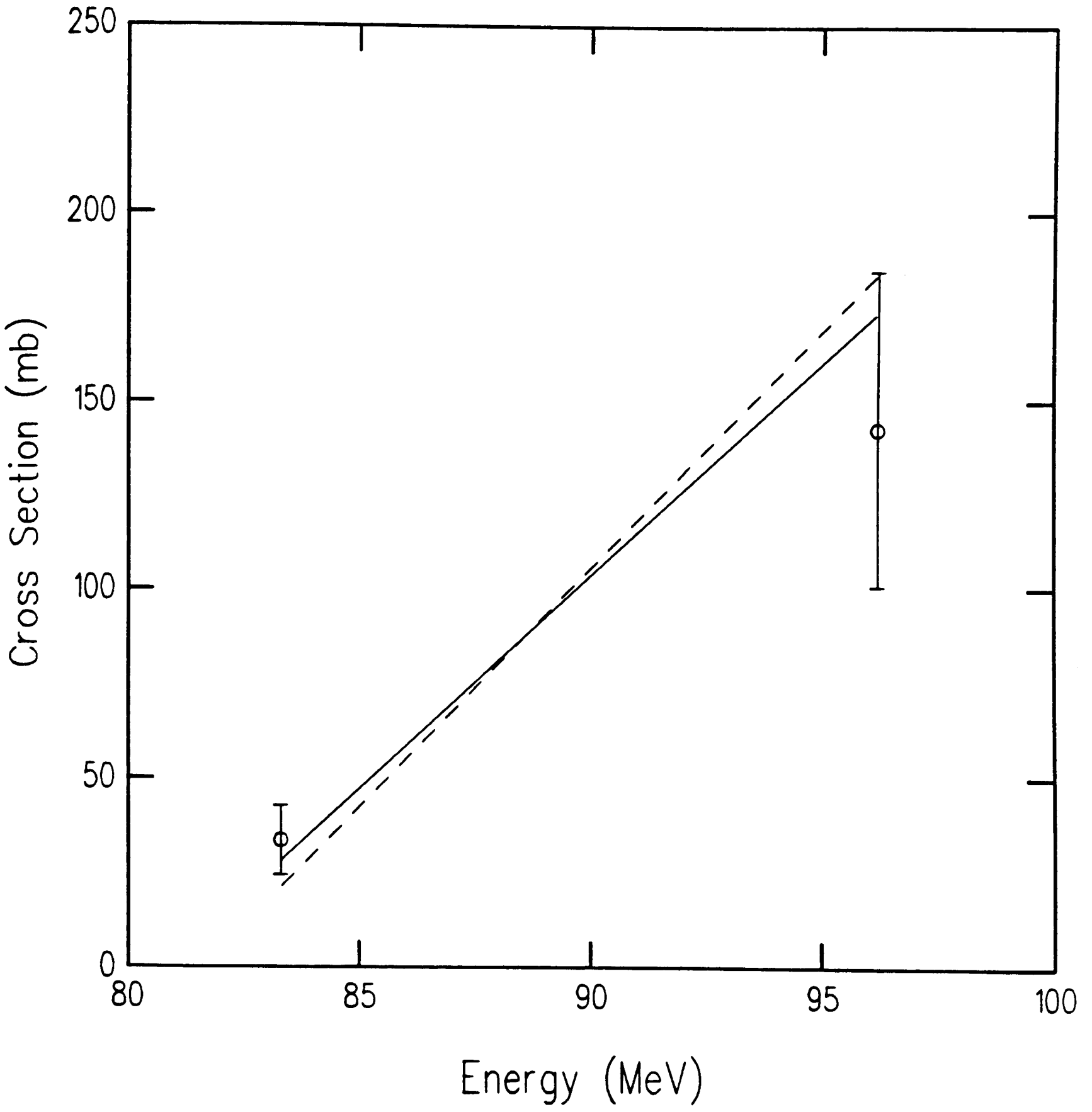


Figure 6.5. CASCADE calculations of fission cross sections for $^{28}Si + ^{50}Cr$ compared with experimental data. As with figure 6.4, the solid line indicates the cross sections predicted using the finite range model fission barriers, and the dashed line those obtained with the rotating liquid drop model barriers.

	197.3 MeV		230.5 MeV	
	σ_{fiss} mb	σ_{fus} mb	σ_{fiss} mb	σ_{fus} mb
RLDM	225.65	1128.12	351.68	1022.08
RFRM	221.78	1128.12	529.48	1022.08
EXPT	197.6 ± 35.4	1200 ± 100*	403.1 ± 64.1	

* (Evaporation residue data of Doubré plus this work)

Table 6.2 CASCADE predictions for ^{40}Ca + ^{40}Ca and experimental results. RLDM denotes calculations using rotating liquid drop model fission barriers, RFRM those using rotating finite range model barriers and EXPT signifies experimental results.

results for lighter systems: a similar analysis of the fission decay of ^{32}S + ^{24}Mg required an enhancement of the level density for evaporation by 1.28 [61]. Such an enhancement may be justified by the effects of deformation on the transmission coefficients for particle evaporation. The transmission coefficients used by CASCADE are calculated for spherical nuclei, whereas the systems studied in this work are highly deformed due to their large angular momenta. The RLDM version of CASCADE is only able to describe both systems if different level density parameters are used. Both programs only calculate barriers for symmetric fission and so, because the observed mass distributions are very broad, have limited validity. Furthermore, the disappearance of the finite range model fission barriers for these systems clearly puts them outside the scope of the statistical model of compound nucleus decay employed by CASCADE. It is interesting to note that the RFRM fission barriers vanish for angular momenta typically $10\hbar$ lower than those calculated in the framework of the zero range liquid drop model. We discuss this point further in section 8 of this chapter.

System	Energy MeV	Fission Cross Section (mb) RLDM	RFRM	EXPT
$^{28}Si + ^{54}Cr$	130	21.23	27.31	26.9 ± 7.3
$^{28}Si + ^{52}Cr$	130	19.70	28.44	25.0 ± 6.8
$^{28}Si + ^{50}Cr$	130	21.68	28.67	33.8 ± 9.2
$^{28}Si + ^{50}Cr$	150	183.63	173.38	143 ± 42

Table 6.3 CASCADE predictions for $^{28}Si + ^{50,52,54}Cr$ and experimental results. The symbols RLDM, RFRM and EXPT are explained in table 6.2.

6.4 Post-Scission Evaporation

6.4.1 The Code LILITA

The centroids of the experimental mass distributions from $^{40}Ca + ^{40}Ca$ fall $\approx$ 2 amu below mass 40. This indicates that evaporation occurs at some point in the reaction process and gives rise to a decay which is not truly two-body in nature. It is unlikely that evaporation from the compound system is important, because even the most pessimistic CASCADE calculations predict that second chance fission constitutes less than 20% of the total fission yield. Hence, it is most probable that evaporation occurs after scission. However, the analysis of binary product correlations, discussed in section 5.4, yielded such broad distributions that evaporation prior to scission cannot be ruled out.

If post-scission evaporation does take place, there is no simple way of determining the primary mass distribution from the final yield. In order to elicit the primary distribution, it is necessary to assume a form for it, calculate the associated final mass distribution within the framework of the statistical model and compare this with the experimental data. The process of iteration can then be used to find the primary distribution which best reproduces the data.

The procedure outlined above was used to try and establish the primary mass distributions. A primary distribution would be assumed and the corresponding final distribution determined using the code LILITA [52]. Like CASCADE, LILITA is a Hauser-Feshbach program. However, unlike CASCADE, LILITA performs a Monte-Carlo simulation of the decay process, making it possible to extract event by event information, such as multiparticle correlations.

A further advantage of LILITA is that there is a 'two-body collision' option (originally developed to describe deep-inelastic reactions [62]), which can be used to model post-scission evaporation. When executing this option, as well as specifying the entrance channel, the user designates the properties of all binary exit channels to be considered. For each fragmentation of interest, the mass, charge, ground state Q-value, most probable Q-value and its variance (assuming a Gaussian distribution), the amount of transferred angular momentum and cross section are specified. The form of the angular distribution for each channel is also specified. In all calculations described here the form expected for fission decay – $d\sigma/d\theta_{cm} = constant$ – was chosen for every mass split. The charge of each fragment was assigned the value $A/2$ for even mass (A) and $(A-1)/2$ for odd A. The ground state Q-values were determined from tables of mass excesses [63]. Of the other input parameters, the most probable Q-values and their variances were taken from the experimental data, while transferred angular momentum values (J_{trans}) were calculated using the sticking limit:

$$J_{trans} = J_{max} \times \frac{\theta_1 + \theta_2}{\mu R_{12}^2 + \theta_1 + \theta_2} \tag{6.9}$$

where J_{max} is the maximum angular momentum brought into the system (calculated using equation 6.3), μ is the reduced mass, θ_1, θ_2, are the nascent fragments' moments of inertia (assuming them to be rigid spheres) and R_{12} is the sum of their radii.

LILITA uses these input parameters to generate a large number (typically 10^6) of binary fission pseudo-events. For each of these events, it calculates the

amount of evaporation to emanate from the two fragments, using the Hauser-Feshbach formalism described above.

As the evaporation rate is strongly influenced by the level density (see equation 6.4), which in turn is determined by the excitation energy, the division of excitation energy between the fragments greatly affects how much evaporation they produce. LILITA shares the excitation energy in two ways, depending on its size. If its value is below 15 MeV, then it is divided according to mass:

$$\begin{aligned} E_{ex}^{1} &= E_{ex}^{tot}\frac{A_1}{A_1+A_2} \\ E_{ex}^{2} &= E_{ex}^{tot}\frac{A_2}{A_1+A_2} \\ E_{ex}^{tot} &= E_{ex}^{1}+E_{ex}^{2} \end{aligned} \tag{6.10}$$

Here, the quantities E_{ex}^{1}, E_{ex}^{2} and E_{ex}^{tot} denote the excitation energies of fragment 1 (mass A_1), of fragment 2 (mass A_2) and of the whole system, respectively. For excitation energies above 15 MeV, equal temperatures are assumed. This leads to the relation

$$\frac{E_{ex}^{1}-\Delta_1}{A_1} = \frac{E_{ex}^{2}-\Delta_2}{A_2} \tag{6.11}$$

where Δ_1, Δ_2 are pairing energies and all other symbols are as in equation 6.10.

6.4.2 LILITA Calculations

The mass distributions from fissionlike reactions of the system ^{40}Ca + ^{40}Ca are fairly close in shape to a Gaussian. Thus, the LILITA calculations for this system were carried out assuming Gaussian primary mass distributions, the variances of which were varied about the values observed experimentally.

Unlike the post-scission mass spectra predicted by LILITA, the experimental mass distributions are subject to finite resolution. Hence to account for this, each mass spectrum from LILITA was convoluted with a Gaussian of full width half maximum equal to the experimental mass resolution.

In figure 6.6 we present the final mass distribution predicted by LILITA for a primary distribution of full width half maximum 26 amu, at a laboratory energy of 197.3 MeV. The solid line is the experimental $d\sigma/d\theta_{cm}$ spectrum for the 20.2° detector at this energy and the dashed line is the LILITA distribution, convoluted with the experimental resolution and normalized to the experimental spectrum between masses 20 and 40. The corresponding diagram for 230.5 MeV, also for a width of 26 amu, is shown in figure 6.7. As can be seen, for both energies, the agreement between experiment and theory is quite good. The calculations are able to account for both the widths of the distributions and the undulating structure.

The overlay on figure 5.18 of the previous chapter shows a LILITA prediction of the charge of one particle plotted against the mass of its complementary fragment for a bombarding energy of 197.3 MeV. Clearly data and calculation are in fairly good agreement, confirming the evaporation of several nucleons.

To test the sensitivity of these calculations, the effect of varying the width of the mass distribution input to LILITA about the value 26 amu was investigated for each energy. In both cases, a change of as little as 4 amu leads to a notable degradation of the agreement between calculation and experimental data. Further checks included varying the form of the primary mass distribution. As these particular calculations have relevance to the question of shell effects in the data, they are presented below in the discussion on this topic.

The experimental mass distributions from the $^{28}Si + {}^{50,52,54}Cr$ systems have a strong asymmetric component which appears to be localised at target and beam. Thus the primary mass distributions used in the LILITA calculations for these systems were assumed to be Gaussians centred at target and projectile. As with the calculations for $^{40}Ca + {}^{40}Ca$ the final LILITA spectra were smoothed with the experimental mass resolution and normalized to the data (in this case to the region between masses 40 and 50). For each isotope of chromium, the best agreement between theory and data was obtained with

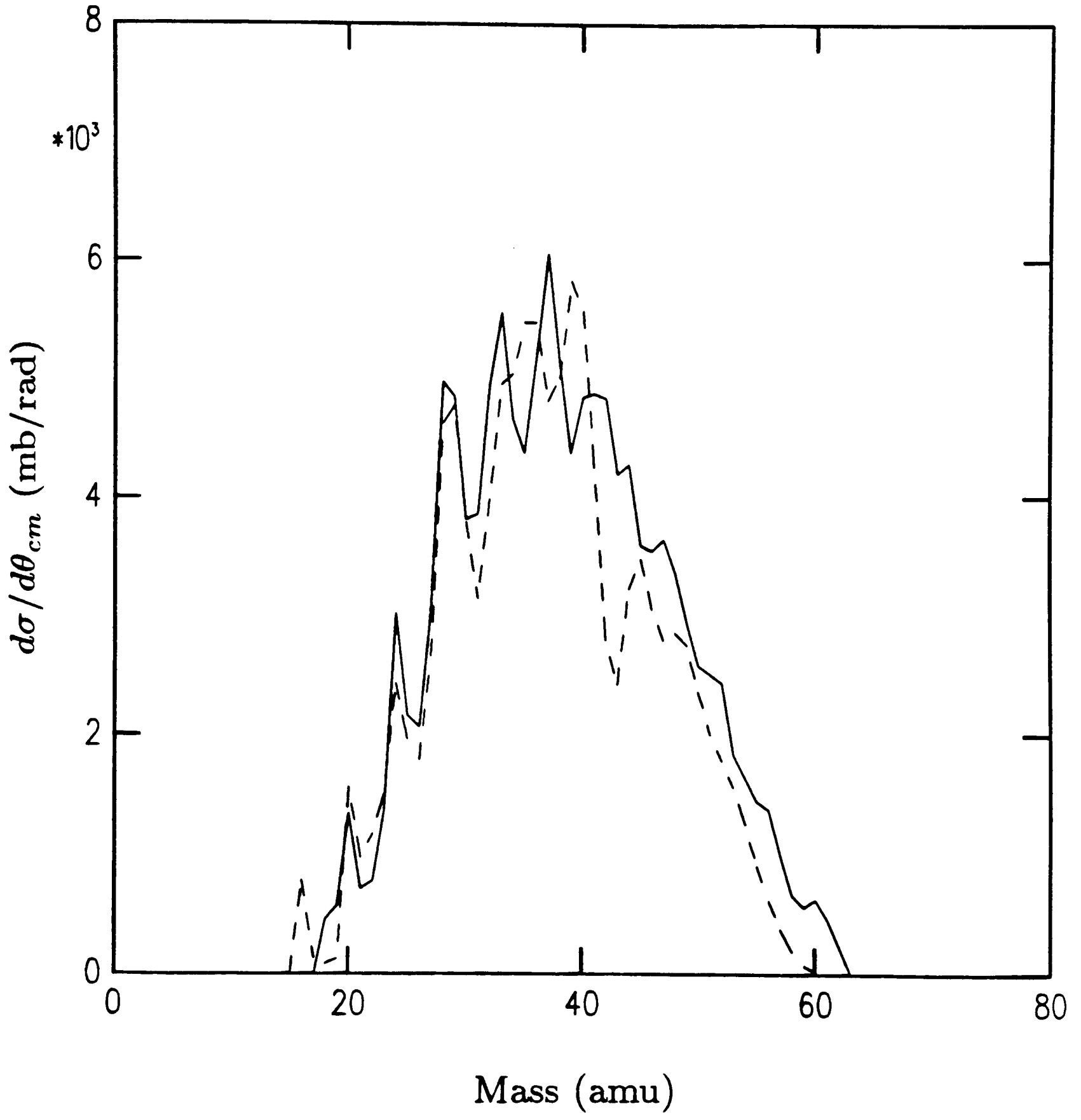


Figure 6.6. LILITA mass distribution for 197.3 MeV ^{40}Ca + ^{40}Ca. The solid line is an experimental mass spectrum showing $d\sigma/d\theta$ for the 20.2° detector. The dashed line is the corresponding LILITA prediction for a Gaussian primary distribution of full width half maximum 26 amu, centred at mass 40.

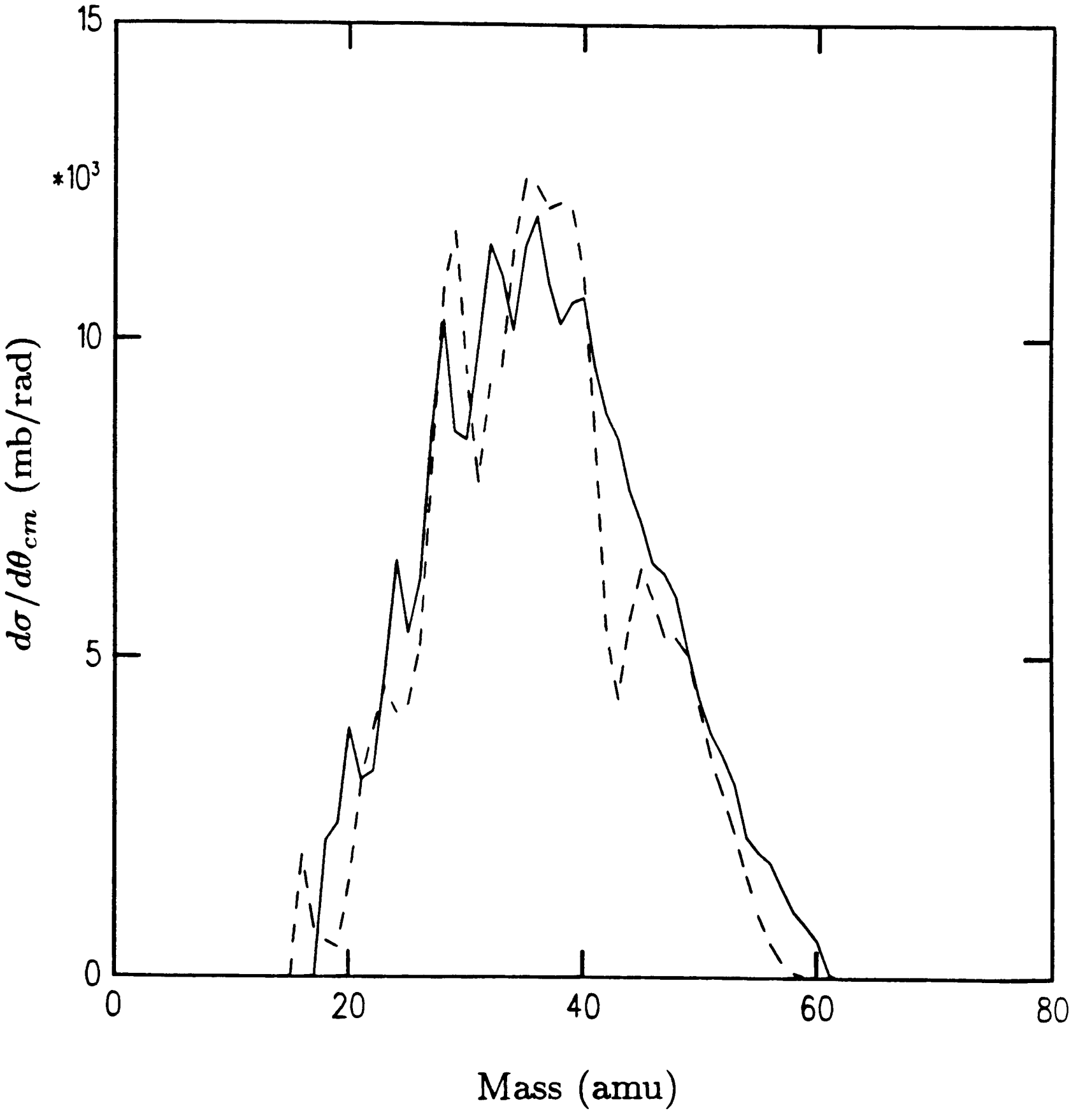


Figure 6.7. LILITA mass distribution for 230.5 MeV ^{40}Ca + ^{40}Ca. The solid line is an experimental mass spectrum showing $d\sigma/d\theta$ for the 20.2° detector. The dashed line is the corresponding LILITA prediction for a Gaussian primary distribution of full width half maximum 26 amu, centred at mass 40.

a full width half maximum of 20 amu for the primary distribution. The results of these calculations for ^{28}Si + ^{50}Cr are presented in figure 6.8 (130 MeV) and figure 6.9 (150 MeV). The results for the other chromium isotopes, being very similar, are not presented. As in figures 6.6 and 6.7, the solid lines denote experimental spectra and the dashed lines LILITA predictions. These calculations cannot be rigorously tested for low fragment masses, as the experimental data contain contamination from slit scattering and from other reaction mechanisms around mass 28.

Although agreement between experiment and theory is good in figures 6.8 and 6.9, it is not as good as for the ^{40}Ca + ^{40}Ca system, particularly in the case of the 150 MeV data. Could it be that the target and beamlike component is the product of evaporation following asymmetric fission? In an effort to test this hypothesis asymmetric primary distributions were input to LILITA. However, such calculations proved unfruitful, as LILITA can only calculate evaporation probabilities for nuclei up to charge 30, mass 60 and so, for these asymmetric distributions evaporation from the most probable fission products could not be calculated.

In summary, these LILITA calculations are able to describe the mass distributions from the fissionlike reactions of ^{40}Ca + ^{40}Ca and ^{28}Si + ^{50,52,54}Cr. For ^{40}Ca + ^{40}Ca a symmetric primary mass distribution was required to reproduce the experimental data. For ^{28}Si + ^{50,52,54}Cr an asymmetric distribution was needed, but it was not possible to determine whether a target and beamlike or asymmetric primary distribution gives the best description of the fissionlike mass spectra from these systems.

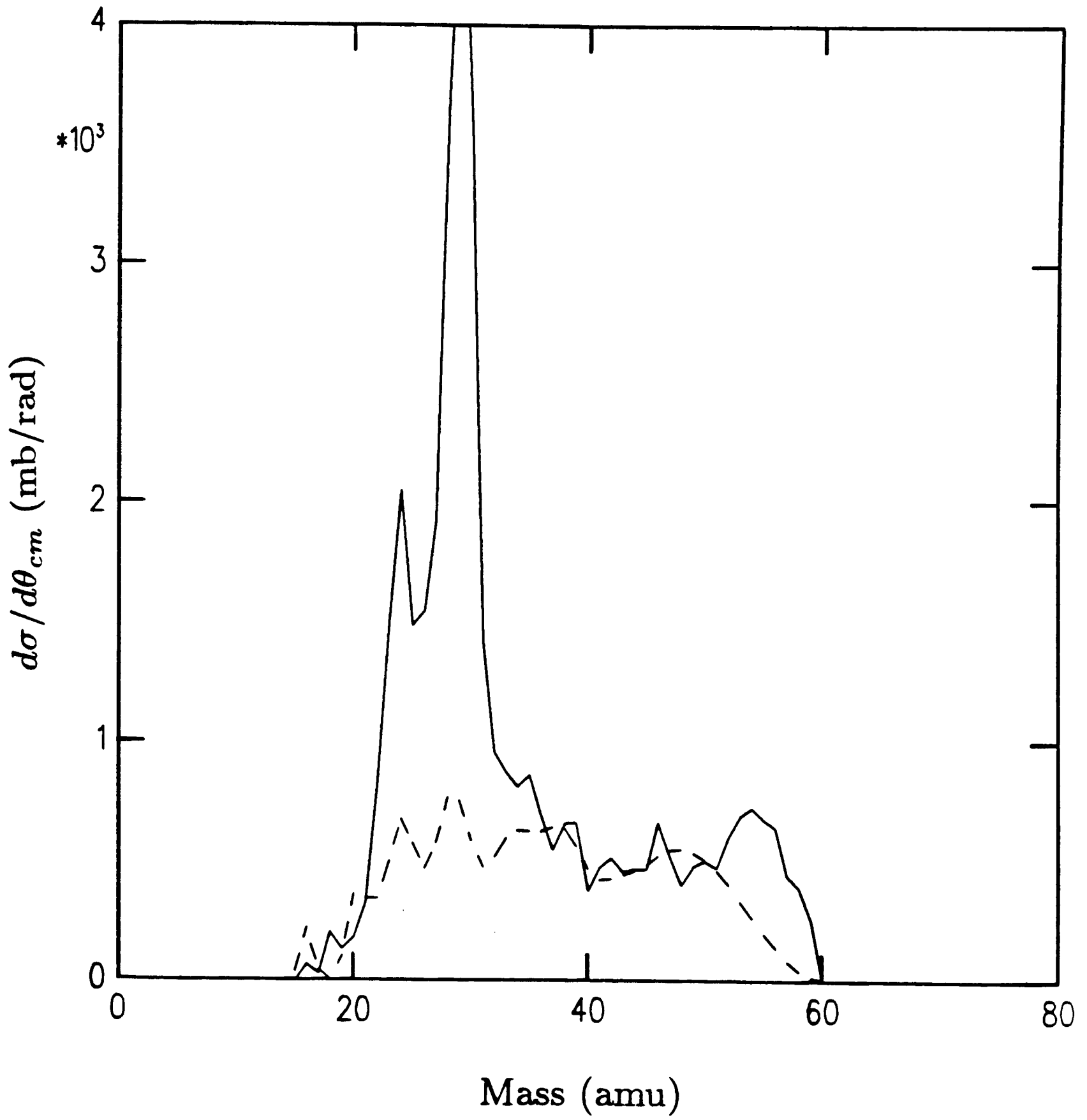


Figure 6.8. LILITA mass distribution for 130 MeV ^{28}Si + ^{50}Cr. The solid line is an experimental mass spectrum showing $d\sigma/d\theta$ for the 30° detector. The dashed line is the corresponding LILITA prediction for a Gaussian primary distribution of full width half maximum 20 amu and which is centred at masses 28 and 50.

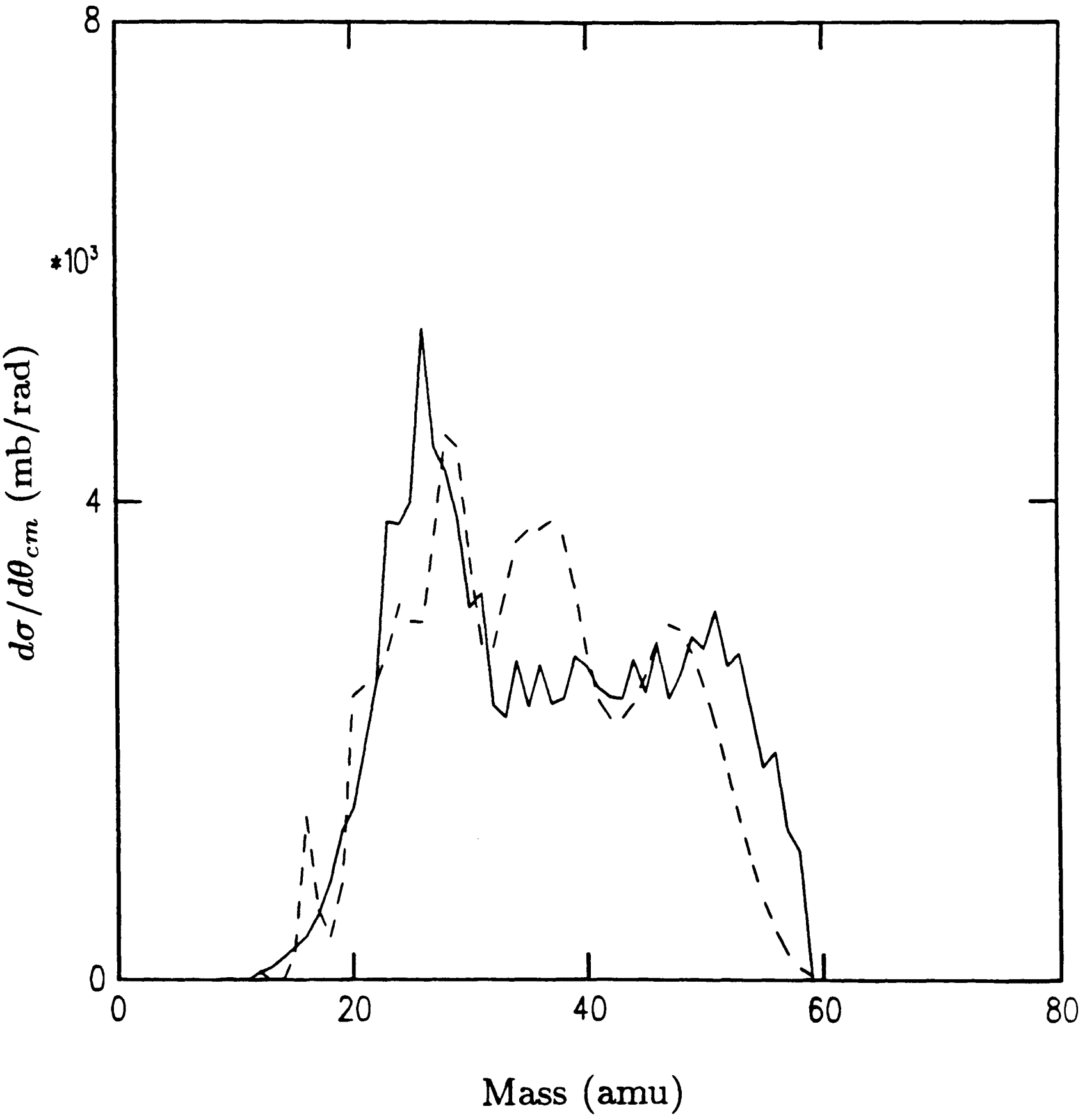


Figure 6.9. LILITA mass distribution for 150 MeV ^{28}Si + ^{50}Cr. The solid line is an experimental mass spectrum showing $d\sigma/d\theta$ for the 30° detector. The dashed line is the corresponding LILITA prediction for a Gaussian primary distribution of full width half maximum 20 amu and which is centred at masses 28 and 50.

6.5 Diffusion Model Calculations

In chapter 2 we discuss the use of the diffusion model to describe deep-inelastic collisions and point out that the properties of fissionlike reactions in the medium mass region have also been explained using this type of model. Thus it is instructive to determine whether the experimental results presented in this thesis can be characterized in such a manner. To explore this possibility, a set of calculations has been performed for the systems of interest using the diffusion model code developed by Feldmeier [64]. A semi-classical model is used [65] which describes the evolution of the system in the following way. When the two nuclei approach one another, particle exchange across their surfaces produces a dissipative force, which is described by the proximity window formula [66]. The nuclei then form a connecting neck, across which particles may be exchanged. This is described by the wall and window dissipation processes discussed in section 2.2.2. After a period of time ($\sim 10^{-21}$ s), the nuclei either reseparate – a deep-inelastic process – or fuse to form a compound nucleus. The program calculates the evolution of the system in small time steps – typically 10^{-23} s. Each trajectory is determined by solving the Lagrange-Rayleigh equations:

$$\frac{d}{dt}\frac{\partial L}{\partial \dot{q}_i} - \frac{\partial L}{\partial q_i} = -\frac{1}{2}\frac{\partial \phi}{\partial \dot{q}_i} \tag{6.12}$$

where L is the Lagrangian, ϕ is the Rayleigh dissipation function and the q_i are generalized co-ordinates (e.g. the distance between the mass centres). $L = T - V$ where T is kinetic energy and V is the sum of nuclear and Coulomb potential energies. The right hand side of the Lagrange-Rayleigh equation is a friction force, with ϕ equal to the rate of energy dissipation by wall and window processes.

For a given partial wave, values for the mean and variance of the mass distribution; the total kinetic energy; the scattering angle, and the angular momentum distribution of the final products are evaluated.

The systems studied in this thesis each have a large fully damped cross section. Therefore if a deep-inelastic mechanism, such as orbiting, is responsible for the observed yields the model should predict that several partial waves achieve the fully relaxed total kinetic energy without fusing. The results of these calculations for ^{40}Ca + ^{40}Ca are shown in table 6.4.

The corresponding results for ^{28}Si + ^{50}Cr are presented in table 6.5.

Similar calculations were performed for the other chromium isotopes, and yielded results similar to those for ^{50}Cr. In tables 6.4 and 6.5 τ is the system's lifetime, l_{graz} the grazing partial wave and σ_{mass} denotes the variance of the mass distribution. In each case the lowest partial wave listed is the first one not to undergo fusion, where for the purposes of these calculations, fusion is deemed to have taken place if the system survives long enough to complete three full revolutions. For the system ^{28}Si + ^{50}Cr at both energies, and for ^{40}Ca + ^{40}Ca at 197.3 MeV, the lowest partial wave has a TKE value only slightly higher than expected for full relaxation, and a large mass variance (equivalent to a full width half maximum of $\sim$ 25 amu). Thus a long-lived deep-inelastic component may be present in these systems. The interpretation of the calculations for ^{40}Ca + ^{40}Ca at 230.5 MeV is more complicated. Partial wave 62 is predicted to display a broad mass distribution, but a higher TKE than expected for full energy damping, and thus should be experimentally distinguishable from the fissionlike component.

A convenient way of showing the results of this type of calculation is the Wilczyński plot, which allows a direct comparison between experiment and theory. This is a diagram of total kinetic energy plotted against scattering angle as a function of partial wave. The Wilczyński plot for the system ^{40}Ca + ^{40}Ca is shown in figure 6.10. Those for the other systems discussed are similar in general detail.

System	Partial Wave	θ_{cm} (deg.)	TKE (MeV)	τ (10^{-22} s)	σ_{mass} (amu)	Z_1
$^{40}Ca + ^{40}Ca$, 197.3 MeV	57	−470.15	59.59	74.00	12.00	20.00
	58	−13.08	67.51	12.75	4.88	20.00
	59	12.02	77.48	9.38	2.83	20.00
$l_{graz} = 80.48$	60	21.26	84.67	8.00	1.96	20.00
	61	25.30	88.18	7.25	1.53	20.00
	63	30.25	92.83	6.25	0.95	20.00
	65	36.46	98.57	5.25	0.31	20.00
	70	39.88	99.83	3.75	0.01	20.00
$^{40}Ca + ^{40}Ca$, 230.5 MeV	62	−176.52	71.87	25.25	12.51	20.00
	63	−50.76	79.83	13.50	6.14	20.00
	64	−44.19	70.50	13.88	7.10	20.00
$l_{graz} = 91.89$	65	−27.58	72.35	12.25	6.00	20.00
	66	−2.08	83.18	9.25	3.75	20.00
	67	7.64	90.36	8.00	2.86	20.00
	68	12.59	94.47	7.38	2.38	20.00
	69	16.68	99.23	6.75	1.90	20.00
	70	19.31	102.02	6.25	1.59	20.00
	80	32.68	115.05	3.25	0.02	20.00

Table 6.4 Results of calculations for $^{40}Ca + ^{40}Ca$ using the model of Feldmeier. The Viola TKE for this system is 51.45 MeV. See text for discussion.

System	Partial Wave	θ_{cm} (deg.)	TKE (MeV)	τ (10^{-22} s)	σ_{mass} (amu)	Z_1
$^{28}Si + {}^{50}Cr$, 130 MeV	51	−94.07	52.12	24.02	10.49	14.15
	52	12.82	66.18	9.25	2.33	14.04
	53	22.02	72.08	7.75	1.58	14.03
$l_{graz} = 69.29$	54	26.19	75.21	7.00	1.18	14.02
	55	29.10	77.72	6.50	0.86	14.02
	56	33.85	81.72	5.75	0.42	14.01
	60	39.96	84.11	3.75	0.02	14.00
	65	40.40	84.13	2.00	0.00	14.00
$^{28}Si + {}^{50}Cr$, 150 MeV	57	−95.76	54.41	20.64	11.06	14.24
	58	−13.17	64.99	10.75	4.12	14.10
	59	3.24	72.39	8.63	2.85	14.07
$l_{graz} = 79.27$	60	12.43	79.56	7.38	2.00	14.05
	61	16.80	83.93	6.75	1.58	14.04
	63	22.31	89.67	5.75	0.94	14.03
	65	28.93	95.82	4.75	0.29	14.01
	70	32.71	97.06	3.25	0.01	14.00
	75	33.03	97.08	1.75	0.00	14.00

Table 6.5 Predictions of Feldmeier's model for the system $^{28}Si + {}^{50}Cr$. The Viola TKE for this system is 47.48 MeV. See text for discussion.

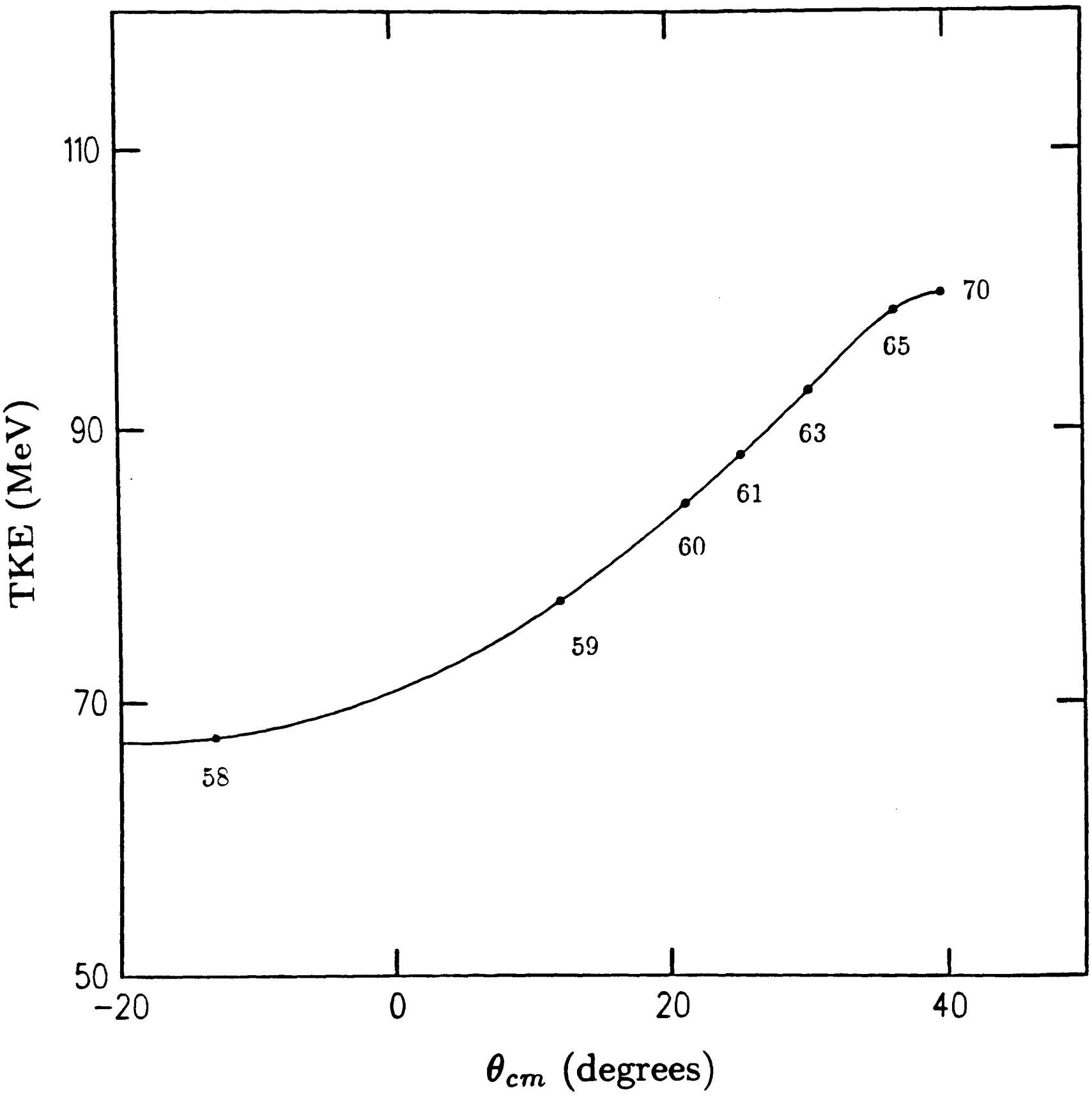


Figure 6.10. Wilczyński plot for ^{40}Ca + ^{40}Ca at 197.3 MeV, calculated using the program of Feldmeier [64]. The labels denote partial wave number. $l = 57\hbar$ is off the scale on this figure.

Clearly these calculations predict that fully damped deep-inelastic scattering can only occur for a very narrow window in partial wave space. In the sharp cutoff model, the cross section for a given partial wave l is

$$\sigma_l = \frac{\pi}{k^2}(2l+1) \tag{6.13}$$

where,

$$k = \frac{\sqrt{2\mu E_{cm}}}{\hbar} \tag{6.14}$$

μ is the reduced mass and E_{cm} the energy in the centre of mass. For these systems and for the partial waves of interest (i.e. 50 to 60$\hbar$), $\sigma_l \approx$ 30 to 40 mb. Thus the deep-inelastic contribution should be of this magnitude. As the smallest fissionlike cross section for ^{40}Ca + ^{40}Ca is 197.6 mb such a component is not likely to be very important. However the fissionlike cross section for ^{28}Si + ^{50}Cr is only 33.8 mb at the lower energy, and so orbiting could be important in this case.

One interesting feature of the calculations for ^{28}Si + ^{50,52,54}Cr is that they predict very little evolution of the mass distributions with angle. Furthermore, similar calculations for ^{32}S + ^{59}Co at 154 MeV do not predict such an effect either (see table 6.6).

Figure 6.11 shows how the incoming beamlike particle's charge evolves during the reaction as a function of time, according to the model of Feldmeier. The calculation shown is for $l = 63\hbar$, the last partial wave to fuse. It is not until 6×10^{-21} s that the system starts to move towards mass symmetry, in which time the system has completed more than one revolution. This is in disagreement with the results of Agnoli et al. [21], which they successfully describe with a diffusion model. The particular prescription they use is based on the single particle model of Ayik and others [67]. One feature of their calculations is that they assume the probability of decay at time t varies as:

$$1 - \exp\left(-\frac{t}{\tau}\right) \tag{6.15}$$

System	Partial Wave	θ_{cm} (deg.)	TKE (MeV)	τ (10^{-22} s)	σ_{mass} (amu)	Z_1
$^{32}S + ^{59}Co$, 154 MeV	64	−49.22	63.93	18.28	8.56	16.19
	65	2.46	74.83	11.00	3.90	16.09
	66	18.66	85.80	8.50	2.38	16.05
$l_{graz} = 87.56$	67	23.62	90.78	7.75	1.81	16.04
	68	27.04	94.62	7.00	1.40	16.03
	69	29.34	97.09	6.50	1.10	16.03
	70	31.19	99.41	6.25	0.83	16.02
	75	39.18	105.44	4.25	0.04	16.00

Table 6.6 Results of trajectory calculations for the system $^{32}S + ^{59}Co$ at 154 MeV. The Viola TKE for this system is 56.18 MeV. See text for discussion.

τ is a lifetime parameter and is adjusted until the best fit to the data is obtained. However no fitting is involved in the model of Feldmeier. All parameters are extrapolated from heavier systems and the lifetime of the system is solely determined from the evolution of the particular trajectory. It may well be that the agreement between data and theory observed by Agnoli et al. is brought about by the presence of a fitted lifetime parameter in the model they use.

Both the model of Feldmeier and that employed by Agnoli assume sharp nuclear surfaces. The effects of the diffuseness of the nuclear surfaces may enhance dissipation sufficiently to bring the calculations more into line with experiment.

In conclusion, these calculations predict that a component of the fully relaxed cross section may be of a deep-inelastic origin. However, this component should be small, and indeed less than 20% in the case of the ^{40}Ca + ^{40}Ca system. The prediction of small or negligible deep-inelastic cross sections for medium mass systems is consistent with the results of some other experiments in a lighter mass region, where deep-inelastic scattering is found to be unimportant in relation to fusion-fission. An example of this may be found in the paper of Sanders et al. [68].

6.6 The Businaro-Gallone Transition

In the liquid drop model, the transition from asymmetric to symmetric fission, for a spin zero nucleus, takes place at a fissility (x) of 0.394 (see section 2.9.1 for a discussion of this). It is important to note that this is close to the fissility values of the systems studied in this thesis: for example ^{80}Zr has an x of 0.393. However, if fission is to compete with particle evaporation in the medium mass region the nuclei must be given large angular momenta (typically 50$\hbar$) and one of the effects of angular momentum is to push the Businaro-Gallone transition to lower fissility values. Thus, these systems should have

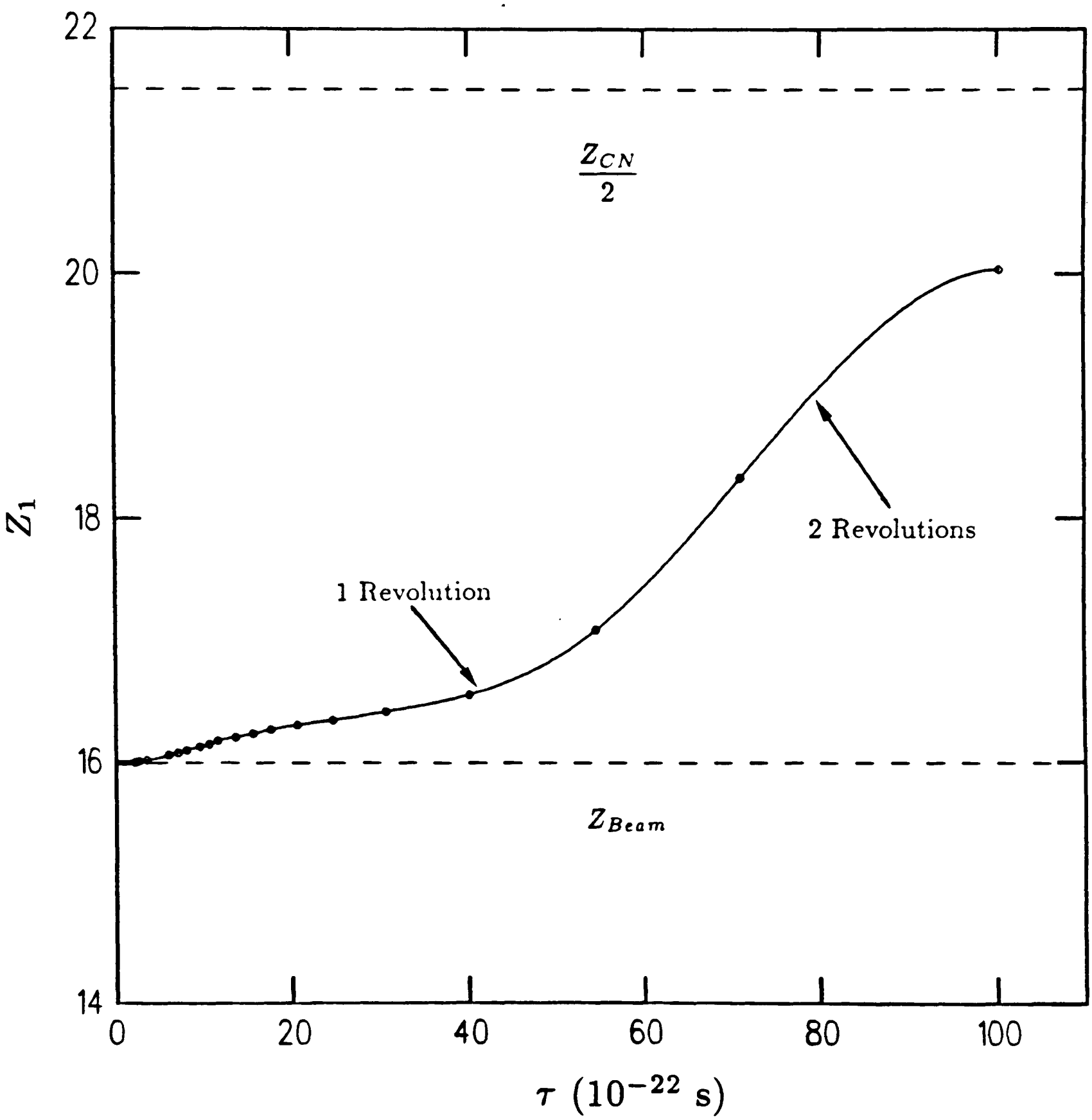


Figure 6.11. Evolution of the charge of the beamlike particle as a function of time (in units of 10^{-22} s), for the system $^{32}S + ^{59}Co$ at 154 MeV, as predicted by the model of Feldmeier [64]. The calculation shown is for $l = 63\hbar$, the last partial wave to fuse. It is not until the system has completed more than one revolution that charge starts to equilibrate. Z_{CN} denotes the charge of the compound nucleus and Z_{Beam} the charge of the beam, both of which are shown by dashed lines. The points at which the system has completed 1 and 2 revolutions are indicated.

higher fissilities than the Businaro-Gallone transition value and hence fission symmetrically.

Figure 6.12 shows a plot of fission barrier against fissility for the rotating liquid drop model. The height of the fission barrier is expressed in units of the surface energy of the spherical nucleus. The solid lines are isobars of constant rotational parameter y. The locus of the Businaro-Gallone transition as a function of y is indicated by the dashed line. As y increases, the fissility at which the Businaro-Gallone transition occurs decreases. In this figure, the labelled symbols correspond to different experiments which are referenced in table 6.7.

Symbol	**Reaction**	**Energy** MeV	**Fissility** x	**Reference**
a	$^{32}S + ^{50}Ti$	166	0.349	Barrette et al. [17]
b	$^{28}Si + ^{54}Cr$	130	0.349	This work
c	$^{28}Si + ^{52}Cr$	130	0.356	This work
d	$^{28}Si + ^{50}Cr$	150	0.364	This work
e	$^{32}S + ^{59}Co$	160	0.401	Oeschler et al. [18]
f	$^{32}S + ^{65}Cu$	160	0.414	Oeschler et al. [18]
g	$^{35}Cl + ^{62}Ni$	170	0.414	Bisplinghoff et al. [69]
h	$^{93}Nb + ^{9}Be$	782	0.400	Sobotka et al. [28]
i	$^{12}C + ^{98}Mo$	107	0.424	Natowitz et al. [70]
j	$^{40}Ca + ^{40}Ca$	197.3	0.393	This work
k	$^{12}C + ^{89}Y$	197	0.403	Natowitz et al. [70]
l	$^{12}C + ^{98}Mo$	197	0.424	Natowitz et al. [70]
m	$^{32}S + ^{74}Ge$	170	0.434	Oeschler et al. [18]
n	$^{32}S + ^{79}Br$	170	0.466	Oeschler et al. [18]
o	$^{32}S + ^{85}Rb$	170	0.479	Oeschler et al. [18]
p	$^{32}S + ^{89}Y$	153	0.499	Oeschler et al. [18]
q	$^{12}C + ^{107}Ag$	107	0.474	Natowitz et al. [70]
r	$^{139}La + ^{9}Be$	1157	0.500	Sobotka et al. [28]

Table 6.7 References to labels in figure 6.12. The observed fragmentation was asymmetric or transitional for (a) to (i) and symmetric for (j) to (r).

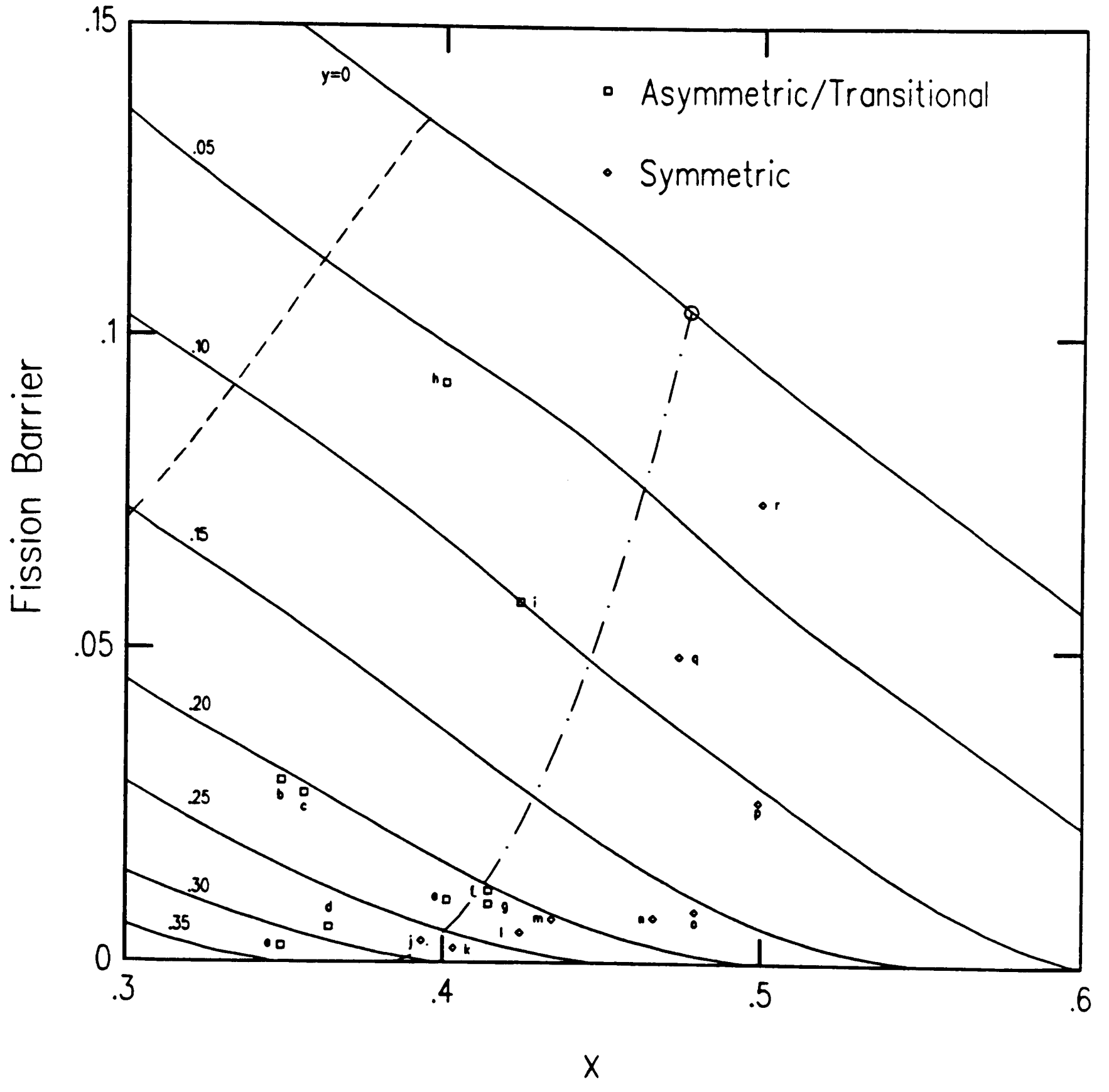


Figure 6.12. The fission barrier in the liquid drop model as a function of x and y. The labelled symbols correspond to values for different experiments, which are referenced in table 6.7. The dashed line gives the Businaro-Gallone transition in the rotating liquid drop model. The dot-dashed line gives an extrapolated value deduced from the rotating finite range model. This plot is based on a figure from the paper of Cohen et al. [9].

The squares show cases where asymmetric or transition decay has been observed and the diamonds indicate systems which fragment symmetrically. Transitional systems are those which cannot clearly be categorized as symmetric or asymmetric, or which display target and beamlike fragmentation. The systems presented on figure 6.12 are restricted to those for which the RLDM predicts that the fission barrier should be finite for the highest partial wave populated. The reason for this is that the fissionlike cross sections are dominated by the highest partial waves to fuse, so if the fission barrier reaches zero much of the yield will originate from a region where a compound nucleus cannot be formed, in which case the Businaro-Gallone transition has no meaning. Although these systems are all predicted to have finite fission barriers in the rotating liquid drop model, this may not be the case for the finite range model. We return to this point later in this chapter.

The fact that a clear progression from symmetric to asymmetric systems is evident in figure 6.12 suggests the liquid drop properties of the nucleus may have some bearing on the trend. However this trend cannot be ascribed to the Businaro-Gallone transition within the framework of the leptodermous (i.e. thin surface) RLDM. The rotating finite range model assumes diffuse surfaces and finite range forces. Calculations with this model predict that the Businaro-Gallone transition occurs at $Z^2/A = 23$ for spin zero [27]. This corresponds to $x \approx 0.477$ along the line of β-stability as given by Green's formula [71]. The RFRM Businaro-Gallone point (shown in figure 6.12 by a circle) is much closer to the experimentally observed transition. Unfortunately no calculations of the position of the Businaro-Gallone point at finite angular momentum are available for this model, and so a full comparison between the model and the data cannot be made. Nevertheless a simple model can be used to illustrate that the RFRM may, at least, provide some means of explaining the data.

This model makes use of the idea of effective fissility; discussed in connection with the extra push model in section 2.5.2. In equation 2.18 of that section, an

expression for the relationship between angular momentum and effective fissility is presented viz:

$$\left(\frac{Z^2}{A}\right)_e(l) = \left(\frac{Z^2}{A}\right)_e + \left(\frac{fl}{l_{ch}}\right)^2 \tag{6.16}$$

where

$$\left(\frac{Z^2}{A}\right)_e = \frac{4Z_1Z_2}{A_1^{\frac{1}{3}}A_2^{\frac{1}{3}}\left(A_1^{\frac{1}{3}} + A_2^{\frac{1}{3}}\right)} \tag{6.17}$$

The value of l_{ch} is

$$l_{ch} = 0.1027\frac{A_1^{\frac{2}{3}}A_2^{\frac{2}{3}}\left(A_1^{\frac{1}{3}} + A_2^{\frac{1}{3}}\right)}{\sqrt{A_1 + A_2}} \tag{6.18}$$

Although originally developed for collision systems, this fissility scaling procedure can be applied to the situation of a rotating compound nucleus and yields an expression for an effective fissility parameter – denoted by $x(l)$ – in terms of the rotational parameter y. To do this we first set $A_1 = A_2$ and $Z_1 = Z_2$, so that equation 6.17 is equal to Z^2/A of the compound nucleus. Now the liquid drop model parameters x and y are given by [9]

$$\begin{aligned} x &= \frac{Z^2}{A} \times \frac{1}{50.883\left(1 - 1.7826\left[\frac{N-Z}{A}\right]^2\right)} \\ y &= \frac{l^2}{A^{\frac{7}{3}}} \times \frac{1.9249}{\left(1 - 1.7826\left[\frac{N-Z}{A}\right]^2\right)} \end{aligned} \tag{6.19}$$

If we substitute x and y into equation 6.16, the expression

$$x(l) = x + 1.217f^2y \tag{6.20}$$

is obtained. A model similar to this has been used by Blann et al. [72] to scale $l = 0\hbar$ RFRM fission barriers for spinning nuclei.

In this simple model, a rotating system lies on the Businaro-Gallone transition if $x(l) = 0.477$. Thus the equation of the Businaro-Gallone line in x, y space is simply

$$y = \frac{0.477 - x}{1.217f^2} \tag{6.21}$$

If f is given a value close to 0.5, then this model places the Businaro-Gallone line in the correct location to explain the transition in the data. This is shown on figure 6.12 by the dot-dashed line.

The agreement between data and this schematic model is good. This suggests that the general trends in fissionlike reactions in the medium mass region may be dependent on the presence of the Businaro-Gallone transition. Before this hypothesis can be tested rigorously, more realistic RFRM calculations including the effects of angular momentum on the Businaro-Gallone transition are needed, along with more data close to the expected transition regime. One very important point is that target and beamlike decay is not predicted by a liquid drop model of fission. However, it may be that there is a combination of a broad, flat fission distribution with target and beamlike deep-inelastic scattering.

A further point about figure 6.12 is that several assumptions have been made in order to produce it and in its interpretation. These are discussed below.

1) The RLDM barriers were calculated for the valley of β-stability, whereas all of the experimental systems shown on figure 6.12 are far away from stability, on the neutron deficient side. The fission barrier heights for the systems under investigation were obtained under the assumption that they depend solely on x and y.
2) Figure 6.12 is a plot of fission barrier against fissility within the framework of the RLDM, while the dot-dashed line is scaled from the RFRM, which predicts different fission barrier heights and different values for $l_{B_f=0}$. Thus the dot-dashed line does not represent true RFRM fission barrier heights. However the difference between the RLDM and RFRM barrier height is a smooth function of x and y, and so a corresponding plot for the RFRM should be qualitatively similar. It is implicitly assumed that this is the case.

Rotating finite range model calculations predict that the Businaro-Gallone transition may lie in the medium mass region. If this were so, it would provide

an explanation for some of the features of fissionlike reactions in this region; namely a gradual evolution from asymmetric to symmetric mass fragmentation. However, the observation of a target and beamlike component, and an evolution with angle, for some systems cannot be explained solely in terms of such a model.

6.7 Mass and Energy Distributions

Nuclear fission involves the splitting of a fully equilibrated ensemble of many particles into two groups, and hence is a statistical process. The probability distributions for the number of particles in each group (i.e. the mass split) and the energy of relative motion of the two sets of particles (i.e. the total kinetic energy) are both Gaussian in form. Estimates of the full width half maxima of both of these distributions can be obtained from the liquid drop model [53,54].

The probability distribution for the mass of one fragment A_1 can be written

$$P(A_1) = \frac{1}{\sqrt{(2\pi\sigma^2_{A_1})}} \exp\left[-\frac{(A_1 - \frac{1}{2}A_{CN})^2}{2\sigma^2_{A_1}}\right] \tag{6.22}$$

where A_{CN} denotes the mass of the compound nucleus and the variance (σ_{A_1}) can be evaluated from the liquid drop model. An analogous expression can be written for the total kinetic energy (E):

$$P(E) = \frac{1}{\sqrt{(2\pi\sigma^2_E)}} \exp\left[-\frac{(E - E_0)^2}{2\sigma^2_E}\right] \tag{6.23}$$

where E_0 is the most probable total kinetic energy and σ_E is the variance of the energy distribution given by the liquid drop model.

The predicted full width half maxima of both mass and energy distributions, as a function of fissility and nuclear temperature at the saddle point, are shown in figure 6.13 (taken from the paper of Nix [53]). The reader will note that the predicted mass full width half maxima, for all the systems studied, tend to

infinity. But these calculations are for a zero angular momentum liquid drop. As we mention in the previous section, the effects of rotational stress on a nucleus are roughly equivalent to an increase in its fissility and can be modelled within the context of effective fissility. Thus, for the purposes of these calculations, effective fissility was equated with the abscissae of the diagrams in figure 6.13.

The effective fissility was determined using the method described in the previous section: firstly, the relationship between effective fissility and angular momentum was determined using equations 6.16 to 6.18, with f set to 5/7 (the sticking value for symmetric fragmentation); then the angular momentum brought into the system was calculated as a function of bombarding energy, using equation 6.3. For ^{40}Ca + ^{40}Ca this procedure yields the expression

$$x(l) = -0.0849 + 8.195 \times 10^{-3} E_{cm} \tag{6.24}$$

for the relation between bombarding energy and effective fissility. Similar expressions can be obtained for the ^{28}Si + ^{50,52,54}Cr systems.

Before the widths of the mass and energy distributions can be calculated the nuclear temperature at the saddle point (Θ) is needed. This is related to the excitation energy at the saddle point (E_{ex}^{sp}) by the semi-empirical nuclear equation of state [73]

$$E_{ex}^{sp} = a\Theta^2 - \Theta \tag{6.25}$$

where the level density parameter (a) is equal to $A/8$ MeV^{-1} [53]. Now, E_{ex}^{sp} is equal to the excitation energy at the rotational ground state (E_l^*) minus the height of the fission barrier:

$$E_{ex}^{sp} = E_l^* - \left(B_{RLDM}^f + E_{shell}^{sp} - E_{shell}^{gs}\right) \tag{6.26}$$

Here the term in brackets is the fission barrier. It is equal to the liquid drop model component (B_{RLDM}^f) (calculated in the paper of Cohen et al. [9]) plus the

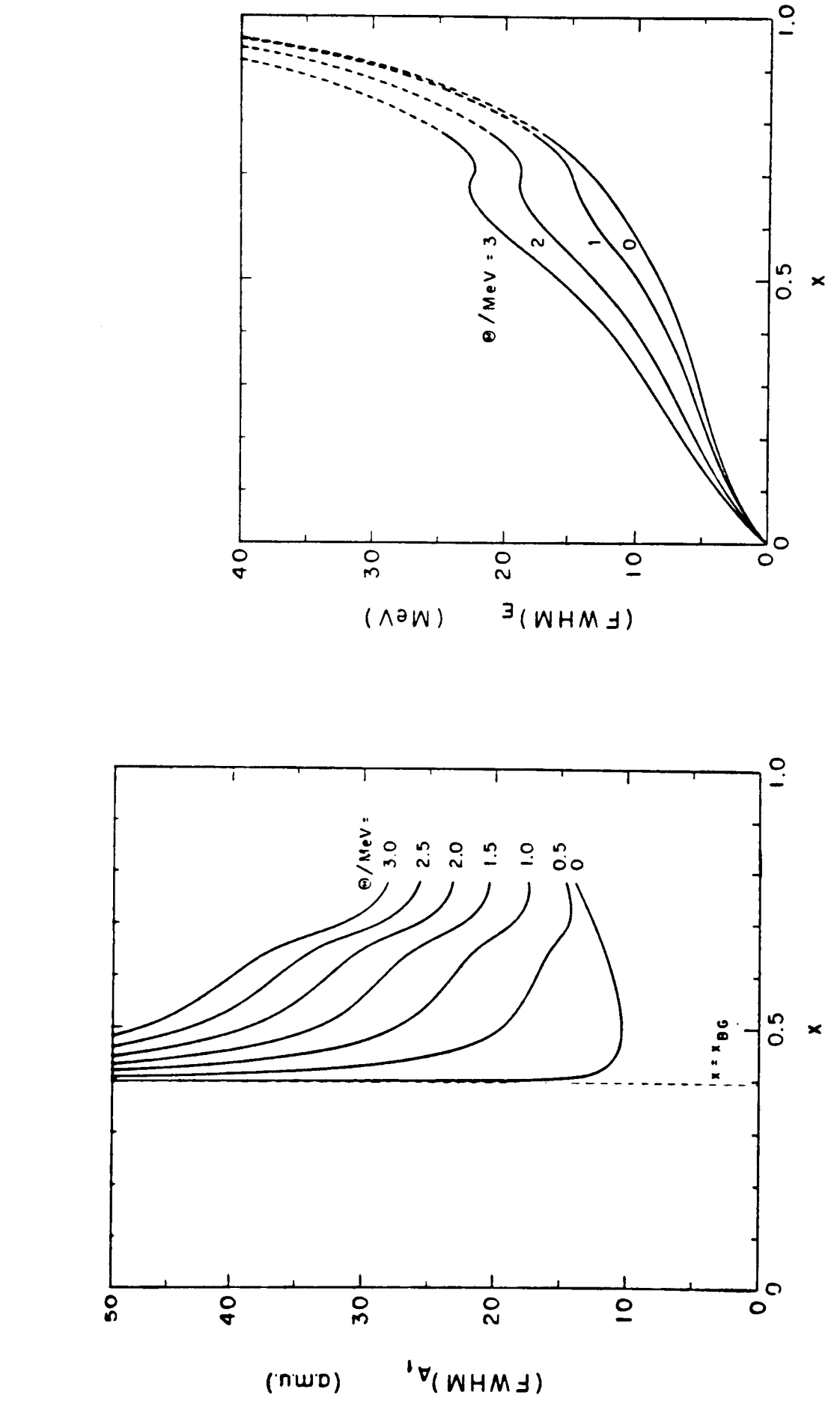


Figure 6.13. Predicted full width half maxima of the mass (left hand side) and total kinetic energy (right hand side) distributions for fission, as a function of the fissility parameter (x). The curves are for various values of the nuclear temperature at the saddle point (Θ). Taken from the paper of Nix [53].

shell correction at the saddle point (E^{sp}_{shell}) minus that at the spin zero ground state (E^{gs}_{shell}).

Values for E^{gs}_{shell} were estimated using the shell correction term from the Droplet model of Myers et al. [74]:

$$E^{gs}_{shell} \approx C\left[\frac{F(N)+F(Z)}{(\frac{1}{2}A)^{\frac{2}{3}}} - cA^{\frac{1}{3}}\right] \tag{6.27}$$

where $C = 5.8$ MeV, $c = 0.325$ and N, Z, A denote the neutron number, charge and mass of the nucleus respectively. The functions $F(N, Z)$ depend on how far N,Z are from closed shell values.

A fissioning medium mass nucleus typically has at least several MeV of excitation energy when it reaches its saddle point. Furthermore, saddle point shapes are very deformed in this mass region. Now, shell effects are expected to diminish with excitation energy [47], and also with deformation [7]. Hence the assumption was made that any shell effects at the saddle point are negligible. Thus $E^{sp}_{shell} = 0$.

The excitation energy at the rotational ground state is given by

$$E^*_l = Q^{fus} + E_{cm} - E^{gs}_{rot} \tag{6.28}$$

where Q^{fus} is the fusion Q-value, E_{cm} is the centre of mass energy and E^{gs}_{rot} is the energy of the rotational ground state with respect to the true ground state (the contribution from shell effects has been incorporated into the fission barrier in equation 6.26). As with B^f_{RLDM}, the values for E^{gs}_{rot} were taken from the paper of Cohen et al.

In this way, E^*_l and the other parameters in equation 6.26 were calculated and used to estimate the excitation energy – and hence nuclear temperature – at the saddle point. Once the effective fissility and nuclear temperature at the saddle point were known for a given system, figure 6.13 was used to obtain theoretical values for the widths of the mass and energy distributions.

System	E_{lab} MeV	Experiment FWHM$_{A_1}$ amu	Experiment FWHM$_E$ MeV	Theory FWHM$_{A_1}$ amu	Theory FWHM$_E$ MeV
$^{40}Ca + ^{40}Ca$	197.3	26	17	22	17
$^{40}Ca + ^{40}Ca$	230.5	26	22	18	24
$^{28}Si + ^{50}Cr$	130		17	25	15
$^{28}Si + ^{50}Cr$	150		20	21	18

Table 6.8 Experimental and calculated values of mass and energy full width half maxima - denoted by FWHM$_{A_1}$ and FWHM$_E$ respectively. The results for the $^{28}Si + ^{52,54}Cr$ systems are the same as those for $^{28}Si + ^{50}Cr$. No experimental FWHM$_{A_1}$ values are given for these systems as their distributions are asymmetric. The experimental FWHM$_{A_1}$ values for $^{40}Ca + ^{40}Ca$ are those deduced from the LILITA calculations.

The results obtained from this model, along with the corresponding experimental quantities, are presented in table 6.8.

The calculated values for the full width half maxima of the total kinetic energies are generally in agreement with experiment. However, the widths of the $^{40}Ca + ^{40}Ca$ mass distributions are broader than predicted. Furthermore, this model predicts symmetric fission for the $^{28}Si + ^{50,52,54}Cr$ set of systems, whereas the observed distributions are asymmetric.

These calculations show that it is possible to describe the total kinetic energy widths from both sets of systems in terms of the liquid drop model. As these calculations are based on the liquid drop model, they take no account of effects associated with the finite range of the nuclear force and the diffuseness of the nuclear surface; effects which can lead to significantly different mass distributions as pointed out in the discussion of the Businaro-Gallone transition.

6.8 Fast-Fission and the Finite Range Model

In the discussion on intermediate mechanisms in section 2.7, we point out that the main evidence for the existence of a new reaction process in the medium mass region is the apparent inability of established models of long-lived dissipative collisions to explain the data: specifically many authors have ruled out fast-fission and quasi-fission on the basis of rotating liquid drop model calculations. However, as the CASCADE calculations for these systems (discussed earlier in this chapter) graphically illustrate, realistic models of the nucleus predict the fission barrier of the compound nucleus to vanish at much lower angular momentum values than predicted by the leptodermous rotating liquid drop model. This begs an obvious, yet intriguing question. Namely, can the data on fissionlike reactions in this mass region, interpreted as evidence for a new intermediate reaction process, be characterised as fast-fission? If so, this would help to unify fissionlike reactions in this mass region with those of much heavier systems, where fast and quasi-fission have been identified and studied for some years [75].

Fast-fission can occur if the system coalesces for angular momentum values at which the compound nucleus does not possess a well defined fission barrier. This is the case if the fission barrier (B_f) is smaller than the nuclear temperature at the saddle point (Θ). The maximum fusion partial wave (or critical angular momentum) may be estimated using a sudden potential [2] to describe the interaction between the colliding nuclei (see for example equation 2.1). If this value is larger than the angular momentum at which $B_f = \Theta$ then fast-fission is possible [23].

Calculations along these lines were performed to test whether fast-fission can occur for the systems studied in this thesis. The routine BARFIT [51] provides both the energy of the rotational ground state (E^{gs}_{rot}) and the fission barrier of a given nucleus, as a function on angular momentum. Equations

6.25 to 6.28 were used to estimate the nuclear temperature at the saddle point for each partial wave, with values of E_{rot}^{gs} and the fission barrier taken from BARFIT. Shell corrections were neglected for the purpose of these calculations.

A simple model was used to estimate the largest angular momentum with which each system fuses. The interaction between target and projectile was described using a sudden potential, with (equation 2.1)

$$V_l(r) = \frac{Z_1 Z_2 e^2}{r} + \frac{f^2 l(l+1)\hbar^2}{2\mu r^2} - V_N(r) \tag{6.29}$$

where all symbols are explained in section 2.2.1. Two forms were used for the nuclear potential: the proximity potential of Ngô [2], and the Yukawa plus exponential, finite range model of Krappe, Nix and Sierk [27]. The equation of the potential due to Ngô is

$$V_N(r) = \frac{C_1 C_2}{C_1 + C_2} U_N(s) \tag{6.30}$$

where $C_i = R_i \left[1 - R_i^{-2}\right]$ (with $R_i = 1.16 A_i^{1/3}$ fm), $s = r - C_1 - C_2$ and the function $U_N(s)$ is given by

$$U_N(s) = \begin{cases} 34 \exp\left[-\frac{(s-s_0)^2}{5.4}\right] \text{ MeV}, & \text{if } s > s_0 = -1.6 \text{ fm} \\ 34 + 5.4\,(s - s_0)^2 \text{ MeV}, & \text{otherwise.} \end{cases} \tag{6.31}$$

The finite range model of Krappe et al. is the same as that used by BARFIT, and so is ideally suited to a consistent comparison with the predictions of the routine. This model gives for the nuclear potential

$$V_N(r) = \begin{cases} D\left(F + \frac{s}{a}\right)\frac{R_{12}}{r} \exp\left(-\frac{s}{a}\right), & \text{if } s > 0 \\ V_0 + \left(\frac{B}{R_{12}}\right) r, & \text{otherwise.} \end{cases} \tag{6.32}$$

where D, F, V_0 and B are constants for a given system, $R_{12} = R_1 + R_2$ (with $R_i = 1.18 A_i^{1/3}$ fm), $s = r - R_{12}$ and $a = 0.65$ fm. In these models s is the distance between the nuclear surfaces, C_1, C_2 are the central radii of the nuclei, R_{12} is the sum of their radii and a is a diffuseness parameter.

In the critical distance model (section 2.3.1) the colliding nuclei have to reach a certain minimum separation in order to fuse. When the system reaches this separation, known as the critical distance, strong frictional forces dissipate angular momentum and if the resulting potential energy surface possesses a pocket the nuclei may fuse. This simple treatment of the collision process has been invoked for these calculations, with $s = 0$ – i.e. when the nuclear surfaces come into contact – taken as the critical distance of approach. For a given centre of mass energy (E_{cm}), the maximum partial wave for which the surfaces come into contact (l_{cont}) is given by the expression

$$E_{cm} = \frac{Z_1 Z_2 e^2}{R_{12}} + \frac{f^2 l_{cont}(l_{cont}+1)\hbar^2}{2\mu R_{12}^2} - V_N(r) + \Delta E \qquad (6.33)$$

Dissipation of angular momentum in the collision is allowed for by the parameter f, which is often set to the sticking value given by

$$f = \frac{\mu R_{12}^2}{\mu R_{12}^2 + \theta_1 + \theta_2} \qquad (6.34)$$

where μ is the reduced mass and θ_1, θ_2 are the moments of inertia of target and projectile, assuming them to be rigid spheres. ΔE is the energy lost from relative motion as the nuclei come together. For peripheral collisions ΔE is approximately equal to the loss of centrifugal energy due to the decrease of orbital angular momentum from l_{cont} to $f l_{cont}$ [76], and so

$$E_{cm} = \frac{Z_1 Z_2 e^2}{R_{12}} + \frac{l_{cont}(l_{cont}+1)\hbar^2}{2\mu R_{12}^2} - V_N(r) \qquad (6.35)$$

Although strong dissipation of angular momentum occurs at the point of contact, bringing the surfaces of the nuclei together is not a sufficient condition to fuse them. For fusion to occur the resultant force between them ($F(r)$) must be attractive. This force is given by the expression

$$F(R_{12}) = \frac{dV_l(R_{12})}{dr} = -\frac{Z_1 Z_2 e^2}{R_{12}^2} - \frac{f^2 l_{cr}^{max}(l_{cr}^{max}+1)\hbar^2}{\mu R_{12}^3} - \frac{dV_N(R_{12})}{dr} \qquad (6.36)$$

For a given reaction and a given centre of mass energy, the critical angular momentum is the smaller of l_{cont} and l_{cr}^{max}.

Spin distributions for the systems ^{40}Ca + ^{40}Ca and ^{28}Si + ^{50}Cr are presented in figures 6.14 and 6.15 respectively. In each figure the solid lines show fusion distributions; the dashed lines show fission cross sections predicted by CASCADE (see section 6.3); the dotted lines indicate the limit $B_f = 0$, and the dot-dashed lines correspond to $B_f = \Theta$. The fusion spin distributions have been obtained using equation 6.2, with the diffusenesses set to $2\hbar$ and the critical angular momenta determined using the nuclear potential of Krappe, Sierk and Nix. Clearly, for all systems but 130 MeV ^{28}Si + ^{50}Cr much of the fissionlike cross section is predicted to emanate from partial waves for which $B_f < \Theta$, thus satisfying the conditions for fast-fission. The results of these calculations for the systems studied in this thesis are presented in table 6.9.

Similar calculations have been performed for some of the other systems in this mass region whose fissionlike reactions have been studied in the literature. The results of these calculations are shown in table 6.10.

The symbol † in tables 6.9 and 6.10 denotes those systems for which fast-fission is not expected. The mass distributions from each of these systems are not inconsistent with an interpretation in terms of fission of a fully equilibrated compound nucleus, accompanied by an amount of postfission evaporation. The symbol ‡ is used to indicate systems whose angular distributions are strongly forward peaked, and so explainable in terms of a combination of fission and deep-inelastic scattering. All other entries in tables 6.9 and 6.10 are expected to display a significant fast-fission cross section. It is interesting to note that for each system in these tables the rotating finite range model prediction of $l_{B_f=0}$ is approximately $10\hbar$ lower than the rotating liquid drop model value.

The fission barriers given by BARFIT are those for symmetric fission. It may be that these systems possess a finite fission barrier for the entrance channel mass asymmetry, but not for symmetric decay, in which case the reaction

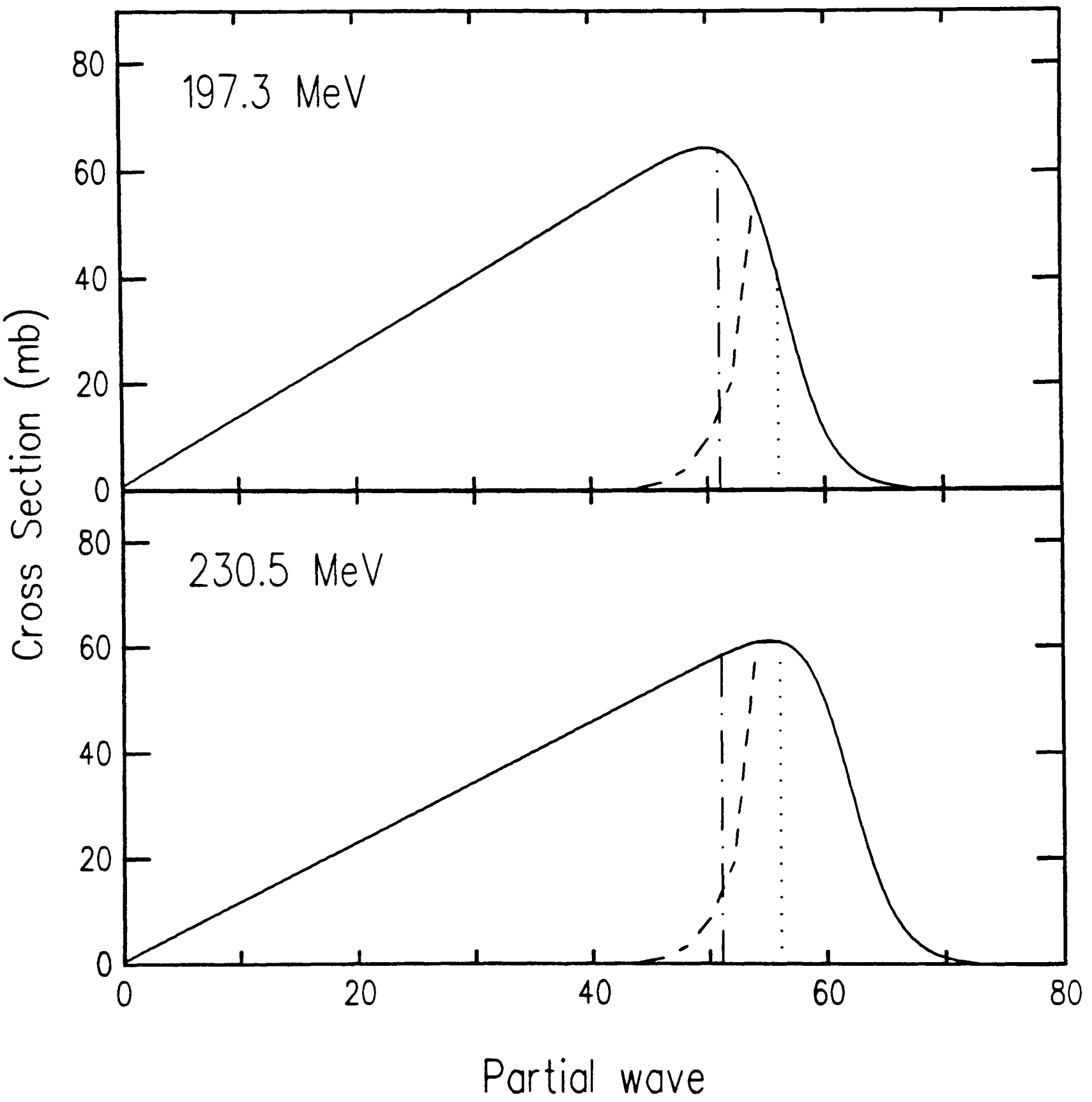


Figure 6.14. Predicted spin distributions for ^{40}Ca + ^{40}Ca at 197.3 and 230.5 MeV. The figure shows $d\sigma/dl$ as a function of partial wave number. All lines are explained in the text. Only even partial waves are allowed for this system.

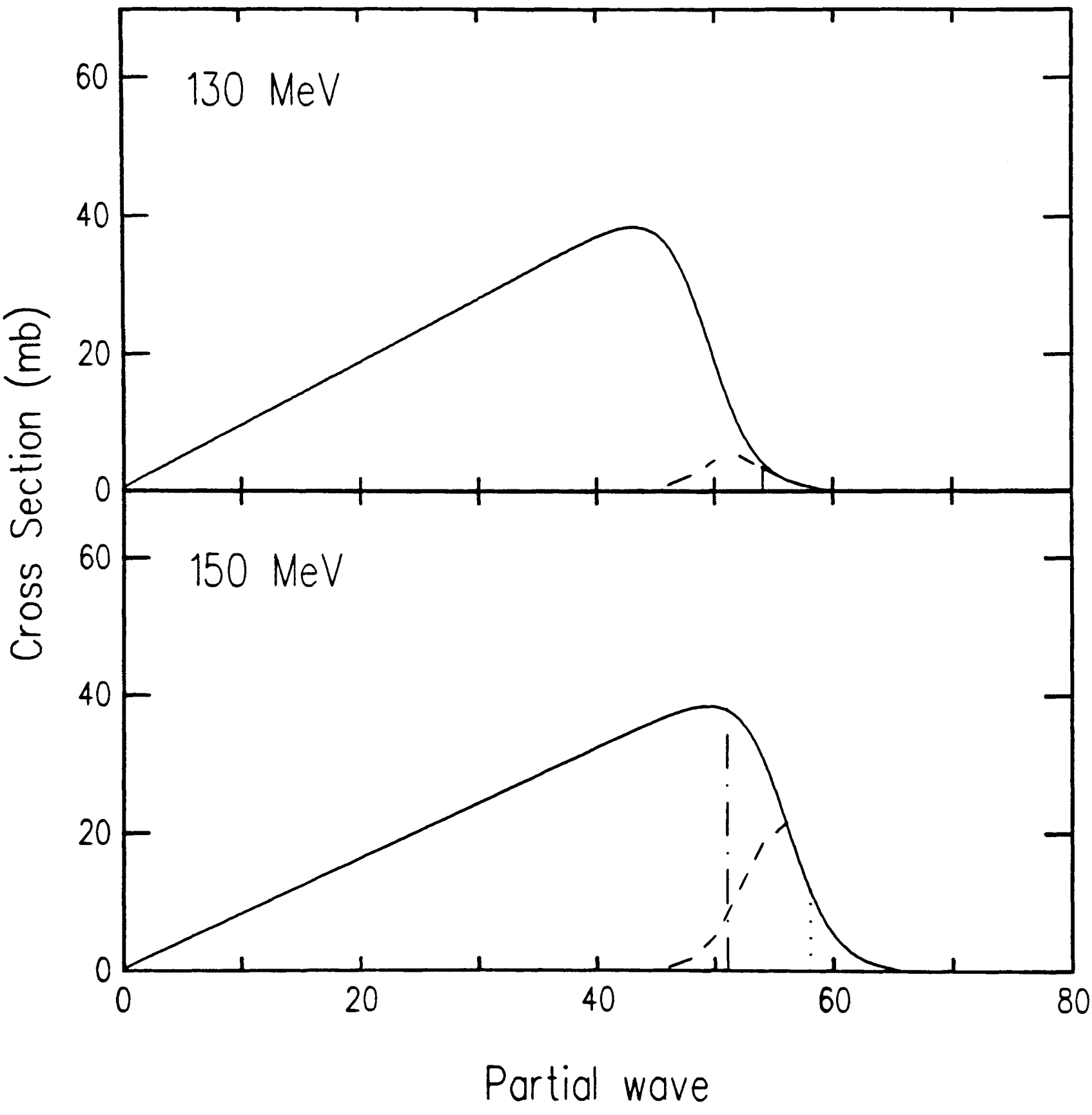


Figure 6.15. Predicted spin distributions for ^{28}Si + ^{50}Cr at 130 and 150 MeV. The figure shows $d\sigma/dl$ as a function of partial wave number. All lines are explained in the text.

System	E_{LAB}	l_{KNS}	l_{NGO}	l_{CASC}	$l^{BARFIT}_{B_f=\Theta}$	$l^{BARFIT}_{B_f=0}$	$l^{RLDM}_{B_f=0}$	Comment
$^{40}Ca + ^{40}Ca$	197.3	56.3	56.7	57.8	51	56.6	66.3	
$^{40}Ca + ^{40}Ca$	230.5	61.7	64.0	59.5	51	56.6	66.3	
$^{28}Si + ^{50}Cr$	130	49.2	50.1	49.3	54	58.2	67.9	†
$^{28}Si + ^{50}Cr$	150	55.8	55.7	57.2	53	58.2	67.9	
$^{28}Si + ^{52}Cr$	130	50.8	51.8	50.9	56	61.1	71.0	†
$^{28}Si + ^{54}Cr$	130	52.3	53.4	52.4	59	63.8	74.2	†

Table 6.9 Characteristic angular momentum values for systems studied in this thesis. In this table the column headings have the following meanings: E_{LAB} denotes the bombarding energy; l_{KNS} is the critical angular momentum calculated using the nuclear potential of Krappe et al. [27]; l_{NGO} signifies the critical angular momentum calculated with the proximity potential of Ngô [2]; l_{CASC} is the critical angular momentum predicted by CASCADE (see section 6.3); $l^{BARFIT}_{B_f=\Theta}$ denotes the angular momentum for which BARFIT predicts the fission barrier is equal to the nuclear temperature; $l^{BARFIT}_{B_f=0}$ is the limit when the fission barrier vanishes in the finite range model, and $l^{RLDM}_{B_f=0}$ is the angular momentum at which the fission barrier vanishes in the liquid drop model. The symbol † in the column headed **Comment** is discussed in the text.

System	E_{LAB}	l_{KNS}	l_{NGO}	l_{CASC}	$l^{BARFIT}_{B_f=\Theta}$	$l^{BARFIT}_{B_f=0}$	$l^{RLDM}_{B_f=0}$	Comment	Reference
$^{32}S + ^{50}Ti$	131	49.2	51.3	48.2	59	63.8	74.2	†	Barrette et al. [17]
$^{32}S + ^{50}Ti$	166	61.4	61.4	60.6	58	63.8	74.2		Barrette et al. [17]
$^{32}S + ^{59}Co$	140	52.8	54.6	52.5	61	66.1	76.0	‡	Agnoli et al. [21]
$^{32}S + ^{59}Co$	168	62.2	62.5	63.6	60	66.1	76.0		Agnoli et al. [21]
$^{32}S + ^{63}Cu$	140	52.6	54.7	52.2	62	67.1	76.8	‡	Agnoli et al. [21]
$^{32}S + ^{63}Cu$	168	64.2	64.4	64.1	61	67.1	76.8		Agnoli et al. [21]
$^{32}S + ^{74}Ge$	170	69.1	69.6	71.0	68	75.0	85.6		Oeschler et al. [18]
$^{32}S + ^{59}Br$	170	68.3	69.0	70.1	68	74.2	83.9		Oeschler et al. [18]
$^{32}S + ^{85}Rb$	170	69.2	70.2	71.0	71	76.8	86.8		Oeschler et al. [18]
$^{32}S + ^{89}Y$	153	59.8	62.2	60.0	71	76.5	86.1	†	Oeschler et al. [18]
$^{35}Cl + ^{62}Ni$	170	64.5	65.3	65.6	64	69.9	80.0		Bisplinghoff et al. [69]
$^{12}C + ^{89}Y$	197	69.6	65.7	69.5	66	75.1	86.6		Natowitz et al. [70]
$^{12}C + ^{98}Mo$	107	48.6	47.8	49.9	74	79.9	92.3	‡	Natowitz et al. [70]
$^{12}C + ^{98}Mo$	197	71.4	67.6	72.6	71	79.9	92.3		Natowitz et al. [70]
$^{12}C + ^{107}Ag$	107	48.7	48.0	49.9	73	65.7	73.4	‡	Natowitz et al. [70]
$^{93}Nb + ^{9}Be$	782	36.3	36.1	36.5	71	76.3	88.2	†	Sobotka et al. [28]
$^{139}La + ^{9}Be$	1157	38.1	38.8	37.6	84	89.3	107.9	†	Sobotka et al. [28]

Table 6.10 Characteristic angular momenta of systems studied in the literature. The column headings are explained in the caption to table 6.9. The symbols † and ‡ are discussed in the text.

mechanism would be quasi-fission. Calculations to test this hypothesis are in progress [61].

Thus much of the experimental data on fissionlike reactions in this mass region may be characterised as fast-fission. This points to a generic link with similar types of dissipative reaction in heavier systems.

6.9 Nuclear Shell Effects

We now consider the possible evidence for nuclear shell effects in the data. The shell effects considered involve the formation of a compound nucleus, and so their confirmation would be inconsistent with the fast-fission interpretation discussed above. In chapter 2 these phenomena are presented under three headings: namely α-particle clustering, ground state Q-value correlations, and magicity at superdeformation. We now discuss each of these in turn.

6.9.1 Alpha-Particle Clustering

The fissionlike mass distributions from ^{40}Ca + ^{40}Ca at both 197.3 and 230.5 MeV show strong, regular structure (see figures 6.6 and 6.7). The fact that this structure has periodicity four amu makes it consistent with the postulate of α-particle clustering in the compound nucleus ^{80}Zr.

However, the detailed anatomy of the mass distributions suggests the situation may be more complex: firstly, the system evaporates at least four units of mass on average, which may have some bearing on the α-particle-like periodicity; and secondly the maxima at every four mass units become significantly weaker above mass 40, giving the whole structure an uneven look.

We show in the discussion of the LILITA calculations that the appearance of the α-particle-like structure is predicted reasonably well within the framework of post-scission evaporation, if a Gaussian primary mass distribution is assumed. Furthermore, LILITA calculations assuming strong α-particle periodicity in the primary mass distribution grossly overpredict the structure observed in the final distribution. This would appear to rule out the hypothesis that the α-particle structure emanates from the primary fissionlike mass distribution. Nevertheless, to investigate the effects of a weak α-particle structure, LILITA calculations were carried out using a Gaussian (full width half maximum = 26 amu) with a small (typically 10%) enhancement of every fourth mass in the primary distribution. The results of these calculations also overpredict the periodic structure.

Hence, the appearance of strong peaks at every fourth mass in the ^{40}Ca + ^{40}Ca spectra can be attributed to post-scission evaporation, without the existence of any α-particle structure in the primary fissionlike yield.

6.9.2 Ground State Q-Value Correlations

We point out in section 2.9.2 that the mass spectra obtained by Oeschler et al. [18], for a series of systems, are strongly correlated with the ground state Q-values. The ability of the LILITA calculations (with a Gaussian primary mass distribution) to describe the experimental mass spectra from fissionlike reactions of ^{40}Ca + ^{40}Ca argues against any dependence on the ground state Q-values, which would favour decay into ^{28}Si and ^{52}Fe. Furthermore, the compelling evidence for post-scission evaporation brings into question whether the fissioning nucleus can be cold enough for shell effects to be influential. However, the strong correlation between the measured total kinetic energies and ground state Q-values (see section 5.2.5) is reminiscent of the shell effects observed in the total kinetic energy spectra obtained from the spontaneous and induced fission decay of some actinide nuclei [8].

The mass spectra for the ^{28}Si + ^{50,52,54}Cr systems show maxima close to masses 50, 52 and 54, consistent with ground state Q-value dependence. However, as pointed out above, this may be the result of a long-lived deep-inelastic orbiting component or asymmetric fission accompanied by evaporation. The experimental Q-values for these systems each show a smooth variation as a function of mass, with no hint of any correlations with the ground state values.

Shell effects of this kind are expected to occur if the minimal level density along the path to fission is low, such that small variations in the potential energy surface, due to Q-value effects, greatly influence the phase-space available. The minimal level density occurs when the potential energy is a maximum; i.e. at the saddle point. As the excitation energy of the fissioning nucleus is increased, the excitation energy at the saddle point (for a given angular momentum) also increases, giving rise to a greater minimal value for the level density. Thus, shell effects are expected to decrease with excitation energy. This is borne out by experiment: the shell effects seen in the fission decay of the actinides diminish with excitation energy (E^*), and for $E^* \geq 20$ MeV become imperceptible. The correlation between ground state Q-values and TKE observed for ^{40}Ca + ^{40}Ca also becomes weaker as energy is increased (figure 5.11).

6.9.3 Superdeformed Shell Effects

We mention in chapter 2 that the signature of superdeformed shell effects would be the occurrence of sharp variations in such properties as fission cross sections and total kinetic energies across a range of isotopes. The fissionlike properties of ^{28}Si + ^{50,52,54}Cr show no evidence for such behaviour. Furthermore, the possibility of a strong deep-inelastic component which may be dominant close to threshold (where shell effects should be most tangible) brings into question whether such measurements are possible. Also, the fissionlike cross sections of

$^{28}Si + ^{50,52,54}Cr$ are well reproduced by the statistical model calculations with similar input parameters for each system (see section 6.3).

6.10 Summary

The experimental data have been compared with several model calculations. For each of the systems studied:

1. Fusion calculations predict the presence of a large cross section for compound nucleus formation.
2. Diffusion model calculations suggest the existence of a fully damped orbiting component for the lowest deep-inelastic partial wave. This component is of magnitude 30 to 40 mb, and hence unable to account for the total fully damped yield, except perhaps in the case of the silicon on chromium systems at 130 MeV.
3. Calculations from the standpoint of the statistical model are able to reproduce the fissionlike cross section.
4. The liquid drop model predicts the full width half maximum of the TKE reasonable well, but gives too broad a mass width.
5. The large amount of post-scission evaporation produced significantly alters the mass distribution, making a quantitative measure of the primary fissionlike yield difficult.

The mass distributions from fissionlike reactions in this region of the periodic table display a smooth transition from asymmetry (or target and beamlike) to symmetry when plotted as a function of the rotating liquid drop model fission barrier height and fissility parameter. Calculations using a finite range model of the nuclear force predict the occurrence of fast-fission for many systems studied in this mass region.

Chapter 7

Summary and Conclusions

That's how it is, said Pooh.

A. A. Milne, *When We Were Six*

7.1 Summary

In this thesis we have described a set of experiments to investigate the properties of fully damped reactions in the mass 80 region. In a unique study, symmetric and asymmetric target and beam combinations – leading to similar compound nuclei – have been compared. The purpose of this has been to establish the entrance channel dependence of these processes, and hence to gain greater insight into the dissipative reaction mechanisms at play in this particular mass region.

The symmetric system $^{40}Ca + ^{40}Ca$ was studied at laboratory energies of 197.3 and 230.5 MeV. A set of six time of flight telescopes, placed at 10°, 15.4°, 20.2°, 32.4°, 42.4° and 52.4° to the beam, was used to measure the energies and masses of the reaction products. A Bragg curve spectrometer-MWPC telescope, placed at −30°, provided both charge identification and binary coincidence information with the time of flight telescopes.

The results indicate a large fully damped cross section in this energy range (197.6 mb at 197.3 MeV and 403.1 mb at 230.5 MeV). The angular distributions obtained from the 197.3 MeV data are flat as a function of θ_{cm}, but display a small rise close to mass 40 for the higher energy. The mass distributions have broad (full width half maxima > 20 amu for a Gaussian fit), symmetric peaks, with periodic structure at every fourth mass – a feature suggestive of a predominance of multiple α-particle nuclei in the exit channel. The variation of Q-value with mass split is well described assuming sticking of the nascent fragments. Superimposed on the sticking component is a structure which follows the pattern of the ground state Q-values at the lower energy and which deviates from this at symmetry for the higher energy. However, this behaviour may be more indicative of the inadequacies of the sticking model than of any physical relation with ground state Q-values. Coincidence and singles results are consistent and indicative of the evaporation of about four to six units of mass, in agreement with the findings of Barrette et al. for the system $^{32}S + {}^{50}Ti$ [17].

Fissionlike reactions of the asymmetric system $^{28}Si + {}^{50}Cr$ were studied at beam energies of 130 and 150 MeV, corresponding to similar ratios of centre of mass energy to Coulomb barrier to those employed in the $^{40}Ca + {}^{40}Ca$ experiment. The systems $^{28}Si + {}^{52,54}Cr$ were also studied at 130 MeV. The purpose of studying a range of chrome isotopes was to obtain information on the isotopic dependence of the reaction mechanism. Four time of flight telescopes placed at 10°, 20°, 30° and 40° were used to determine energy and mass.

Technical developments were required in order to carry out the $^{28}Si + {}^{50,52,54}Cr$ measurements. Specifically, a new type of avalanche counter has been developed. The detector consists of two plane wire grids, separated by 1.5 mm, and across which a potential difference is applied. The chief objective of this design is to combine the best features of the parallel plate avalanche counter and the multiwire proportional chamber. Two methods of grid manufacture

have been employed: the detectors used in the experiment were made by winding thin wire around a former; and more recently, a photo-etching technique of manufacture has been used. Timing resolution values of 350 ps have been obtained using these hybrid detectors in conjunction with silicon surface barrier detectors. Although the wire wound avalanche counters that were deployed in the $^{28}Si + ^{50,52,54}Cr$ measurements were subject to reliability problems, the more recently developed photo-etched detectors have proved both reliable and efficient, thus proving the quality of the novel design.

Fully damped cross sections of ≈ 30 and ≈ 140 mb were obtained at 130 and 150 MeV respectively, with little variation across the isotopic range. The mass distributions are asymmetric, with slight maxima at target and beam masses. As with the $^{40}Ca + ^{40}Ca$ data, the variation of Q-value with mass split is described by the sticking limit, but conversely shows no correlation with the ground state Q-values. These results for $^{28}Si + ^{50,52,54}Cr$ are similar to those of Barrette et al. for the system $^{32}S + ^{50}Ti$ [17].

The data from these experiments have been compared with the predictions of several models. The results of some of these calculations provide much insight into the reaction process. The code LILITA has been used to determine primary mass distributions, assuming the observed yields to be the result of post-scission evaporation. Calculations for $^{40}Ca + ^{40}Ca$ predict a Gaussian primary distribution at each bombarding energy, while for $^{28}Si + ^{50,52,54}Cr$ it was not possible to deduce unequivocally whether the primary distribution is asymmetric or target and beamlike, due to computational limitations.

The diffusion model predicts the presence of a small deep-inelastic component contributing approximately 40 mb to the fully damped cross section for each system. Hence, with the possible exception of $^{28}Si + ^{50,52,54}Cr$ at 130 MeV it is unable to account for the magnitudes of the fissionlike cross sections measured in these experiments.

The rotating liquid drop model predicts that each of the systems studied can form a compound nucleus for all partial waves which fuse. However, a comparison of the limit of nuclear stability (i.e. $B_f \rightarrow 0$) with the critical angular momentum for fusion of each system, within the framework of the more realistic rotating finite range model, provides strong evidence that a dominant fissionlike component emanates from partial waves for which the compound nucleus does not possess a well defined fission barrier. Such a process clearly fulfils the conditions for fast-fission. However, fast-fission is not expected for 130 MeV ^{28}Si + ^{50,52,54}Cr. Similar calculations have been performed for many of the systems studied in the literature, the results of which also suggest the occurrence of fast-fission in many of these experiments.

A plot of fission barrier height (calculated using the liquid drop model) against fissility parameter, for the systems studied in this mass region, displays a distinct transition from systems which decay asymmetrically (or like target and beam) to those which decay symmetrically. The location of this transition is close to where the rotating finite range model predicts the spin zero Businaro-Gallone point to occur.

7.2 Conclusions

In this work, we show that much of the data on fissionlike reactions in this mass region can be interpreted as fast-fission; a process traditionally associated with much heavier systems. Such an explanation obviates the need for the intermediate reaction mechanism interpretation proposed by various authors, and helps to unify fissionlike reactions in this mass region with those of heavier systems, where such phenomena have been studied for many years.

Fast-fission, however, is not expected to occur for the $^{28}Si + ^{50,52,54}Cr$ systems at 130 MeV, as their fission barriers are greater than the nuclear temperature at their saddle points. The large number of nucleons evaporated from $^{28}Si + ^{50,52,54}Cr$ at 130 MeV has made it impossible to ascertain whether the primary mass distributions are asymmetric or target and beamlike in this case. Such information would enable the unequivocal characterization of the reaction mechanism, in this lower energy regime, as either asymmetric fission or deep-inelastic orbiting. Although diffusion model calculations do predict that orbiting occurs for these systems, they generally underpredict the observed magnitude of the fully relaxed cross sections for all cases except 130 MeV $^{28}Si + ^{50,52,54}Cr$. Hence, it would seem that orbiting does not contribute significantly to the fully damped cross sections of most systems studied in this thesis. Conversely, the plot of fission barrier against fissility parameter presented in figure 6.12 provides some evidence for the dominance of a fusion-fission mechanism at lower energies; where the fission barrier is greater than the nuclear temperature at the saddle point, thus precluding fast-fission. This criterion is satisfied by the systems labelled (b), (c), (h), (i), (p), (q) and (r) on figure 6.12. Clearly, there is transition from asymmetric to symmetric decay with increasing fissility; a result completely consistent with the assertions that these systems fission and that they straddle the Businaro-Gallone line.

Much future work can be done to test this interpretation. At present, calculations are in progress to calculate conditional saddle points for $^{28}Si + ^{50,52,54}Cr$ [61]. If these systems possess zero fission barrier for symmetric decay, yet a finite barrier for the entrance channel mass asymmetry, then the reaction mechanism may be categorized as quasi-fission. In the low energy regime, a systematic series of measurements for systems spanning the predicted Businaro-Gallone transition would provide a stringent test of whether fission occurs. Such studies might enable the localization of the Businaro-Gallone transition. Further studies of $^{40}Ca + ^{40}Ca$ could prove fruitful in this direction. At low energies,

close to the fission threshold, the mass distributions from this system may be asymmetric. This would be irrefutable evidence for fission. However, as the LILITA calculations for the systems discussed in this work clearly indicate, any study of fissionlike mass distributions in this region of the periodic table must take account of the effects of particle evaporation; a process which can drastically alter the forms of such distributions.

By making a direct comparison of different entrance channels leading to similar compound systems, it has been possible to gain much insight into the fully damped reactions of medium mass nuclei. Previous descriptions of these phenomena have dismissed the possibility of a generic link with processes observed for heavier systems on the basis of calculations using the rotating liquid drop model; a model which assumes zero range forces. By employing the rotating finite range model we have been able to show that processes common to heavier systems may indeed take place. Such calculations point to the possibility of both fast-fission and asymmetric fission in this mass and energy regime, thus obviating the need for the intermediate mechanisms interpretation previously proposed to describe data in this mass region.

Appendix I

Finer Points of the Data Analysis

There is no higher or lower knowledge,
but one only, flowing out of experimentation.

Leonardo da Vinci

I .1 Introduction

Finer points of the singles data analysis are presented in this appendix. Each of the following sections is referred to in chapter 5 of the main text. It is intended that this part of the thesis be read in conjunction with that chapter and used when specific detail is required.

I .2 Pulse Height Defect

Ideally the height of the output pulse from a silicon surface barrier detector should only depend on the particle's energy. Unfortunately, this is not true for heavy ions, as a fraction of the energy imparted is not detected. Reasons for this include the recombination of pairs and trapping in lattice defects. These

phenomena are known collectively as pulse height defect. All energy measurements described in this thesis were corrected for pulse height defect using the empirical formula of Kaufman et al. [77].

The measured energy (E) of a detected particle can be expressed in dimensionless energy units (ε), using the expression

$$\varepsilon = E\frac{0.8853 a_0 M_2 \left(Z_1^{\frac{2}{3}} + Z_2^{\frac{2}{3}}\right)^{-\frac{1}{2}}}{Z_1 Z_2 e^2 (M_1 + M_2)} = \kappa(M, Z)E \qquad (I.1)$$

where a_0 is the radius of the first Bohr orbit of hydrogen ($a_0 = 5.292 \times 10^{-11}$ m) and the subscripts 1 and 2 refer to the ion and the detection medium (silicon) respectively. Kaufman et al. find that the energy defect is well described by the empirical formula,

$$\Delta\varepsilon = \frac{6\varepsilon}{\varepsilon + 8} + \frac{A}{1 + 525\varepsilon^{-1.407}} \qquad (I.2)$$

where A is a constant – taken as 14.0 in this work. Thus the corrected energy of the particle (E_t) is given by,

$$E_t = E + \Delta\varepsilon/\kappa \qquad (I.3)$$

Pulse height defect was corrected for in this way.

The ionization produced by light particles is less dense than that from heavier ones, and so recombination is a less serious problem in this case. Thus the pulse height defect for very light ions is small, and generally negligible in the case of α-particles.

I .3 Plasma Delay

Plasma delay is described in section 3.3.1. The dense plasma produced by heavy ions, as they come to rest in a silicon surface barrier detector, tends to shield electron-hole pairs from the external electric field, giving rise to a variable time difference between the particle's arrival and charge collection.

Plasma delay time corrections were made using the method due to Neidel and Henschel [36]. They obtain an empirical formula:

$$\tau_p = 1.33 \frac{M^{\frac{1}{6}} E^{\frac{1}{2}}}{F} \qquad (I.4)$$

where M is the mass in amu, E is the energy in MeV and F is the electrical field strength in kV/cm. As the calibration constant for each TAC had been chosen so that the ^{40}Ca elastic peak fell at the correct mass, the plasma delay time for ^{40}Ca was already included in t_0 (see equation 5.2). Hence the quantity of interest was the difference between the calculated plasma time and that estimated for ^{40}Ca. This was calculated using equation I.4 and set equal to $\delta\tau_p$, for use in equation 5.3.

Neidel et al. deduce that the formula is valid if the field is above a certain, critical value (F_{min}), given by

$$F_{min} = 1.26 \frac{E}{M^{\frac{2}{5}}} \qquad (I.5)$$

The applicability of the expression to these data is questionable in view of the fact that the detector electric fields were close to the minimum value. Furthermore similar studies of plasma delay times have yielded different results [78]. However, the mass calibrations are linear and free from distortion.

I .4 Predicted Loci of Fission Events

I .4.1 Total Kinetic Energies and Q-Values

In order to deconvolute the various components of the data and extract the yield from fissionlike reactions of ^{40}Ca + ^{40}Ca, the Viola systematics were used to predict the locus of events from each possible fissionlike reaction. These loci were used to decide where events with the correct Q-values for fully relaxed processes should fall on a 2-dimensional spectrum of mass against energy.

As a first stage in the construction of these curves, the maximum partial wave brought into the system (L_{max}) was estimated by equating the centre of mass energy (E_{cm}) with the sum of Coulomb and rotational energies of touching target and projectile nuclei. Thus

$$L_{max} = \sqrt{2\mu\,(E_{cm} - V_C)}\,(R_{12} + D) \qquad (I.6)$$

where V_C is the Coulomb barrier between target and projectile, μ is their reduced mass, R_{12} the sum of their radii (with $r_0 = 1.25$ fm) and D is a distance parameter (set to 0.8 fm).

The outgoing total kinetic energy (TKE) for symmetric fragmentation is given by the systematics of Viola et al. [10]:

$$TKE = 0.1189 Z^2/A^{1/3} + 7.3 \text{ MeV} \qquad (I.7)$$

This can be related to the deformation at which the TKE is determined. To do this the TKE is equated to the sum of Coulomb and rotational energies using the expression

$$TKE = \frac{1.44 Z_1 Z_2}{r_0\left(A_1^{\frac{1}{3}} + A_2^{\frac{1}{3}}\right) + S} + \frac{10.6771 f^2 L_{max}\,(L_{max}+1)}{\mu\left[r_0\left(A_1^{\frac{1}{3}} + A_2^{\frac{1}{3}}\right) + S\right]^2} \qquad (I.8)$$

where the parameter S is a separation variable which accounts for the effects of deformation. f is a friction parameter. In this work, the 'sticking' value was taken for f. This is given by

$$f = \frac{\mu R_{12}^2}{\mu R_{12}^2 + \theta_1 + \theta_2} \qquad (I.9)$$

where μ is the reduced mass of the nascent fragments, R_{12} is the sum of their radii, and $\theta_{1,2}$ are their moments of inertia (assuming they are rigid spheres).

Firstly, for symmetric fragmentation ($A_1 = A_2$ etc.), S is adjusted until the left and right hand sides of equation I.8 are equal. The TKEs for asymmetric partitions are determined using equation I.8, with S held at the value determined for symmetric fragmentation. The predicted Q-value for a fully relaxed process (Q_{pred}) is simply $E_{cm} - TKE$. The predicted Q-values discussed in section 5.2.5 were calculated in this way.

I .4.2 Mass Against Energy Plots

The laboratory energy E_3 of a particle (mass M_3) produced in a binary reaction is given by the formula

$$\sqrt{E_3} = \frac{\sqrt{M_3}b \pm \sqrt{M_3 b^2 + 4c\,(d - M_3 a)}}{2c} \qquad (I.10)$$

with

$$\begin{aligned} a &= Q + E_{lab} \\ b &= 2\cos\theta\sqrt{M_P E_{lab}} \\ c &= M_T + M_P \\ d &= M_T E_{lab} + cQ \end{aligned} \qquad (I.11)$$

where Q is the reaction Q-value (calculated using the method described above), E_{lab} is the bombarding energy in the laboratory frame, M_T is the target mass, M_P is the projectile mass and θ is the angle of observation in the laboratory

frame. Using the fully relaxed Q-values, the predicted values of E_3 were calculated as a function of M_3. The predicted locus of fissionlike events for ^{40}Ca + ^{40}Ca is shown in figure 5.2, along with similar plots for the systems ^{40}Ca + ^{90}Zr and ^{40}Ca + ^{16}O. These curves clearly indicate which are the events of interest.

I .5 Evaporation Residues

For the experiments described in this thesis, evaporation residues were expected to comprise a significant component of the yield at forward angles. Therefore it was important to know where evaporation residues should fall on a mass against energy spectrum, in order to isolate them. This was achieved using their expected mean velocities.

If a compound nucleus is formed which subsequently evaporates particles, because the directions of the evaporations are random in the centre of mass frame, the average velocity of the compound nucleus in the 0° direction (V_{cn}) should remain unchanged.

$$V_{cn} = \sqrt{\frac{2E_{lab}M_P}{(M_P + M_T)^2}} \qquad (I.12)$$

So if an evaporation residue, with mass M, is detected at an angle θ, on average its energy should be given by

$$E = \frac{M}{2} \times \frac{V_{cn}^2}{\cos^2\theta} = \frac{M}{\cos^2\theta} \times \frac{E_{lab}M_P}{(M_P + M_T)^2} \qquad (I.13)$$

in the non-relativistic limit. Equation I.13 was used to find the evaporation residue events in the data.

I .6 Correction for ^{40}Ca + ^{nat}O Fission Products

Fissionlike products from reactions of ^{40}Ca with oxygen are evident in the data for all detectors, particularly those at more forward angles. Two groups of these events are present, corresponding to two sets of centre of mass angles. On a 2-dimensional mass against energy spectrum (see figure 5.2), the higher energy group overlaps with the lighter products from the ^{40}Ca + ^{40}Ca system; a problem which had to be corrected for. Fortunately, the lower energy group of ^{40}Ca + ^{nat}O reaction products is clean. This made it possible to estimate the yield in the higher energy group and hence correct for its contamination of the fully relaxed yield from ^{40}Ca + ^{40}Ca.

To carry out this correction, the differential cross section observed in the laboratory frame for a particular mass from the clean, low energy group was transformed to the centre of mass frame using the method described in section 7 of this appendix. The cross section was then converted to $d\sigma/d\theta_{cm}$. The assumption was made that for the partitioning ^{40}Ca + ^{nat}O system $d\sigma/d\theta_{cm}$ is constant. Using this hypothesis, $d\sigma/d\Omega_{cm}$ was determined for the higher energy ^{40}Ca + ^{nat}O component, which was then converted to the laboratory frame and a corresponding yield estimated.

I .7 Laboratory to Centre of Mass Conversion

We mention in section 4.2.2 (equation 4.1) that the yield (Y) is related to the differential cross section ($d\sigma/d\Omega_{lab}$) by the formula

$$Y = \frac{\rho J \Delta\Omega}{2.67ZA} \times \frac{d\sigma}{d\Omega_{lab}} \qquad (I.14)$$

The various quantities are explained in section 4.2.2. Thus $d\sigma/d\Omega_{lab}$ can be determined if Y and the other quantities are known. However, the charge state of the beam after passing through the target (Z) is not necessarily known.

A convenient way of circumventing this problem is to use a 'monitor' reaction of known cross section for normalization. Rutherford scattering into the forward detectors was used in this work. The monitor yield (Y_{mon}) is given by the expression

$$Y_{mon} = \frac{\rho J \Delta\Omega_{mon}}{2.67ZA} \times \frac{d\sigma_R}{d\Omega_{lab}} \qquad (I.15)$$

where $\Delta\Omega_{mon}$ is the solid angle of the detector used to measure the yield from the monitor reaction and $d\sigma_R/d\Omega_{lab}$ is given by equation 4.2. If equation I.14 is divided by equation I.15 then the expression

$$\frac{d\sigma}{d\Omega_{lab}} = \frac{d\sigma_R}{d\Omega_{lab}} \times \frac{Y}{\Delta\Omega} \times \frac{\Delta\Omega_{mon}}{Y_{mon}} \qquad (I.16)$$

is obtained.

$d\sigma/d\Omega_{lab}$ must now be transformed to the centre of mass frame. Thus it is multiplied by the Jacobian for laboratory to centre of mass conversion, to yield $d\sigma/d\Omega_{cm}$. Now

$$d\Omega = \sin\theta d\theta d\phi \qquad (I.17)$$

so

$$\frac{d\sigma}{d\theta_{cm}} = 2\pi \sin\theta_{cm} \times \frac{d\sigma}{d\Omega_{cm}} \qquad (I.18)$$

For these fissionlike reactions $d\sigma/d\theta_{cm}$ is approximately constant, so the total fragment cross section is equal to $d\sigma/d\theta_{cm}$ multiplied by π (i.e. integrated over θ_{cm}). However there are two fragments from each fissionlike decay. So the fissionlike cross section (σ_f) is half the fragment cross section. Thus

$$\sigma_f = \frac{\pi}{2} \times \frac{d\sigma}{d\theta_{cm}} \qquad (I.19)$$

Appendix II

The Program FLAME

God casts the die, not the dice.

Albert Einstein

II .1 Introduction

We now discuss the Monte-Carlo program employed to confirm the consistency of singles and coincidence data. This program uses a given mass distribution to generate laboratory frame spectra which may then be compared with experiment to confirm the consistency of a given body of data. In the next section we describe the features of the program. In section II.3 the use of FLAME in the analysis of the ^{40}Ca + ^{40}Ca data is discussed and in section II.4 a listing of the program is presented.

II .2 Program Details

FLAME constructs laboratory frame mass spectra for binary, fissionlike reactions of rapidly rotating nuclei. It assumes angular distributions of the form $d\sigma/d\theta_{cm} =$ constant.

The user inputs the properties of the entrance channel (i.e. target, beam and laboratory energy) and gives details of the experimental configuration (i.e. detector angles and geometry). Once these parameters are input, the mass distribution is read in from a disc file: for each mass partition the relative probability and total kinetic energy are required. Other inputs to the program are the width of the total kinetic energy distributions (assuming them to be described by Gaussian functions of the same width for each mass split); whether binary coincidence or singles results are required, and how many trajectories are to be calculated.

Once these pieces of information have been entered into the program it produces the Monte-Carlo spectra. For each event, the spherical polar co-ordinates θ_{cm} and ϕ are generated, along with the mass of each fragment and the total kinetic energy. This event is then transformed to the laboratory frame. The trajectory of each fragment is compared with the position of each detector to determine whether the event is observed. If the event is detected, and the necessary coincidence requirements are satisfied, the appropriate mass spectrum is incremented. The mass spectra for all detectors are written to disc at the end of the program for comparison with experimental data.

In the case of the calculations described below, 2×10^6 trajectories require 16 minutes CPU time on the Oxford Nuclear Physics Laboratory's VAX 8700.

II .3 Analysis of the ^{40}Ca + ^{40}Ca Data

The use of this program to analyse the ^{40}Ca + ^{40}Ca experiment presented a problem: the centroids of the mass distributions for both bombarding energies are shifted from 40, indicating that the reaction is not completely two-body in nature. Thus, to circumvent this difficulty, the entrance channel specified was ^{38}K + ^{38}K – i.e. the system most like the true entrance channel, but with the correct centroid for symmetric fission. The bombarding energy for this fictitious reaction was chosen to produce the correct centre of mass velocity for the ^{40}Ca + ^{40}Ca experiment. The mass distributions used for these calculations were taken from the Gaussian fits shown in figure 5.8, assuming $Z = A/2$ for all partitions. The total kinetic energies and their average width were taken from the experimental data.

For each bombarding energy, 2×10^6 trajectories were calculated in both singles and binary coincidence modes. Seven mass spectra were generated in all for each run, corresponding to the six surface barrier detectors and the MWPC-BCS telescope. After each calculation, the Monte-Carlo distribution for one detector would be renormalized relative to the corresponding experimental spectrum. All generated spectra were then compared with experiment to check consistency. In all cases the overall agreement between data and simulation was good (see figures 5.13 to 5.16), hence providing confirmation of the consistency of singles and coincidence data for all detectors.

II .4 Listing of Program

```
c
c                              PROGRAM FLAME
c

c     monte-carlo program to generate angular distributions
c     assuming:
c     d(sigma)/d(theta_cm)=constant
c     there is the option of running in singles or coincidence mode
c     detectors can be circular or rectangular in shape
c     to denote detectors on opposite side of beam give theta opposite sign

c     inputs are:
c     mp mass of projectile
c     mt mass of target
c     elab beam energy
c     qvar variance of total kinetic energy
c     th(10) angles of detectors (up to 10)
c     sa(10) solid angles of detectors (if circular)
c     width, height and distance needed for rectangular detectors

c     input files needed:
c     error function file for gaussian distribution named gaussfit.dat
c     mass and tke file
c     format:
c     mass,d(sigma)/d(A),tke
c     complementary fragment not needed
c     values for up to acn/2 only are needed (acn/2-1/2 for an odd nucleus)

      real sa(10),th(10),width(10),height(10)
      real distance(10),yrange(10),zcentre(10),xcentre(10)
      real tkemean(150),prob(150)
      integer iv(10,150)
      integer*4 seed
      character nam*2,masfile*10,answer*1
      logical circular(10),coinc,seen(2,10)
      parameter (pi=3.141593)
      common /gas/ngas,gas(1001)

c     input relevant data

      type *,'Enter projectile charge and mass'
      accept *,izp,mp
      type *,'Enter target charge and mass'
      accept *,izt,mt
      type *,'Enter beam energy'
      accept *,elab
```

```
      type *,'Enter TKE variance (MeV)'
      accept *,tkevar
      type *,'Do you want coincidences (Y/N)?'
      accept 60,answer
   60 format(a1)
      coinc=.false.
      if(answer.eq.'y'.or.answer.eq.'Y') coinc=.true.

c     parameters

      ia=mp+mt
      iz=izp+izt
      z=float(iz)
      a=float(ia)
      ap=float(mp)
      at=float(mt)
      zt=float(izt)
      zp=float(izp)
      ecm=elab*at/a
      vcm=sqrt(2.*ap*elab)/a

c     read in gaussian array for tke distribution

      open(unit=29,file='gaussfit.dat',readonly,status='old')
      read(29,*) ngas
      read(29,*) (gas(i),i=1,ngas)
      close(29)

c     input cm mass distribution from file and normalize

      loop=0
      type *,'Enter mass distribution filename (a10)'
      accept 5,masfile
    5 format(a10)
      open(1,file=masfile,status='old')
c     the complementary fragment probabilites are not needed
   10 read(1,*,err=30) mass,prob(mass),tkemean(mass)
      loop=loop+1
c     masslow is lowest mass considered and masshigh is the highest
      if(loop.eq.1)masslow=mass
      goto 10
   30 continue
      close(1)
      masshigh=mass
      if(masshigh.gt.ia/2)masshigh=ia/2
c     correction for even mass due to complementary fragment
      itemp=ia/2
```

```
      itemp=itemp*2
      if(itemp.eq.ia) prob(masshigh)=prob(masshigh)/2.
      total=0.
      do i=masslow,masshigh
      total=total+prob(i)
      end do
      do i=masslow,masshigh
      prob(i)=prob(i)/total
c     generate string of unit length with probability
c     for each mass split marked off
      if(i.gt.masslow)prob(i)=prob(i)+prob(i-1)
      end do
      prob(masshigh)=1.01

c     input detector information

      type *,'How many detectors do you want (10 max)?'
      accept *,ndet
      if(ndet.lt.1) ndet=1
      if(ndet.gt.10) ndet=10
      if(ndet.eq.1.and.coinc) coinc=.false.
c     loop for each detector
c     find out if detector is circular or square
c     input dimensions of detector
c     note:  for circular detectors the solid angle must be input
      do 100 i=1,ndet
   45 type 50,i
   50 format(' Is detector ',i2,' circular (Y/N)?')
      accept 60,answer
      if(answer.eq.'y'.or.answer.eq.'Y') then
      type 75,i
   75 format(' Enter solid angle of detector ',i2,' (mstr)')
      accept *,sa(i)
c     convert to steradians
      sa(i)=sa(i)/1000.
      circular(i)=.true.
      else if(answer.eq.'n'.or.answer.eq.'N') then
      type 110,i
  110 format(' Enter width and height of detector ',i2,' (cm)')
      accept *,width(i),height(i)
      type 120,i
  120 format(' Enter distance of detector ',i2,' (cm)')
      accept *,distance(i)
      yrange(i)=height(i)/2.
      circular(i)=.false.
      else
      goto 45
```

```
      end if
      type 70,i
   70 format(' Enter angle of detector ',i2,' (degrees)')
      accept *,the
      th(i)=the*pi/180.
      if(.not.circular(i))then
c     calculate limits of rectangular detectors in cartesians
      zcentre(i)=distance(i)*cos(th(i))
      xcentre(i)=distance(i)*sin(th(i))
      end if
  100 continue

c     how many trajectories?

      type *,'How many trajectories?'
      accept *,niter
      type *,'Here we go then!'
      minus1=-1
c     generate random seed
      seed= 100.0 * secnds(0.0)
      do 200 nit=1,niter
c     type trajectory number every 10000
      nala=nit/10000
      nala=nala*10000
      dala=(nit-nala)*(nit-nala)
      if(dala.le.0.1) type *,nit

c     generate theta, phi, m1 and calculate related variables

c     it is assumed positive and negative thetas are identical
c     so the variable minus1 is to ensure alternate + and - angles
c     for light fragments
      theta=ran(seed)*pi
c     as the detectors are at phi=0, only positive phi values need be
c     considered
      phi=ran(seed)*pi/2.
c     m1 is found by comparing the random number valuem1 with a string of
c     unit length which is divided into sections, the lenghts of which
c     correspond to the probability of each mass split
c     which region of the string overlaps with valuem1 is equated to m1
      valuem1=ran(seed)
      do i=masslow,masshigh
      if(valuem1.lt.prob(i))then
      m1=i
      goto 20
      end if
      end do
```

```
  20  continue
      m2=ia-m1
c     ensure equal probability of positive and negative angles
      minus1=-minus1
      if(minus1.lt.0)then
      mtemp=m1
      m1=m2
      m2=mtemp
      end if
      a1=float(m1)
      a2=float(m2)

c     generate tkex from gaussian routine

      v=ran(seed)
      tkex=tkemean(m1)+gaus(v)*tkevar
      if(tkex.lt.0.001)tkex=0.001

c     kinematics

c     centre of mass velocities
      v1=sqrt(2.*tkex*a2/a1/a)
      v2=sqrt(2.*tkex*a1/a2/a)
c     laboratory velocities from cosine rule
      vl1=sqrt(v1*v1+vcm*vcm+2.*v1*vcm*cos(theta))
      vl2=sqrt(v2*v2+vcm*vcm-2.*v2*vcm*cos(theta))
      if(vl1.le.0.001) vl1=0.001
      if(vl2.le.0.001) vl2=0.001
c     laboratory energies
      elab1=.5*a1*vl1*vl1
      elab2=.5*a2*vl2*vl2
c     laboratory angles from cosine rule
c     this avoids ambiguities associated with theta>90 degrees from the
c     sine rule
      thlaw1=(vcm*vcm+vl1*vl1-v1*v1)/2./vcm/vl1
      if(thlaw1.le.-1.)  then
      thlab1=pi
      else if(thlaw1.ge.1.)  then
      thlab1=0.
      else
      thlab1=acos(thlaw1)
      end if
      thlaw2=(vcm*vcm+vl2*vl2-v2*v2)/2./vcm/vl2
      if(thlaw2.le.-1.)  then
      thlab2=-pi
      else if(thlaw2.ge.1.)  then
      thlab2=0.
```

```
      else
      thlab2=-acos(thlaw2)
      end if

c     decide if event is seen by detectors

      numberseen=0
      do i=1,ndet
      seen(1,i)=.false.
      seen(2,i)=.false.
      end do
      do 600 i=1,ndet
c     if detector is circular:
c     work out distance of trajectory from centre of detector (x1,x2)
c     compare with distance of detector edge from centre (sqrt(sa/pi))
c     if trajectory hits detector increment spectrum
      if(circular(i)) then
      x1=sqrt((th(i)-thlab1)*(th(i)-thlab1)+phi*phi)
      x2=sqrt((th(i)-thlab2)*(th(i)-thlab2)+phi*phi)
      dtheta1=sqrt(sa(i)/pi)-x1
      dtheta2=sqrt(sa(i)/pi)-x2
      if(dtheta1.ge.0.)  then
      seen(1,i)=.true.
      numberseen=numberseen+1
      end if
      if(dtheta2.ge.0.)  then
      seen(2,i)=.true.
      numberseen=numberseen+1
      end if
      else
c     if not circular (i.e.  rectangular):
c     convert theta, phi and radius (=distance) to cartesians
c     compare with geometry of detector
c     if trajectory hits detector increment spectrum
      x1=abs(distance(i)*cos(phi)*sin(thlab1)-xcentre(i))
      x1=x1-abs(width(i)/2.*cos(th(i)))
      x2=abs(distance(i)*cos(phi)*sin(thlab2)-xcentre(i))
      x2=x2-abs(width(i)/2.*cos(th(i)))
      y1=abs(distance(i)*sin(phi)*sin(thlab1))-yrange(i)
      y2=abs(distance(i)*sin(phi)*sin(thlab2))-yrange(i)
      z1=abs(distance(i)*cos(thlab1)-zcentre(i))
      z1=z1-abs(width(i)/2.*sin(th(i)))
      z2=abs(distance(i)*cos(thlab2)-zcentre(i))
      z2=z2-abs(width(i)/2.*sin(th(i)))
      if(x1.lt.0.0.and.y1.lt.0.0.and.z1.lt.0.0) then
      seen(1,i)=.true.
      numberseen=numberseen+1
```

```
      end if
      if(x2.lt.0.0.and.y2.lt.0.0.and.z2.lt.0.0) then
      seen(2,i)=.true.
      numberseen=numberseen+1
      end if
      end if
 600  continue
      if(numberseen.eq.0) goto 200
      if(coinc.and.numberseen.lt.2) goto 200
      do i=1,ndet
      if(seen(1,i)) iv(i,m1)=iv(i,m1)+1
      if(seen(2,i)) iv(i,m2)=iv(i,m2)+1
      end do
 200  continue

c     output results

c     results are written to file det1, det2, ...  detn etc.
      do 500 i=1,ndet
      write(nam,400) i
 400  format(i2)
      open(1,file='det'//nam,status='new')
      thet=th(i)*180./pi
      do 500 n=1,ia
      write(1,*) n,iv(i,n)
 500  continue

      stop
      end

c     gaussian function for tke calculation
c     ''borrowed'' from lilita

      function gaus(v)
      common/gas/ngas,gas(1001)
      ix=ngas*v+1
      dif=gas(ix)-gas(ix+1)
      dif=abs(dif)
      gaus=gas(ix)+dif*(ngas*v-ix+1)
      return
      end
```

Appendix III

Fusion Model Calculations

Those whom God has joined together,
Let no man put asunder.

Marriage Service

III .1 Introduction

In this appendix we give details of the fusion calculations presented in section 6.2. Here we concentrate more on how the calculations were carried out than on the physics deduced from them, which is discussed in that section. We consider each type of calculation in turn, starting with those using the extra push model [13] in section III.2. The critical distance [5] and statistical yrast [6] model calculations are discussed in sections III.3 and III.4 respectively. Many equations used in these calculations appear elsewhere in this thesis. However, for clarity, they are repeated here. All calculations discussed were performed using the standard model parameters, without any fitting. The values of these parameters are listed in table III.1.

Model	Parameter	^{40}Ca + ^{40}Ca	^{28}Si + ^{50}Cr
Extra Push	V_B	55.5	46.9
	R_B	9.62	9.58
	V_C	44.7	35.5
	R_C	7.93	7.80
Critical Distance	V_B	54.8	42.9
	R_B	9.70	10.2
	V_C	31.6	16.0
	R_C	7.12	6.56
Statistical Yrast	V_{II}	24.7	17.5
	R_{II}	6.36	6.67
	V_{III}	70.7	77.9
	R_{III}	4.55	4.53

Table III .1 Parameters used in the fusion calculations. All potentials are in MeV and all radii are in fm. Each parameter is explained in the discussion of the appropriate model.

III .2 Extra Push Model

The interaction potential between two nuclei may be written

$$V_l(r) = \frac{Z_1 Z_2 e^2}{r} + \frac{l(l+1)\hbar^2}{2\mu r^2} - V_N(r) \qquad (III.1)$$

where $V_N(r)$ is the nuclear potential. The proximity potential of Ngô [2] was used for these calculations. This has the form

$$V_N(r) = \frac{C_1 C_2}{C_1 + C_2} U_N(s) \qquad (III.2)$$

where $C_i = R_i \left[1 - R_i^{-2}\right]$ (with $R_i = 1.16 A_i^{1/3}$ fm), $s = r - C_1 - C_2$ and the function $U_N(s)$ is given by

$$U_N(s) = \begin{cases} 34 \exp\left[-\frac{(s-s_0)^2}{5.4}\right] \text{ MeV}, & \text{if } s > s_0 = -1.6 \text{ fm} \\ 34 + 5.4\,(s - s_0)^2 \text{ MeV}, & \text{otherwise.} \end{cases} \qquad (III.3)$$

The fusion cross section at low energy (σ_{fus}) is given by the expression (see section 2.3 for discussion)

$$\sigma_{fus} = \pi R_B^2 \left[1 - \frac{V_B}{E_{cm}}\right] \qquad (III.4)$$

where E_{cm} is the centre of mass energy. The fusion barrier height (V_B) and radius (R_B) are determined for $l = 0$. The results of these calculations are shown by the solid lines in figures 6.1 and 6.2.

The fusion cross sections in the extra push region can be obtained just by equating the bombarding energy to the sum of nuclear, Coulomb, tangential and radial energies at the point where the nuclear surfaces come into contact. This gives the expression [79]

$$\sigma_{fus} = \frac{\pi R_C^2}{E_{cm}} \left[\sqrt{\left(\frac{\alpha\beta + \frac{1}{2}}{\beta^2}\right)^2 - \left(\frac{\alpha^2 + V_C - E_{cm}}{\beta^2}\right)} - \left(\frac{\alpha\beta + \frac{1}{2}}{\beta^2}\right) \right] \qquad (III.5)$$

where R_C is the centre separation at contact (i.e. $s = 0$) and the parameters α and β are coefficients describing the extra push energy. The predictions of equation III.5 are shown by the dot-dashed lines in figures 6.1 and 6.2.

The angular momenta for which the fission barrier is zero and for which it is equal to the neutron binding energy can be calculated using the liquid drop model [9]. For each of these angular momentum values the classical impact parameter was determined and used to calculate the associated cross section. This gives the relation

$$\sigma \propto \frac{l^2}{E_{cm}} \qquad (III.6)$$

where l is the angular momentum of interest. These calculations are also shown in figures 6.1 and 6.2.

III .3 Critical Distance Model

The method described in the first half of the previous section was used to calculate fusion cross sections in the low energy regime, the only difference being the utilization of a different nuclear potential. The potential due to Bass [80] was used:

$$V_N(r) = \frac{R_1 R_2}{R_1 + R_2} g(s) \qquad (III.7)$$

where $s = r - R_1 - R_2$, $g(s)$ is given by

$$g(s) = \left[0.0300 \exp\left(\frac{s}{3.3}\right) + 0.0061 \exp\left(\frac{s}{0.65}\right)\right]^{-1} \qquad (III.8)$$

s is the surface separation in fm and

$$R_i = 1.16 A_i^{\frac{1}{3}} - 1.39 A_i^{-\frac{1}{3}} \text{ fm} \qquad (III.9)$$

The cross section in the higher energy regime is given by the expression

$$\sigma_{fus} = \pi R_C^2 \left[1 - \frac{V_C}{E_{cm}}\right] \qquad (III.10)$$

where $R_C = R_1 + R_2$ and V_C is the sum of Coulomb and nuclear potentials at this point. The critical distance model calculation for ^{40}Ca + ^{40}Ca is shown by the solid line in figure 6.3.

III .4 Statistical Yrast Model

In these calculations the fusion cross sections for the low energy regime were determined exactly as in the critical distance model analysis.

The higher energy region is described by the need to form the compound nucleus at an energy ΔQ above the yrast line. Hence,

$$E^* = E_{cm} + Q = \frac{\hbar^2 l_{cr}(l_{cr}+1)}{2J} + \Delta Q \qquad (III.11)$$

where Q is the reaction Q-value, l_{cr} the angular momentum and J the moment of inertia of the compound nucleus. This leads to the expression

$$\sigma_{fus} = \frac{\pi J}{\mu}\left[1 + \frac{Q - \Delta Q}{E_{cm}}\right] \qquad (III.12)$$

where μ is the reduced mass and ΔQ is given the value 10 MeV. In table III.1 the quantity $V_{II} = \Delta Q - Q$ and $R_{II} = \sqrt{J/\mu}$.

There is a third regime in this model known as the fusion entry line. It is assumed the nuclei have to reach a critical distance (R_{III}) in order to fuse at very high energies. This distance is given by

$$A < r^2 >_A = A_1 < r^2 >_{A_1} + A_2 < r^2 >_{A_2} + \frac{A_1 A_2}{A} R_{III}^2 \qquad (III.13)$$

where

$$< r^2 >_{A_i} = \frac{3}{5}\left(1.12 A_i^{\frac{1}{3}}\right)^2 \left(1 + 3.84 A_i^{-\frac{2}{3}}\right) \qquad (III.14)$$

A_1 and A_2 are masses of target and projectile and A is the mass of the compound nucleus. In this region

$$\sigma_{fus} = \pi R_{III}^2 \left[1 + \frac{V_{III}}{E_{cm}}\right] \qquad (III.15)$$

where V_{III} is the sum of Coulomb and nuclear potentials at the critical distance, calculated within the framework of the model. The statistical yrast model prediction for ^{40}Ca + ^{40}Ca is shown by the dotted line in figure 6.3.

Appendix IV

Glossary of Terms

We dance round in a ring and suppose,
But the Secret sits in the middle and knows.

Robert Frost

IV .1 Introduction

There now follows a brief glossary of terms used in this thesis and which may be encountered in the literature. This list is not meant to be comprehensive, neither is it intended that the descriptions given are definitive. The objective is purely to explain the meanings given to these terms as used in this thesis. For instance, the definition of fusion is presented in the context of a heavy ion reaction and not in the more general sense. Some terms, such as fast-fission, are given slightly different meanings by different authors. However, throughout this thesis the definitions taken are those presented in this glossary.

IV .2 Glossary

Businaro-Gallone saddle point

For a given compound nucleus, the conditional saddle point which has the maximum potential energy is called the Businaro-Gallone saddle point.

Businaro-Gallone transition

Light nuclei tend to fission asymmetrically, while heavy nuclei usually fission symmetrically. The change from from one regime to the other takes place at the Businaro-Gallone transition.

Compound nucleus formation

Population of a state in the compound nucleus in a heavy ion collision. For compound nucleus formation to occur, the system must fuse.

Conditional saddle point

The saddle point of the compound nucleus whose asymmetry is equal to that of the entrance channel. For fusion to happen, the system must penetrate inside the conditional saddle point.

Critical angular momentum

The maximum partial wave to fuse. This is not necessarily equal to the maximum angular momentum of the compound nucleus, and will not be if processes such as fast-fission are dominant.

Deep-inelastic reaction

A heavy ion reaction, in which large large amounts of mass may be transferred and much energy of relative motion may be dissipated, but a fused system is not formed.

Dolichohodous

This means having a long mean free path. It is assumed that the nucleons within a nucleus are dolichohodous.

Extra push

The extra amount of radial energy needed to overcome the conditional saddle point, a process which leads to fusion, but not necessarily compound nucleus formation.

Extra-extra push

The extra amount of radial energy to form a compound nucleus, i.e. to surmount the unconditional saddle point.

Fast-fission

A state is populated inside the fusion barrier, however the compound nucleus has no stable configuration, and hence cannot be formed. Its fission barrier is zero.

Fission

Fragmentation of a compound nucleus into two (or possibly more) heavy fragments, where 'heavy' signifies a particle of greater mass than the α-particle.

Fully relaxed

In a heavy ion collision, when a collective degree of freedom (e.g. kinetic energy) has reached full equilibrium it is said to be fully relaxed. This is equivalent to fully damped.

Fusion

Population of a bound state inside the interaction barrier during a heavy ion collision. This may, but does not necessarily, lead to compound nucleus formation.

Intermediate mechanism

Any reaction process intermediate between fusion-fission and deep-inelastic scattering. Examples include fast-fission and quasi-fission.

Leptodermous

This means thin skinned. In the RLDM it is assumed that the surface diffuseness of the nucleus is small relative to its size and hence that the nucleus is leptodermous.

Orbiting

A long-lived deep-inelastic reaction in which the collision partners rotate through a large angle while in contact. Such a process may have the fully relaxed Q-value and may have an angular distribution which approaches $1/\sin\theta_{cm}$, however mass distributions for orbiting display an entrance channel dependence.

Quasi-fission

The system forms a state within the conditional saddle point. However, a compound nucleus may not be formed, as the unconditional saddle point is more compact than the fused system, and so an extra-extra push is needed to form a stable compound nucleus.

Saddle point

This is a maximum point on the potential energy surface of a nucleus which is unstable with respect to the fission degree of freedom. Thus once the saddle point is exceeded the nucleus fissions.

Strongly damped

A collective degree of freedom is said to be strongly damped when it is partially equilibrated during a heavy ion collision.

Unconditional saddle point

The true saddle point of the compound nucleus, equivalent to the lowest energy conditional saddle point. For a compound nucleus to be formed the system should populate a state inside the unconditional saddle point.

References

[1] . W. J. Swiatecki,
Prog. Part. Nucl. Phys. **4** (1980) 383.

[2] . C. Ngô,
in *Proc. Int. Conf. Nucl. Phys.*, Florence, Vol. 2
(ed. P. Blasi and R. A. Ricci), Tipografia, Bologna (1983) 321.

[3] . W. U. Schröder and J. R. Huizenga,
in *Treatise on Heavy-Ion Science*, Vol. 2
(ed. D. A. Bromley), Plenum, New York (1985) Ch. 3.

[4] . A. J. Sierk,
in *Proc. Int. Symp.*
"The Many Facets of Heavy-Ion Fusion Reactions",
Argonne (1986) 135.

[5] . D. Glas and U. Mosel,
Nucl. Phys. **A237** (1975) 429.

[6] . S. M. Lee, T. Matsuse and A. Arima,
Phys. Rev. Lett. **45** (1980) 165.

T. Matsuse, A. Arima and S. M. Lee,
Phys. Rev. **C26** (1982) 2338.

[7] . R. G. Stokstad,
in *Treatise on Heavy-Ion Science*, Vol. 3
(ed. D. A. Bromley), Plenum, New York (1985) Ch. 2.

[8] . R. Vandenbosch and J. R. Huizenga,
Nuclear Fission, Academic Press, New York (1973).

[9] . S. Cohen, F. Plasil and W. J. Swiatecki,
Ann. Phys. (N.Y.) **82** (1974) 557.

[10] . V. E. Viola, K. Kwiatkowski and M. Walker,
Phys. Rev. **C31** (1985) 1550.

[11] . A. Gobbi and W. Nörenberg,
in *Heavy Ion Collisions*, Vol. 2
(ed. R. Bock), North Holland, Amsterdam (1980) Ch. 3.

[12] . J. R. Birkelund, L. E. Tubbs, J. R. Huizenga,
J. N. De and D. Sperber,
Phys. Rep. **56** (1979) 107.

[13] . W. J. Swiatecki,
Nucl. Phys, **A376** (1982) 275.

[14] . C. Ngô, C. Grégoire, B. Remaud and E. Tomasi,
Nucl. Phys. **A400** (1983) 259.

[15] . B. B. Back, R. R. Betts, K. Cassidy, B. G. Glagola, J. E. Gindler,
L. E. Glendenin, B. D. Wilkins,
Phys. Rev. Lett. **50** (1983) 818.

[16] . A. Gavron, P. Eskola, A. J. Sierk, J. Boissevain, H. C. Britt,
K. Eskola, M. M. Fowler, H. Ohm, J. B. Wilhelmy,
S. Wald and R. L. Ferguson,
Phys. Rev. Lett. **52** (1984) 589.

[17] . J. Barrette, P. Braun-Munzinger, C. K. Gelbke, H. E. Wegner,
B. Zeidman, A. Gamp, H. L. Harney and Th. Walcher,
Nucl. Phys. **A279** (1977) 125.

C. K. Gelbke, P. Braun-Munzinger, J. Barrette, B. Zeidman,
M. J. LeVine, A. Gamp, H. L. Harney and Th. Walcher,
Nucl. Phys. **A269** (1976) 460.

[18] . H. Oeschler, P. Wagner, J. P. Coffin, P. Engelstein and B. Heusch,
Phys. Lett. **87B** (1979) 193.

[19] . G. Guillaume, J. P. Coffin, F. Rami, P.Engelstein, B. Heusch,
P. Wagner, P. Fintz, J. Barrette and H. E. Wegner,
Phys. Rev. **C26** (1982) 2458.

[20] . J. P. Coffin, G. Guillaume, A. Fahli, F. Rami, B. Heusch, P. Wagner, P. Engelstein, P. Fintz and N. Cindro, *Phys. Rev.* **C30** (1984) 539.

[21] . S. Agnoli, I. Massa, G. Vannini, P.Boccaccio, F. Reffo, L. Vannucci, I. Iori and R. A. Ricci, *Nucl. Phys.* **A464** (1987) 103.

[22] . R. Ricci, *Prog. Part. Nucl. Phys.* **15** (1985) 187.

[23] . Yu. Ts. Oganessian and Yu. A. Lazarev, in *Treatise on Heavy-Ion Science*, Vol. 4 (ed. D. A. Bromley), Plenum, New York (1985) Ch. 1.

[24] . K. Thomas, R. Davies and A. J. Sierk, *Phys. Rev.* **C31** (1985) 915.

[25] . U. L. Businaro and S. Gallone, *Nuovo Cimento* **1** (1955) 629, and **1** (1955) 1277.

[26] . M. G. Mustafa, P. A. Baisden and H. Chandra, *Phys. Rev.* **C25** (1982) 2525.

[27] . H. J. Krappe, J. R. Nix and A. J. Sierk, *Phys. Rev.* **C20** (1979) 992.

[28] . L. G. Sobotka, M. A. McMahan, R. J. McDonald, C. Signarbieux, G. J. Wozniak, M. L. Padgett, J. H. Gu, Z. H. Liu, Z. Q. Yao and L. G. Moretto, *Phys. Rev. Lett.* **53** (1984) 2004.

[29] . S. M. Lee, W. Yokota, T. Matsuse, in *Proc. Int. Symp. "The Many Facets of Heavy-Ion Fusion Reactions"*, Argonne (1986) 63.

[30] . V. Metag, D. Habs and H. J. Specht, *Phys. Rep.* **65** (1980) 1.

[31] . V. M. Strutinsky,
Nucl. Phys. **A95** (1967) 420.

[32] . R. K. Bhaduri and C. K. Ross,
Phys. Rev. Lett. **27** (1971) 606.

[33] . W. Nazarewicz, J. Dudek, R. Bengtsson,
T. Bengtsson and I. Ragnarsson,
Nucl. Phys. **A435** (1985) 397.

[34] . W. E. Burcham,
Elements of Nuclear Physics, Longman, London (1987) 76.

[35] . H. Pleyer, B. Kohlmeyer, W. F. W. Schneider and R. Bock,
Nucl. Instr. Meth. **96** (1971) 263.

[36] . H. O. Neidel and H. Henschel,
Nucl. Instr. Meth. **178** (1980) 137.

[37] . G. Gabor, W. Schimmerling, D. Greiner,
F. Beiser and P. Lindstrom,
Nucl. Instr. Meth. **130** (1975) 65.

[38] . H. Stelzer,
Nucl. Instr. Meth. **133** (1976) 409.

[39] . A. Breskin,
in *Lecture Notes in Physics* **178**
(ed. W. von Oertzen), Springer-Verlag, Berlin (1982) 44.

[40] . J. P. Coffin and P. Engelstein,
in *Treatise on Heavy-Ion Science*, Vol. 7
(ed. D. A. Bromley), Plenum, New York (1985) Ch. 7.

[41] . P. A. LeBas,
D. Phil thesis, Oxford, 1984 (unpublished).

[42] . W. W. M. Allison and P. A. LeBas,
computer program *FISH*, Oxford, 1981 (unpublished).

[43] . S. J. Sanders, R. R. Betts, I. Ahmed, K. T. Lesko, S. Saini, B. D. Wilkins, F. Videbaek and B. K. Dichter, *Phys. Rev.* **C34** (1986) 1746.

[44] . H. Stelzer, in *Lecture Notes in Physics* **178** (ed. W. von Oertzen), Springer-Verlag, Berlin (1982) 25.

[45] . M. F. Vineyard, B. D. Wilkins, D. J. Henderson, D. G. Kovar, C. Beck C. N. Davids and J. J. Kolata, *Nucl. Instr. Meth.* **A255** (1987) 507.

[46] . B. D. Wilkins, D. J. Henderson, D. G. Kovar, C. Beck, B. G. Glagola and T. F. Wang, Argonne National Laboratory Report No. ANL-87-13, 1987, 155 (unpublished).

[47] . F. Pühlhofer, *Nucl. Phys.* **A280** (1977) 267.

[48] . B. Cooke and D. Sinclair, computer program *GENDAT*, Oxford, 1978 (unpublished).

[49] . L. C. Northcliffe and R. F. Schilling, *Nuclear Data Tables* **A7** (1970) 233.

[50] . J. F. Ziegler, *Handbook of Stopping Cross-Sections for Energetic Ions in All Elements, Vol. 5 of The Stopping and Ranges of Ions in Matter*, Pergamon Press, New York (1980).

[51] . A. J. Sierk, *Phys. Rev.* **C33** (1986) 2039.

[52] . J. Gomez del Campo, R. G. Stokstad, J. A. Biggerstaff, R. A. Dayras, A. H. Snell and P. H. Nelson, *Phys. Rev.* **C19** (1979) 2170.

[53] . J. R. Nix, *Nucl. Phys.* **A130** (1969) 241.

[54] . J. R. Nix and W. J. Swiatecki,
Nucl. Phys. **71** (1965) 1.

[55] . H. Doubré, A. Gamp, J. C. Jacmart,
N. Poffé, J. C. Roynette and J. Wilczyński,
Phys. Lett. **73B** (1978) 135.

[56] . E. Tomasi, D. Ardouin, J. Barreto, V. Bernard, B. Cauvin,
C. Magnago, C. Mazur, C. Ngô, E. Piasecki and M. Ribrag,
Nucl. Phys. **A373** (1982) 341.

[57] . W. Hauser and H. Feshbach,
Phys. Rev. **87** (1952) 366.

[58] . T. D. Thomas,
Nucl. Phys. **53** (1964) 558.

[59] . D. Wilmore and P. E. Hodgson,
Nucl. Phys. **55** (1964) 673.

F. G. Perey,
Phys. Rev. **131** (1963) 745.

[60] . W. Dilg, W. Schantl, H. Vonach and M. Uhl,
Nucl. Phys. **A217** (1973) 269.

[61] . S. J. Sanders,
private communication (1988).

[62] . J. Gomez del Campo,
in *Proc. Int. Symp.*
Heavy Ion Physics from 10 to 200 MeV/amu,
Brookhaven National Laboratory, 1979,
(eds. J. Barrette and P. D. Bond), BNL-51115, **1** (1979) 93.

[63] . A. H. Wapstra and K. Bos,
At. Data Nucl. Data Tables **19** (1977) 175.

[64] . H. T. Feldmeier,
Argonne National Laboratory Report No. ANL-PHY-85-2,
1985 (unpublished).

[65] . J. Blocki, M. Dworzecka, F. Beck and H. T. Feldmeier,
Phys. Lett. **99B** (1981) 13.

[66] . F. Beck, J. Blocki, M. Dworzecka and G. Wolschin,
Phys. Lett. **76B** (1978) 35.

[67] . S. Ayik and Nörenberg,
Z. Physik **A288** (1978) 401.

[68] . S. J. Sanders, D. G. Kovar, B. B. Back, C. Beck,
B. K. Dichter, D. J. Henderson, R. V. F. Janssens, J. G. Keller,
S .Kaufman, T. F. Wang, B. D. Wilkins and F. Videbaek,
Phys. Rev. Lett. **59** (1987) 2856.

[69] . J. Bisplinghoff, P. David, M. Blann, W. Scobel,
T. Mayer-Kuckuk, J. Ernst and A. Mignerey,
Phys. Rev. **C17** (1978) 177.

[70] . J. B. Natowitz, M. N. Namboodiri and E. T. Chulick,
Phys. Rev. **C13** (1976) 171.

[71] . A. E. S. Green,
Nuclear Physics, McGraw-Hill, New York (1955) pp. 185, 250.

[72] . M. Blann and T. T. Komoto,
Phys. Rev. **C26** (1982) 472.

[73] . K. J. LeCouteur and D. W. Lang,
Nucl. Phys. **13** (1959) 32.

[74] . W. D. Myers and W. J. Swiatecki,
Nucl. Phys. **81** (1966) 1.

[75] . R. Bock, Y. T. Chu, M.Dakowski, A. Gobbi, E. Grosse,
A. Olmi, H. Sann, D. Schwalm, U. Lynen, W. Müller,
S. Bjørnholm, H. Esbensen, W. Wölfi and E. Morenzoni,
Nucl. Phys. **A388** (1982) 334.

[76] . U. Mosel,
in *Proc. 2nd Europhysics Study Conf. Dynamics of Heavy Ion Collisions*,
Hvar, 1981, (eds. N. Cindro, R. A. Ricci and W. Greiner),
North Holland (1981) 1.

[77] . S. B. Kaufman, E. P. Steinberg, B. D. Wilkins,
J. Unik, A. J. Gorski and M. J. Fluss,
Nucl. Inst. Meth. **115** (1974) 47.

[78] . W. Bohne, W. Galster, K. Gradisch and H. Morgenstern,
Nucl. Inst. Meth. **A240** (1985) 145.

[79] . S. Bjørnholm and W. J. Swiatecki,
Nucl. Phys. **A391** (1982) 471.

[80] . R . Bass,
Nuclear Reactions with Heavy Ions,
Springer-Verlag, Berlin (1980) 331.